18 April 2014 | $10

Science

A Wink in the Sky

AAAS

Patchy Insulation

Myelin insulates neuronal axons such that their electrical signals travel faster and more efficiently. However, not all axons are myelinated equally. **Tomassy *et al.*** (p. 319; see the Perspective by **Fields**) obtained detailed images from two snippets of the adult mouse brain and generated three-dimensional reconstructions of individual neurons and their myelination patterns. The images show that some axons have long, unmyelinated stretches, which might offer sites for building new connections. Thus, myelination is not an all-or-none phenomenon but rather is a characteristic of what may be a specific dialogue between the neuron and the surrounding myelin-producing cells.

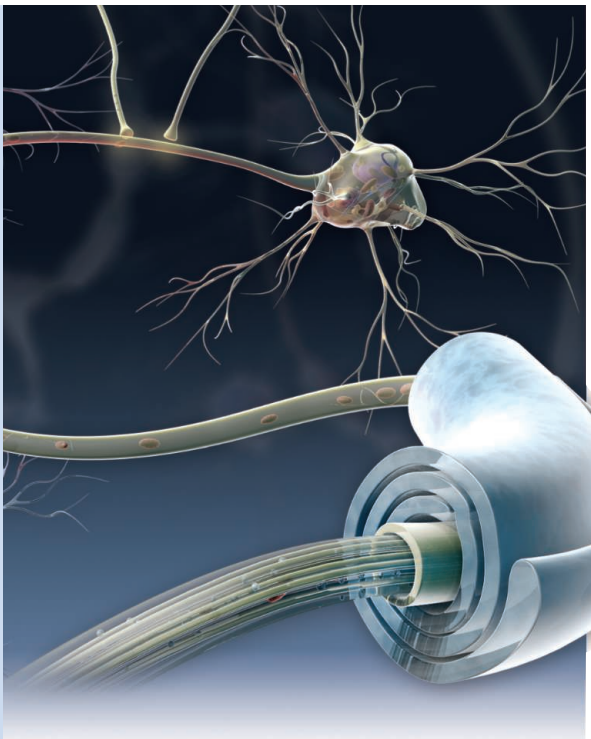

Sleep Tight, Fly

Shortly after eclosion, young flies sleep a lot and are resistant to being woken. Several days later, the same flies sleep less and are more easily woken. **Kayser *et al.*** (p. 269) show that the different sleep pattern characteristic of youthful flies is critical to correct development of their brains. When sleep is disrupted in young flies, dopaminergic signaling is also disturbed and a glomerulus in the courtship behavior circuit does not develop properly, leading to inadequate courtship behavior and failure to reproduce.

Smoothing Graphene

Several methods have been reported for the growth of monolayer graphene into areas large enough for integration into silicon electronics. However, the electronic properties of the graphene are often degraded by grain boundaries and wrinkles. **Lee *et al.*** (p. 286, published online 3 April) showed that flat, single crystals of monolayer graphene can be grown by chemical-vapor deposition on silicon wafers covered by a germanium layer that aligns the grains. The graphene can be dry-transferred to other substrates, and the germanium layer can be reused for further growth cycles.

On a Zeppelin

Nitrous acid (HONO) is an important atmospheric trace gas that acts as a precursor of tropospheric hydroxyl-radicals (OH), which is responsible for the self-cleansing capacity of the atmosphere and which also controls the concentrations of greenhouse gases, such as methane and ozone. How HONO is made is a mystery. Flying onboard a Zeppelin over the Po Valley in Northern Italy, **Li *et al.*** (p. 292) discovered HONO in the undisturbed morning troposphere, indicating that HONO must be produced there, rather than mixed from the surface. The high HONO concentrations are likely to have been formed by a light-dependent gas-phase source that probably consumed OH or HO_2 radicals, which hints that the impact of HONO on the abundance of OH in the entire troposphere may be substantially overestimated.

Starry Brightness

The high photometric precision of NASA's Kepler observatory has enabled the detection of many planets because they cause slight dimming of their host stars as they orbit in front of them. From these data, **Quintana *et al.*** (p. 277) have spotted a five-planet system around a small star. Here, the outermost planet is only 10% larger than Earth and completes its 130-day orbit entirely within the habitable zone, where liquid water could exist on its surface. Similarly, Kepler can detect faint periodic brightenings, as **Kruse and Agol** (p. 275) have reported for the binary system KOI-3278. In this system, a white dwarf acts as a gravitational microlens when it passes in front of its Sun-like G-star companion every 88 days. The lensing effect allows the mass of the white dwarf to be estimated, which helps us to understand how similar binary systems may have evolved.

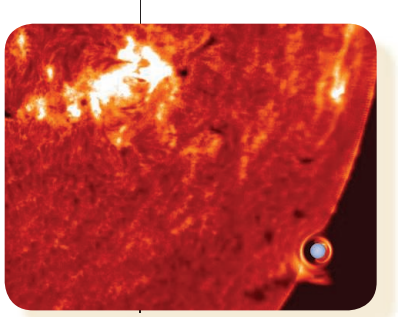

Changing Assemblages

Although the rate of species extinction has increased markedly as a result of human activity across the biosphere, conservation has focused on endangered species rather than on shifts in assemblages. **Dornelas *et al.*** (p. 296; see the Perspective by **Pandolfi and Lovelock**), using an extensive set of biodiversity time series of species occurrences in both marine and terrestrial habitats from the past 150 years, find species turnover above expected but do not find evidence of systematic biodiversity loss. This result could be caused by homogenization of species assemblages by invasive species, shifting distributions induced by climate change, and asynchronous change across the planet. All of which indicates that it is time to review conservation priorities.

Resilient Hyperpolarization

Despite constant exposure to all sorts of stressors, most people are resilient and do not develop depression, but we do not understand the neurophysiological underpinnings of stress resilience. **Friedman *et al.*** (p. 313) studied this phenomenon in a mouse model of social-defeat stress depression. In the mice they found that, despite apparently pathological levels of hyperpolarization and elevated potassium channel currents in the ventral tegmental area (a structure known to be involved in depression), resilient mice showed normal activity in dopaminergic neurons. Thus, if "depressed" mice were experimentally provoked into hyperpolarization—unexpectedly, they completely reversed depression-related behaviors.

CREDITS (TOP TO BOTTOM): CHRISTOPHER BICKEL; ERIC AGOL, NASA/SDO/HMI

Additional summaries

Hope for SUSY?

Supersymmetry (SUSY), the symmetry between fermions, particles that form matter, and bosons, which mediate the interactions between them, has been proposed as one of the more likely extensions of the Standard Model of particle physics; however, it has so far received little experimental support. Condensed matter systems, such as the superfluid helium-3, may save the concept. In preparation for experimentation, **Grover *et al.*** (p. 280, published online 3 April) develop a theoretical approach that suggests SUSY describes the quantum phase transition on the boundary of a topological superconductor between a magnetic phase characterized by a bosonic order parameter and a neighboring phase hosting Majorana fermions.

Strained Superconductor

Distorting a material and observing its response can allow insight into its electronic properties. Thin films can be strained by placing them on a substrate with a different lattice constant; bulk samples present more of a challenge. **Hicks *et al.*** (p. 283) designed an apparatus to apply both tensile and compressive strain and used it to study the properties of the superconductor Sr_2RuO_4, which has long been hypothesized to host the unusual p-wave superconductivity. The response of the superconducting transition temperature T_c to the applied strain depended on the direction in which the strain was applied, and did not exhibit a cusp predicted to occur around zero strain. As the technique leaves a surface of the probe open to external probes, it could be adopted for a wide range of methods.

Thin and Selective Outpourings

When using a membrane to separate materials, the efficiency of the separation is limited by how fast the gas or liquid passes through the membrane and by how selective it is. Thinner membranes usually allow for faster flow rates but are usually less selective. Attempting to maintain selectivity, **Celebi *et al.*** (p. 289) developed a sophisticated way to drill holes of controlled diameter in a graphene sheet about two layers thick. For such a thin membrane, the primary barriers to separation come from entrance and exit from the holes and not from the motion through the membrane.

How Tight?

In metazoans, sheets of epithelial cells separate different tissue spaces and control their composition. Tight junctions are cell-cell adhesion structures in these cell sheets that form a seal between cells but also provide some selective permeability to ions and small molecules. Claudins are the main constituents of tight junctions, and mutations in claudins cause inherited human disorders involving the disruption of ionic balance. **Suzuki *et al.*** (p. 304) report the structure of mouse claudin-15 at 2.4 angstrom resolution, which shows an extracellular β-sheet domain anchored to a transmembrane four-helix bundle. The electrostatic distribution on the claudin surface reveals a negatively charged groove in the extracellular domain that may provide a pathway for positive ions.

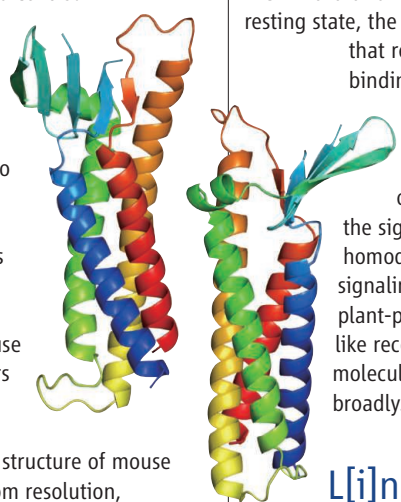

CREDIT: SUZUKI *ET AL.*

Resisting the Chop

Dengue, West Nile, and Yellow Fever viruses are all flaviviruses that have single-stranded RNA genomes and form specific, short flaviviral RNAs (sfRNAs) during infection that cause viral pathogenicity. These sfRNAs are produced by the incomplete degradation of viral RNA by the host-cell exonuclease Xrn1. What stops the host enzyme from completely chopping up the viral RNA? **Chapman *et al.*** (p. 307) reveal a pseudoknot in the structure of the Xrn1-resistant segment of a sfRNA from Murray Valley Encephalitis Virus, which, perhaps, the host Xrn1 exonuclease cannot untangle.

Universal Immune Function

Certain pathogen effectors are detected in plants by cytoplasmic receptors. First solving the crystal structures of *Arabidopsis* receptors, **Williams *et al.*** (p. 299; see the Perspective by **Nishimura and Dangl**) discovered that in the resting state, the structures form a heterodimer that readies the complex for effector binding and keeps the signaling domains from firing too early. Once the pathogen effector binds, the structure of the complex shifts such that the signaling domains can form a homodimer to initiate downstream signaling. Similarities between these plant-pathogen receptors and Toll-like receptors in animals suggest the molecular mechanisms may translate broadly.

L[i]nc to Dendritic Cell Activation

Long noncoding RNAs (lncRNAs) are important regulators of gene expression, but whether they are important regulators of the immune system is poorly understood. **Wang *et al.*** (p. 310) identify a lncRNA expressed exclusively in human dendritic cells (DC), called lnc-DC, that is required for optimal DC differentiation from human monocytes and that regulates DC activation of T cells. Lnc-DC interacts with the transcription factor STAT3, which is also required for DC development and function, to prevent interaction with and to block dephosphorylation by tyrosine phosphatase SHP1.

Published by AAAS

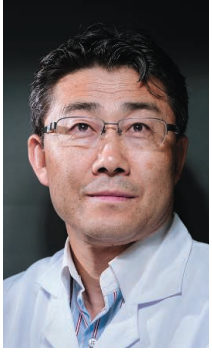

George F. Gao is director of the CAS Key Laboratory of Pathogenic Microbiology and Immunology at the Institute for Microbiology of the Chinese Academy of Sciences, Beijing; vice president of the Beijing Institutes of Life Science, Beijing; president of the Chinese Society for Virology, Beijing; and deputy director general of the Chinese Center for Disease Control and Prevention, Beijing. E-mail: gaof@im.ac.cn

Influenza and the Live Poultry Trade

LIVE POULTRY TRADE AT LOCAL MARKETS HAS LONG BEEN A PART OF CHINA'S NATIONAL IDENTITY. From small villages to big cities, the gathering and selling of different birds in this vibrant atmosphere is at the heart of the country's cuisine culture. Unfortunately, the backdrop to this tradition has changed. Last year, the H7N9 virus, a new strain of influenza A, jumped from birds to humans, causing 144 cases of human infection and 47 deaths in China. Now a second wave of this flu is coursing through the country, with 258 confirmed cases and 99 deaths as of 8 April 2014. Scientific evidence points to a connection between the conditions at these live markets and the spread of flu, suggesting that until other means are found to prevent the transmission of or effectively treat the illness, China must shut down live poultry markets to prevent further spread of the virus and a possible global pandemic.

Early in 2013, the Chinese Center for Disease Control and Prevention and several prominent Chinese research groups quickly identified H7N9 as the causative agent of the emerging flu. The source of the virus was immediately traced to live poultry markets. With a call for an immediate shutdown of these markets in major cities, including Hangzhou and Shanghai (where the first H7N9 human infection cases were found), the government quickly controlled the spread of the virus. But the government deemed long-term closure to be economically unviable, and the markets reopened soon after the summer. At the beginning of the new flu season in October, the virus bounced back in the eastern Yangtze River delta region. This year, it has spread to the Canton region (Guangdong province) in China, which is alarming because live poultry markets are commonplace there.

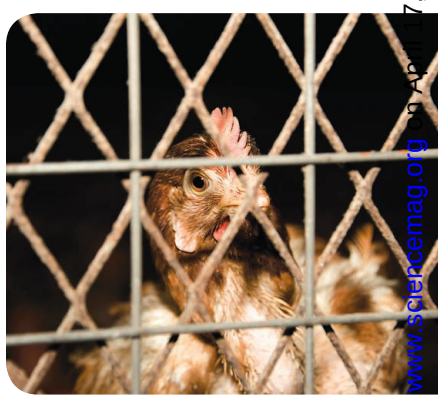

Approximately 87% of the people infected with H7N9 had close contact with live poultry or exposure to a contaminated environment such as the poultry markets, where the virus can spread quickly through birds. Poultry transportation between provinces is probably playing an important role in its spread across China. Although it is generally believed that H7N9 has not developed human-to-human transmissibility, the possibility cannot be excluded. There has been limited unsustained human-to-human transmission in several case clusters. Genomic analysis of the isolated viruses reveals that divergent strains exist and that the virus is not yet "fixed" in its identity and character. H7N9 has yet to adapt to humans by mixing its viral genes with those of a human-specific influenza virus. This can happen if a single host (a human or bird, for example) is infected by both an avian and a human virus. Such genomic reassortment generated the pandemic flu strains in 1918 and 2009, which killed 20 to 40 million and 250,000 people, respectively, worldwide. The risk of this occurring is precisely why the shutdown of live poultry markets is needed to avoid potential reassortments.

But H7N9 is not the only problem. Two new subtypes of influenza A virus have been isolated in humans: H6N1 in Taiwan and H10N8 in mainland China. Both have a clear poultry origin and are found in live poultry markets. Six genes of H10N8 are derived from H9N2, an avian influenza virus that is common in live poultry markets but has infected humans as well. Avian H7N9 and H9N2 coexist in chickens.That means that at any time, their genomes could mix and give rise to a potentially more virulent strain that infects humans.

The birds in live poultry markets are incubators for new subtypes of influenza virus, and the continuation of this culture is worrisome. It is simply not enough to implement regular birdcage disinfection measures and the killing of unsold birds every evening. Curtailing poultry transportation is even more difficult than shutting down markets. H7N9 is avirulent to poultry, so it is difficult to identify virus-carrying birds. Unless the government closes these markets, there is ample opportunity for the rise of a global and devastating pandemic.

– George F. Gao

10.1126/science.1254664

EDITED BY JESSE SMITH AND KRISTEN MUELLER

ECOLOGY

It's All in the Timing

Phenology is the timing of biological events, such as the time of year when flowers bloom. Because phenology is dependent on environmental cues, including temperature, how it is affected by climate change is unclear. Understanding this connection is challenging, however, due to natural variation in events such as flowering time. CaraDonna *et al*. report on the results of a 39-year effort to record a suite of ecological data, such as first, peak, and last flowering dates, within an alpine meadow community in the Colorado Rocky Mountains. Over the time span of the experiment, data were collected on 60 plant species, largely every other day during the growing season. Although there was a general trend toward earlier flowering dates and a longer growing season, individual species' responses were distinct, and changes within a species in first, peak, and last flowering dates shifted independently of one other. These results suggest that first flowering date, the most commonly collected phenological metric in plants, is not necessarily an accurate estimator of total responses to a changing climate. Furthermore, changes in coflowering patterns were observed, which indicates that even small changes in timing could alter alpine plant communities. — SNV

Proc. Natl. Acad. Sci. U.S.A. **111**, 10.1073/pnas.1323073111 (2014).

IMMUNOLOGY

Dead But Not Dangerous

How the innate immune system senses and responds to dead cells and how non-infectious inflammatory responses are controlled remain unclear. Neumann *et al.* identified an inhibitory C-type lectin receptor, Clec12a, as a specific immune receptor for dead cells. Both human and mouse Clec12a acted as direct sensors for uric acid crystals, which are key "danger" signals that alert the immune system to cell death. Dead cells or uric acid crystals triggered Clec12a signaling. Clec12a-deficient mice exhibited hyperinflammatory responses to uric acid crystals or sterile dead cell challenges in vivo. Thus, Clec12a represents a regulatory immune receptor that dampens the inflammatory immune response to dead cells. By doing so, it may help to minimize potential damage during non-infectious inflammation. — SMH

Immunity **40,** 389 (2014).

CELL BIOLOGY

Seeing Signaling

A classic model for the study of cell signaling is the bacterial chemotaxis system. Fukuoka *et al*. describe the latest step in "seeing" just how this simple yet elegant mechanism really works. The basics of the system are known. Receptors on the cell surface bind attractant or repellent molecules, and this leads to alterations in the phosphorylation of a regulatory protein known as CheY. CheY in turn interacts with the molecular motor of the flagellum, altering its direction of rotation. Bacteria were engineered to express CheY protein that was fluorescently tagged. This enabled the use of total internal reflection fluorescence microscopy to monitor the interaction of CheY with the flagellar motor in single bacterial cells, while at the same time observing the direction of rotation of the flagellar motor. The rotor turned clockwise when phosphorylated CheY (CheY-P) was bound and counterclockwise when CheY-P dissociated. Although the motor has been estimated to contain approximately 34 subunits that can bind CheY-P, calculations showed that clockwise-turning motors bound 13 ± 7 CheY-P molecules, so not all the subunits needed to be bound to alter the rotor's direction. In addition, the affinity for binding of CheY-P to the motor in its clockwise-moving state was about fivefold greater than that of a counterclockwise-moving motor. Dissociation of CheY-P from the motor occurred with a ~70-ms time frame—much too fast to be controlled by dephosphorylation of CheY-P. — LBR

Sci. Signal. **7**, ra32 (2014) .

NEUROSCIENCE

Disrupted Development

Socioemotional difficulties and abnormal overgrowth of the brain are apparent early in childhood for those with autism. Although the brain overgrowth has resolved by adulthood, the difficulties remain. Stoner *et al*. analyzed the expression of a variety of genes that relate to the identification of neuron and glial subtypes, as well as a handful of genes linked to autism in postmortem samples of brains from unaffected children and children with autism. Multiple readouts were assembled computationally to reconstruct the three-dimensional pattern of gene expression. Samples from children with autism showed small patches, 5 to 7 mm in length, in which the expression of several genes was abnormally reduced. The expression of genes related to excitatory neurons was most affected in these patches, genes related to interneurons less so, and genes related to glia even less affected. No one subset of genes or specific locations characterized all the samples. Neurons were present, however, in patches of reduced gene expression. The diversity in locations of the disrupted patches may reflect the diversity in how autism affects children, so that, depending on where a disruption happened to land, different brain functions could be affected. — PJH

N. Engl. J. Med. **370**, 1209 (2014).

CREDIT: MARTHA INOUYE

Published by AAAS

CHEMISTRY

Doing Better Caged

Asymmetric synthesis, which builds organic molecules with a preferred chirality, is often performed with homogeneous metal complexes bearing large chiral ligands that position reactants to produce the desired isomer. However, for catalyst recovery, heterogeneous catalysts are often more convenient, and the caged environment of metal-organic frameworks (MOFs) can also perform asymmetric catalysis if linkers based on chiral ligands are used. Falkowski *et al.* now report on MOF-based syntheses with one of most successful ligands for late-transition metals, Noyori's BINAP ligand, 2,2′-bis(diphenylphosphine)-1,1′-binaphthyl. They first synthesized a MOF where the structure-directing unit is a zirconium-based cluster $[Zr_6O_4(OH)_4]$ and the linkers are BINAP-derived dicarboxylic acids. They then introduced Ru or Rh by adding metal complexes and then HBr. Rotational disorder prevented assignment of the metal coordination by x-ray diffraction, but x-ray absorption fine-structure spectroscopy confirmed metal coordination to the two P atoms of BINAP. They obtained very high enantiomeric excesses for a variety of organic reactions, including the asymmetric addition of arylboronic acids to 2-cyclohexanone (where yields with a Rh catalyst were moderate to high) and asymmetric hydrogenation of β-ketoesters (where the yields with a Ru catalyst were quantitative). — PDS

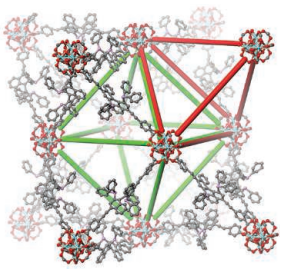

J. Am. Chem. Soc. 10.1021/ja500090y (2014).

ATMOSPHERIC CHEMISTRY

On the Wall

Aerosols exert a major influence on air quality and the radiative properties of the atmosphere, so deciphering how they form is central to understanding pollution control and climate change. Secondary organic aerosols (SOAs) make up a major fraction of these particles, but their formation is particularly underconstrained. Most of what we know about their mechanism of formation comes from laboratory studies done in enclosed chambers, but these studies generally detect SOA formation at rates much too low to explain their atmospheric abundances. Zhang *et al*. report experimental results that show that the deposition of oxidized vapors on the chamber walls can substantially reduce estimates of the rate of formation of SOAs measured in such environments, by a factor of as much as 4. Correcting for such effects would help reconcile chamber experimental results and observations made in the atmosphere, without the need to invoke other factors such as missing precursors, as some other work has done. — HJS

Proc. Natl. Acad. Sci. 10.1073/pnas.1404727111 (2014).

CHEMISTRY

Lead-Free Film

Ferroelectric materials have a permanent electric dipole moment that can be switched by the application of an external electric field, a property that makes them widely used in sensing, memory, and actuators. Most commonly used ferroelectrics are perovskites, such as lead zirconium titanate (PZT). Molecular ferroelectrics present an interesting, more environment-friendly alternative, but in the technologically relevant thin-film form they have been found to perform considerably more poorly than in bulk. Zhang *et al.* find that imidazolium perchlorate is a molecular ferroelectric with relatively high spontaneous polarization and transition temperatures. The authors grow films of this material by depositing it on a substrate by the spin-coating method, and induce dendritic crystal growth on the surface by placing it in a saturated solution. The resulting films show properties comparable to those of the bulk material and, in addition, their piezoelectric response, relevant to applications and measured by piezoresponse force microscopy, compares well to those of films of the more established ferroelectrics such as PZT. — JS

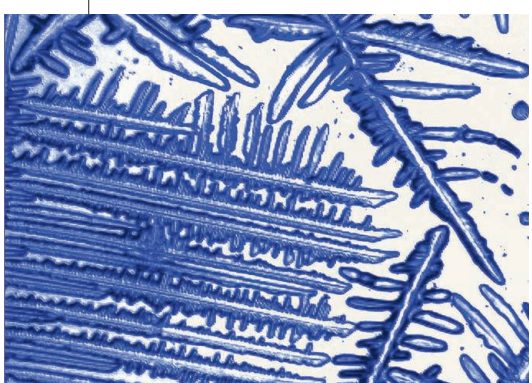

Angew. Chem. Int. Ed. 10.1002/anie.201400348 (2014).

CREDITS (TOP TO BOTTOM): J. M. FALKOWSKI *ET AL.*, *JOURNAL OF THE AMERICAN CHEMICAL SOCIETY* **136**, 14 (1 APRIL 2014) © 2014 AMERICAN CHEMICAL SOCIETY; REN-GEN XIONG

Published by AAAS

AROUND THE WORLD

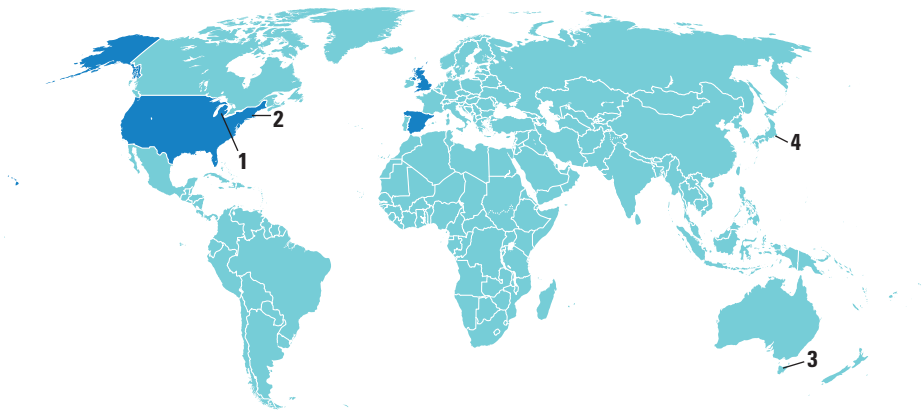

Isle Royale, Michigan **1**

No Genetic Rescue for Island's Wolves

After 2 years of consideration, the National Park Service (NPS) announced last week that it will not introduce mainland wolves to revive the genetically inbred and declining wolf population on Isle Royale, in Lake Superior. "The decision is not to intervene as long as there is a breeding population," says Isle Royale National Park Superintendent Phyllis Green.

On the edge. Isle Royale's wolves are in record decline.

But a recent record decline in wolf numbers—and ripple effects on the island's moose and forest—has convinced many researchers that genetic rescue of the wolves is needed.

NPS issued no analysis or report in support of its decision, part of a larger management planning and environmental impact statement exercise, but Green says details of the plan will be forthcoming this fall.

The birth last summer of three pups to Isle Royale wolves was a factor in the decision, Green adds. The pups survived the brutal winter, although two adults did not. That puts the official count of the island's wolves at nine. **http://scim.ag/IRwolves**

Cambridge, Massachusetts **2**

Harvard Reexamines Investments

Last fall, Harvard University rejected a student-led push to divest fossil fuel holdings from its $33 billion endowment. But the university announced last week that its endowment will be the first in the United States to join the Principles for Responsible Investment, a coalition of institutional investors supported by the United Nations to promote investments in sustainable technologies and products. The school is also asking donors to help create a $20 million energy innovation fund and signing on to the international nonprofit Carbon Disclosure Project on corporate openness.

Still, more than 100 professors—about 4% of the faculty—have signed a 10 April petition urging the university to reverse its decision on divestment. "My hope is that the divestment movement can, with other grassroots efforts, grow into a social movement capable of mobilizing a small but active minority to push climate policy at the ballot box," wrote one of the signers, Harvard energy expert David Keith, in a blog post this past December.

Hobart, Tasmania **3**

Australian Antarctic Research Faces Cuts

Commercial sponsorship and philanthropic donations: Those are among the "[a]lternative funding models" for research that officials at the Australian Antarctic Division (AAD), the nation's lead polar science agency, told staff they will consider to offset planned funding cuts.

Gordon de Brouwer, secretary of the federal Environment Department, which oversees AAD, told scientists and support staff on 8 April that the division also faces an unspecified number of "voluntary" job losses. AAD has already lost 30 employees over the past few months, leaving the remaining 300 staff members stretched. The news follows a warning issued late last month by the Australian Academy of Science that the country's strategic position in Antarctica is at risk because of a declining scientific effort there (*Science*, 11 April, p. 134).

The financial squeeze comes as the Environment Department's budget will be slashed from AU$460 million to AU$361 million over 4 years. And the nation's top science organization, the Commonwealth Scientific and Industrial Research Organisation (CSIRO), is bracing for its own government funding cuts in May, *The Sydney Morning Herald* reported this week. CSIRO stands to lose $150 million, or 20% of its government funding, the paper reported. **http://scim.ag/AADcuts**

Tokyo **4**

Japanese Researchers To Resume Whaling

Japan's marine mammal research agency has signaled that it plans to resume "research whaling" in Antarctica next year, despite an international court ruling that concluded similar past hunts weren't science-based. Earlier this month, the International Court of Justice (ICJ) in the Netherlands ordered Japan to halt the controversial hunts (*Science*, 4 April, p. 22), and Japanese officials announced they were canceling permits for the 2014 to 2015 season. But in

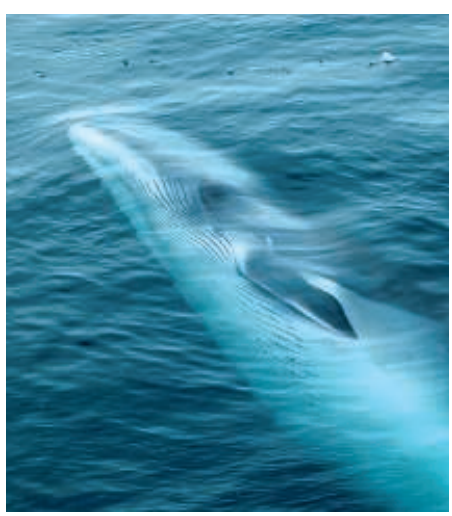

Hunted. Japanese researchers will resume hunts for cetaceans such as the minke whale in 2015.

CREDITS (TOP TO BOTTOM): ROLF PETERSON; ERLEND KVALSVIK

Published by AAAS

legal briefs filed with a U.S. federal court in Seattle, Washington, Japan's Institute of Cetacean Research (ICR) said it will resume whaling in 2015. The agency is seeking a court order preventing the Sea Shepherd Conservation Society from harassing its ships. The ICR filing provided no details, but said the new hunt will be "in accord with the ICJ decision." **http://scim.ag/ICRwhaling**

NEWSMAKERS

NSF Honors Up-and-Coming Molecular Biologist

For his trailblazing work developing new tools to edit the genome and manipulate brain cells, molecular biologist **Feng Zhang**, 32, has won the National Science Foundation's million-dollar Alan T. Waterman Award, given annually to an outstanding scientist or engineer under the age of 35. Zhang is affiliated with the Broad and McGovern institutes at Harvard University and the Massachusetts Institute of Technology in Cambridge.


Zhang

Zhang and his family moved from China to Des Moines when he was a child, he says. During high school, Zhang worked at a gene therapy lab, an experience that taught him to think about biology from an engineer's point of view and sparked a passion for "developing new technologies for tinkering with biological systems." Under the tutelage of neuroscientist Karl Deisseroth at Stanford University, Zhang, then a Ph.D. student, helped develop optogenetics, a tool that allows researchers to use light to control neuronal gene expression and firing. Zhang went on to invent CRISPR, a fast, cheap method of inserting, deleting, and substituting DNA sequences in animal genomes. The award will provide "a great way to test new ideas" for using the technology to treat genetic and brain diseases, he says.

Budget Director to Head HHS

President Barack Obama last week nominated **Sylvia Mathews Burwell**, director of the White House budget office, to replace Kathleen Sebelius, outgoing secretary of the Department of Health and Human Services (HHS).

Burwell, 48, has a background in public policy and was deputy director of the White House Office of Management and Budget (OMB) under President Bill Clinton. From 2001 to 2011, she worked for the Bill & Melinda Gates Foundation, where for several years she headed the foundation's Global Development Program, overseeing projects including agricultural development and polio eradication. She directed the Walmart Foundation before becoming OMB director a year ago.


Burwell

As HHS director, Burwell will continue efforts to carry out the Affordable Care Act. Sebelius endured months of criticism for problems with the government's health insurance website.

Thanks for the Memories

The physicist who helped put the "big" in "big data" has won the "Tech Nobel." **Stuart Parkin** was named the 2014 recipient of the $1.4 million Millennium Technology Prize from the Technology Academy Finland. Parkin currently splits his time among Stanford University in Palo Alto, California; the IBM Almaden Research Center in San Jose, California; and the Max Planck Institute of Microstructure Physics in Halle, Germany.

While working at IBM in 1989, Parkin invented the "spin valve," a gizmo that can form a bit of magnetic memory. It ushered in a more than 1000-fold increase in computer hard drive storage capacity, paving the way for social media, video streaming, and cloud computing.


Parkin

Parkin said he feels honored and humbled by the award. "Who would have known that my invention would one day … affect the way people share information and communicate with each other on the Internet, on our mobile devices and across the world." Parkin is now developing a new technology called Racetrack memory that he hopes could again revolutionize computer memory. >>

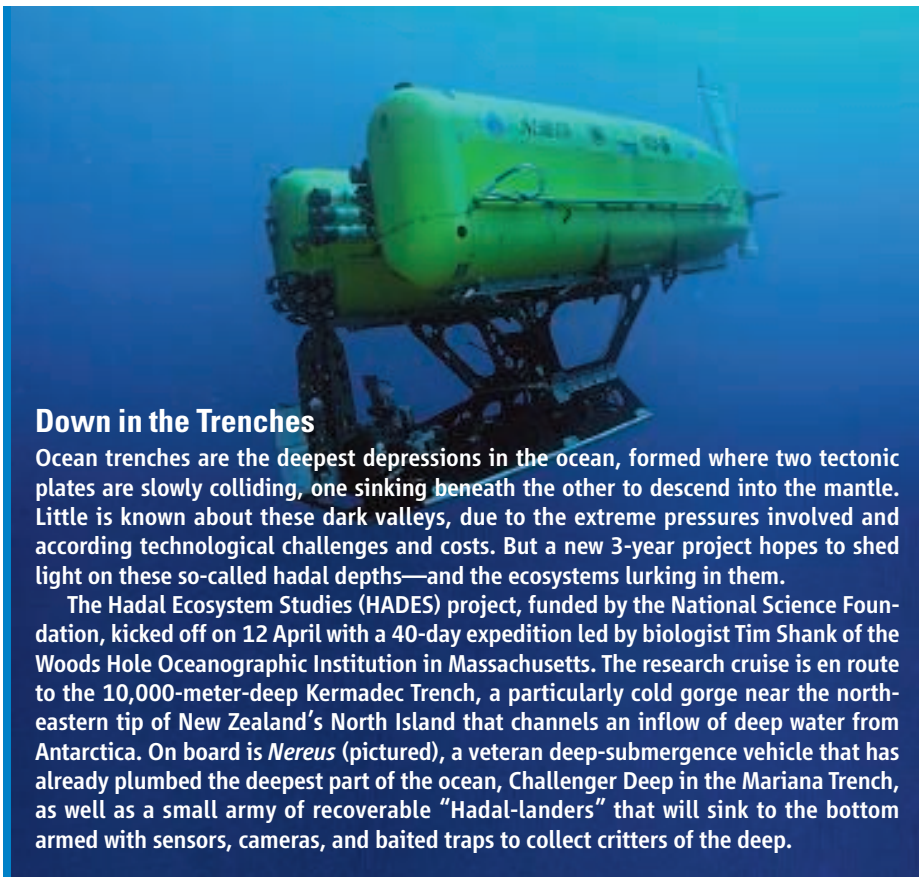

Down in the Trenches

Ocean trenches are the deepest depressions in the ocean, formed where two tectonic plates are slowly colliding, one sinking beneath the other to descend into the mantle. Little is known about these dark valleys, due to the extreme pressures involved and according technological challenges and costs. But a new 3-year project hopes to shed light on these so-called hadal depths—and the ecosystems lurking in them.

The Hadal Ecosystem Studies (HADES) project, funded by the National Science Foundation, kicked off on 12 April with a 40-day expedition led by biologist Tim Shank of the Woods Hole Oceanographic Institution in Massachusetts. The research cruise is en route to the 10,000-meter-deep Kermadec Trench, a particularly cold gorge near the northeastern tip of New Zealand's North Island that channels an inflow of deep water from Antarctica. On board is *Nereus* (pictured), a veteran deep-submergence vehicle that has already plumbed the deepest part of the ocean, Challenger Deep in the Mariana Trench, as well as a small army of recoverable "Hadal-landers" that will sink to the bottom armed with sensors, cameras, and baited traps to collect critters of the deep.

CREDITS (LEFT TO RIGHT): MARIA NEMCHUK; WALMART FOUNDATION; ADVANCED IMAGING AND VISUALIZATION LABORATORY, WOODS HOLE OCEANOGRAPHIC INSTITUTION; WIKIMEDIA COMMONS

Published by AAAS

>>NEWSMAKERS

Former German Minister Drops Her Fight to Reclaim Ph.D.

Marking the end of one of the most hotly debated plagiarism cases in Germany, former German Education and Research Minister **Annette Schavan** is giving up her fight to keep her Ph.D. title, she announced 10 April on her website.


Schavan

Schavan was awarded the degree in educational science at the University of Düsseldorf in 1980. More than 30 years later, Schavan, by then the nation's education and research minister, was charged with plagiarism by an anonymous accuser who posted an analysis of her dissertation online. The University of Düsseldorf revoked the degree in February 2013; 4 days later, Schavan resigned.

But the wrangling continued: Schavan acknowledged mistakes but denied any intent to mislead and took her case to court. Last month, the Düsseldorf Administrative Court upheld the university's action, finding that Schavan had taken several passages from secondary sources without citing them correctly.

"I have decided not to appeal and to end the legal fighting," Schavan wrote in the statement on her home page. A devout Catholic, she has been tapped as Germany's ambassador to the Vatican.

Chinese Science Official Snared In Corruption Probe

China's anticorruption champion has snared a high-ranking official in the country's science and technology establishment. **Shen Weichen**, the Communist Party secretary and chief executive of the China Association for Science and Technology, or CAST, is under investigation "for suspected serious violation of discipline and laws," according to the agency spearheading the anticorruption drive, the Communist Party of China's Central Commission for Discipline Inspection. The agency did not reveal further details about the allegations.

Shen has been at CAST for barely a year. He was appointed Communist Party secretary at the organization in April 2013 and elected its executive vice chairman, in charge of "day-to-day work," in June, according to CAST's website. *China Business News*, an influential Chinese business daily, reported that Shen's corruption investigation likely doesn't focus on his work at CAST but on earlier jobs in Shanxi, a coal-rich province in central China where Shen spent most of his career, and particularly on real estate development in Shanxi's capital, Taiyuan.

Random Sample

Chemistry Sets, Reimagined

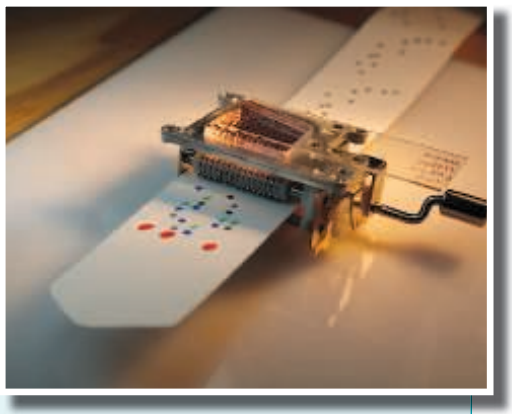

Chemistry kits aren't what they used to be. Fifty years ago, budding mad scientists had access to many now-forbidden hazardous chemicals handy for setting off minor explosions or concocting bubbling potions.

The Science, Play and Research Kit Competition aims to bring back all the fun of the chemistry set—minus the liability issues—by reimagining a kit for the 21st century. On 8 April, the competition revealed its first prize winners, who will share a $50,000 award: Manu Prakash, a bioengineer at Stanford University in California, and graduate student George Korir, who came up with an inexpensive lab-on-a-chip capable of a slew of experiments, from testing snakebite venom to checking acidity in soil.

Scientists shouldn't be "dumbing down" the chemistry kit, Prakash says: "Science toys today are so narrowed … you can do this one thing and that's it." So Prakash and Korir designed a small microfluidic chip with miniature pipes, valves, and pumps that can potentially conduct hundreds of tests. Whether you want to examine water quality, check for adulterants in milk, or even make a medical diagnosis, the chip is prefilled with the necessary ingredients.

Step one: Choose an experiment by selecting a card with prepunched holes. Similar to how a ribbon is reeled through a music box to determine which notes to play, the card is cranked through multiple toothed gears; when a tooth comes in contact with a hole, the gear turns, activates a particular pump, and triggers a drop of a chemical to be released. Meanwhile, the user can watch the reaction occurring within the clear microchip. The best part? The set costs about $5.

FINDINGS

Hunter-Gatherers Don't Need Probiotics

Probiotics are a rapidly growing product in the food industry, added to foods to restore the "natural balance" of organisms in our intestines. But not everyone needs them: The Hadza, a group of hunter-gatherers in Tanzania, lack a gut bacterium that is a key ingredient in most probiotic foods, a new study finds. What's more, the Hadza don't suffer from colon diseases found in humans eating modern diets in Western nations. Those diseases are associated with less diversity in gut bacteria, called the microbiome.

The new study is the first to report on the gut bacteria of hunter-gatherers. An international team collected and sequenced

Gut reaction. The Hadza have a diverse array of gut bacteria—and don't suffer from colon diseases.

DNA from the bacteria in fecal samples from 27 Hadza. Compared with Italians, the Hadza have a more diverse microbiome, the team reports online this week in *Nature Communications*—although they completely lack *Bifidobacterium*, a type of bacteria commonly added to probiotic drinks that is associated with dairy products, which the Hadza do not consume.

"We must redefine our notions of what is considered healthy and unhealthy, since these distinctions are clearly dependent on diet," says Alyssa Crittenden, a nutritional anthropologist at the University of Nevada, Las Vegas, and lead author of the study. **http://scim.ag/Hadzagut**

CREDITS (LEFT TO RIGHT): LAURENCE CHAPERON; GEORGE KORIR; MAX PLANCK INSTITUTE FOR EVOLUTIONARY BIOLOGY

Published by AAAS

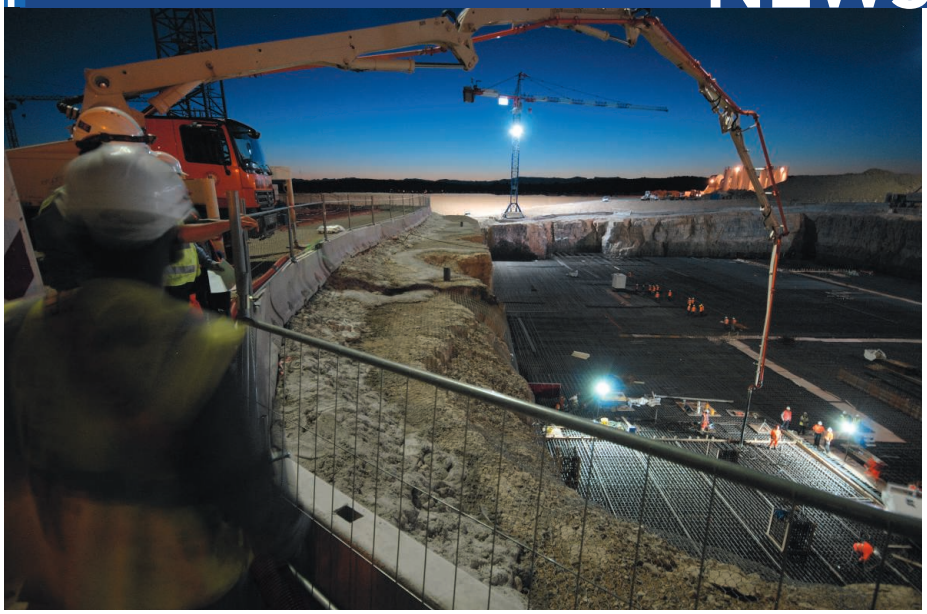

Under way. U.S. concerns about ITER costs come as construction moves ahead in Cadarache, France.

FUSION

U.S. Support for ITER Wavers as Costs Spiral

Soaring costs are jeopardizing the U.S. contribution to the international fusion energy project, ITER. Last week, a key member of Congress reacted with alarm to new projections showing that the U.S. share of the cost for the massive machine could reach $3.9 billion—roughly four times the original estimate made in 2006.

"I'm really beginning to believe that our involvement in ITER is not practical, that we will not gain what we hope to gain from it, and instead this money could be much better be spent elsewhere," said Senator Dianne Feinstein (D–CA), the chair of an appropriations subcommittee that controls ITER funding, at a hearing on 9 April. The Senate panel could move as early as next month to cut U.S. funding for ITER, which is already under construction in Cadarache, France, says a staffer who works for the Senate's Democratic majority.

Backing out of the commitment may be difficult. It would require the approval of Congress and the White House, and some U.S. officials worry that reneging on the deal could carry steep diplomatic costs with the other ITER partners, such as Europe and Japan. But the prospect of losing U.S. support has unsettled ITER leaders. "I'm very worried," says Robert Iotti, chair of the ITER Council of member nations and a nuclear engineer with CH2M HILL in Englewood, Colorado. "And frankly every day I'm more and more worried because things seem to be going in the wrong direction."

This isn't the first crisis to face U.S. supporters of ITER, which aims to use an enormous doughnut-shaped electromagnet to create a "burning plasma" that produces more energy than the machine consumes. Backers first proposed the project in 1985 as a joint venture with the Soviet Union and Japan. But the United States backed out in 1998, citing concerns over cost and feasibility—only to jump in again in 2003. At the time, planners estimated ITER would cost roughly $5 billion. That estimate had grown to $12 billion by 2006, when the European Union, China, India, Japan, South Korea, Russia, and the United States signed a formal agreement to construct the device, which was scheduled to start operations in 2016. As a result of delays and management problems, the ITER Organization now estimates the reactor will cost at least $21 billion and won't run until 2020 at the earliest—although some say even those figures are wildly optimistic.

The United States committed to building 9% of the ITER machinery, which in 2006 the Department of Energy (DOE) estimated would cost $1.1 billion. By 2011, the estimate had risen to $2.5 billion. U.S. officials had not released an updated cost profile in recent years. But now the U.S. contribution is expected to total $3.9 billion by the time ITER is fully operating in 2034, Ned Sauthoff, project manager for U.S. ITER at Oak Ridge National Laboratory in Tennessee, told a meeting of DOE's Fusion Energy Sciences Advisory Committee in Rockville, Maryland, on 9 April. The estimate assumes ITER will start running with ordinary hydrogen fuel in 2024 or 2025 and will shift to deuterium and tritium fuel—the mixture needed for a burning plasma—10 years later.

In spite of the delays, the U.S. effort is making "strong progress," Sauthoff says. "U.S. components needed for the construction sequence are being completed for delivery in 2014 and 2015," he says.

Much of the increase is the result of a DOE decision to stretch out ITER spending over a longer time period, which amplifies the effects of inflation and requires larger amounts of "contingency" funding to cover budget uncertainties. Early plans called for DOE to spend $350 million a year on ITER from 2014 through 2016. But that would have eaten up most of DOE's fusion budget, leaving little for domestic programs. So in

U.S. ITER Budgets—Old and New

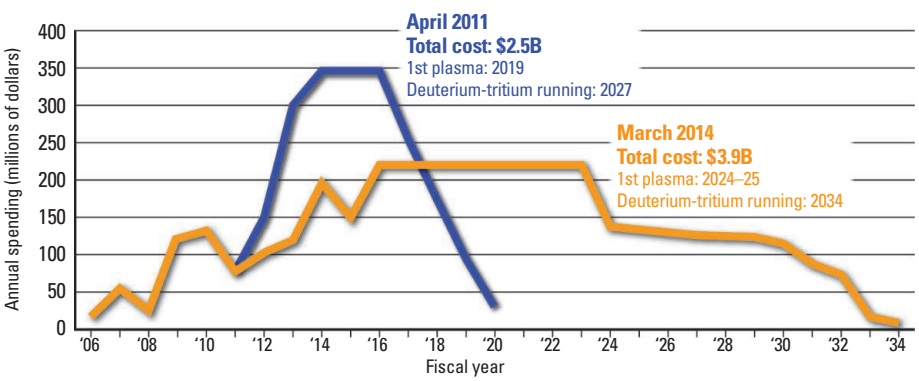

Longer, costlier. U.S. ITER costs are rising as spending gets spread out.

CREDITS (TOP TO BOTTOM): © 2014, ITER ORGANIZATION; U.S. ITER PROJECT OFFICE

Published by AAAS

formulating this year's budget, department officials proposed capping ITER spending at $225 million; in the end, Congress gave ITER just $200 million of DOE's $505 million fusion budget. The White House proposes spending even less on ITER, $150 million, in the 2015 fiscal year which begins 1 October.

That low request may reflect a division within the Obama administration, says the Democratic Senate staffer. Diplomats at the U.S. State Department argue that the U.S. commitment is akin to a treaty and can't be broken, he says. (State Department officials declined comment.) But some DOE officials may be happy to walk away from the troubled project, he adds. Congress could break the deadlock when lawmakers revise, or mark up, the administration's proposed budget for 2015. In the Senate, "our intention is to make a decision for ourselves in our markup," the staffer says. "They won't have a choice."

The Senate's final stance could depend on how well the ITER Organization responds to a scathing management review it received this past February (*Science*, 28 February, p. 957), a Republican staffer in the Senate says. Among its 11 recommendations: replacing ITER Director-General Osamu Motojima, reducing the number of senior managers by half, developing a realistic schedule, and creating a culture of urgency in the project. "If they make those changes, then there is viability in the [U.S.] program," predicts the staffer. But if "they don't, there isn't."

The ITER Organization is striving to implement those recommendations, Iotti says. "We are taking immediate action on all of them." But some changes—such as finding a new director-general—will take time, he notes. And some problems may never be completely fixed. Iotti notes that, according to the ITER agreement, the director-general cannot give orders to member nations; he can only try to persuade them to make changes.

Even if the Senate follows through on its threat, U.S. work on ITER won't stop immediately. The House of Representatives, which has been more supportive of fusion research, must pass its version of the budget, and any final spending must win approval of both houses of Congress and the White House. That process will take months, one Republican House staffer predicts. The Senate may use its markup to send a message, he says: ITER must shape up.

Still, Iotti worries that the U.S. flare-up puts the fate of ITER as a whole at risk. "In my opinion, it might be fatal [to the project] if the U.S. were to drop out," he says. Suddenly, that seems like a possibility.

–ADRIAN CHO

TOXICOLOGY

'Humanized' Mouse Detects Deadly Drug Side Effects

After five patients died in a small clinical trial of an experimental hepatitis B drug in 1993, high-level committees scrambled to work out what went wrong. In the end, they blamed not the researchers but the lab animals. Earlier studies, including several in animals, simply failed to show that the drug was toxic.

Now, researchers say they have developed an animal model that would have detected the drug's toxicity: an engineered mouse with a humanlike liver. They say it could serve as a versatile testbed for liver toxicity, a worrisome side effect of many drugs.

Gary Peltz, a rheumatologist at Stanford University School of Medicine in California, heads one of several groups that have engineered mice to have "humanized" livers. Other groups have primarily used their models to investigate fundamental questions about metabolism, and some have reported drug effects. But none has taken the toxicology model as far as the FIAU study that Peltz and co-authors published in the 15 April edition of *PLOS Medicine*. This is "the first definitive example of a human-specific, drug-induced toxicity that could

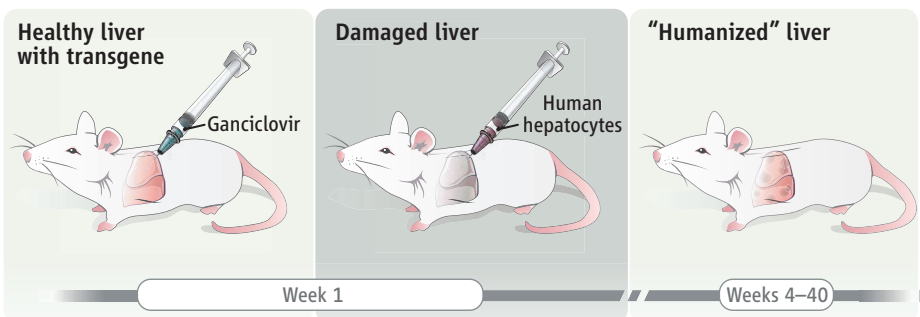

Recipe for a chimeric mouse. Researchers first kill mouse liver cells, and then transplant human hepatocytes.

"The study is a tour de force," says Jay Hoofnagle, director of the Liver Disease Research Branch at the National Institute of Diabetes and Digestive and Kidney Diseases in Bethesda, Maryland. Hoofnagle was not involved in the work, although his division partly funded it. He led the infamous 1993 trial, which tested a hepatitis B drug known as fialuridine (FIAU).

That phase II study was designed to evaluate different doses of FIAU in 15 people who had chronic hepatitis B infections. The drug caused severe lactic acidosis in seven patients; two died quickly, and five received liver transplants, but only two survived. Earlier experiments in mice, rats, dogs, and monkeys had tested FIAU at various doses and found no detectable harm. Similarly, small human studies conducted by other researchers had not tied any serious adverse events to the drug. Expert committees convened separately by the U.S. National Institutes of Health (*Science,* 10 June 1994, p. 1530) and the Institute of Medicine (*Science*, 24 March 1995, p. 1759) each determined that Hoofnagle and collaborators had acted appropriately in conducting their trial.

be detected in chimeric mice, but not in conventional rodent, dog, or monkey toxicity studies," the researchers assert. (One of the co-authors, Stanford's Jeffrey Glenn, has collaborated with Hoofnagle on hepatitis studies.)

Peltz's team destroys the liver cells in an immunodeficient mouse strain called NOG by stitching in a transgene of an enzyme, thymidine kinase, from herpes simplex virus-1. Then they give the mice the drug ganciclovir, which becomes active only in the presence of this enzyme, selectively killing mouse liver cells but not otherwise harming the animals. Finally, they transplant human liver cells into the mice, which they dubbed TK-NOG. The resulting mice live for up to 8 months, and their livers metabolize drugs in much the same way as a human liver.

For their new study, Peltz and co-workers wanted to demonstrate the mouse's value for drug testing. "I called a number of people and asked what was the best example of a drug where preclinical toxicology failed to predict what would happen in humans," says Peltz, who formerly ran genetics and genomics research at Roche's now-closed

CREDIT: V. ALTOUNIAN/*SCIENCE*, ADAPTED FROM G. PELTZ, *TRENDS IN PHARMACOLOGICAL SCIENCES*, **34** (MAY 2013)

Palo Alto, California, lab. FIAU seemed a perfect fit. (After the FIAU disaster, a study in woodchucks infected with their own version of hepatitis B did detect the drug's toxicity, but woodchucks are rare in toxicology labs.)

In the new study, Peltz's team compared various doses of FIAU in the TK-NOG mice, using NOG mice that retained their mouse livers as controls. The first experiment, which gave the mice a high dose of FIAU, began on a Monday. Peltz thought it would take a few months before any toxicities showed up in the TK-NOG animals. "On Wednesday, [the lab] called and they said, 'You may want to stop this. The mice are really sick,' " Peltz remembers. "It was the happiest I've ever been about a sick mouse." One mouse had died and 14 others had acute liver failure. FIAU had no effect on the NOG mice. Lower doses of FIAU caused illness or serious liver abnormalities in the TK-NOG mice, and the severity of the effects increased with the dose—a key indication, the authors argue, that the drug caused the toxicities. Different doses of a safe, widely celebrated hepatitis C drug, sofosbuvir (*Science*, 13 December 2013, p. 1302), did not harm the TK-NOG mice.

Markus Grompe, a pediatrician at Oregon Health & Science University in Portland, says the new work is a "solid report" and "good proof of principle." But Grompe, who has a company that markets his own chimeric mice, says he expects all the existing mouse models with humanized livers, including his own, would have performed equally well. Peltz, who says "at present" he has "no financial interest" in his mice, insists that other chimeric mice have ongoing liver toxicities caused by the process used to engineer them; the two researchers slugged it out in the May and August 2013 issues of *Trends in Pharmacological Sciences*.

Charles Rice, who studies hepatitis C virus at Rockefeller University in New York City, calls Peltz's study "interesting" but says "critical controls" are missing. He says the immunodeficiency in the TK-NOG mice could have contributed to FIAU's effects. To rule this out, Rice says he'd like to see FIAU tested in TK-NOG mice reconstituted with liver cells from rats, dogs, and monkeys.

Peltz says the team will test other drugs that, like FIAU, did not show toxicity in animal studies but caused harm in humans. He'd also like to create chimeric mice with human liver cells from different genetic backgrounds to see if results from the mice could help link drug effects to specific populations.

Hoofnagle says the humanized mice might help answer a fundamental question about FIAU: Why did it cause harm in the first place? The drug exists in two different structures, or isomers, and some evidence suggests only one is dangerous to humans. Says Hoofnagle: "This model might be an elegant means to sort out these issues."

–JON COHEN

EPIGENETICS

Ancient DNA Holds Clues to Gene Activity in Extinct Humans

Ancient DNA researchers are teasing yet more secrets from long-vanished human species. Over the past 2 years, they revolutionized the study of human evolution by deriving high-quality genome sequences from 50,000-year-old fossils. Now, through clever analysis of that ancient DNA, they have gleaned a record of which genes were turned on or off in those archaic humans.

Online this week in *Science* (http://scim.ag/DGokhman), an Israel-based team, working with an ancient DNA research group, reports mapping the chemical modifications likely to have silenced genes in the DNA of a 50,000-year-old female from a mysterious group called the Denisovans (*Science*, 31 August 2012, p. 1028) and a slightly older female Neandertal. By comparing that data with similar maps for modern human tissue, they have pinpointed two genes that might underlie skeletal differences between us and our extinct cousins.

One or two genomes aren't enough to verify that the observed chemical modifications, known as methylation, are characteristic of the entire species, and much more work is required to confirm that the methylation patterns actually led to skeletal changes in Neandertals and Denisovans. Still, to be able to study gene activity at all in ancient humans is "ingenious," says Chris Stringer, a paleoanthropologist at the Natural History Museum in London.

CREDIT: © DENIS FINNIN/AMERICAN MUSEUM OF NATURAL HISTORY

Boning up. DNA methylation that silences genes may account for some of the skeletal differences between Neandertals (*left*) and modern humans.

"This study shows that it is now possible to 'paint' ancient genome sequences with an additional layer of information," adds Ryan Lister, a genome biologist at the University of Western Australia, Crawley.

The past decade has driven home the importance of how genes are regulated, not just which proteins they code for, in defining how an organism looks, acts, and reproduces. In one key regulatory process, cells attach a methyl side group to a DNA base, typically cytosine. Methylation helps curtail the activity of rogue mobile DNA

Published by AAAS

and in mammals inactivates one of the X chromosomes in females. But it can also silence individual genes, for example when a gene has done its job and is no longer needed. And because methyl groups can be removed, genes can be called out of retirement at any time.

Lately, molecular and cell biologists have been mapping methylation patterns—so-called methylomes—in various tissue from people to learn what role this regulation plays in health and disease. But the method for mapping methylomes in living cells requires a lot of DNA, typically more than can be found in a fossil.

Adrian Briggs recently hit upon a possible solution to generating ancient methylomes. As a graduate student at the Max Planck Institute for Evolutionary Anthropology in Leipzig, Germany, Briggs worked in Svante Pääbo's lab, which is famous for sequencing ancient DNA. Over time fossil DNA degrades, breaking into fragments and changing chemically. The base cytosine sometimes transforms into a different base found in RNA, uracil, which genome sequencing machines misread as the base thymine.

While developing a way to delete the uracils, Briggs became confused, because the resulting sequence still had more thymine bases than expected. Then a biochemist colleague explained that a methylated cytosine would not degrade into uracil and instead would over time convert to thymine, resulting in an unusually high proportion of thymine in the sequence. A light bulb went off.

Briggs realized that by comparing an ancient DNA sample with a modern human genome, researchers could pinpoint places where the former had thymine but the latter has cytosine. A few of those differences might be actual mutations distinguishing the two species, but most would indicate where a cytosine had converted to a thymine, and thus, where methylation had occurred. "Normally DNA damage gives us a hard time," notes Ludovic Orlando, a developmental biologist at the University of Copenhagen. "For once, DNA damage becomes really our friend!"

> ***"This paper gives us a first glimpse of how we can begin to unlock epigenetic aspects of ancient genomes which have been hidden from us up to now."***
>
> **—CHRIS STRINGER, NATURAL HISTORY MUSEUM, LONDON**

Briggs, who is now at a biotech company called AbVitro Inc. in Boston, published his idea in 2010, but no one could try it out because it required in-depth sequencing of a genome, something that was still out of reach for fossil DNA. But last year, with improvements in DNA sequencing, Orlando and colleagues tried a similar approach on a 4000-year-old Eskimo hair, describing the hair's methylome in *Genome Research* in December 2013. Because methylation patterns vary with age, they were also able to estimate how old the Eskimo was at death.

Then David Gokhman, Eran Meshorer, and Liran Carmel of the Hebrew University of Jerusalem teamed up with Pääbo's group to map methylation across a Denisovan and a Neandertal genome, both of which had been sequenced in depth—the former came from DNA in a fossil finger bone, the latter from a toe bone. When they compared the ancient methylation patterns with ones determined in bones from a modern young female and in other tissues, they found that about 99% of ancient and modern methylome maps match up. The match was perfect at housekeeping genes, which are essential to all cells and therefore less likely to have their regulation changed over the course of human evolution—an indication that the analysis was on target. "I was very convinced," says Lluis Quintana-Murci, a population geneticist at the Institut Pasteur in Paris.

At about 2000 places, though, the ancient and modern methylomes diverged. In both of the archaic methylomes but not the modern human one, there were signs of heavy methylation that could have silenced two of a cluster of genes critical to development, known as HOXD. The few studies that have looked at diminished HOXD gene function in mammals have found skeletal changes that approximate some of the features that distinguish Neandertals from modern humans, such as larger ends of the thigh bone, bigger hands and fingers, shorter limbs, and broader elbow and knee joints. Still, Orlando acknowledges, "There's a long way from spotting the differentially methylated region and saying this is what caused the differences [in anatomy]."

While Andrew Feinberg, a genomicist and epigenetics expert at Johns Hopkins University in Baltimore, Maryland, applauds the approach, he and others remain wary. "I don't think [the method] has been tested fully and I don't think they can draw inferences from a single sample," he says. He and others emphasize that because methylomes can vary through time, across environments, from cell type to cell type, and even between the sexes, researchers will need many more high-quality archaic genomes to establish the typical methylation pattern of Neandertals, Denisovans, or any ancient human species.

Nevertheless, many ancient DNA specialists are optimistic that such sequences will be forthcoming. And Briggs predicts an early application for the technique: Biologists interested in the changes in gene activity that helped transform wild animals into domesticated breeds will soon try the ancient methylome approach on livestock fossils. "This paper gives us a first glimpse of how we can begin to unlock epigenetic aspects of ancient genomes which have been hidden from us up to now," Stringer concludes. **–ELIZABETH PENNISI**

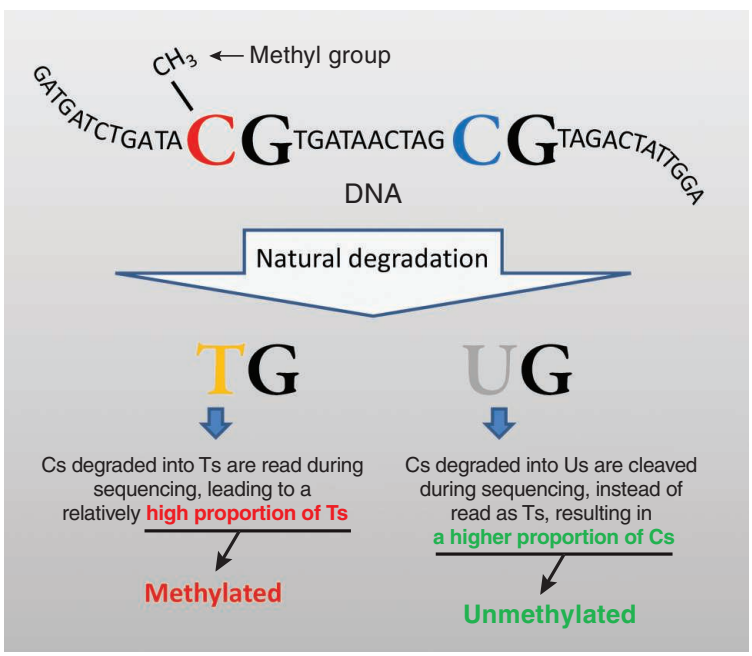

Methylation revelation. DNA bases covered with methyl groups degrade differently from unmethylated ones, leaving telltale signs in ancient genomes.

CREDIT: ERAN MESHORER

CREDIT: HOW HWEE YOUNG/NEWSCOM

Breathe easy. Efforts by China and other developing nations to reduce air pollution are helping jump-start greenhouse gas controls.

CLIMATE SCIENCE

More Sophisticated Forecasts Yield Glimmer of Hope in Climate Gloom

BERLIN—To anyone aware of the diplomatic squabbling and domestic gridlock over climate change, the latest assessment of prospects for limiting it was predictably grim. Averting risky climate change "requires a fundamental transformation of the energy supply system," concludes a summary of the report from the United Nations' Intergovernmental Panel on Climate Change (IPCC), released here on 13 April. And so far, humanity has "not done a lot" to achieve that goal, IPCC Chair Rajendra Pachauri told a press conference.

But the report offered something more than alarm and a litany of unreachable goals. Drawing on sophisticated new models that reflect the latest research on energy technologies, economics, and sociopolitical factors, it points to some surprising win-wins: policies and technologies that might achieve meaningful cuts in greenhouse gas emissions at an acceptable political and economic cost. As IPCC co-author and economist Reyer Gerlagh of Tilburg University in the Netherlands explains, "nowadays we can do a full cost-benefit analysis—including the co-benefits. We couldn't do that 10 years ago."

The roughly 2000-page report is the last of three installments in IPCC's massive effort to assess climate research conducted since 2007. The first, on the physical climate system, was released this past September (*Science*, 4 October 2013, p. 23); the second, on climate impacts, was unveiled last month (*Science*, 4 April, p. 21). Since the last assessment, economic growth and burgeoning global coal use have driven emissions ever higher. Global emissions of carbon dioxide (CO_2) or its equivalent were 7 billion tons greater between 2000 and 2010 than over the prior decade.

The "integrated assessment models" that underpin the report deliver discouraging news. They allow researchers to examine how politics could inflate the cost of reaching an oft-cited goal: stabilizing CO_2 concentrations at 450 parts per million (the current level is about 400 ppm) by 2100, a target that would give the planet a shot at limiting global warming to 2°C. For instance, the models show that restricting the use of biofuels because of concerns that fuel crops compete with food could increase costs by 44% to 78%, compared with more aggressive mitigation scenarios. Opposition to carbon capture and storage (CCS) technology, which captures carbon dioxide emitted by power plants and then pumps it underground, and has led to fears about leaks, could increase costs by 29% to 297%. (IPCC lead author Leon Clarke of the Joint Global Change Research Institute in College Park, Maryland, notes, however, that it is "very hard to predict costs over a century.")

But the report suggests that both technologies could be important to reducing future emissions. That's because the models show that an approach called bioenergy with CCS, or BECCS, could deliver appreciable benefits at relatively low costs. BECCS involves making biofuels from plants that have already sucked carbon out of the atmosphere, and then capturing and storing the emissions from burning the fuels. "If we are going to try for some of these lower targets, the models really like BECCS," Clarke says, though he notes the approach has yet to be tested at scale. The report says the similarity of BECCS to existing technologies is an advantage—which is why understanding the cost of potentially blocking its development is important.

Improved models are also helping researchers quantify the benefits of policies already in place, including some not necessarily focused on climate. For instance, China is moving aggressively to reduce air pollution to improve public health and increase energy efficiency to limit fuel imports. Studies suggest that these efforts are providing a co-benefit: They are moving the country toward zero-emissions sources like wind and solar. "Co-benefits are a reason countries are getting started—very few countries are doing climate policy for climate's sake," says political scientist David Victor of the University of California, San Diego, a report co-author.

Similarly, the report suggests that aggressive efforts to reduce greenhouse gas emissions could have their own co-benefits. Stepped-up mitigation could, by cleaning the air, save the equivalent of 10 million lives by 2030 compared with a less aggressive scenario, concluded one study cited in the IPCC report. Another found that the monetary benefits of improved human health would roughly balance the cost of reducing emissions. "If you take health impacts into account economically it makes mitigating climate change much more affordable," says IPCC co-author Keywan Riahi of the International Institute for Applied Systems Analysis in Laxenburg, Austria.

But after many years of watching such glimmers of hope fade, climate scientists are wary, says Christopher Field, an ecologist at the Carnegie Institution for Science in Palo Alto, California, who co-led the second report. "It's often hard for me to decide whether to be optimistic or pessimistic."

–ELI KINTISCH

Published by AAAS

ASTRONOMY

Almost-Earth Tantalizes Astronomers With Promise of Worlds to Come

Ever since the first exoplanet was discovered in 1996, astronomers have been scanning the heavens for another Earth: a rocky planet orbiting its star at just the right distance for it to harbor liquid water and thus, potentially, life. Now, sifting through data collected by NASA's Kepler orbiting observatory, they have discovered just such a planet, although it's not quite Earth 2.0. Named Kepler-186f, the planet orbits a star that is less than half the size of the sun and much cooler.

"Very exciting," says James Kasting, an exoplanet researcher at Pennsylvania State University, University Park, who was not involved in the work. "This is probably the most potentially Earth-like planet yet." David Charbonneau, an exoplanet researcher at Harvard University, calls it "one of the most significant discoveries from Kepler."

The new world is the outermost of five planets orbiting Kepler-186, a red dwarf star some 500 light-years from Earth. Such M stars typically have a fraction of the mass of the sun, burn more slowly, and are too faint to be seen with the naked eye. (Hotter sunlike stars are classified as type G.) Kepler detected the planet from a minuscule dimming of the star each time the planet transited, or crossed the face of the star.

From the extent and timing of that dimming, the researchers calculated that the planet is almost the same size as Earth—just 10% bigger in diameter—and goes around its star once every 130 days. Although its mass is unknown, astronomers say its size almost guarantees that it is rocky like Earth. Its distance from its star—about as far from the star as Mercury is from the sun—puts it in the outer reaches of Kepler-186's habitable zone.

Planets previously found in the habitable zones of other stars have been substantially larger than Earth (see table) and unlikely to have a rocky surface. But because it orbits a dwarf, "we consider this planet more of an Earth cousin than an Earth twin," says Elisa Quintana, a researcher at NASA Ames Research Center in Mountain View, California, and lead author of a paper announcing the discovery this week in *Science* (p. 277). Small, faint stars like type Ms make up more than three-quarters of the billions of stars in the Milky Way, however, so the finding could open a wide new hunting ground for extraterrestrial life. "Our galaxy is probably littered with cousins of Kepler-186f," Quintana says.

Several factors could make such planets less promising abodes for life than planets circling sunlike stars. For one, their close-in habitable zones could leave them extra vulnerable to perils such as stellar flares. On the plus side, M stars keep burning billions of years longer than sunlike stars do. "That is good news for life, because there is a longer period of time for it to take hold on the surface of the planet," says Stephen Kane, a co-author and researcher at San Francisco State University in California.

No Place Like Home

	Planet	Near Earth size?	Sunlike star?	In habitable zone?
	Kepler-20e	✔ (0.8 Earth radius)	✔	No (too hot)
	Kepler-22b	No (2.4 Earth radii)	✔	✔
	Kepler-186f	✔ (1.1 Earth radii)	No (red dwarf)	✔
Not yet found	"Earth 2.0"	*Yes*	*Yes*	*Yes*

Near misses. Several Earth-like exoplanets have been discovered, but none meets all the criteria for Earth 2.0.

Kepler-186f is a late bonus from Kepler, which monitored the brightness of some 150,000 stars from March 2009 to May 2013 in search of planets. Analyzing Kepler data, scientists have identified more than 3800 planetary candidates, of which 961 have been confirmed as planets. As the software to search Kepler's data improves, scientists keep finding planets that they missed before.

Researchers had detected Kepler-186's four inner planets by the spring of 2013. Then, a routine analysis of all of Kepler's light curves—a procedure that typically takes weeks of supercomputer time—flagged the possible existence of a small fifth planet. Quintana's team conducted a series of checks to ensure that what the software had found was a genuine transit.

To learn more about the planet, Quintana and colleagues had to learn more about the star. By taking spectra of Kepler-186 with ground-based telescopes, they nailed down its mass and size—information that helped them determine the planet's radius. "I remember walking to Elisa's office one afternoon, and she looked up at me and said, 'The planet's about the size of the Earth,' " says Steve Howell, project scientist for Kepler at NASA Ames and a co-author of the paper. Further analysis placed the planet in the outer reaches of the star's habitable zone.

"We are not saying that there's water on the surface," Howell says. "All we know is that the surface has the right temperature that water could exist there in a liquid state." To support water, however, the planet would also need to have an atmosphere to protect it. It's unclear from the available data whether the planet has an adequate atmospheric blanket.

Even those key ingredients wouldn't guarantee that Kepler-186f is habitable. If it orbited slightly closer in, Quintana says, gravitational interactions would leave the planet tidally locked: rotating so that one side always faced the star. Such two-faced planets—with the night side eternally frigid and the day side blistering hot—are considered long shots for life. But Quintana and her colleagues say Kepler-186f is far enough out that it might avoid that fate.

Unfortunately, the planet is too far away from Earth for follow-up studies. However, researchers hope it heralds many similar worlds soon to come. "The biggest impact of this discovery is to know that there are planets that are the same size as Earth in the habitable zones of small stars," Charbonneau says. He says the next step will be "to find a close example" so that upcoming instruments like the Giant Magellan Telescope and NASA's James Webb Space Telescope can "study the atmosphere of such planets and perhaps even deduce the presence of life on them."

–YUDHIJIT BHATTACHARJEE

CREDITS (TOP TO BOTTOM): NASA; NASA/AMES/JPL-CALTECH; NASA

Published by AAAS

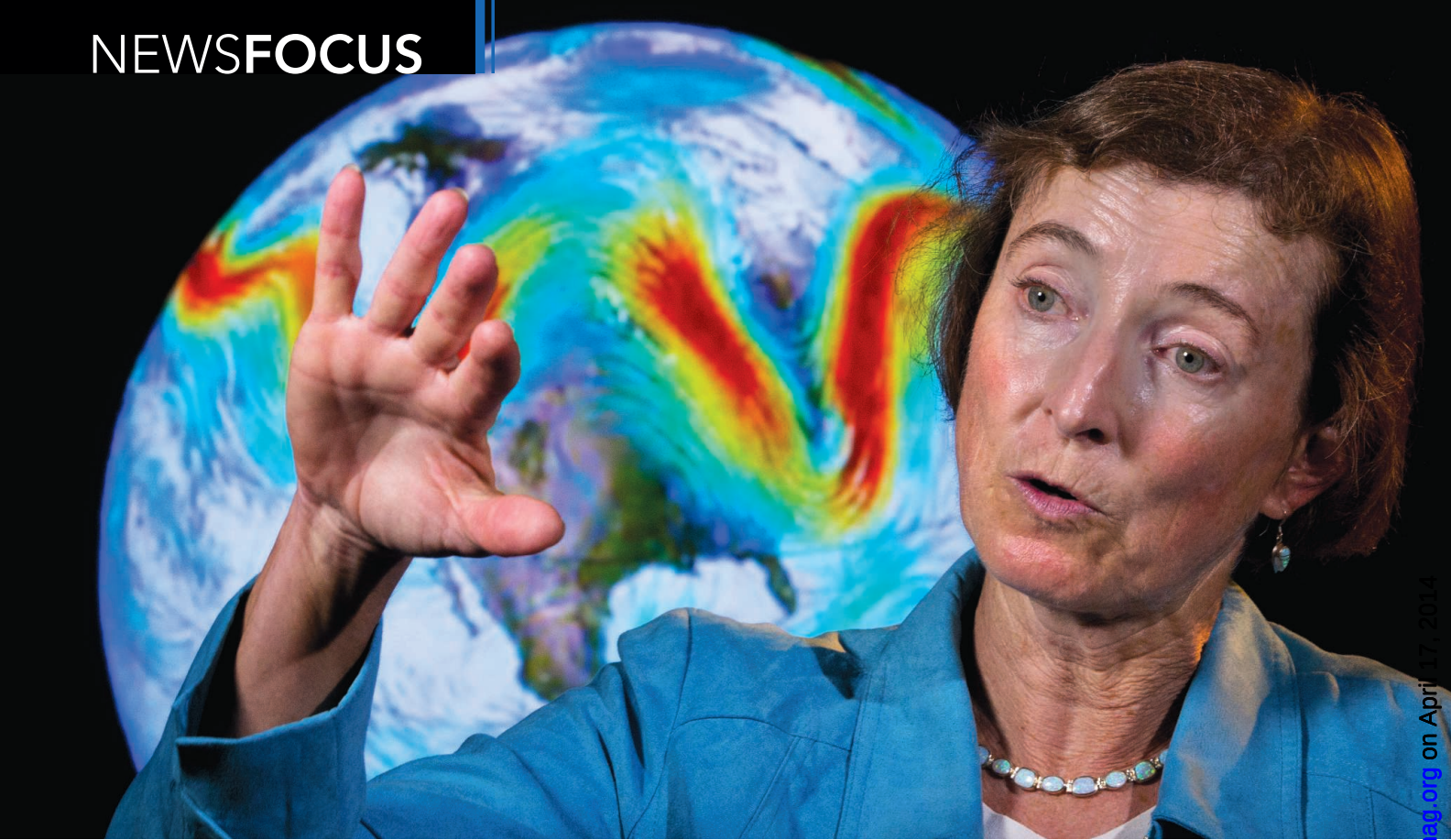

CREDIT: JACQUELYN MARTIN/AP PHOTO

Into the Maelstrom

Jennifer Francis has made waves linking the melting Arctic to extreme weather around the world. But a storm of criticism has forced the climate scientist to defend her hypothesis

When 40 climate experts huddled in a small conference room near Washington, D.C., last September, all eyes were on an atmospheric scientist named Jennifer Francis. Three years ago, Francis proposed that the warming Arctic is changing weather patterns in temperate latitudes by altering the behavior of the northern polar jet stream, the high, fast-moving river of air that snakes around the top of the world. The idea neatly linked climate change to weather, and it has resonated with the press, the public, and powerful policymakers. But that day, Francis knew that many of her colleagues—including some in that room—were deeply skeptical of the idea, and irritated by its high profile.

Sometimes, Francis is anxious before high-pressure talks and wakes before dawn. Not this time, even though the National Academy of Sciences had assembled the group essentially to scrutinize her hypothesis. "I wasn't nervous," she recently recalled. "I was prepared for the pushback."

It came fast and hard. Just one slide into her talk, before she could show a single data point, a colleague named Martin Hoerling raised a challenge. "I'll answer that with my next figure," Francis calmly responded, her bright blue eyes wide open. Two minutes later, Hoerling interrupted again, calling a figure "arbitrary." Francis, unruffled, parried—only to have Hoerling jab again.

Francis presented the evidence for her hypothesis as an orderly chain of events. "I challenged every link in the chain," recalls Hoerling, an atmospheric dynamicist at the National Oceanic and Atmospheric Administration's (NOAA's) Earth System Research Laboratory in Boulder, Colorado. Eventually, the workshop's organizer had to intervene. No more questions "so the dissertation defense can go on," nervously joked David Robinson, a climatologist at Rutgers University in New Brunswick, New Jersey, where Francis also works.

Later, some attendees praised Francis's performance. "The way [Hoerling] aggressively interrupted was unusual," says Arctic scientist Walt Meier of NASA's Goddard Space Flight Center in Greenbelt, Maryland. "But she handled it very well, with grace."

Hoerling's assessment? "She was unpersuasive," he says. "The hypothesis is pretty much dead in the water."

A stiff headwind

Francis's hypothesis has divided colleagues ever since she first proposed it in 2011, and the divisions have only deepened as Francis became a go-to climate scientist for reporters, a marquee speaker at major conferences, and an informal consultant to John Holdren, President Barack Obama's science adviser. "It's become a shooting match over her work," says atmospheric dynamicist Walter Robinson of North Carolina State University in Raleigh. "Which side are you on?"

More than scientific bragging rights are at stake. If a warming Arctic is already affecting weather in the midlatitudes, then climate change "no longer becomes something that's remote, affecting polar bears," Meier says. Instead, it's a day-to-day reality affecting billions of people—and a challenge to policymakers responsible for assessing and reducing the risks.

Published by AAAS

Jet setter. Jennifer Francis has proposed that Arctic warming is altering the polar jet stream.

Yet to many Francis critics, the attention she has received is premature, a product of unusual weather in the United States and Francis's cheerfully outgoing and insistent style. Hoerling, for one, says Francis is driving "a campaign. … This single person has been able to promulgate a conjecture into an apparent explanation of everything."

"I can't help it if the media and public are interested in my research," Francis responds. But she readily admits that all the evidence is not in and concedes that the public interest has inverted the normal life cycle of a scientific controversy. "Usually a hypothesis gets tested … the conclusions are solid and then it becomes news," she says. But in this case, says Stephen Vavrus, a climate modeler at the University of Wisconsin, Madison, who collaborates with Francis, "Jennifer and I have been forced into the uncomfortable position of defending—or at least explaining—our position before the scientific process has run its course."

Clouds on the horizon

Seeking out adversity is part of Francis's character. In 1980, after her junior year in college, she and her to-be husband Peter overhauled a 14-meter sailboat named *Nunaga* and sailed around the globe, logging almost 100,000 kilometers over 5 years. They used a sextant to navigate and drew crude weather maps on acetate, using naval data broadcast over the radio in Morse code. Many circumnavigators make the "milk run," sticking to the relatively bucolic tropics. The pair instead pushed the limits, enduring punishing winds to round Cape Horn, dipping into the "Roaring Forties" off New Zealand, and dodging ice floes some 900 kilometers from the North Pole. At one point they struggled to fix a broken rudder during a fierce winter storm in the Tasman Sea. "We regularly placed our lives in the other's hands," Peter later wrote in a self-published volume. His wife, meanwhile, "matured from a young woman to an adult."

The Arctic foray deeply affected Francis, now 56. "I just sort of fell in love with the light up there," she says. She had been studying to be a dentist, but she switched to meteorology after returning to school, focusing subsequent graduate work on Arctic forecasting. Later, as a research professor at Rutgers, she published respected analyses of the Arctic climate with a focus on sea ice, which has lost roughly 75% of its fall volume since 1980.

It was a second circumnavigation of the globe, beginning in 2009, that inspired what one might call the Francis hypothesis. (This time the crew included her 12-year-old son and 14-year-old daughter.) "Gazing out at the waves, you have a lot of time to think out there," she says. Francis had been studying how a changing climate was affecting the Arctic. At sea, she flipped the equation: "I started to wonder how much the Arctic was affecting the system."

Upon return, she e-mailed Vavrus in January 2011 with a "thought I have been noodling." The Arctic is warming faster than the midlatitudes, she noted, a phenomenon known as Arctic amplification. Could that amplification—2°C more warming than the rest of the globe over the past 2 decades—be changing the behavior of the polar jet stream, with global consequences?

> "I can't help it if the media and public are interested in my research."
>
> JENNIFER FRANCIS, RUTGERS UNIVERSITY

Studies dating back to the 1970s had hinted at the idea, which turns some conventional wisdom about climate change on its head. Traditionally, researchers have attributed the rapid Arctic warming to local drivers such as the loss of ice and snow. In other words, the Arctic is generally seen as the victim, not the perpetrator.

Francis had doubts, however, based on her observations of the northern polar jet stream. First recognized by scientists in the 1890s, this meandering torrent, which can be up to 200 kilometers across, flows west to east some 7 to 12 km above Earth's surface at speeds of up to 400 km per hour. It forms a wavy ring around the North Pole, and typically marks the border between colder, low-pressure polar air masses inside the ring (called the polar vortex), and warmer, higher pressure air to the south.

By the time Francis and Vavrus began talking, she already suspected the jet stream was changing. In 2009, she and colleagues published a paper suggesting that its west-to-east winds were weakening, or slowing, especially after Arctic summers with less sea ice. Francis blamed Arctic warming. By reducing the air pressure gradient between the Arctic and the midlatitudes, she argued, amplification might be robbing the jet stream of the engine that drives its flow (see graphic, p. 252).

If so, Arctic amplification could be shaping weather farther south. Researchers have come to understand that shifts in the path and speed of the jet stream exert a powerful influence over weather in the Northern Hemisphere. When the jet meanders far to the south over North America in winter, for instance, the result is cold snaps; when it meanders far to the north, temperatures can warm well above normal.

Building on that work, Francis and Vavrus began examining changes in the amplitude of jet stream meanders, or how far the crests of its bends reach north and south. Combing through atmospheric data, they found that the amplitudes in the fall and winter had increased by roughly 150 kilometers over the past 30 years, as the Arctic warmed. The northern peaks (called ridges by meteorologists) tended to stretch farther toward the Arctic, they found. The southern dips, known as troughs, were apparently affected less, but overall the jet stream seemed to be becoming more sinuous.

Like the weakening of the winds themselves, that increased "waviness," as some researchers call it, would tend to slow the eastward movement of weather patterns. The result: Weather conditions of all sorts—dry periods and warm spells, or storms and cold snaps—would persist. In North America, for example, large pools of Arctic air would linger longer over the continent, as they did during this past winter.

The end result of all that slower motion, Francis believes, is more persistent weather that could be more extreme—and she said as much at a meeting of the American Geophysical Union in San Francisco in late 2011. As examples, she pointed to weather events of the previous 2 years—long, snowy winters in the eastern United States and Europe, a lengthy Texas heat wave, and a record-breaking rainy spell in the U.S. Northeast. All were "consistent" with her analysis, Francis said.

Checking the barometer

After that talk, "I was mobbed," Francis recalls. A few months later, in March 2012, Francis and Vavrus formally outlined their idea in *Geophysical Research Letters* (*GRL*). The timing was uncanny: Temperatures in the United States were skyrocketing again. Within weeks, *The New York Times* ran a front-page story on the "surreal heat wave" and a subsequent frigid cold snap. Francis was the first

scientist quoted. "The question really is not whether the loss of the sea ice can be affecting the atmospheric circulation on a large scale," she said. "The question is, how can it not be?"

"And then my life changed," Francis says. Before the *GRL* paper appeared, she estimates she spent just one-quarter of her time working on outreach and communication. Soon after, that fraction rose to 80%. Since 2011, she has logged more than 150 media mentions and speaking engagements. She's an articulate scientist, after all, with a surprising take on a topic that everyone loves to talk about: the weather.

40-knot winds

As Francis has accumulated media appearances, however, opposition to the hypothesis has grown steadily among researchers. In early 2011, for instance, she and Vavrus submitted a proposal to analyze data and model the phenomenon to the National Science Foundation's (NSF's) climate dynamics division. It got generally positive reviews, although it didn't make the funding cut. A year later, however, despite revisions "the reviews of our second attempt were much worse," Francis says. "That's when we realized there was a backlash." (NSF's Arctic science program ultimately funded the work.)

Criticism is coming from three directions. First, scientists have challenged the pair's analysis of historical data, questioning whether it really shows that the polar jet stream's west-to-east winds are slowing and its meanders stretching. Last year in *GRL*, for example, climate modeler James Screen of the University of Exeter in the United Kingdom and a colleague reported that they had measured the meanders and found few statistically significant changes. "It could easily just be natural variability," Screen says. The pair did find a reduction in the size of the jet stream's vertical waves, which rise and fall perpendicular to Earth's surface. But that is inconsistent with the Francis hypothesis, they say, because it would translate into fewer temperature extremes at any specific latitude. Last year, climate dynamicist Elizabeth Barnes of Colorado State University, Fort Collins, also analyzed the data, and concluded that the Francis and Vavrus findings were an "artifact of [their] methodology."

Climate modelers also have offered heckles, saying their computer simulations have mostly failed to confirm the hypothesis. In their models, they've dialed up future greenhouse warming or reduced Arctic sea ice—both factors that should amp up Arctic amplification—but failed to produce a slower, more meandering jet stream. And models that simply reproduce existing conditions, Screen says, have to run for the equivalent of more than "60 years before I start to see anything" similar to Francis's observations.

The most vociferous critiques, however, have come from researchers who study atmospheric dynamics, or the many mechanisms that jostle and shape air masses. Given the Arctic's relatively puny influence over the planet's atmospheric energy flows, the notion that it can alter the jet stream "is just plain wrong," says dynamicist Kevin Trenberth of the National Center for Atmospheric Research in Boulder. The more likely culprit, he says, is natural variability driven by the tropics, where Earth gets its largest input of solar energy.

Such variability, Trenberth says, could explain the jet stream's giant curvy shape this past January, which brought record chill to the southeastern United States, warm temperatures to Alaska, and made "polar vortex" a household term. At the time, a massive amount of so-called latent heat was accumulating in the tropical Pacific, Trenberth notes, in an incipient El Niño event. Parcels of warm air from the tropics may have forced the jet stream northward in one place, causing it to meander southward farther east. "It may not be that Arctic amplification is causing a wavier jet stream, it may be that a wavier jet stream is causing Arctic amplification," he says.

"I understand that people would be skeptical," Francis says. "It's a new paradigm." But she counsels patience. She notes that evidence of Arctic amplification itself has emerged from the statistical noise only in the last 15 or so years, so it may take time for the changes to the jet stream to become statistically significant. And she believes the modeling experiments that fail to simulate a more meandering jet stream are biased, because they don't include sufficiently robust Arctic amplification.

Such arguments have persuaded some colleagues to at least wait and see. Oceanographer James Overland of NOAA's Pacific Marine Environmental Laboratory in Seattle, Washington, for example, says, "I find the tropical explanation for the recent behavior of the jet stream no less implausible than the Arctic one." And he suspects that, as data accumulate, the dynamicists will come to gain a greater appreciation for the Arctic's role.

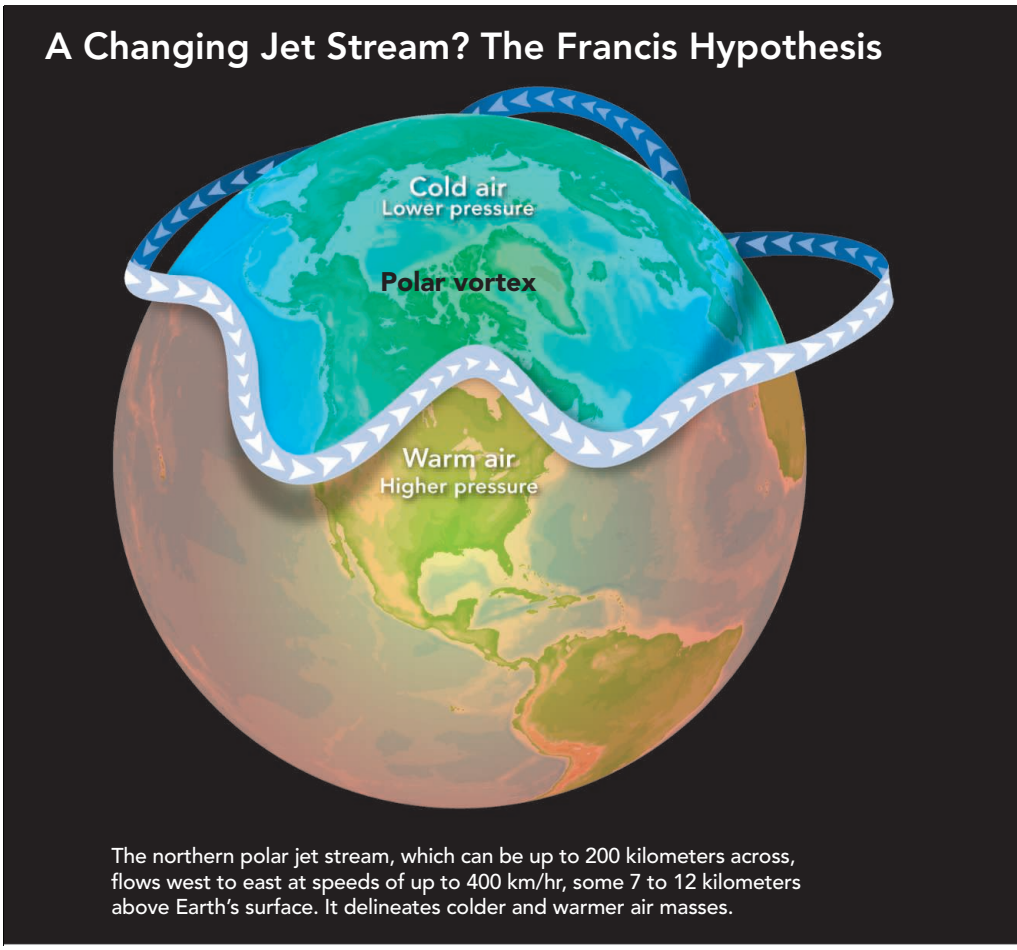

The northern polar jet stream, which can be up to 200 kilometers across, flows west to east at speeds of up to 400 km/hr, some 7 to 12 kilometers above Earth's surface. It delineates colder and warmer air masses.

CREDIT: C. SMITH/*SCIENCE*

Published by AAAS

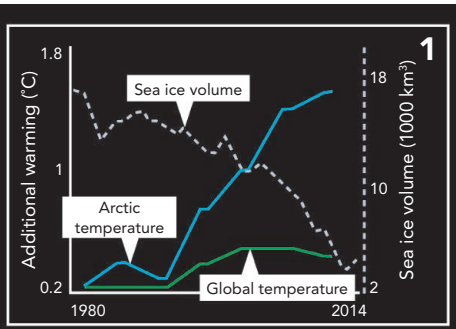

Declines in sea ice cover and other factors are driving "Arctic amplification," or the more rapid warming of the Arctic than warming of the globe as a whole.

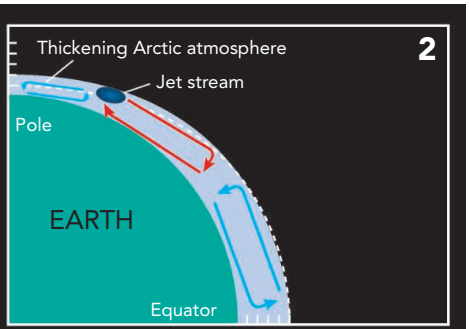

Jennifer Francis believes Arctic warming is altering the jet stream's behavior, in particular by reducing the pressure gradient between the colder, thinner polar atmosphere and the warmer, thicker atmosphere to the south.

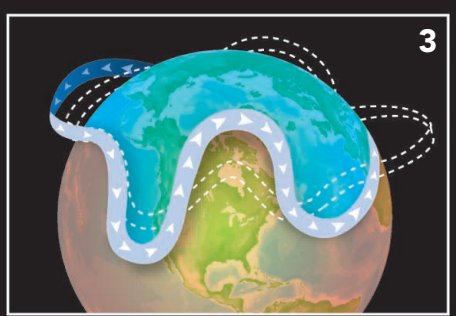

The result, she hypothesizes, is a slower, more sinuous jet stream with tips that stretch farther north.

The "wavier" jet stream causes longer lasting weather patterns, such as the southward bend that brought record cold to much of eastern North America this past winter.

CREDIT: C. SMITH/*SCIENCE*

Batten the hatches

Scientists may debate the reasons for this past January's cold spell in the eastern United States, but one clear effect was to direct more attention to the Francis hypothesis. In early January, Francis was at home in Marion, Massachusetts, responding to a blizzard of e-mails from reporters, her cat Kessie on her lap. Then came a message from an unexpected address. "I have been following with interest your work," wrote White House science adviser Holdren.

"I fell off my chair first, and started breathing again," Francis recalls.

Holdren wanted to learn more about her research, he wrote, and any relevant unpublished work. "I work for a very smart President," he explained in a follow-up message. "I don't go near him with any chart I can't completely explain!" Francis says she "fell off my chair again."

That same day, 8 January, Holdren appeared in a YouTube video produced by the White House in which he essentially endorsed her hypothesis. "There will be continuing debate," he said over clips of stark Arctic ice and blowing snowdrifts. "But I believe the odds are that we can expect, as a result of global warming, to see more of this pattern of extreme cold in the midlatitudes."

"I was blown away that he was so convinced," Francis says. She was hardly alone. When dynamicist John Wallace of the University of Washington, Seattle, saw the video, he was appalled. He quickly recruited four colleagues to pen an op-ed challenging Holdren's message. "Normally, I don't have time to write letters to newspapers," says Wallace, who didn't mention Holdren by name in the piece. The Francis hypothesis "deserves a fair hearing," the quintet wrote in a letter that eventually appeared in *Science* (14 February, p. 729). "But to make it the centerpiece of the public discourse on global warming is inappropriate." Later, in another article, Wallace warned: "When the public becomes confused, the carefully considered scientific consensus [on climate] becomes vulnerable to attack."

"That really hurt," Francis says. But she won't back down from speaking out. The discussion "in the media has really galvanized some people to realize climate change is happening right now," she says. An oceanographer who collaborates with Francis, Charles Greene of Cornell University, agrees. "When we see something happening," he says, "we should put it out there."

Francis has taken to that mission with zeal. She sends reporters long e-mails answering their questions, carefully tracks her media hits, and continually rehones and rehearses her presentations. After a recent talk at the annual meeting of AAAS (which publishes *Science*), she was approached by Lewis Branscomb, 87, a U.S. science policy luminary with lengthy experience in Washington. "That was the best general audience lecture I have ever heard," Branscomb told her.

She's also learned from some mistakes. In an incident this past January, Francis asserted that the "intent" of one of her critics—Colorado State's Barnes—"seems less than objective." That personal assault was included in a long technical e-mail to a weather blogger, and the comments drew a public scolding from prominent climate blogger Judith Curry of the Georgia Institute of Technology in Atlanta. Francis promptly apologized. "That e-mail was written at 5 o'clock in the morning while I was on a college tour with my daughter," Francis says. "Usually I like to let things simmer."

She has conceded some scientific points, too. She largely dropped one part of her hypothesis—that a curvier jet stream is leading to more atmospheric "blocking"—after Barnes published an analysis challenging the idea.

Francis predicts that "within a few years, as Arctic amplification continues, we will have enough data to know whether or not we're right." In the meantime, she is as comfortable as ever weathering the squalls. "I've developed a thicker skin," she says. At a recent meteorology conference, she suggested that curvier jet streams would steer more future Atlantic hurricanes west, along the path taken by Superstorm Sandy in October 2012. That contention drew fire from critics, including modelers whose work suggests the opposite. Her reaction? "That was kind of fun because people were irately skeptical," she says.

To put it all in perspective, Francis thinks back to the more serious dangers she faced at age 22 aboard the *Nunaga*. "Maybe this acceptance of higher risk was something I was more comfortable with than most, and maybe it translated to my research as having more confidence in myself—my judgment and my ability," she writes in an e-mail. The title of the book, which documents that life-changing journey, seems apt these days in more ways than one: *A Path to Extremes*.

–ELI KINTISCH

Published by AAAS

LETTERS

edited by Jennifer Sills

Climate Discussion Echoes Tobacco Debate

IN 1962, LUTHER TERRY, THE SURGEON GENERAL OF THE PUBLIC HEALTH SERVICE, ESTABLISHED the Surgeon General's Advisory Committee on Smoking and Health. On 11 January 1964, he released the committee's report, "Smoking and Health: Report of the Advisory Committee to the Surgeon General of the United States" (*1*), which reviewed the existing science and concluded that lung cancer and chronic bronchitis are causally linked to cigarette smoking.

This landmark report marked a critical pivot in our national response to tobacco products, leading to packet warning labels, restrictions on cigarette advertising, and anti-tobacco campaigns. But it by no means ended the debate about what we now know to be horrifically negative public health impacts of tobacco use. Instead, it galvanized the tobacco companies, through their industry-funded Tobacco Institute, to publish a large number of "white papers" to rebut scientific reports critical of tobacco (*2*). The demise of the Tobacco Institute came in 1998, as part of the Tobacco Master Settlement Agreement, where 46 state attorneys general obtained $206 billion dollars over 25 years from the tobacco industry for its culpability in creating a public health crisis (*3*).

This bit of history has important parallels to our national discussion of climate change. On 18 March, AAAS released a report produced by a panel of 13 prominent experts chaired by the Nobel prize–winning scientist Mario Molina, titled "What We Know: The Reality, Risks and Response to Climate Change" (http://whatweknow.aaas.org/get-the-facts). As was the case when Luther Terry issued his tobacco report in 1964, no new science is being offered in the climate report. Instead, it presents a brief review of the key relevant scientific conclusions. Just as the 1964 report included discussion of the possibility that tobacco caused cardiovascular disease, the "What We Know" paper speaks to the possibility of abrupt climate change risks. Another important parallel is that the 1964 report was issued under the imprimatur of a highly trusted and authoritative source. AAAS, as the largest general membership society of scientists in the world, holds a similar position of trust.

Yet another important parallel between the AAAS "What We Know" report and the 1964 Surgeon General's report is the political and social context into which it is launched. As historians Naomi Oreskes and Eric Conway depict in their book *Merchants of Doubt* (*4*), the tobacco issue created an industry playbook for running misinformation campaigns to mislead the public and deny well-established scientific conclusions. As the authors document, the industry misinformation campaign on climate change is in high gear and achieving results: Many Americans think that climate experts still have much disagreement about whether human-caused climate change is happening (*5*).

Today it's inconceivable that an American decision-maker would risk the public opprobrium that would result from expressing skepticism that tobacco causes cancer. We believe that it is an obligation of all scientists to hasten the day when the same is true for climate change, where the stakes are even higher.

ROBERT J. GOULD[1]* AND EDWARD MAIBACH[2]

[1]One Degree Strategies, LLC, Rockville, MD 20852, USA. [2]Center for Climate Change Communication, George Mason University, Fairfax, VA 22030, USA.

*Corresponding author. E-mail: rob@onedegreestrategies.com

References

1. L. Terry *et al.*, "Smoking and Health: Report of the Advisory Committee to the Surgeon General of the United States" (U-23 Department of Health, Education and Welfare, Public Health Service Publication No. 1103, 1964).
2. Tobacco Smoke and the Nonsmoker: Scientific Integrity at the Crossroads (Tobacco Institute, Washington, DC, 1986); http://legacy.library.ucsf.edu/documentStore/w/a/l/wal03e00/Swal03e00.pdf.
3. Master Settlement Agreement (National Association of Attorneys General, 1998).
4. N. Oreskes, E. M. Conway, *Merchants of Doubt* (Bloomsbury Press, New York, 2010).
5. A. Leiserowitz *et al.*, "Climate change in the American mind: Americans' global warming beliefs" (Yale Project on Climate Change Communication and the George Mason University Center for Climate Change Communication, 2013); http://environment.yale.edu/climate-communication/files/Climate-Beliefs-April-2013.pdf.

Letters to the Editor

Letters (~300 words) discuss material published in *Science* in the past 3 months or matters of general interest. Letters are not acknowledged upon receipt. Whether published in full or in part, Letters are subject to editing for clarity and space. Letters submitted, published, or posted elsewhere, in print or online, will be disqualified. To submit a Letter, go to www.submit2science.org.

Integrating Psychological Treatment Approaches

M. BALTER'S NEWS FOCUS STORY "TALKING back to madness" (14 March, p. 1190) will hopefully help combat the myth that psychotherapy and "biological" treatments are somehow antithetical. They are not. Psychotherapy has biological effects on the brain that are often similar to those seen with medication (*1*), and medication has psychological as well as biological effects.

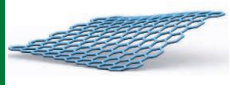

Biological applications of graphene

261

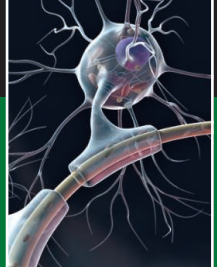

Myelin structure

264

Similarly, it is unhelpful to see social, psychological, and biological approaches to mental disorder as distinct. They are different languages used to describe a single phenomenon. If I am depressed, I can use the language of sociology, pointing to an impoverished upbringing and social exclusion; fix these politically, and my mood may improve. Alternatively, I can use the language of psychology, highlighting childhood conflict and poor self-esteem; address these with a therapist, and my depression may resolve. I could also use the language of biology and comment on my serotonin or norepinephrine levels, and, although our knowledge of the brain remains limited, antidepressant medication may prove effective.

The News Focus story states that "advocates of psychological approaches are engaging with patients' symptoms" and that this is "a radical departure." This may indeed be "radical," but it certainly is not new. In 1810, Dr. William Hallaran, an asylum doctor in Ireland (*2*), "made it a special point on my review days, to converse…with each patient, on the subject which appeared to be most welcome to his humor. By a regular attention to the duties of this parade, I am generally received with…politeness and decorum…and the advantages flowing from it are almost incredible" [(*3*), p. 47]. The more things change, the more they stay the same.

BRENDAN D. KELLY

Department of Adult Psychiatry, University College Dublin School of Medicine and Medical Science, Mater Misericordiae University Hospital, Dublin 7, Ireland. E-mail: brendan.kelly@ucd.ie

References

1. H. Karlsson, *Psychiatr. Times* **28**, 8 (2011).
2. B. D. Kelly, *Ir. J. Med. Sci.* **177**, 79 (2008).
3. W. S. Hallaran, *An Enquiry into the Causes Producing the Extraordinary Addition to the Number of Insane* (Edwards and Savage, Cork, Ireland, 1810).

Uganda Homosexuality Report in Context

THE NEWS & ANALYSIS STORY "SCIENCE MISused to justify Ugandan antigay law" (M. Balter, 28 February, p. 956) discusses the claims of Uganda's president that a scientific report convinced him that homosexuality is behavioral, not genetic. Citing these findings, he then signed an Anti-Homosexuality Bill, a huge setback in human rights for gays and lesbians.

I was an author of the report in question (*1*). We provided an unbiased review of the scientific literature. It does not say that homosexuality is a social abnormality, as some media and political forces claimed. To the contrary, it clearly stipulates that homosexuality is not a disease and that the World Health Organization and American Psychological Association have removed it from their list of psychiatric illnesses.

Some say we could have chosen to boycott participation altogether. I believe that if scientists had refused to carry out this research because we feared (rightfully) that our work would be misrepresented, we would have failed to do our duty as experts, which is to inform the public. Although the results were discouraging, it is worth recognizing that a developing country has relied on its scientists to inform policy. That alone is a step in the right direction.

MISAKI WAYENGERA

Unit of Genetics and Genomics, Department of Pathology, School of Biomedical Sciences, Makerere University College of Health Sciences, Kampala, Uganda. E-mail: wmisaki@yahoo.com

Reference

1. Uganda Ministry of Health, "Scientific evidence on homosexuality" (23 February 2014); http://news.sciencemag.org/sites/default/files/FINAL%20MOH%20STATEMENT%20ON%20HOMOSEXUALITY%2024TH%20FEBRUARY%202014.doc.

CORRECTIONS AND CLARIFICATIONS

Reports: "Nanoscale atoms in solid-state chemistry" by X. Roy *et al*. (12 July 2013, p. 157, published online 6 June 2013). In several places on p. 159, the Greek symbols χ and μ were mistakenly replaced by the letters c and m. The HTML and PDF versions online have been corrected.

LIFE IN SCIENCE

Weeds Making Waves

Phragmites australis is an aggressive, invasive weed that cannot be purged. It grows 6 meters tall and pushes out many wetland species. We have tried to cut it, poison it, burn it, bury it, till it, and drown it, and yet its tufted heads still sway in the wind. Many a scientist has tried to figure out how to deal with this invasive species, and each has met with frustration.

Middle-school teacher John Reynolds tried a different strategy: Instead of eradicating the invasive weed, he used it to build a boat. For three months, John harvested the two-story-tall reedy weeds and lashed them together according to his own design.

When he finished, I received an e-mail. "We'll launch this afternoon if you're ready." In February? In Massachusetts? My blood chilled instantly. But I had to see if it floated.

I donned my waders to protect myself against the 37° Atlantic water. John and some of his students were in wetsuits ready to jump in. The boat was twice as long as the truck bed and had a curved bow like a Polynesian reed boat. I thought both the boat and my friend's willingness to jump in the water were crazy.

But it floated. Even when three people piled on it. It was still floating 2 hours later when the sun inched down the horizon. A seaworthy boat made out of weeds.

Science relies on ingenuity. While converting a two-story weed into boats may not be the most effective management strategy for *Phragmites*, it's certainly an idea that's worth floating.

DAVID SAMUEL JOHNSON

Marine Biological Laboratory, Woods Hole, MA 02543, USA. E-mail: manayunkia@gmail.com

EDITOR'S NOTE

This is an occasional feature highlighting some of the day-to-day humorous realities that face our readers. Can you top this? Submit your best stories at www.submit2science.org.

CREDIT: PETER AND MARIA HOEY/WWW.PETERHOEY.COM

CLIMATE CHANGE

On Scientists and Advocacy

Gavin A. Schmidt

Last year, I asked a crowd of a few hundred geoscientists from around the world what positions related to climate science and policy they would be comfortable publicly advocating. I presented a list of recommendations that included increased research funding, greater resources for education, and specific emission reduction technologies. In almost every case, a majority of the audience felt comfortable arguing for them. The only clear exceptions were related to geo-engineering research and nuclear power. I had queried the researchers because the relationship between science and advocacy is marked by many assumptions and little clarity. This despite the fact that the basic question of how scientists can be responsible advocates on issues related to their expertise has been discussed for decades—most notably in the case of climate change by the late Stephen Schneider.

Behind the Curve
Science and the Politics of Global Warming

by Joshua P. Howe
University of Washington Press, Seattle, 2014. 311 pp. $34.95. ISBN 9780295993683. Weyerhaeuser Environmental Books.

Schneider described in great length the importance of recognizing that it is a combination of science and values that leads to policy choices. He repeatedly stressed the importance of scientists being forthright about their values and the process by which they arrived at their advocacy position. His elucidation of the policy challenges posed by climate change [e.g., (*1*)] was far from a naive "science-only" approach, and it has been followed by many subsequent scientist-communicators (including myself).

The scientists depicted in Joshua Howe's *Behind the Curve* are nothing like Schneider. Those scientists apparently have, for over 50 years, clung to a delusion that policies arise solely from scientific facts, and they remain perplexed as to why CO_2 emissions continue to rise. Oddly enough, one of them is Schneider. This contradiction is both surprising and a little disappointing.

Howe (a historian at Reed College) offers a solid description of institutional responses to the emerging science of climate change over the past half century. The titular curve is the depiction of the ever-increasing concentration of CO_2 measured at Mauna Loa, originally by the dogged Charles D. Keeling. The trope in the title refers to the background story of climate politics but also to the slow policy responses, which do indeed lag behind the curve of the science. A more detailed analogy that Howe draws between the ups and downs of the Keeling curve and those of policy responses is less successful because the CO_2 concentration steadily continues to rise while policy responses have frequently stalled.

Howe holds that the lack of commensurate responses to the challenge of accelerating CO_2 emissions stems from the problem having been exclusively presented science-first. He states (unsurprisingly) that "as a result of their science-first approach, scientists have made tremendous strides in their understanding." However, Howe implicitly equates scientists' natural emphasis on science-first approaches to science with the idea that their advocacy must be science-only—a jump that is only weakly supported. Furthermore, Howe claims that this science-only advocacy has in turn has led to science itself becoming a political target.

There are multiple problems with this argument. For instance, Howe provides no description of what a non–science-first approach would have looked like. Indeed, given that there are no nonscientific reasons for reducing CO_2 emissions, it is hard to even imagine one. Howe's lack of recognition that scientists such as Schneider were actually fully aware that science-only is not sufficient for advocacy is odd given that Howe has clearly carefully read Schneider's last book (*2*). Stranger still is Howe's failure to recognize that anti-science political strategies often arise when science is perceived to threaten some vested religious, political, or economic interest. Any claim that political attacks on climate scientists are a unique consequence of their advocacy is ahistorical.

Much better is Howe's account of the links between previous environmental issues (ozone depletion, acid rain, and nuclear winter) and the synthesis of atmospheric, oceanographic, and cryospheric knowledge that now informs our understanding of climate change. (For instance, he offers interesting details about the supersonic transport plane project.) The book's best parts deal with the details of policy discussions. In them, Howe jumps from acronym to acronym with the balance of wonkish ballerina, although on more than a few minor points, better fact checking would have helped.

Overall, I was disappointed in the shallowness of Howe's engagement with his central idea. Early on, he claims that the only legitimate way for scientists to advocate is to ask for more science funding, a position that reflects a very narrow and unrealistic view of what scientists supposedly value. This narrowness of vision persists throughout the book, and clichéd descriptions of scientists as political naifs are a constant refrain. *Behind the Curve* comes across not as a critique of science-first approaches to policy that have failed but rather as criticism of scientists first for failures in policy.

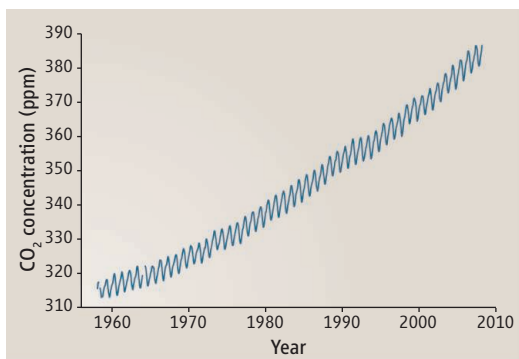

Keeling's curve.

The real hurdle to enacting policies commensurate with the magnitude of the climate change challenge is simply that we all have a large vested interest in the (increasingly unsustainable) status quo. This makes it a more difficult problem than any of the environmental issues previously identified by scientists. Nonetheless, science and scientists still have much to offer in finding ways forward, and, as my informal survey demonstrated, there is no shortage of scientists who have a far more nuanced approach to advocacy than Howe assumes. As a scientist-advocate myself (*3*), I think that is a hopeful sign.

The reviewer is at the NASA Goddard Institute for Space Studies, 2880 Broadway, New York, NY 10025, USA. E-mail: gs210@columbia.edu

References

1. www.agci.org/library/presentations/about/presentation_details.php?recordID=10192.
2. S. H. Schneider, *Science As Contact Sport: Inside the Battle to Save Earth's Climate* (National Geographic, Washington, DC, 2009).
3. www.youtube.com/watch?v=CJC1phPS6IA.

10.1126/science.1251819

Published by AAAS

SCIENCE AND REGULATION

Particulate Matter Matters

Quasi-experimental evidence is needed on the relations between human health and airborne particulate matter.

Francesca Dominici,[1]* Michael Greenstone,[2,3]*† Cass R. Sunstein[4]*

April 22nd is the 45th Earth Day, which marks the birth of the modern environmental movement that helped lead to the creation of the U.S. Environmental Protection Agency, the Clean Air Act Amendments, and the Clean Water Act. The result has been substantial improvements in environmental quality in the United States. Today, developing countries are contending with levels of pollution that are even higher than those in the United States before the first Earth Day. And in a period of considerable economic difficulty, the United States is trying to strike the right balance between the benefits and costs of further reductions in pollution.

Under federal law, the U.S. Office of Management and Budget (OMB) must report to Congress annually on the benefits and costs of major federal regulations. It is remarkable but true that from 2003 through 2012, reductions of emissions of just one category of pollutant—particulate matter (PM)—have accounted for about one-third to one-half of the total monetized benefits of all significant federal regulations and, by some estimates, more than that (*1*). With the estimated benefits of PM reductions playing such a central role in regulatory policy, it is critical to ensure that the estimated health benefits are based on the best available evidence. If the estimates are biased upward (downward), then the regulations may be too stringent (lenient).

In the last 40 years, the evidence that has led to revisions of the U.S. National Ambient Air Quality Standards has come mainly from observational studies aimed at estimating an exposure-response relation (*2*). But associational approaches to inferring causal relations can be highly sensitive to the statistical model and covariates used to adjust for confounding. Indeed, the U.S. government itself has drawn attention to the "uncertainty in the reduction of premature deaths associated with reduction in particulate matter" (*3*).

There is a growing consensus in economics, political science, statistics, and other fields that the associational or regression approach to inferring causal relations—on the basis of adjustment with observable confounders—is unreliable in many settings (*4*–*6*). We discuss how quasi-experimental (QE) techniques provide an opportunity to improve understanding of the relation between human health and regulation of air pollution from particulates.

Beijing shrouded in smog.

CREDIT: ISTOCKPHOTO

[1]Department of Biostatistics, Harvard School of Public Health, Boston, MA 02115, USA. [2]Department of Economics, Massachusetts Institute of Technology, Cambridge, MA 02142, USA. [3]National Bureau of Economic Research, Cambridge, MA 02138, USA. [4]Harvard Law School, Cambridge, MA 02138, USA. *All authors contributed equally and are listed alphabetically. †Corresponding author. E-mail: mgreenst@mit.edu.

Limits of Observational Studies

Randomized control trials would be the best way to measure the health benefits of PM reductions (*4*), but for obvious reasons, true experiments are generally not feasible. One exception is chamber studies of controlled exposure, but such studies rely on healthy subjects and focus only on end points of limited value.

An observational study of the health effects of particulates boils down to a comparison of health outcomes across space and/or time among places with differing levels of air pollution. For example, an influential study compared the health outcomes of individuals who lived in six cities with varying levels of air pollution (*2*). For such studies, one challenge is that the people who live in the more polluted places frequently have differing initial levels of health (e.g., due to differences in smoking rates, diet, or socioeconomic status) from the levels of people who live in the less polluted places. Another challenge is that there may be locational determinants of health (e.g., hospital quality or water pollution) that differ across the places and are correlated with air pollution levels. Further, people may choose to live in locations on the basis of their (likely unobserved) susceptibility to pollution and other related health problems, and/or they may spend greater resources on self-protection in polluted locations in ways that are not measured in available data sets.

Statistical methods, based mostly on regression approaches, aim to "adjust" for observed confounders, by including the available measures of behavioral, socioeconomic, and locational differences as covariates in the regression model. Since many determinants of health are unobserved, these methods that rely on adjustment for observed confounders can lead to biased estimates of the relation between health and particulates.

In 2010, the American Heart Association conducted a review of the available observational studies exploring the relation between fine particulate matter [diameter <2.5 μm ($PM_{2.5}$)] exposure and mortality and car-

Published by AAAS

diovascular morbidity (*7*). The authors concluded: "It is the opinion of the writing group that the overall evidence is consistent with a causal relationship between $PM_{2.5}$ exposure and cardiovascular morbidity and mortality."

Thanks to the rigorous statistical methods that have been developed and applied to the assembled data, and to the enormous effort of government agencies and specific investigators in conducting independent reanalyses [e.g., (*8*)], analyses of observational data have had a large impact on air-quality regulations and on the supporting analyses of their accompanying benefits.

Nonetheless, legitimate concerns remain. Although important progress has been made in adjusting for confounding in observational studies (*9*–*13*), there may be unobserved differences across the populations and locations, and sufficient adjustments may not have been made for the measurable differences.

This point is illustrated in the table, which summarizes evidence from (*14*) that examines the cross-sectional relation between total suspended particulates (TSPs) and mortality rates (deaths per 10,000) among the more than 30 million individuals age 50 and over living in the 501 U.S. counties monitored for TSP in the years 1970–72. The first data column reports on a model that does not include any adjustment for observed confounders. The estimates in the second data column are adjusted for the age distribution, gender, and race of the population and detailed county-level per capita measures of employment; public transfers (e.g., food stamps, Medicare payments); and health expenditures. The rows report on the separate estimation of these two models on mortality rates in each year from 1969 through 1974. The entries report the impact of a 1 $\mu g/m^3$ increase in TSPs on the mortality rate.

Of the 12 regression estimates, two show a significant positive association between TSPs and mortality, two perversely show a significant negative association, and the remaining eight would be judged statistically insignificant at conventional levels. In this setting, the addition of covariates causes a reduction in the coefficients, but this is not generalizable to other studies, as bias due to confounding can go in either direction. Overall, it is apparent that with these data and the available covariates, the association between TSPs and mortality rates varies widely within a year across models and within a model across years.

This admittedly provocative example illustrates our point: Associational approaches to inferring causal relations can be highly sensitive to the choice of the statistical model and set of available covariates that are used to adjust for confounding.

Quasi-Experiments as an Alternative

QE evaluation techniques provide an opportunity to improve understanding of the relation between human health and particulates air pollution. In a QE evaluation, the researcher compares outcomes between a treatment group and a control group, just as in a classical experiment; but treatment status is determined by politics, an accident, a regulatory action, or some other action beyond the researcher's control. The key difference with an observational study in this setting is that the QE approach is devoted to identifying treatment-induced variation in particulates that plausibly mitigates confounding or omitted variables bias in the estimated relation between human health and particulates, rather than relying on the variation presented by nature and optimizing agents. Despite the "nonrandom" assignment of treatment status, it is possible to draw causal inferences from the differences in outcomes (by "outcomes," we refer to both air pollution levels and human health) between the treatment and control groups in a quasi- or natural experiment, provided certain assumptions are met.

This approach has been used extensively in recent years and has permitted more credible inferences about the impacts of a wide range of relations, including the effect of an additional year of schooling on earnings (*15*), the impact of changes in air pollution on housing prices (*16*), the effect of Medicare on mortality (*17*), and the effect of anti-discrimination laws on the earnings of African-Americans (*18*).

In fact, there is an emerging QE literature on the human health effects of air pollution that relies on designs where an "action" has affected—often drastically—the ambient levels and the chemical composition of air pollution. Some of the most well-known examples are the ban of coal sales in Dublin (*19*); the differential reduction in TSPs across the United States as a consequence of the 1981–82 recession (*20*); the air pollution reduction interventions before, during, and after the Beijing Olympic games (*21*); a steel plant strike (*22*); features of the U.S. Clean Air Act (*6*, *23*); and the Chinese policy that provided free coal for heating in cities north of the Huai River (*24*) (see sidebar). [See also (*25*–*28*) for detailed reviews.]

Although QE approaches promise more credible estimates, they are not without limitations. It is important that QE designs are able to demonstrate that observable covariates are balanced by the treatment and credibly explain why unobserved ones are likely to be balanced, too. In cases where the covariates are not balanced and/or the unobserved ones are unlikely to be balanced, QE estimates are not likely to be more credible than associational estimates. Further, QE approaches can often be demanding of the data and lack statistical power. As is the case with associational estimates, applying QE estimates to other settings (e.g., places, periods, and demographic groups) requires careful consideration and, in some cases, may be inappropriate. This challenge can be greater

Estimate of the effect of TSPs on mortality rates of adults over 50

	Adult deaths per 10,000 residents	
Adults aged over 50 (year)	No adjustment for confounders	Adjusted for confounders
1969	0.183**	0.024
	(0.062)	(0.030)
	[0.04]	[0.75]
1970	0.112*	0.022
	(0.068)	(0.024)
	[0.02]	[0.74]
1971	0.088	–0.047
	(0.091)	(0.025)
	[0.01]	[0.74]
1972	0.102	–0.130**
	(0.125)	0.050
	[0.01]	[0.72]
1973	0.208	–0.054
	(0.129)	(0.061)
	[0.02]	[0.74]
1974	0.126	–0.157***
	(0.115)	(0.050)
	[0.01]	[0.75]

TSPs and mortality rate. The association between TSPs and mortality rates can vary widely within a year across models and within a model across years. Cross-sectional parameter estimates of the effect of a 1 $\mu g/m^3$ increase in TSPs on mortality rates, heteroskedastic-consistent standard errors (in parentheses), and *R*-squared statistics (in brackets) associated with a separate regression of the mortality rate of adults over age 50 on TSPs. Adjustments for confounds include controls for age distribution, gender, race, income, employment, income assistance, and medical expenditures. *$P < 0.1$, **$P < 0.05$, ***$P < 0.01$. Modified from (*14*).

Published by AAAS

On the Wrong Side of the River

Chen *et al*. (*24*) illustrates some of the appealing features of QE designs and more specifically of a regression discontinuity (RD) design (*34*). It exploits a Chinese policy that provided free coal for winter heating in areas north of the Huai River and denied coal-based heating to the south of the river. The idea is to compare locations just north and south of the river. In this setting, the RD design relies on the assumption that any confounders (both observed and unobserved) vary smoothly with latitude, except for the availability of coal-based indoor heating, as one crosses the Huai River. The authors controlled for these potential confounders through adjustment for a flexible polynomial in distance to the river, measured as degrees latitude north of the Huai River.

The authors find that north of the river, the policy led to discrete increases in TSPs and discrete decreases in life expectancy (derived from age-specific mortality rates). The paper's headline finding is that long-term exposure to an additional 100 μg/m^3 of TSPs is associated with a reduction in life expectancy at birth of about 3.0 years (95% confidence interval: 0.4 to 5.6). Further, the paper finds that the effect of TSPs on life expectancy is largely insensitive to whether observable covariates are included in the model, which would be the case in a randomized control trial; this stands in contrast with the relations in the table that were derived from an observational study, rather than one based on a QE design.

with QE approaches where the selection of the study population is dictated by the available treatment (see the box) and therefore is beyond the researcher's controls.

A Path to Better Science and Policy

Overall, the literature makes a compelling case that airborne PM is bad for human health—it shortens lives and raises morbidity rates. However, quantitative estimates of the magnitude of the anticipated or actual public health benefits from further reductions are needed and will require careful work. Deeper understanding of this relation could greatly improve regulatory policy in coming years as regulators face two external events.

First, the Obama Administration has started a regulatory look-back initiative that aims to assess how regulations have worked in practice ("retrospective analysis") and then adjust the regulations on the basis of the results. It would be useful to know whether previous efforts to reduce particulates air pollution actually produced the projected improvements in human health [e.g., (*6*, *14*, *29*)]. Second, estimates of the health effects of PM will play a central role in numerous upcoming regulatory decisions. In making those estimates, two sets of critical questions need better answers: (i) What is the shape of the dose-response curve (e.g., would a reduction in $PM_{2.5}$ from 12 to 10 μg/m^3 produce the same health benefits as a reduction from 14 to 12)? (ii) In light of the wide range of chemical composition across particulates, can we identify chemical components of $PM_{2.5}$ and the type of emission sources that regulators should target to protect public health (without imposing unnecessary compliance costs, which would ultimately be incurred by companies, workers, and consumers)? [See also (*30*, *31*).]

A critical question is how to develop better evidence to identify not merely the existence but also the magnitude of public health benefits from cleaner air and especially from further reductions in PM (*32*). To be sure, regulators must sometimes act under considerable time pressure; the Clean Air Act sharply constrains their ability to consider costs as such; and in some circumstances, use of carefully conducted observational studies remains the only feasible option. However, the path to the best available evidence about the benefits (*33*) of reducing PM and other air pollutants lies in an increased focus on developing and using QE evidence. Such a shift would honor Earth Day by going back to its foundations, which demanded that we draw on the most reliable science to protect humanity's well-being.

References and Notes

1. Office of Management and Budget, "2013 Draft report to Congress on the benefits and costs of federal regulation and unfunded mandates on state, local, and tribal entities," pp. 14, 18, 19 (OMB, Washington, DC, 2013); www.whitehouse.gov/sites/default/files/omb/inforeg/2013_cb/draft_2013_cost_benefit_report.pdf.
2. D. W. Dockery *et al*., *N. Engl. J. Med.* **329**, 1753–1759 (1993).
3. Office of Management and Budget, "2012 Report to Congress on the benefits and costs of federal regulation and unfunded mandates on state, local, and tribal entities" (OMB, Washington, DC, 2012); www.whitehouse.gov/sites/default/files/omb/inforeg/2012_cb/2012_cost_benefit_report.pdf.
4. D. Rubin, *Ann. Appl. Stat* **2**, 808–840 (2008).
5. M. Greenstone, T. Gayer, *J. Environ. Econ. Manage.* **57**, 21–44 (2009).
6. C. M. Zigler *et al*., *Biostatistics* **13**, 289–302 (2012).
7. R. D. Brook *et al*., American Heart Association Council on Epidemiology and Prevention, Council on the Kidney in Cardiovascular Disease, and Council on Nutrition, Physical Activity and Metabolism, *Circulation* **121**, 2331–2378 (2010).
8. D. Krewski *et al*., *Res. Rep. Health Eff. Inst.* **140**, 5–114, discussion 115–136 (2009).
9. R. Peng *et al*., *J. R. Stat. Soc. Ser. A* **169**, 179–203 (2006).
10. H. Janes *et al*., *Epidemiology* **18**, 416–423 (2007).
11. C. A. Pope 3rd, R. T. Burnett, *Epidemiology* **18**, 424–426, discussion 427–428 (2007).
12. S. Greven *et al*., *J. Am. Stat. Assoc.* **106**, 396–406 (2011).
13. C. Wang *et al*., *Biometrics* **68**, 661–671 (2012).
14. K. Chay *et al*., *J. Risk Uncertain.* **27**, 279–300 (2003).
15. O. Ashenfelter, A. Krueger, *Am. Econ. Rev.* **84**, 1157 (1994).
16. K. Chay, M. Greenstone, *J. Polit. Econ.* **113**, 376–424 (2005).
17. D. Card *et al*., *Q. J. Econ.* **124**, 597–636 (2009).
18. J. J. Heckman, B. S. Payner, *Am. Econ. Rev.* **79**, 138–177 (1989).
19. L. Clancy *et al*., *Lancet* **360**, 1210–1214 (2002).
20. K. Chay, M. Greenstone, *Q. J. Econ.* **118**, 1121–1167 (2003).
21. D. Q. Rich *et al*., *JAMA* **307**, 2068–2078 (2012).
22. M. R. Ransom, C. A. Pope, III, *Contemp. Econ. Policy* **13**, 86–97 (1995).
23. O. Deschenes, M. Greenstone, J. Shapiro, "Defensive investments and the demand for air quality: Evidence from the NOx budget program and ozone reductions" (NBER working paper 18267, NBER, Cambridge, MA, 2012).
24. Y. Chen, A. Ebenstein, M. Greenstone, H. Li, *Proc. Natl. Acad. Sci. U.S.A.* **110**, 12936–12941 (2013).
25. Health Effects Institute, "Assessing the health impact of air quality regulations: Concepts and methods for accountability research" (Commun. 11, HEI, Boston, MA, 2003); http://pubs.healtheffects.org/view.php?id=153.
26. D. Thomas, *Statistical Methods in Environmental Epidemiology* (Oxford Univ. Press, New York, 2009), chap. 14.
27. K. Moore *et al*., *Am. J. Epidemiol.* **171**, 1233–1243 (2010).
28. T. A. Glass, S. N. Goodman, M. A. Hernán, J. M. Samet, *Annu. Rev. Public Health* **34**, 61–75 (2013).
29. K. Chay, M. Greenstone, "Air quality, infant mortality, and the Clean Air Act of 1970" (NBER working paper 10053, NBER, Cambridge, MA, 2003).
30. M. L. Bell *et al*., *Am. J. Respir. Crit. Med.* **179**, 1115–1120 (2009).
31. F. Dominici *et al*., *Epidemiology* **21**, 187–194 (2010).
32. J. M. Samet, *N. Engl. J. Med.* **365**, 198–201 (2011).
33. M. Greenstone, *J. Polit. Econ.* **110**, 1175–1219 (2002).
34. D. Lee, T. Lemieux, *J. Econ. Lit.* **48**, 281–355 (2010).

Acknowledgments: The authors thank M. Lipka and D. Stuart for research assistance. F.D. is supported by grants from the Health Effects Institute (HEI) (4909); the National Institute of Environmental Health Sciences (NIEHS), NIH (R01 ES019560, R21 ES020152, R21 ES02147); and the U.S. Environmental Protection Agency (EPA) (RD 83490001, RD 83479801, R834894). The content is solely the responsibility of the authors and does not necessarily represent the official views of the HEI, NIEHS, or EPA.

10.1126/science.1247348

ECOLOGY

Avoiding (Re)extinction

Alternative methods of identification should be used to avoid collection of voucher specimens of threatened or rediscovered species.

Ben A. Minteer,[1] James P. Collins,[1] Karen E. Love,[1] Robert Puschendorf[2]

Field biologists have traditionally collected voucher specimens to confirm a species' existence. This practice continues to this day but can magnify the extinction risk for small and often isolated populations. The availability of adequate alternative methods of documentation, including high-resolution photography, audio recording, and nonlethal sampling, provide an opportunity to revisit and reconsider field collection practices and policies.

Cases such as the extinction of the great auk remind us what is at stake in taking animals from small and declining populations. The last wild great auk (*Pinguinus impennis*) was sighted in 1844 on Eldey Island, Iceland. Centuries of exploitation for food and feathers, and, to some degree, a changing climate, had stressed the species, but overzealous museum collectors also played a role in its extinction (*1*). As the bird's numbers dwindled in the 19th century, ornithologists and curators increasingly prized great auk skins and eggs, with museums and universities sending out collection parties to procure specimens. On Eldey, fishermen killed the final breeding pair of the flightless birds and sold them to a local chemist, who stuffed the specimens and preserved them in spirits. Their internal organs now reside at the Zoological Museum in Copenhagen (*2*).

The great auk's disappearance predates the rise of a robust societal ethic of conservation and the emergence of a scientific concern for global biodiversity decline in the late 20th century. Yet, there is still a strong and widespread impulse to procure specimens of rare or rediscovered species for scientific purposes.

In their global review of species reappearances, Scheffers *et al*. (*3*) document at least 351 species that have been rediscovered since 1889, mostly in the tropics. In recent years, scientific and media attention has been drawn to the rediscovery of amphibian species thought to be extinct, including 11 species in Costa Rica alone (see the figure). Many amphibian rediscoveries have been documented by collecting specimens upon first encounter, a practice one of us has carried out in the past [R.P. with *Craugastor ranoides*, (*4*)]. Such rediscovered species typically exist in small populations with small range sizes and are therefore highly vulnerable. The desire to collect voucher specimens to verify the reappearance of species presumed extinct can be heightened by the recognition of the organism's rarity, as in the case of private individuals seeking to own and display rare animal specimens for their perceived scarcity and thus value. Rediscoveries can also be accidental, as many missing species are hard to identify in the field and collected specimens may turn out to be from very small populations, with the risk of collection only realized well after the fact (*5*).

PHOTO CREDIT: JUAN G. ABARCA ALVARADO

Species loss and rediscovery in Costa Rica. The fungal pathogen *Batrachochytrium dendrobatidis* (Bd) has been linked to the decline and extinction of amphibians worldwide (*12*). For example, amphibian populations in Costa Rica experienced substantial declines, with 20 of the 199 species feared extinct, after Bd moved through the country from the mid-1980s to the early 1990s (*13*, *14*). However, 11 of the 23 species have been rediscovered (*4*). Holdridge's toad (*Incilus holdridgei*) (see photo), a species endemic to a single volcano, vanished during the declines and was declared extinct by the International Union for Conservation of Nature and Natural Resources in 2007 but was rediscovered in 2008. Today, relict populations persist in areas where Bd once contributed to their demise.

Many taxa are difficult to identify from morphology alone. The collection of voucher specimens by field biologists is therefore increasingly augmented by other kinds of samples. Cultural traditions within a research community can, however, reinforce the collection of voucher specimens even where it is not necessary by insisting that a preserved specimen in a natural history collection is the gold standard—or only standard—for publishing a species description or documenting a species' presence. Collecting specimens is no longer required to describe a species or to document its rediscovery.

The concern about overcollection goes well beyond the case of rediscovered spe-

[1]School of Life Sciences, Arizona State University, Tempe, AZ 85287, USA. [2]School of Biological Sciences, Plymouth University, Drake Circus, Plymouth, Devon PL4 8AA, UK. E-mail: ben.minteer@asu.edu

Published by AAAS

cies. It also applies to the more common scenario of documenting newly discovered species, which (like most rediscovered species) often exist in small, isolated populations and therefore suffer from the same problems if voucher specimens are collected from the field. Field collection of individuals from small and declining populations vulnerable to extinction is also a common practice. Collection both by professional and amateur scientists has been linked to the decline or loss of a range of animal species, including Mexico's elf owl (*Micrathene whitneyi soccorroensis*) (*6*). Plants have also been affected by scientific overcollection; Norton *et al*. (*7*) cite the case of the scientific collection–driven decline and extinction of uncommon plant taxa in New Zealand over the past two centuries.

Perhaps the most powerful alternative method to collection is a series of good photographs, which can even be used to describe a species, complemented by other lines of evidence, such as molecular data and a description of a species' mating call for birds, amphibians, or insects. Advances in handheld technology have made it much easier and cheaper to identify species; most smartphones have a camera and a voice recorder sufficient to gather high-resolution images as well as an organism's call. Such nonlethal techniques were used successfully for the identification of the bird *Bugun liocichla*, a species that was newly discovered in India in 2006 (*8*). The bird's discoverer deliberately chose not to collect a voucher specimen for fear of imperiling the population; instead, a combination of photos, audio recordings, and feathers were used to distinguish the species.

In the case of rediscovered species, many were already well described, and a good-quality image should suffice. For rediscovered, rare, and newly discovered species, molecular techniques (such as skin swabbing for DNA) are an increasingly effective way to sample a specimen to confirm an identity with no or minimal harm to the organism (*9*, *10*). For this system to work, the DNA of relict populations and newly discovered species must be sequenced and the data made publicly available. This would, for example, make future population rediscoveries easier to document.

The multivariate description of a species that results from combining high-resolution photographs, sonograms (as appropriate), molecular samples, and other characteristics that do not require taking a specimen from the wild can be just as accurate as the collection of a voucher specimen without increasing the extinction risk. Clearly there remains a long-running debate over the appropriate standards for scientific description absent a voucher specimen (*11*). The benefits and costs of verification-driven specimen collection, however, should be more openly and systematically addressed by scientific societies, volunteer naturalist groups, and museums. Sharing of specimen information, including obligations to store genetic information from voucher specimens in widely accessible digital repositories, can also help to reduce the future need to collect animals from the wild.

References

1. S. A. Brengtson, *Auk* **101**, 1 (1984).
2. E. Fuller, *The Great Auk: The Extinction of the Original Penguin* (Bunker Hill, Piermont, New Hampshire, 2003).
3. B. R. Scheffers, D. L. Yong, J. B. Harris, X. Giam, N. S. Sodhi, *PLOS ONE* **6**, e22531 (2011).
4. A. García-Rodríguez, G. Chaves, C. Benavides-Varela, R. Puschendorf, *Divers. Distrib.* **18**, 204 (2012).
5. K. Nishida, *Brenesia* **66**, 78 (2006).
6. R. Rodriguez-Estrella, M. C. Blázquez Moreno, *Biodivers. Conserv.* **15**, 1621 (2006).
7. D. A. Norton, J. M. Lord, D. R. Given, P. J. De Lange, *Taxon* **43**, 181 (1994).
8. R. Athreya, *Indian Birds* **2**, 82 (2006).
9. J. Prunier *et al*., *Mol. Ecol. Resour.* **12**, 524 (2012).
10. A. M. Mendoza, J. C. García-Ramírez, H. Cárdenas-Henao, *Mol. Ecol. Resour.* **12**, 470 (2012).
11. N. J. Collar, *Ibis* **141**, 358 (1999).
12. J. P. Collins, M. L. Crump, *Extinction in Our Times: Global Amphibian Declines* (Oxford Univ. Press, 2009).
13. F. Bolaños, *Ambientico* **107**, 12 (2002).
14. B. L. Phillips, R. Puschendorf, *Proc. Biol. Sci.* **280**, 20131290 (2013).

10.1126/science.1250953

MATERIALS SCIENCE

Exploring the Interface of Graphene and Biology

To take advantage of the properties of graphene in biomedical applications, well-defined materials need to be matched with intended applications.

Kostas Kostarelos[1,3] and Kostya S. Novoselov[2,3]

Graphene is highly conductive, flexible, and has controllable permittivity and hydrophilicity, among its other distinctive properties (*1*, *2*). These properties could enable the development of multifunctional biomedical devices (*3*). A key issue for such applications is the determination of the possible interactions with components of the biological milieu to reveal the opportunities offered and the limitations posed. As with any other nanomaterial, biological studies of graphene should be performed with very specific, well-designed, and well-characterized types of materials with defined exposure. We outline three layers of complexity that are interconnected and need to be considered carefully in the development of graphene for use in biomedical applications: material characteristics; interactions with biological components (tissues, cells, and proteins); and biological activity outcomes.

Graphene has now been developed in many different forms in terms of shapes, sizes, chemical modifications, and other characteristics that can produce dramatically different results when studied biologically. Methods for producing graphene include direct exfoliation in organic liquids (*4*, *5*), reduction of graphene oxide (GO) (*6*), and epitaxial growth by CVD (chemical vapor deposition) on copper (*7*) or epitaxial growth on silicon carbide (*8*). The three aspects of this layer of structural complexity—the thickness, the lateral extent, and the surface functionalization of graphene—are illustrated in panel A of the figure and show how the materials produced by different methods fall in very different parts of this parameter space. These different physical and chemical characteristics dictate the suitability of a material for specific biomedical applications.

These wide discrepancies between the available graphene types will crucially determine the second layer of complexity, that of interactions of graphene with living cells and their compartments. In panel B

[1]Nanomedicine Laboratory, Faculty of Medical and Human Sciences, University of Manchester, Manchester, UK. [2]School of Physics and Astronomy, University of Manchester, Oxford Road, Manchester, M13 9PL, UK. [3]National Graphene Institute, University of Manchester, Oxford Road, Manchester M13 9PL, UK. E-mail: kostas.kostarelos@manchester.ac.uk; kostya@manchester.ac.uk

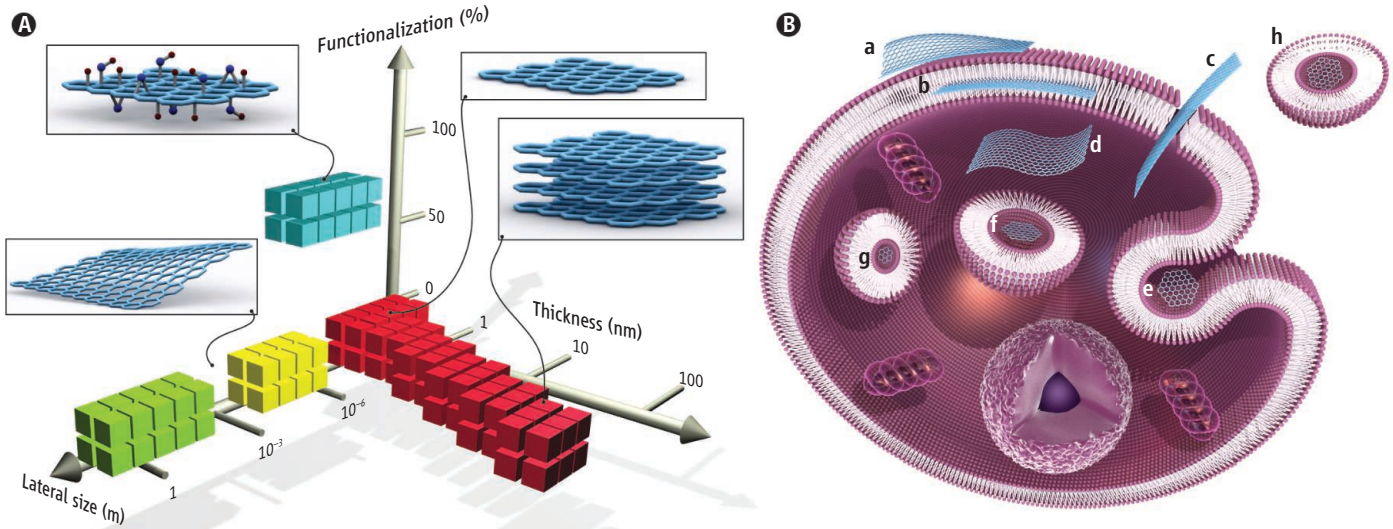

Graphene materials and their biological interactions. (**A**) A parameter space for the most widely used graphene materials can be described by the dimensions and surface functionalization of the material, the latter defined as the percentage of the carbon atoms in sp^3 hybridization. Green squares represent epitaxially grown graphene; yellow, mechanically exfoliated graphene; red, chemically exfoliated graphene; blue, graphene oxide. Note that a number of other graphene-related materials (such as graphene quantum dots and graphene nanoribbons) are also being used in experiments. (**B**) Possible interactions between graphene-related materials with cells (the graphene flakes are not to scale). (a) Adhesion onto the outer surface of the cell membrane. (b) Incorporation in between the monolayers of the plasma membrane lipid bilayer. (c) Translocation of membrane. (d) Cytoplasmic internalization. (e) Clathrin-mediated endocytosis. (f) Endosomal or phagosomal internalization. (g) Lysosomal or other perinuclear compartment localization. (h) Exosomal localization. The biological outcomes from such interactions can be considered to be either adverse or beneficial, depending on the context of the particular biomedical application. Different graphene-related materials will have different preferential mechanisms of interaction with cells and tissues that largely await discovery.

of the figure, we show in a schematic fashion some of the possible cell-graphene interactions.

Nanoflakes of chemically exfoliated graphene, micrometer-size flakes of GO, or substrate-bound CVD graphene will have dramatically different interactions and effects (if any) on live cells and tissue that can result in contradicting conclusions. Even experiments on similar, but not well-defined, materials can produce puzzling results. For instance, recently published papers on pulmonary inflammation after exposure to graphene platelets found no effects after 6 weeks (*9*) but some degree of acute (24 hours) inflammatory response (*10*).

The consequence of interactions at the cellular level will determine the third layer of complexity, that of overall biological activity outcomes. These outcomes can be adverse to the cell or tissue (e.g., fibrosis, membrane damage, or accumulation) or beneficial (e.g., facilitating intracellular transport of therapeutic or diagnostic agents, or providing antimicrobial or protective shielding). Some outcomes, such as cell activation or apoptosis, can be harmful or beneficial depending on the cell type and the intended use (in cancer therapy, harm to cells may be good; in vaccine design, activation of some parts of the immune system may be desired).

Both adverse and beneficial outcomes have been reported recently by different groups, even for similar graphene materials and cellular interactions. For example, cell internalization has been shown both as a mechanism that can lead to cell intoxication in some studies (*11*, *12*) and as a means to transport therapeutic agents intracellularly without ensuing damage in others (*13*). In another example, some recent computational and experimental studies have demonstrated that specific forms of graphene can directly interact with plasma membranes, which suggests that graphene may cause cell membrane damage (*14*, *15*). However, other studies demonstrated that interaction and binding of various graphene material types onto the mammalian plasma membrane can lead to a potentially beneficial enhancement of cell growth (*16*) or shielding effect (*17*, *18*) with no cell damage. Lastly, some types of graphene materials have been shown to physically adsorb and wrap around bacterial cell membranes, suggesting possible antibacterial activity (*19*–*21*), but this result has not been confirmed by others (*16*).

Also, the safety profile of graphene materials on interaction with living biological matter cannot be directly drawn from that for other carbon-based materials (graphitic platelets, amorphous carbon, and diamond-like carbon that have been studied for decades). These materials have properties very different from either graphene, bilayer graphene, or even few-layer graphene, and so will be their biological outcomes. Furthermore, despite some (very vague) similarities between graphene and carbon nanotubes, the former is generally not fiber-shaped, so fiber toxicology paradigms are not directly applicable (*22*). The limited number of available in vivo studies suggest that flat graphitic structures are not able to trigger the adverse (inflammatory) reaction associated with fibrous asbestos or long, rigid carbon nanotubes (*23*).

Another biological process of great importance is the biodegradation of graphene that will determine the safety profile of graphene materials from its residence time and persistence within tissues. Additionally, the kinetics of graphene degradation will define the limitations posed in relation to specific biomedical applications that may require long-term integration within the biological milieu (e.g., orthopedic or neuronal implants, catheters, wound healing agents, and corneal devices). The biodegradability of different graphene types will vary, as will the products of any biodegradation process. Some initial experimental evidence suggests that graphene can be enzymatically degradable by the oxidation activity of horseradish peroxidase (*24*) or macrophage-mediated degradation in vivo (*25*).

The development of graphene-based technologies for biomedical applications, either in the form of a device or an adminis-

CREDIT: ADAPTED FROM CONRAD GESNER

Published by AAAS

tered substance for therapeutic or diagnostic purposes, will be thoroughly scrutinized by the existing regulatory and approval framework implemented by national and international agencies. In the meantime, we urge very careful characterization and rational selection of the graphene materials to be studied in specific biological models, based on a hypothesis-driven intended biomedical purpose. Only rational, well-designed studies of graphene interactions with cells, tissues, and organisms will help guide the best choices for the use of this exciting family of materials.

References and Notes

1. A. K. Geim, *Science* **324**, 1530 (2009).
2. K. S. Novoselov, *Rev. Mod. Phys.* **83**, 837 (2011).
3. K. S. Novoselov *et al.*, *Nature* **490**, 192 (2012).
4. P. Blake *et al.*, *Nano Lett.* **8**, 1704 (2008).
5. Y. Hernandez *et al.*, *Nat. Nanotechnol.* **3**, 563 (2008).
6. S. Park, R. S. Ruoff, *Nat. Nanotechnol.* **4**, 217 (2009).
7. X. Li *et al.*, *Science* **324**, 1312 (2009).
8. P. N. First *et al.*, *MRS Bull.* **35**, 296 (2010).
9. A. Schinwald *et al.*, *Nanotoxicology* **8**, 824 (2014).
10. A. Schinwald, F. A. Murphy, A. Jones, W. MacNee, K. Donaldson, *ACS Nano* **6**, 736 (2012).
11. T. Lammel *et al.*, *Part. Fibre Toxicol.* **10**, 27 (2013).
12. O. Akhavan, E. Ghaderi, *ACS Nano* **4**, 5731 (2010).
13. D. Bitounis *et al.*, *Adv. Mater.* **25**, 2258 (2013).
14. Y. Li *et al.*, *Proc. Natl. Acad. Sci. U.S.A.* **110**, 12295 (2013).
15. Y. Tu *et al.*, *Nat. Nanotechnol.* **8**, 594 (2013).
16. O. N. Ruiz *et al.*, *ACS Nano* **5**, 8100 (2011).
17. H. K. Na *et al.*, *Nanoscale* **5**, 1669 (2013).
18. J. Russier *et al.*, *Nanoscale* **5**, 11234 (2013).
19. W. Hu *et al.*, *ACS Nano* **4**, 4317 (2010).
20. S. Liu *et al.*, *ACS Nano* **5**, 6971 (2011).
21. S. Liu *et al.*, *Langmuir* **28**, 12364 (2012).
22. C. Bussy, H. Ali-Boucetta, K. Kostarelos, *Acc. Chem. Res.* **46**, 692 (2013).
23. H. Ali-Boucetta *et al.*, *Adv. Healthc. Mater.* **2**, 433 (2013).
24. G. P. Kotchey *et al.*, *ACS Nano* **5**, 2098 (2011).
25. C. M. Girish, A. Sasidharan, G. S. Gowd, S. Nair, M. Koyakutty, *Adv. Healthc. Mater.* **2**, 1489 (2013).

Acknowledgments: The collaboration was supported by EC-FET European Graphene Flagship.

10.1126/science.1246736

APPLIED PHYSICS

Refractory Plasmonics

Stable at high temperatures, refractory plasmonic materials could boost existing optoelectronic technologies.

Urcan Guler, Alexandra Boltasseva, Vladimir M. Shalaev

Refractory materials are defined as those with a high melting point and chemical stability at temperatures above 2000°C. Applications based on refractory materials, usually nonmetallic, span a wide range of areas including industrial furnaces, space shuttle shields, and semiconductor technology. Metals have also been studied as refractories; however, the optical properties of those metals that have been tried for high-temperature applications were not good enough to be used in plasmonic applications (these are almost entirely based on noble metals, which are not good refractories). Refractory materials that exhibit reasonably good plasmonic behavior would undoubtedly enable new devices and boost such existing applications as heat-assisted magnetic recording (HAMR) (*1*), solar/thermophotovoltaics (S/TPV) (*2*), plasmon-assisted chemical vapor deposition (*3*), solar thermoelectric generators (*4*), and nanoscale heat transfer systems (*5*).

The field of plasmonics offers the potential to greatly enhance the efficiencies of existing technologies, such as electronics and photonics, as well as to create new technological opportunities (*6*). Although several proof-of-concept studies have been reported, the realization of practical devices has been hindered by the challenges associated with the properties of noble metals—in particular, poor chemical and thermal stability and high losses (*7*, *8*). Usually listed as a problem for plasmonic applications, resistive losses result in heating of the plasmonic material, enabling a temperature rise in a confined volume around the nanostructure. Several plasmonic applications with a great potential for practical use, such as photothermal treatment (*9*) and HAMR (*1*), rely on the heating effects. Because of the local temperature rise, the mechanical and chemical stability of plasmonic nanostructures are of paramount importance; refractory plasmonic materials are therefore indispensable.

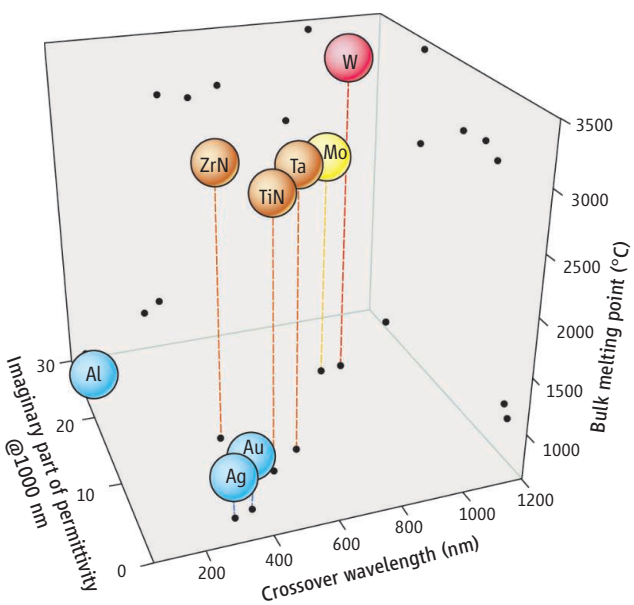

A handful of alternatives. The low melting point and softness of metals pose problems when real-world applications are considered, especially in nanostructures in which the melting point is reduced. Refractory plasmonic materials would provide a solution for high-temperature applications where corrosion and wear resistance are desired. Refractory metals exhibit plasmonic resonances mostly in the near-infrared region with relatively higher losses. Transition metal nitrides mimic the optical properties of gold and provide the superior material properties of the refractory materials. It is above the "crossover wavelength" that a material becomes plasmonic.

S/TPV technology is based on the idea of absorbing solar irradiation with a broadband absorber, which results in heating of an intermediate component and the subsequent emission of this thermal energy in a narrow spectrum for efficient absorption by the photovoltaic cell. Such devices can theoretically achieve energy conversion efficiencies up to 85% (*2*). However, the operational temperatures required for high-efficiency devices are estimated at ~1500°C, and emitter materials that can withstand prolonged exposure to such temperatures have not yet been developed. Engineered absorber and emitter photonic crystals can be fabricated with refractory metals (*10*, *11*), but achievable operational temperatures are still far below

School of Electrical & Computer Engineering and Birck Nanotechnology Center, Purdue University, West Lafayette, IN 47907, USA, and Nano-Meta Technologies Inc., 1281 Win Hentschel Boulevard, West Lafayette, IN 47906, USA. E-mail: shalaev@purdue.edu

the desired values, and adequate durability cannot be obtained even with protective layers made of refractory dielectric materials (*11*). One-dimensional photonic crystal emitters based on Si/SiO_2 layers, although they are more vulnerable to degradation at high temperatures, have demonstrated the highest S/TPV efficiency when integrated with a carbon nanotube broadband absorber that has limited spectral selectivity and back-emission at longer wavelengths (*12*). Refractory plasmonic materials could be the solution for most of the major limitations, thus advancing the existing S/TPV technology. Ultrathin metamaterial absorbers and emitters made of the same refractory plasmonic material could be integrated as a narrow intermediate spectral converter that can be easily heated, owing to the increased surface-to-volume ratio (*13*). The absorber could be spectrally engineered so that back-emission is minimized at longer wavelengths and a reduced absorber area ratio is no longer a problem. Larger absorber areas would enable higher temperatures and much higher efficiencies, also eliminating the need for light collection optics. More important, thinner structures achievable with metamaterials would reduce the mechanical load on the nanostructures, thus enabling high-temperature durability.

Another field with a potential near-term impact in industry is HAMR. The demand for larger data storage capacity has resulted in a need for larger areal densities, and consequently smaller grain sizes, which in turn may lead to thermal instabilities. One promising approach is to use high-coercivity materials (which have greater stability at room temperature) and to locally heat the material with a plasmonic nanoantenna, lowering its coercivity for a short time to write data. This idea was demonstrated in an experiment in which local heating on a 70-nm track was achieved with a gold nanoantenna (*1*). However, efficient heating of the high-coercivity material results in self-heating of the plasmonic component. Local temperatures reaching 400°C, along with tough operation conditions, impose an extra load on the antenna, which is located very close to a disk spinning at a high speed. Under these conditions, deformation of the nanostructure is unavoidable, especially for noble metals (*14*). In contrast to S/TPV, studies on HAMR have yielded some findings on the advantages of using plasmonic nanostructures, but have lacked materials with the required refractory properties.

The solution for potential high-impact refractory plasmonic applications lies in material building blocks. Finding the proper constituent materials could open up a new avenue for high-temperature applications of advanced plasmonic and metamaterial devices, analogous to recent advances in silicon and silica fiber technologies. One example is transition metal nitrides, such as titanium nitride and zirconium nitride, that exhibit plasmonic properties comparable to those of gold in the visible and near-infrared spectrum (*15*) (see the figure). Coupled with their refractory properties, these materials can boost the performance of many heat-assisted plasmonic devices, thus replacing the traditional noble metals or refractory materials with poor plasmonic properties.

Materials research has been at the center of the most recent studies in the field of plasmonics and metamaterials. Among the alternative materials with desirable optical performance, those with complementary metal-oxide semiconductor compatibility, biocompatibility, chemical stability, tunability, and low losses have attracted attention (*8*). High-temperature stability is the next desired feature to develop in the field of plasmonics.

References and Notes

1. W. Challener *et al.*, *Nat. Photonics* **3**, 220 (2009).
2. S. Fan, *Nat. Nanotechnol.* **9**, 92 (2014).
3. D. A. Boyd, L. Greengard, M. Brongersma, M. Y. El-Naggar, D. G. Goodwin, *Nano Lett.* **6**, 2592 (2006).
4. D. Kraemer *et al.*, *Nat. Mater.* **10**, 532 (2011).
5. E. Rousseau *et al.*, *Nat. Photonics* **3**, 514 (2009).
6. M. L. Brongersma, V. M. Shalaev, *Science* **328**, 440 (2010).
7. A. Boltasseva, H. A. Atwater, *Science* **331**, 290 (2011).
8. G. V. Naik, V. M. Shalaev, A. Boltasseva, *Adv. Mater.* **25**, 3264 (2013).
9. L. R. Hirsch *et al.*, *Proc. Natl. Acad. Sci. U.S.A.* **100**, 13549 (2003).
10. V. Rinnerbauer *et al.*, *Opt. Express* **21**, 11482 (2013).
11. K. A. Arpin *et al.*, *Nat. Commun.* **4**, 2630 (2013).
12. A. Lenert *et al.*, *Nat. Nanotechnol.* **9**, 126 (2014).
13. C. Wu *et al.*, *J. Opt.* **14**, 024005 (2012).
14. N. C. Lindquist *et al.*, *Laser Photon. Rev.* **7**, 453 (2013).
15. U. Guler *et al.*, *Nano Lett.* **13**, 6078 (2013).

Acknowledgments: Supported by Army Research Office grants 63133-PH (W911NF-13-1-0226) and 57981-PH (W911NF-11-1-0359) and NSF MRSEC grant DMR-1120923.

10.1126/science.1252722

NEUROSCIENCE

Myelin—More than Insulation

R. Douglas Fields

Unusual features of myelin in the mammalian cerebral cortex permit more complex forms of network integration.

Myelin is often compared to electrical insulation on nerve fibers. However, nerve impulses are not transmitted through neuronal axons the way electrons are conducted through a copper wire, and the myelin sheath is far more than an insulator. Myelin fundamentally changes the way neural impulses (information) are generated and transmitted, and its damage causes dysfunction in many nervous system disorders including multiple sclerosis, cerebral palsy, stroke, spinal cord injury, and cognitive impairments. A detailed understanding of myelin structure is therefore imperative, but is lacking. On page 319 of this issue, Tomassy *et al*. (*1*) provide a high-resolution global view of myelin structure spanning the six layers of mammalian cerebral cortex. The findings are likely to spark new concepts about how information is transmitted and integrated in the brain.

New techniques of automating collection of electron microscopic images taken in series through layers of tissue are becoming available to analyze neuron ultrastructure in large volumes (*2*). Using such methods, Tomassy *et al*. reveal myelin structure in the mouse cerebral cortex along individual nerve fibers, providing a coherent picture.

Myelin is a coating of compacted cell membrane that is wrapped around the axon by non-neuronal cells called oligodendrocytes. These multipolar cells extend slender cellular processes to grip axons and spin up to dozens of layers of membrane around it like electrical tape. Many oligodendrocytes grasp a single axon to span its full length. The tiny space exposed between each grasping "hand" corresponds to a node of Ranvier, where voltage-gated sodium channels are concentrated. When the electrical potential across the axon membrane depolarizes by about 20 mV, these channels allow rapid influx of sodium ions that discharges the transmembrane potential, creating a voltage transient of ~0.1 V—the action poten-

National Institutes of Health, Eunice Kennedy Shriver National Institute of Child Health and Human Development (NICHD), Building 35, Room 2A211, MSC 3713, Bethesda, MD 20892, USA. E-mail: fieldsd@mail.nih.gov

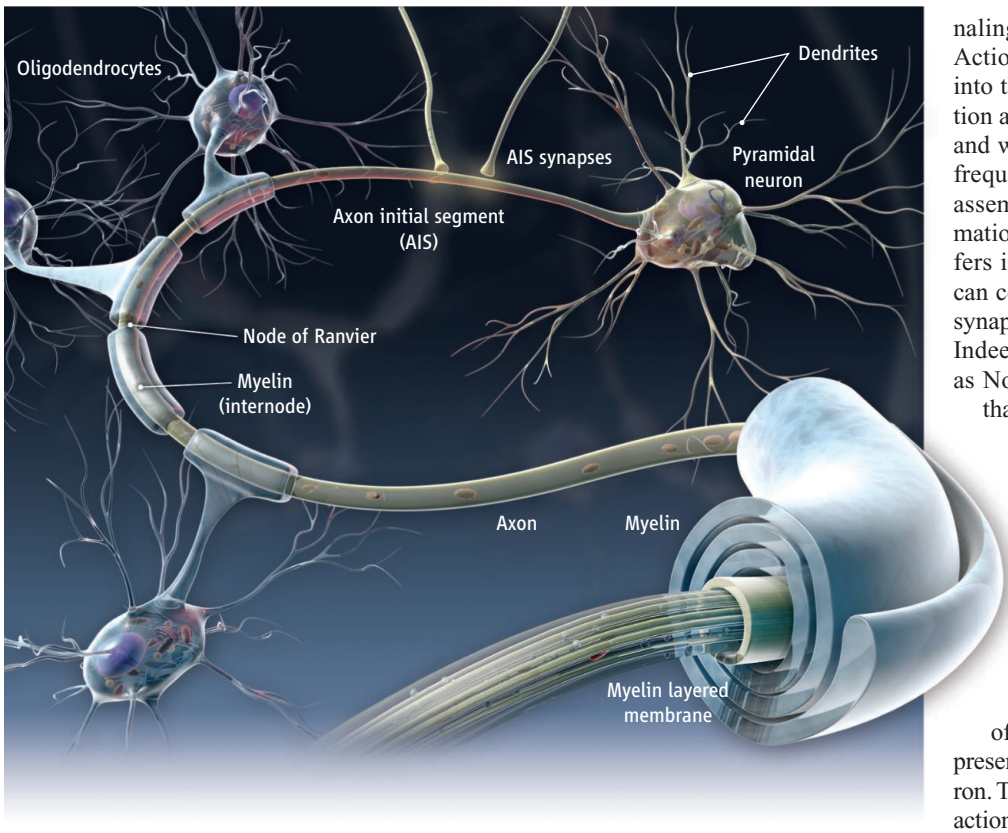

Intermittent myelination. Myelination of layer II/III pyramidal neurons of the cerebral cortex is illustrated, with a long axon initial segment and segments with variable lengths of unmyelinated axon.

CREDIT: C. BICKEL/*SCIENCE*

tial. Myelin forces the action potential to be generated only at these 1-μm-long nodes of Ranvier and to leap rapidly in sequence over tens or hundreds of micrometers to excite an action potential in the next node. Rather than spreading down an unmyelinated axon as a slow wave of depolarization, the nodes of Ranvier act as repeaters. The speed at which signals are transmitted is limited by the distance between nodes, the thickness of the myelin wrapping, and the length of the exposed axon in the node.

The common presumption that these features are relatively uniform along a single axon is invalidated by the observations of Tomassy *et al*. in the mouse cerebral cortex. The authors observed long stretches (up to 55 μm) along an individual axon of pyramidal neurons in layer II/III where there is no myelin sheath interspersed with segments that are myelinated (see the figure). These unmyelinated regions could be passive internodes or they could have clusters of ion channels to promote action potential propagation. Notably, the critical segment of bare axon extending from the cell body to the first segment of myelin [the axon initial segment (*3*); referred to as the premyelin axonal segment by Tomassy *et al*.] differs between cortical layers.

Variation in myelination along an axon could adjust transmission speed to optimize the time of arrival of signals from multiple axons at a relay point in a neural circuit. Unusually long nodes of Ranvier (50 μm) may even delay action potential propagation (*4*), as they increase the electrical capacitance of the axon membrane and consequently increase the time required to charge and discharge it. The as yet unknown ion channel properties in these unmyelinated regions of cortical neurons will also influence conduction velocity. However, the total transmission time across the relatively short distance of the cerebral cortex (about 0.5 mm in a mouse and 2 to 4 mm in humans) may present a negligible delay, suggesting additional reasons for the intermittent myelin. Perhaps unmyelinated axon segments can permit more complex forms of network integration.

The "neuron doctrine" states that information flows through synaptic inputs on dendrites and passes out of the axon as an action potential to excite dendrites of the next neuron in the circuit. However, other modes of communication are becoming apparent. Synapses can form on unmyelinated segments of axons (*5*), and bare axons can release neurotransmitters, signaling by nonsynaptic communication (*6*). Action potentials also propagate backward into the cell body, affecting neural integration and synaptic plasticity (*7*). Oscillations and waves of electrical activity at different frequencies couple neurons into functional assemblies that coordinate and gate information, and the frequency of oscillation differs in layers II/III and V (*8*). Myelin also can constrain where axons sprout and form synapses with dendrites or with other axons. Indeed, proteins in the myelin sheath, such as Nogo, block axon sprouting, indicating that the myelin wrapping stabilizes axon structure and the pattern of connectivity in neural circuits (*9*).

The most critical segment of unmyelinated axon is the axon initial segment. The 5- to 80-μm-long unmyelinated section between the cell body and first myelin segment is the decision point where action potentials are triggered. The morphological features of this segment, and types of ion channels present in it, regulate excitability of the neuron. This region also controls the shape of the action potential, which affects the amount of neurotransmitter released from the synapse, the frequency of action potential firing, and other aspects of action potential signaling (*3*). Action potentials are initiated at the distal end of the axon initial segment (*10*), and the distance to this trigger point has important functional consequences. Tomassy *et al*. found that this region of the axon was longer in layers III/IV than V/VI.

The length and membrane properties of the axon initial segment influence the capacity of action potentials to propagate back into the cell body and dendrites (*3*). Back-propagating action potentials in hippocampal neurons develop during slow-wave sleep and quiet periods of wakefulness and are important in memory formation (*7*).

The length of the myelinated axon between nodes may be determined by neuronal signals, intrinsic properties of the oligodendrocytes, and region-specific factors. Tomassy *et al*. report that the layer-specific pattern of myelination on axons is disrupted in genetically modified mice that have abnormal cortical layering, pointing to a role for neurons in specifying myelination properties. The age of oligodendrocytes can also determine the length of internodal segments, with oligodendrocytes generated later in life producing shorter internodes (*11*). Internodal length and other properties of myelin differ in different brain regions, with corresponding effects on conduction velocity (*12*).

There are countless axons in the nervous system that are unmyelinated and they do not "short out." Myelin organizes the very structure of network connectivity, facilitates modes of nervous system function beyond the neuron doctrine, and regulates the timing of information flow through individual circuits. It is certainly time to set aside the frayed metaphor of myelin as insulation and appreciate the more fascinating reality.

References and Notes

1. G. S. Tomassy *et al*., *Science* **344**, 319 (2014).
2. J. W. Lichtman, W. Denk, *Science* **334**, 618 (2011).
3. M. H. P. Kole, G. J. Stuart, *Neuron* **73**, 235 (2012).
4. S. G. Waxman, G. D. Pappas, M. V. Bennett, *J. Cell Biol.* **53**, 210 (1972).
5. P. Somogyi, G. Tamás, R. Lujan, E. H. Buhl, *Brain Res. Brain Res. Rev.* **26**, 113 (1998).
6. R. D. Fields, Y. Ni, *Sci. Signal.* **3**, ra73 (2010).
7. O. Bukalo, E. Campanac, D. A. Hoffman, R. D. Fields, *Proc. Natl. Acad. Sci. U.S.A.* **110**, 5175 (2013).
8. W. Sun, Y. Dan, *Proc. Natl. Acad. Sci. U.S.A.* **106**, 17986 (2009).
9. M. E. Schwab, S. M. Strittmatter, *Curr. Opin. Neurobiol.* **27**, 53 (2014).
10. L. M. Palmer, G. J. Stuart, *J. Neurosci.* **26**, 1854 (2006).
11. K. M. Young *et al*., *Neuron* **77**, 873 (2013).
12. Y. Bakiri, R. Káradóttir, L. Cossell, D. Attwell, *J. Physiol.* **589**, 559 (2011).

Acknowledgments: R.D.F. is supported by funds from the Division of Intramural Research of NICHD.

10.1126/science.1253851

ECOLOGY

Novelty Trumps Loss in Global Biodiversity

Although global biodiversity is declining, local ecosystems are not systematically losing diversity, but rather experiencing rapid turnover in species.

John M. Pandolfi and Catherine E. Lovelock

The ongoing decline of ecosystems around the world is often described in terms of biodiversity loss. But exactly how much of this decline is the result of species loss in local communities (α diversity), and how much is due to shifts in species composition of these communities? On page 296 of this issue, Dornelas *et al*. (*1*) address this issue with a comprehensive analysis of changes in plant, mammal, bird, fish, and invertebrate diversity in a wide range of biomes. Contrary to expectation, loss of α diversity, though widespread, is not a systematic trend in ecological communities. Rather, communities appear to be undergoing massive turnover in the species that constitute them (β diversity), resulting in the global emergence of communities with novel species configurations.

The authors analyzed a massive data set covering more than 35,000 mammal, bird, fish, invertebrate, and plant species from marine, freshwater, and terrestrial biomes ranging from the poles to the tropics. The data comprised 100 individual time series of species composition. Multiple time-series data sets exist for individual biomes and taxa. To standardize sampling in each time series, the authors calculated α and β diversities from the original data. Loss in α diversity, although prevalent in some time series, was not systematic, mostly because species invasions tended to exceed native losses. For example, poleward expansion of species ranges in response to climate change (*2*) can cause α diversity to remain constant or potentially increase even if local species go extinct.

However, the authors report significant trends in α diversity in some data series. α diversity is increasing through time in both terrestrial plant communities and temperate communities, but is decreasing in global-scale time series (mostly seabirds and marine invertebrates). It is also declining in tropical biomes, but not significantly so. Even though gains and losses in α diversity are variable among regions and taxa, negative trends in α diversity through time in 41 of the 100 data series leave no room for complacency.

Given the known species losses over the past few centuries (*3*) and the potential for species invasions to cancel out local species extinctions and thus maintain consistent levels of α diversity, the species composition in any one place should be subject to large-scale change through time. This is exactly what Dornelas *et al*. find when they compare species composition within a community at any one place between the start of the time series and the ensuing years. Their analysis shows systematic turnover in the species composition of communities through time across climatic regions, realms, and taxonomic groups, with ~10% of species change in communities every decade. The results were robust to tests of temporal autocorrelation (where values at one time in a data

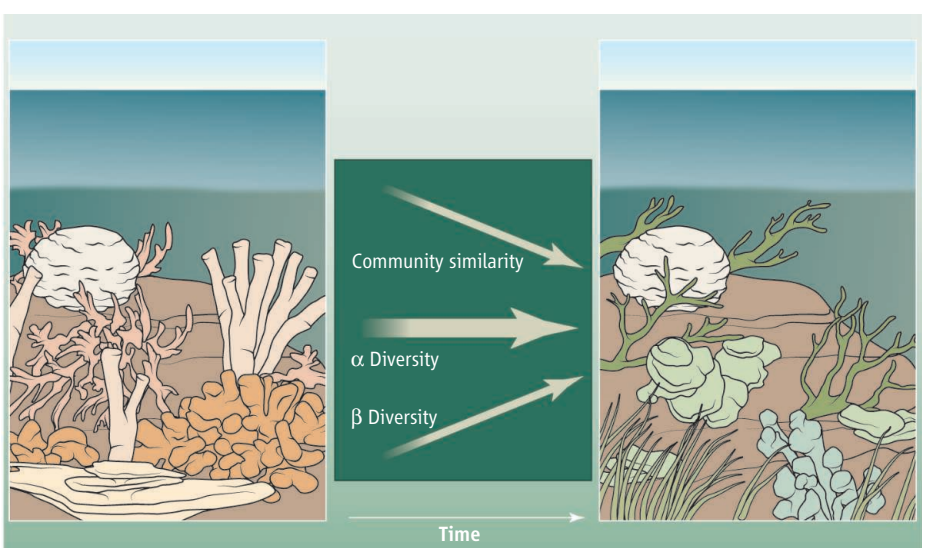

Ecosystem change in the Anthropocene. Dornelas *et al*.'s analysis of long-term studies from many of Earth's biomes shows that species diversity within local communities (α diversity) is equally likely to rise or fall over time, yet the species composition in those communities shows increasing turnover (β diversity) through time. For example, less degraded locally diverse reef communities can be transformed to highly degraded but still locally diverse novel communities.

School of Biological Sciences, ARC Centre of Excellence for Coral Reef Studies, University of Queensland, St. Lucia, Australia. E-mail: j.pandolfi@uq.edu.au; c.lovelock@uq.edu.au

series are correlated with values at another time) and were substantially different from predictions derived from a neutral theory of biodiversity that attributes trends in community dynamics to stochastic demographic processes.

The relationship between α diversity and β diversity needs further exploration, especially in the context of the formation and management of novel communities (see the figure) (*4*). As the species composition of an ecosystem changes in response to loss of species, it is important to understand not only what was lost, but also how that loss affects the emerging novel community. For example, reduction of fast-growing branching corals in the Caribbean (*5*) causes substantial loss in a major source of carbonate production and might lead to the inability of these reefs to continue accreting, even as sea level continues to rise. Species invasion, such as the introduction of avian malaria into Hawaii or zebra mussels to North American streams and lakes, can similarly impart a legacy of substantial community transformation.

Comprehensive as Dornelas *et al*.'s study is, ecosystem coverage is still patchy, with few data sets from the tropics. Those that do exist from the tropics are focused on terrestrial plants, reef fish, and birds. Inclusion of data sets for communities with large mammals and amphibians could lead to much worse α diversity trends for the tropics (*6*, *7*). The importance of long-term investment in monitoring in the tropics (such as the Smithsonian's Center for Tropical Forest Science) cannot be overemphasized.

In the new age of human impacts that is increasingly referred to as the Anthropocene (*8*), how can we reconcile warnings of the next mass extinction (*3*) with the observation that α diversity largely remains constant? Elucidation of the implications of the mass extinction caused by human impacts will have to be revised to consider the way in which whole communities will respond. Extinction is just one component of the way in which ecological communities will be transformed in the future. Managing the species loss involves building an understanding of species turnover in local communities.

The rapid rate of species turnover in ecological communities that Dornelas *et al*. document means that we can expect widespread emergence of novel communities. Identifying the causes of the biodiversity changes is challenging, but there is some evidence that large-scale drivers may influence regions differentially. For example, the composition of temperate communities can be strongly influenced by climate change (*9*, *10*), whereas tropical communities suffer disproportionately from other human activities (*11*). These changes in community composition may affect their resilience or ecosystem function. Ecosystem management approaches must anticipate the widespread emergence of novel ecological communities (*12*) and their consequences for dependent biota, including humans.

References

1. M. Dornelas *et al*., *Science* **344**, 296 (2014).
2. E. S. Poloczanska *et al*., *Nat. Clim. Change* 10.1038/nclimate1958 (2013).
3. A. D. Barnosky *et al*., *Nature* **471**, 51 (2011).
4. R. J. Hobbs, E. Higgs, J. A. Harris, *Trends Ecol. Evol.* **24**, 599 (2009).
5. D. R. Bellwood, T. P. Hughes, C. Folke, M. Nyström, *Nature* **429**, 827 (2004).
6. M. Hoffmann *et al*., *Philos. Trans. R. Soc. London Ser. B* **366**, 2598 (2011).
7. S. N. Stuart *et al*., *Science* **306**, 1783 (2004).
8. W. Steffen, J. Grinevald, P. Crutzen, J. McNeill, *Philos. Trans. R. Soc. London Ser. A* **369**, 842 (2011).
9. B. Sommer, P. L. Harrison, M. Beger, J. M. Pandolfi, *Ecology* 10.1890/13-1445.1 (2014).
10. K. C. Cavanaugh *et al*., *Proc. Natl. Acad. Sci. U.S.A.* **111**, 723 (2014).
11. E. C. Ellis *et al*., *Proc. Natl. Acad. Sci. U.S.A.* **110**, 7978 (2013).
12. N. A. Graham, J. E. Cinner, A. V. Norström, M. Nyström, *Curr. Opin. Environ. Sustain.* **7**, 9 (2014).

10.1126/science.1252963

PLANT SCIENCE

Paired Plant Immune Receptors

The ability of plant cell immune sensors to combine in different pairs could expand the host's defense against pathogens.

Marc T. Nishimura and Jeffery L. Dangl

Plants are constantly interpreting microbial signals from potential pathogens and potential commensals or mutualists. Because plants have no circulating cells dedicated to this task, every plant cell must, in principle, recognize any microbe as friend, foe, or irrelevant bystander. That tall order is mediated by an array of innate immune system receptors: pattern-recognition receptors outside the plant cell and nucleotide-binding oligomerization domain (NOD)–like receptors (NLRs) inside the cell. Despite their importance for plant health, how NLRs function mechanistically has remained obscure. On page 299 of this issue, Williams *et al*. (*1*) reveal a role for heterodimerization between NLRs and show how the rather limited NLR repertoire of any plant genome might be enhanced by combinatorial diversity.

When first isolated 20 years ago, it was surprising to find that structurally similar NLRs could individually confer resistance to strains of plant pathogens from all kingdoms—insects, fungi, oomycetes, bacteria, and viruses (*2*, *3*). Plant NLRs are deployed to various intracellular addresses to monitor for pathogen virulence proteins ("effectors") that target host defense pathways. NLRs in plants and animals function as molecular switches, cycling between a closed "off" conformation bound to adenosine diphosphate (ADP) and an open "active" conformation bound to adenosine triphosphate (ATP). This switch is thought to be controlled by interactions between a C-terminal leucine-rich repeat (LRR) domain folded back across a central nucleotide-binding (NB) domain and an N-terminal dimerization output domain, which in plants is typically either a coiled-coil (CC) motif or a domain with homology to the Toll–interleukin-1 receptor (TIR) cytoplasmic domains (*4*). How the conformation of NLRs changes after effector recognition and during the activation cycle, and the consequences of these changes, are major unanswered questions in plant pathology. One hypothesis posits that the N-terminal TIR or CC domains can dimerize upon effector-mediated activation to transduce signals to the nucleus and reprogram the cell for disease resistance responses.

Williams *et al*. demonstrate that in addition to forming a signaling-competent homodimer, one TIR domain can heterodimerize with another (in the resting state) to suppress host defense signaling. The authors studied the TIR domains of an NLR pair (RPS4 and RRS1) that are encoded by genes linked head-to-head in the plant *Arabidopsis*. Both proteins are required for disease resistance to multiple pathogens (*5*, *6*). By

Howard Hughes Medical Institute and Department of Biology, University of North Carolina, Chapel Hill, NC 27599, USA. E-mail: dangl@email.unc.edu; marcusn@email.unc.edu

solving the crystal structure of the RPS4 dimer, the RRS1 dimer, and the RPS4-RRS1 heterodimer, Williams *et al*. identified amino acids required for both homodimer and heterodimer formation. Mutational analyses showed that this shared surface is required for RPS4 TIR homodimer signaling and also for RRS1 to suppress RPS4. Thus, RRS1 negatively regulates RPS4 through a shared TIR dimerization contact surface. Effector recognition likely drives a rearrangement of the resting heterodimer such that an RPS4 TIR homodimer is formed (see the figure).

NLR heterodimerization, if common, might enlarge the overall NLR receptor repertoire beyond the ~200 genes and fragments present in the reference *Arabidopsis* genome. Heterodimerization may also provide "protein complementation functions" for the many partial NLRs (those lacking either LRR or NB and LRR domains) that are beginning to be functionally appreciated (*7*, *8*).

Some plant NLRs bind directly to the pathogen effector that triggers their action; others, however, monitor the integrity of host proteins with which they associate. These NLRs "guard" host proteins that are targets of effectors, or act as decoys of those targets. Thus, a single NLR can efficiently detect multiple pathogen effectors, simplifying the problem of a limited receptor repertoire (*2*, *3*). One interpretation of the RPS4-RRS1 heterodimer is that RPS4 is guarding RRS1. Indeed, Williams *et al*. observed that two effectors can associate with the functional RPS4-RRS1 complex, as well as with RRS1 alone, to activate RPS4. Interaction of these two effectors with RPS4 cannot be excluded, but is thus far elusive. Also, RPS4 and RRS1 differ in their requirements for canonical NLR activation—that is, the ability of the NBS domain to bind and hydrolyze ATP via a phosphate binding (P-loop) motif. The RPS4 P-loop is required for disease resistance but the RRS1 P-loop is dispensable, which suggests that RRS1 has functionally diverged and is now a platform for binding effectors that activates disease resistance through RPS4. The most striking difference between RRS1 and RPS4 is the presence of a transcription factor DNA binding domain (WRKY) that is fused to the RRS1 C terminus. This domain can bind DNA; a mutation in RRS1 that abolishes DNA binding is constitutively active (*9*).

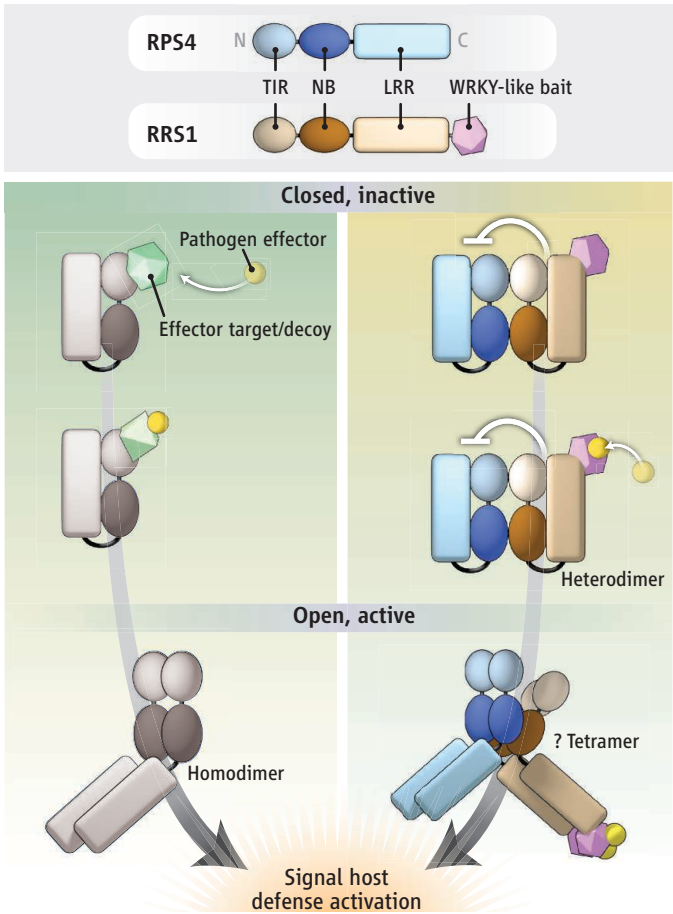

Partners in defense. In *Arabidopsis*, NLR sensors are activated by pathogen effectors. When some NLRs detect modification of a host cell protein and an effector, they form homodimers and activate defense responses **(left)**. RPS4 and RRS1 are "paired" TIR-NLR sensors **(right)**. RPS4 activity is normally blocked when it forms a heterodimer with RRS1. When an effector binds to RRS1, this suppression is released and RPS4 is activated.

There are three WRKY-NLR fusions encoded in the reference *Arabidopsis* genome. Additional plant NLRs contain unusual domains and/or combinations of TIR, NB, and LRR domains. WRKY transcription factors are a large family that are important for disease resistance and stress responses (*10*). It is thus reasonable for them to be targets of a variety of plant pathogen effectors. Could the RRS1 WRKY domain be an "effector bait" that mimics one or more effector virulence targets? One of the effectors that activates RRS1 is an acetyltransferase whose activity is required for RRS1 activation (*11*). This effector might acetylate RRS1 and remove it from DNA to drive RPS4 activation.

NLRs are the most rapidly evolving protein-encoding gene family across plant genomes, and new NLR proteins that have incorporated unusual domains are present in all examined plant genomes. Another functional NLR pair (the CC-NLRs RGA4 and RGA5) was described in rice (*12*). RGA5 has an unusual C-terminal effector-targeted domain with structural similarity to a ferredoxin fold found in the plant protein family related to ATX1 (RATX1), a yeast copper-binding chaperone (*12*). As with RPS4 and RRS1, one can predict that the RATX1-like domain in RGA5 is bait for effectors that target RATX1 proteins to promote pathogenicity. Exploring these oddities will help define the spectrum of important host machinery targeted by pathogens.

A major challenge for understanding NLR function is a structural description of the events before, during, and after NLR activation. How do two different effectors lead to an event recognized by RPS4? The events immediately downstream of RPS4 dimerization that activate defense responses are also not clear. Rational design of immune receptors is ultimately the goal of studying NLR function. Perhaps protein pairs like RPS4 and RRS1 may be useful starting substrates; in a modular guardee like RRS1, the WRKY domain could be replaced with a different effector-binding decoy that would result in RPS4 activation. The vistas opened by structural biology in a field rich with genetics and natural variation in both hosts and pathogens provide an exciting new view of plant immunology, 20 years after the first pathogen sensors were discovered.

References

1. S. J. Williams *et al*., *Science* **344**, 299 (2014).
2. J. D. Jones, J. L. Dangl, *Nature* **444**, 323 (2006).
3. P. N. Dodds, J. P. Rathjen, *Nat. Rev. Genet.* **11**, 539 (2010).
4. F. L. Takken, A. Goverse, *Curr. Opin. Plant Biol.* **15**, 375 (2012).
5. D. Birker *et al*., *Plant J.* **60**, 602 (2009).
6. M. Narusaka *et al*., *Plant J.* **60**, 218 (2009).
7. Y. Wang, Y. Zhang, Z. Wang, X. Zhang, S. Yang, *Plant J.* **75**, 553 (2013).
8. A. M. Zbierzak *et al*., *Plant J.* **75**, 539 (2013).
9. Y. Noutoshi *et al*., *Plant J.* **43**, 873 (2005).
10. P. J. Rushton, I. E. Somssich, P. Ringler, Q. J. Shen, *Trends Plant Sci.* **15**, 247 (2010).
11. C. Tasset *et al*., *PLOS Pathog.* **6**, e1001202 (2010).
12. S. Cesari *et al*., *Plant Cell* **25**, 1463 (2013).

10.1126/science.1253849

A Critical Period of Sleep for Development of Courtship Circuitry and Behavior in *Drosophila*

Matthew S. Kayser,[1,2] Zhifeng Yue,[3] Amita Sehgal[3,4]*

Most animals sleep more early in life than in adulthood, but the function of early sleep is not known. Using *Drosophila*, we found that increased sleep in young flies was associated with an elevated arousal threshold and resistance to sleep deprivation. Excess sleep results from decreased inhibition of a sleep-promoting region by a specific dopaminergic circuit. Experimental hyperactivation of this circuit in young flies results in sleep loss and lasting deficits in adult courtship behaviors. These deficits are accompanied by impaired development of a single olfactory glomerulus, VA1v, which normally displays extensive sleep-dependent growth after eclosion. Our results demonstrate that sleep promotes normal brain development that gives rise to an adult behavior critical for species propagation and suggest that rapidly growing regions of the brain are most susceptible to sleep perturbations early in life.

The ontogenetic hypothesis of sleep, proposed nearly 50 years ago, postulates that early developmental sleep is important for brain patterning (*1*). Average daily sleep amounts are highest early in development across multiple species (*1*–*4*), and human studies have indeed demonstrated that impaired sleep during critical periods of development can have severe and long-lasting consequences (*5*–*7*). Yet it remains unknown whether sleep is required for normal structural maturation of the brain, as animal studies have focused on a role for sleep in the cortical plasticity induced by sensory deprivation in early life, or relied on drugs and lesion studies with non-specific effects (*8*).

Sleep in *Drosophila* shares many characteristics with sleep in humans (*4*, *9*), including ontogenetic changes (*4*, *10*). We used this model organism to explore the neural circuitry governing sleep ontogeny and examined how sleep loss during development affects adult behavior. We found that sleep need is especially high in young flies. Activity of a subset of wake-promoting dopaminergic neurons increases as normal development progresses, resulting in changes in sleep patterns across stages of development. To examine whether sleep during a critical period promotes proper brain development, we focused on courtship because it is a robust, innate behavior with well-mapped circuitry. Dopaminergic hyperexcitation and consequent sleep deprivation in young but not mature flies cause behavioral courtship abnormalities and impair development of a rapidly growing brain region involved in courtship. Thus, sleep early in life is required for the proper development of a behaviorally relevant adult brain circuit.

Young Flies Have Increased Sleep Need

We first examined multiple aspects of sleep in young flies. Female *iso31* flies were collected 2 to 3 hours after eclosion and compared to aged (day 9 to 10) flies. Consistent with previous work (*4*, *10*), we observed increased total sleep amounts on the first day of adult life as compared to mature flies, with the majority of change resulting from increased daytime sleep in newly eclosed adult flies (Fig. 1A). Young flies initiated their first sleep bout after onset of the light period earlier than mature flies and also initiated sleep more quickly after dark onset (Fig. 1B). Sleep bout duration was lengthened during the day in young as compared to mature flies, indicating more consolidated daytime sleep, whereas bouts at night were not significantly different (fig. S1A). Developmental differences in sleep did not stem from more generalized locomotor changes, because activity during periods of wakefulness was not different between young and mature flies (fig. S1B). In addition, mutants without a functional circadian clock demonstrated ontogenetic sleep changes

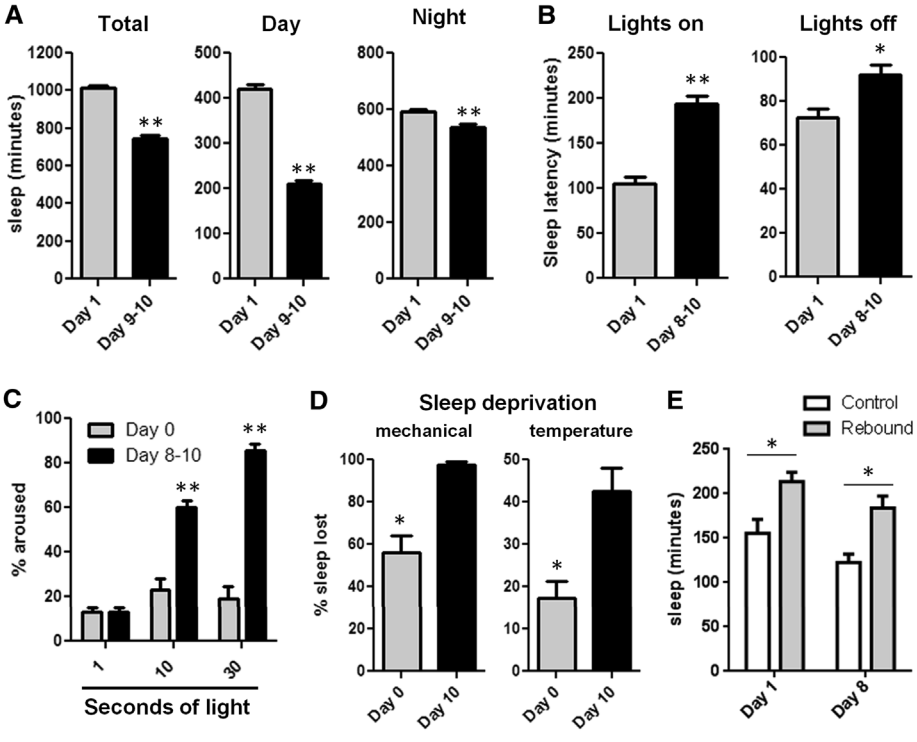

Fig. 1. Reduced arousal and increased resistance to sleep deprivation in young flies. Sleep measured in female *iso31* flies at day 1 and day 9 to 10: (**A**) Sleep amounts ($n = 150$ flies for day 1, 97 for day 9 to 10); (**B**) sleep latency ($n = 31$ for day 1, $n = 32$ for day 10); and (**C**) arousal threshold at day 0 or day 8 to 10 ($n = 5$ replicates, $n = 16$ flies per age in each). (**D**) Sleep deprivation: mechanical ($n = 11$ flies for each condition, with multiple independent replicates); and temperature ($n = 7$ for day 0, $n = 11$ for day 10, with multiple independent replicates). (**E**) Rebound sleep over 6 hours after sleep deprivation ($n = 15$, 38, 16, and 28 flies from left to right). Bar graphs in this figure and all others are presented as means ± SEM. $^{**}P < 0.0001$, $^{*}P < 0.005$; unpaired two-tailed Student's t test [(A); total sleep, (B) and (D)]; plus Welch's correction [(A), night and day sleep]; and two-way analysis of variance (ANOVA) with post-hoc Bonferroni multiple comparisons [(C) and (E)].

[1]Department of Psychiatry, Perelman School of Medicine at the University of Pennsylvania, Philadelphia, PA 19104, USA. [2]Center for Sleep and Circadian Neurobiology, Perelman School of Medicine at the University of Pennsylvania, Philadelphia, PA 19104, USA. [3]Howard Hughes Medical Institute, Perelman School of Medicine at the University of Pennsylvania, Philadelphia, PA 19104, USA. [4]Department of Neuroscience, Perelman School of Medicine at the University of Pennsylvania, Philadelphia, PA 19104, USA.

*Corresponding author. E-mail: amita@mail.med.upenn.edu

(fig. S1C), indicating that the sleep differences we observed were not clock-dependent.

We next investigated changes in arousal threshold using dim light (~100 lux) as a stimulus (*11*). On the first night after eclosion, only ~20% of flies were aroused by the same stimulus that aroused >80% of mature flies (Fig. 1C). This finding was not specific to the *iso31* background or the time of the light pulse in the night (fig. S1, D and E). The reduced arousal did not reflect an inability of young flies to respond to light, because young and mature flies were similarly aroused by a stronger (~1000 lux) light stimulus (fig. S1F). In addition, young flies also showed an increased arousal threshold in response to mechanical stimulation (fig. S1G). We next examined the effect of sleep-depriving stimuli by determining the percent of sleep lost during the night in young and mature flies, using two forms of deprivation (mechanical and temperature). Mature flies exhibited large amounts of sleep loss, particularly with mechanical deprivation, but young flies were resistant (Fig. 1D). Increasing the intensity of mechanical stimulus resulted in near-total sleep deprivation for 12 hours even in day-0 flies (fig. S1H), supporting the idea that young flies have an increased arousal threshold. To examine homeostatic regulation of sleep in young flies, we quantified rebound sleep during the first 6 hours of day after 12 hours of sleep deprivation using the weaker mechanical stimulus. Young and mature flies both showed significant sleep rebound, even under conditions in which young flies lost less sleep during deprivation (Fig. 1E). These results demonstrate a high sleep need during early post-eclosion development.

Reduced Dopamine Mediates Sleep Ontogeny

To explore the mechanism underlying ontogenetic changes in sleep, we performed a candidate-based thermogenetic screen of known wake-promoting *GAL4* drivers, looking for candidates that could overcome the high sleep drive of young flies. *GAL4* lines driving expression of TrpA1 [a heat-sensitive cation channel that can be used to induce neurotransmitter release (*12*)] were exposed to 28°C for 24 hours on the first full day after eclosion or after 8 to 10 days of aging and were compared to *UAS* (Fig. 2A) and *GAL4* (fig. S2A) controls. In mature female adult flies, virtually all drivers increased wake as expected (fig. S2B). In young flies, most drivers also increased wake (fig. S2B). However, *TH-GAL4* (tyrosine hydroxylase) was significantly more effective at driving wake in young flies than were other drivers at this age (Fig. 2A). It was also more effective in young versus mature flies, whereaas TrpA1-mediated activation by other drivers was blunted in young flies as compared to activation of the same neurons in the mature adult (Fig. 2A). The effects of *TH-GAL4>UAS-dTrpA1* were similar in males and independent of day or night (fig. S2, C and D). *TH-GAL4* drives expression in most dopamine neurons in the *Drosophila* brain (*13*), and dopamine is known to promote wake and arousal in the fly (*14*–*16*). We did not detect any gross changes in dopamine neuroanatomy between young and mature flies as visualized by green fluorescent protein (GFP) labeling of TH^+ cell bodies and projections (fig. S3A). Thus, one interpretation of our results is that dopaminergic neurons are hypoactive in young flies, resulting in a larger relative effect of hyperexcitation as compared to other *GAL4*s. If this were the case, we would predict that inhibition of TH^+ neurons would have a blunted effect in young as compared to mature flies, because these neurons are already less active. Using *TH-GAL4* to drive the temperature-sensitive inactivator of neuronal function *UAS-shibire^{ts}* (*17*, *18*), we found that silencing TH^+ neurons at 29°C in mature flies caused a significantly larger increase in sleep than in young flies, as compared to *UAS* (Fig. 2B) and *GAL4* (fig. S3B) controls. This does not simply reflect a ceiling effect of sleep in young flies, because the activation of mushroom body (MB) sleep-promoting neurons (*19*), using *201y-GAL4>UAS-dTrpA1*, resulted in similar amounts of sleep gained in both young and mature flies (Fig. 2B and fig. S3B). Moreover, total sleep amounts were equal in young and mature *TH-GAL4>UAS-shibire* flies exposed to elevated temperatures, whereas *201y-GAL4>UAS-dTrpA1* flies slept significantly more when young (fig. S3C).

We next examined sleep ontogeny in *fumin* flies (*14*), which lack dopamine transporter (DAT) function. Although both young and mature *fumin* flies showed reduced sleep due to increased synaptic dopamine, ontogenetic changes were maintained (Fig. 2C). This supports the idea that young flies have dopaminergic hypofunction, which would limit the amount of dopamine available even in flies that lack DAT. Our hypothesis suggests that a developmental delay in dopaminergic activity underlies sleep changes during adulthood, and the inhibition of dopaminergic neurons eliminates differences in total sleep time between young and mature flies (fig. S3B). The loss of ontogenetic sleep changes is not a generalized result of abnormal arousal signaling, however, because mutations in other known wake/arousal-promoting systems [though resulting in sleep and arousal changes (*20*, *21*)] did not disrupt sleep ontogeny (Fig. 2D). Finally, we used high-performance liquid chromatography (HPLC) to measure dopamine levels in the brains of young flies and found >30% less dopamine as compared to the brains of mature adults (Fig. 2E). Together, these results suggest that dopamine signaling is hypoactive in the brains of young flies, resulting in increased sleep and reduced arousal.

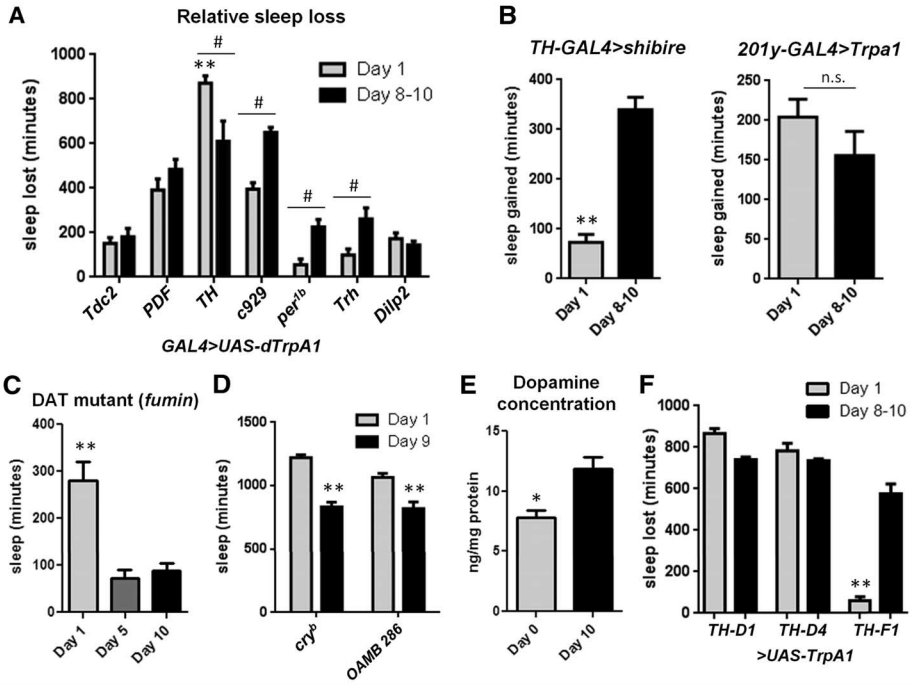

Fig. 2. Reduced dopamine signaling underlies ontogenetic sleep changes. (**A**) Wake-promoting *GAL4>UAS-dTrpA1* screen examining sleep loss compared to *UAS* controls in day-1 and day-8 to -10 flies at 28°C (**denotes comparison to all other day-1 *GAL4>UAS-dTrpA1* measures; from left to right, n = 21, 12, 23, 12, 26, 12, 24, 23, 23, 24, 22, 24, 24, and 24 flies). (**B**) Sleep gained as compared to *UAS* controls in day-1 and day-8 to -10 flies at 29°C (*TH-GAL4>shi*: n = 23 day-1 flies, n = 22 day-8 to -10; *201y-GAL4>TrpA1*: n = 18 day-1, n = 11 day-8 to -10). (**C**) Total sleep time in 24 hours in *fumin* flies at day 1, 5, and 10 (from left to right, n = 34, 20, and 28 flies). (**D**) Total sleep time in 24 hours at day 1 and day 9 in *cry^b* and *OAMB 286* flies (from left to right, n = 12, 12, 10, and 10 flies). (**E**) HPLC detection of dopamine concentration in fly brains (n = 4 separate replicates of 20 brains each). (**F**) Sleep loss in *TH*-restricted lines as compared to *UAS* controls in day-1 and day-8 to -10 flies at 29°C (from left to right, n = 12, 12, 11, 12, 40, and 11 flies). **$P < 0.0001$, # and *$P < 0.05$; two-way ANOVA with post-hoc Bonferroni multiple comparisons [(A) and (D)]; one-way ANOVA with Tukey's post-hoc test [(C) and (F)]; and unpaired two-tailed Student's t test (E); plus Welch's correction (B).

Identification of a Hypoactive Dopamine Circuit

We next sought to determine how dopaminergic hypoactivity leads to increased sleep, first by examining the temporal course of *TH-GAL4* neuronal activity in young flies. We used a targetable luciferase-based reporter under the control of dCREB2 binding sites (*UAS-FLP/+; Cre-F-luc/+*) to achieve spatial control while monitoring CREB as a proxy for cellular activity in vivo for extended periods of time (*22*, *23*). Expression of Cre-luciferase in dopaminergic neurons using *TH-GAL4* revealed a reduction in normalized luminescence over 12 hours in day-0 as compared to day-7 to -9 flies (fig. S4A). By hour 48 of monitoring the same flies, we no longer detected a difference in signal intensity between groups. In contrast, another wake-promoting *GAL4* line, *c929-GAL4*, showed higher reporter levels in young than in mature flies during the same period, indicating that not all wake-promoting neurons are less active by this assay in young flies (fig. S4A). Reduced *TH-GAL4*–driven luminescence appears to be head-specific, demonstrated by monitoring of heads and bodies independently (fig. S4B). These data confirm that a measure of cell signaling, CREB activity, is reduced in *TH-GAL4* neurons of young flies.

To narrow down the role of distinct dopaminergic inputs in sleep ontogeny, we took advantage of *TH-GAL4* drivers with expression restricted to different subsets of dopaminergic neurons (*11*). The dorsal fan-shaped body (dFSB) is a sleep-promoting region in the fly brain (*24*, *25*), and dopamine neurons project to the dFSB in their role as a wake-promoting signal, presumably to inhibit dFSB function (*11*, *26*). *TH-D1* and *TH-D4* both include projections to the dFSB, with *TH-D4* being the most restricted; *TH-F1* is also expressed in a small number of dopaminergic neurons but excludes those projecting to dFSB. At 29°C, we found that each of these lines promotes wakefulness in mature flies when driving expression of *UAS-dTrpA1* (Fig. 2F, black bars), indicating the presence of dFSB-independent dopaminergic arousal circuitry (Fig. 2F is compared to *UAS* controls, fig. S4C is compared to *GAL4* controls). However, in young flies, *TH-D1* and *TH-D4* result in robust sleep loss when driving TrpA1 expression, whereas *TH-F1* has minimal effect (Fig. 2F, gray bars). This result is consistent with the idea that dopaminergic hypofunction in young flies is specific for the dFSB. The *TH-F1* data indicate that excitation of dFSB-independent dopamine neurons cannot overcome hypoactivity of dFSB-dependent dopamine neurons to promote wakefulness in young flies. To examine the activity of these TH^+ neuronal subsets during development, we again used the Cre-based reporter system. We found reduced luminescence in young as compared to mature *TH-D4-GAL4>UAS-FLP/+;Cre-F-luc/+* flies (fig. S4D); in contrast, luminescence was higher in young *TH-F1-GAL4>UAS-FLP/+;Cre-F-luc/+* flies (fig. S4D). These findings indicate lower CREB-dependent transcription in *TH-GAL4* neurons with projections to the dFSB. Additionally, we noted no differences in *TH-D4* or *TH-F1* expression at different ages (fig. S5A), and found that contacts between TH^+ neurons and the dFSB were indistinguishable in the different age groups (fig. S5B). Thus, a subset of dopaminergic neurons (those with projections to the dFSB) is hypoactive in young flies, whereas other dopaminergic neurons are active at or above mature adult levels.

To more directly investigate developmentally regulated activity changes in specific neural circuits that might underlie sleep changes, we took advantage of the CaLexA (calcium-dependent nuclear import of LexA) system (*27*). This system is based on the activity-dependent nuclear import of a chimeric transcription factor, the nuclear factor of activated T cells (NFAT), which then drives GFP reporter expression (*27*, *28*). With *TH-GAL4* driving expression of CaLexA, we focused on fluorescence in dopaminergic projection to the dFSB itself, because reporter expression has been demonstrated to label all compartments of a neuron (*27*). We found reduced fluorescence in the dFSB on day 1 as compared to day 8, when CaLexA was expressed via the *TH-GAL4* driver (Fig. 3, A and B), which is consistent with reduced dopaminergic neuronal activity in this brain region. In contrast, we noted increased fluorescence of the wake-promoting large ventral lateral neurons (l-LNvs) (*29*) in young flies when CaLexA was expressed via the *c929-GAL4* driver (Fig. 3, A and C), which is consistent with our Cre-luciferase data. Finally, we assessed changes in postsynaptic dopaminergic input throughout development with the DopR-Tango system (*30*), with which transient dopamine-induced cellular activation is converted into a stable fluorescent readout. The system can be temporally restricted, because it is coupled to a pan-neuronally expressed hormone (RU486)–inducible *GAL4 (31)*. We first demonstrated that feeding DopR-Tango flies L-dopa for 2 days after 24 hours of RU486 induced an increase in reporter expression in the dFSB (fig. S5C), similar to that found in other brain regions (*30*). Next, we assayed endogenous dopamine signaling in young and mature flies. We fed flies

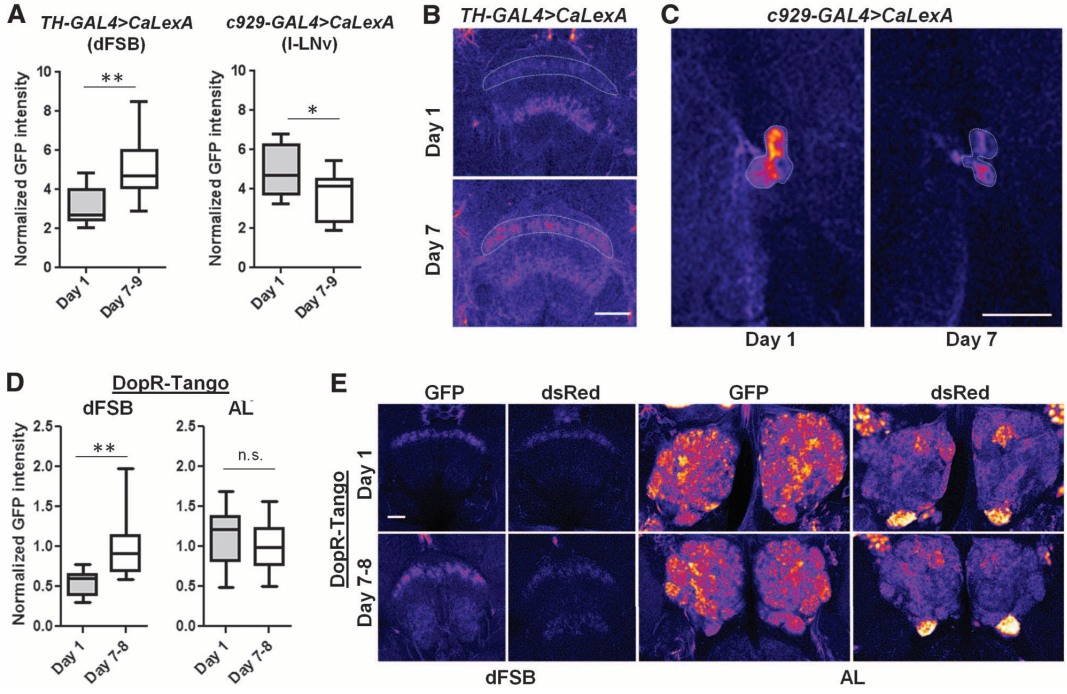

Fig. 3. Hypoactivity of dFSB-projecting dopaminergic neurons in young flies. (**A**) Normalized GFP intensity of the indicated brain region in *GAL4>UAS-CaLexA* flies of different ages (TH-GAL4: $n = 13$ at both ages; c929-GAL4: $n = 14$ day-1, $n = 15$ day-7 to -9). Representative images of (**B**) the dFSB and (**C**) large LNvs in brains immunostained for GFP. GFP is pseudocolored "fire." Warmer colors reflect increased signal intensity. Scale bars, 37.5 μm. (**D**) Normalized GFP intensity in DopR-Tango flies in the dFSB and AL (dFSB: $n = 22$ day-1 flies, $n = 25$ day-7 to -8; AL: $n = 34$ day-1, $n = 49$ day-7 to -8). (**E**) Representative images of the dFSB and AL in DopR-Tango flies. Endogenous GFP and dsRed are pseudocolored fire. Scale bar, 20 μm. Box plots in this figure and all others represent the median value (horizontal line inside box), interquartile range (height of the box, 50% of the data within this range), and minimum and maximum value (whiskers). $^{**}P < 0.0001$, $^{*}P < 0.05$; unpaired two-tailed Student's *t* test plus Welch's correction [(A) and (D)].

RU486 for 24 hours, followed by regular food for ~20 hours to allow time for expression of the Tango reporter (*30*). Young flies were dissected on day 2 after eclosion, ~3 hours after light onset, so the reporter signal should mostly reflect dopaminergic activity from day 1. With this approach, we found significantly lower reporter expression in young flies than in mature flies in the dFSB (Fig. 3, D and E), directly demonstrating reduced dopaminergic input to the dFSB. We did not detect a similar difference in dopaminergic inputs to the antennal lobe (AL; Fig. 3, D and E). Together, these results provide evidence for circuit-level specificity of dopaminergic activity changes during development.

The dFSB Promotes Increased Sleep in Young Flies

Our data suggest that a known sleep-promoting region, the dFSB, is more active in young flies because of reduced dopaminergic input. To test this idea, we used the dFSB driver *104y-GAL4*, which promotes sleep at elevated temperatures when driving expression of TrpA1 (*24*). Inhibition of dFSB activity using *104y-GAL4* has also been shown to reduce sleep, via expression of a K^+ channel that electrically silences neurons (*11*). We examined the consequences of dFSB activation by measuring sleep with *104y-GAL4>UAS-dTrpA1* at elevated temperatures during the first 12 hours of the day, which is a time when young and mature flies exhibit the largest difference in sleep patterns. We found that in young flies, dFSB activation had a blunted effect on sleep as compared to the large increase induced in mature flies (Fig. 4, A and C, compared to *UAS* controls; fig. S6A, compared to *GAL4* controls); another dFSB driver, *c205-GAL4*, yielded similar results (Fig. 4C and fig. S6A). We did not detect any differences in *104y-GAL4*–dependent expression of *UAS-mCD8::GFP* at day 1 as compared to day 8 (fig. S6B). The reduced effect on sleep during day 1 was specific to the dFSB, because MB activation with either *ok107-GAL4>UAS-dTrpA1* or *201y-GAL4>UAS-dTrpA1* resulted in similar sleep increases in young and mature flies (Fig. 4, B and C, compared to *UAS* controls; fig. S6A, compared to *GAL4* controls). Together these results support the idea that the dFSB in young flies is hyperactive because of reduced dopaminergic input, explaining why less sleep is induced with TrpA1 activation, whereas other sleep-promoting regions (such as the MB) function comparably in young and mature flies.

To test whether the dFSB is hyperactive in young flies, we used the CaLexA and Cre-based reporter systems described earlier. Flies with *104y-GAL4* driving expression of CaLexA showed significantly increased fluorescence in the dFSB on day 1 as compared to day 8 (Fig. 4, D and E), indicating increased activity of this sleep-promoting region in young flies. In contrast, expression of CaLexA in the MB using *ok107-GAL4* or *201y-GAL4* revealed no significant differences in neural activity at different ages (Fig. 4, D and E). Likewise with Cre-luciferase, we found a higher luminescence signal during the first 12 hours of the day in day-1 compared to day-8 flies with *104y-GAL4>UAS-FLP/+;Cre-F-luc/+* (fig. S6C). Normalized luminescence over this time in *201y-GAL4>UAS-FLP/+;Cre-F-luc/+* and *ok107-GAL4>UAS-FLP/+;Cre-F-luc/+* flies was the same in flies at day 1 or day 8 (fig. S6C). These results demonstrate that in young flies, a specific sleep-promoting brain area, the dFSB, is more active, leading to increased sleep and reduced arousal.

Courtship Behaviors and Circuitry Require Early Sleep

Why do young flies have mechanisms in place to maintain high levels of deep (arousal-resistant) sleep? Disruption of sleep in young flies by mechanical stimulation impairs a variety of adult behaviors, including courtship (*10*). We examined whether reversible hyperexcitation of *TH-GAL4* neurons during a period when these cells are normally hypoactive would result in long-lasting courtship deficits. *TH-GAL4>UAS-dTrpA1* males were collected within hours of eclosion and exposed to 36 hours of elevated temperature beginning either on day 0 or day 7 (Fig. 5A). Flies

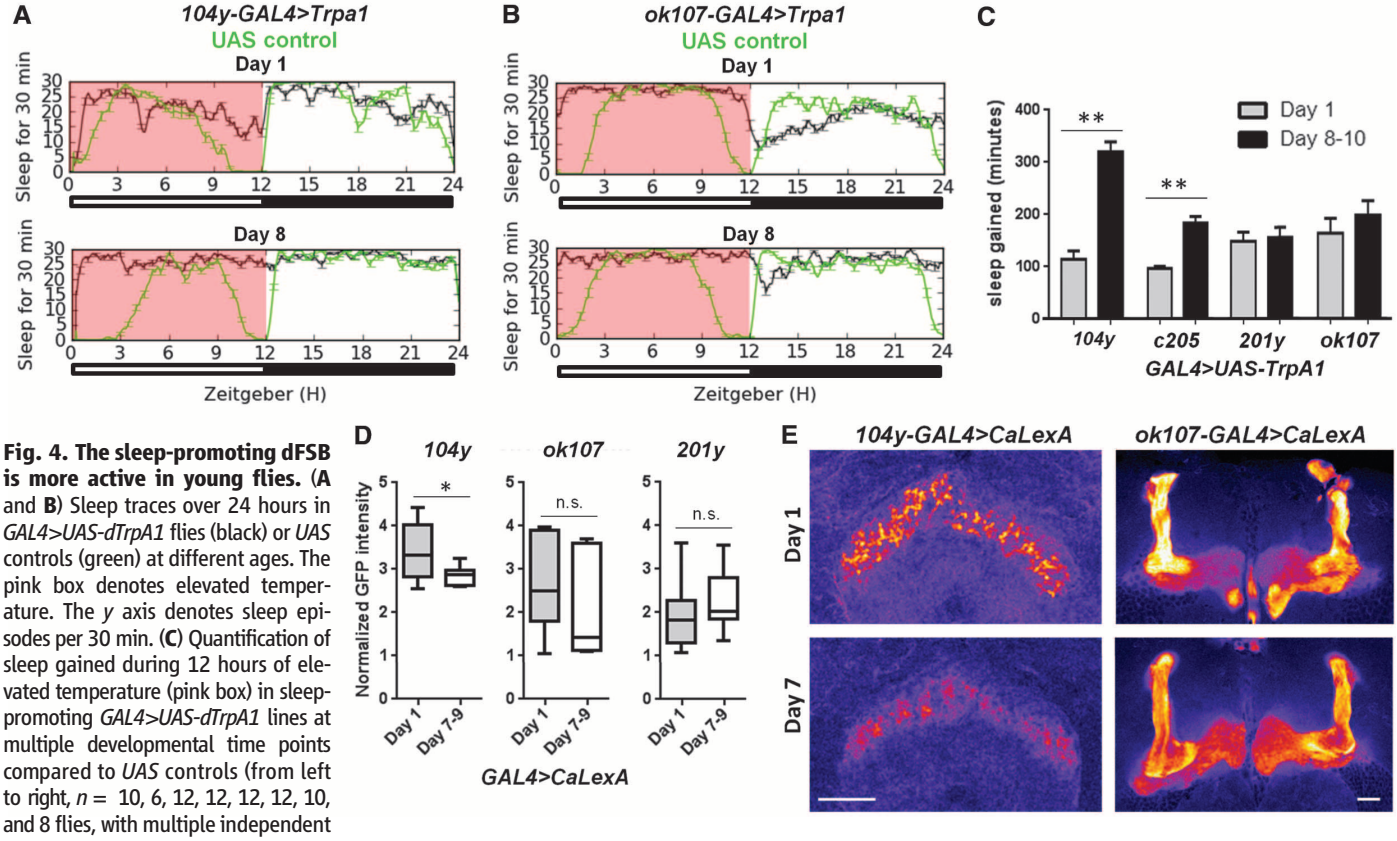

Fig. 4. The sleep-promoting dFSB is more active in young flies. (**A** and **B**) Sleep traces over 24 hours in *GAL4>UAS-dTrpA1* flies (black) or *UAS* controls (green) at different ages. The pink box denotes elevated temperature. The *y* axis denotes sleep episodes per 30 min. (**C**) Quantification of sleep gained during 12 hours of elevated temperature (pink box) in sleep-promoting *GAL4>UAS-dTrpA1* lines at multiple developmental time points compared to *UAS* controls (from left to right, $n =$ 10, 6, 12, 12, 12, 12, 10, and 8 flies, with multiple independent replicates). (**D**) Normalized GFP intensity of the indicated brain region in *GAL4>UAS-CaLexA* flies of different ages (104y-GAL4: $n = 9$ day-1, $n = 10$ day-7 to -9; ok107-GAL4: $n = 15$ day-1, $n = 14$ day-7 to -9; 201y-GAL4: $n = 22$ day-1, $n = 16$ day-7 to -9). (**E**) Representative images of the dFSB (left) and MB (right) in brains immunostained for GFP. GFP is pseudocolored fire. Scale bars , 37.5 μm. $^{**}P < 0.0001$, $^{*}P < 0.05$; one-way ANOVA with Tukey's post-hoc test (C); and unpaired two-tailed Student's *t* test plus Welch's correction (D).

were then allowed to recover for 3 days before testing. On day 5 or day 12, we examined courtship behaviors (Fig. 5A). *TH-GAL4>UAS-dTrpA1* males exposed to elevated temperatures beginning on day 0 but not day 7 exhibited a reduced courtship index and a severe reduction in copulation frequency (Fig. 5B). We observed no effect on courtship in *GAL4* and *UAS* controls exposed to elevated temperatures on day 0 (fig. S7A). Thus, hyperexcitation of dopaminergic neurons during a sensitive window of development leads to long-lasting deficits in courtship.

Because courtship is an innate behavior, the underlying neural circuits are thought to be developmentally programmed (*32*). Courtship behaviors in *Drosophila* are sexually dimorphic and require the male-specific isoform of the *fruitless* gene, Fru(M) (*33*). *fruitless* expression patterns are similar in males and females, but differences have been identified in subpopulations of the ~2000 Fru$^+$ neurons, including clusters dorsal to the antennal lobe (AL), the suboesophageal ganglion (SOG), and neurons projecting to three AL olfactory glomeruli (*34*–*37*). Olfactory glomeruli are known to be highly plastic structures (*38*, *39*), though Fru$^+$ glomeruli have not previously been examined. We therefore focused on this region to determine whether courtship deficits in young sleep-deprived flies might be attributed to changes in Fru$^+$ circuitry. Total volumes were calculated for DA1 and VA1v, which are the Fru$^+$ glomeruli known to exhibit the largest differences between males and females (*34*, *37*). *TH-GAL4>UAS-dTrpa1* males that were sleep-deprived when young, but not those sleep-deprived when mature, showed a reduction in size of a specific Fru$^+$ glomerulus, VA1v (Fig. 5, C and D). The volume of the other analyzed Fru$^+$ glomerulus, DA1, was not affected, nor were two other non-Fru$^+$ glomeruli, DL3 and VA1d, which are adjacent to DA1 and VA1v (Fig. 5, C and D and fig. S7B). These differences are apparent both in raw volumetric data (fig. S7B) and in values normalized to DL3 to control for brain-to-brain size variability (Fig. 5C) (*37*). Similar effects on courtship behavior and AL glomeruli were also obtained when a higher-intensity mechanical stimulus able to sleep-deprive young flies was used (fig. S7, C and D).

To address the possibility that *TH-GAL4>UAS-dTrpa1* in our paradigm affects courtship behaviors and circuitry independent of sleep, we sought a driver that excludes dopaminergic dFSB projections but still has widespread expression in TH$^+$ projections near olfactory glomeruli in the AL. *TH-C1* fits these criteria (*11*), and we found that *TH-C1-GAL4>UAS-CD8::GFP* is expressed in ventral projections to the AL (fig. S8A). Moreover, *TH-C1* is not known to be wake-promoting when activated (*11*). Using *TH-C1-GAL4>UAS-dTrpa1*, we found that hyperexcitation of this subset of TH$^+$ neurons in young flies failed to cause courtship deficits or glomerular volumetric changes in mature adulthood in the absence of earlier sleep loss (fig. S8, B to D). Thus, dopamine neurons excluded by *TH-C1* are necessary for the observed behavioral and volumetric effects, which are not likely to be secondary to direct hyperactivation of dopaminergic inputs to the AL. Finally, we assessed *TH-D4*, mentioned above, which is expressed in neurons projecting only to the ellipsoid body, MB, and FSB (fig. S8A) (*11*). Activation of these neurons in young flies

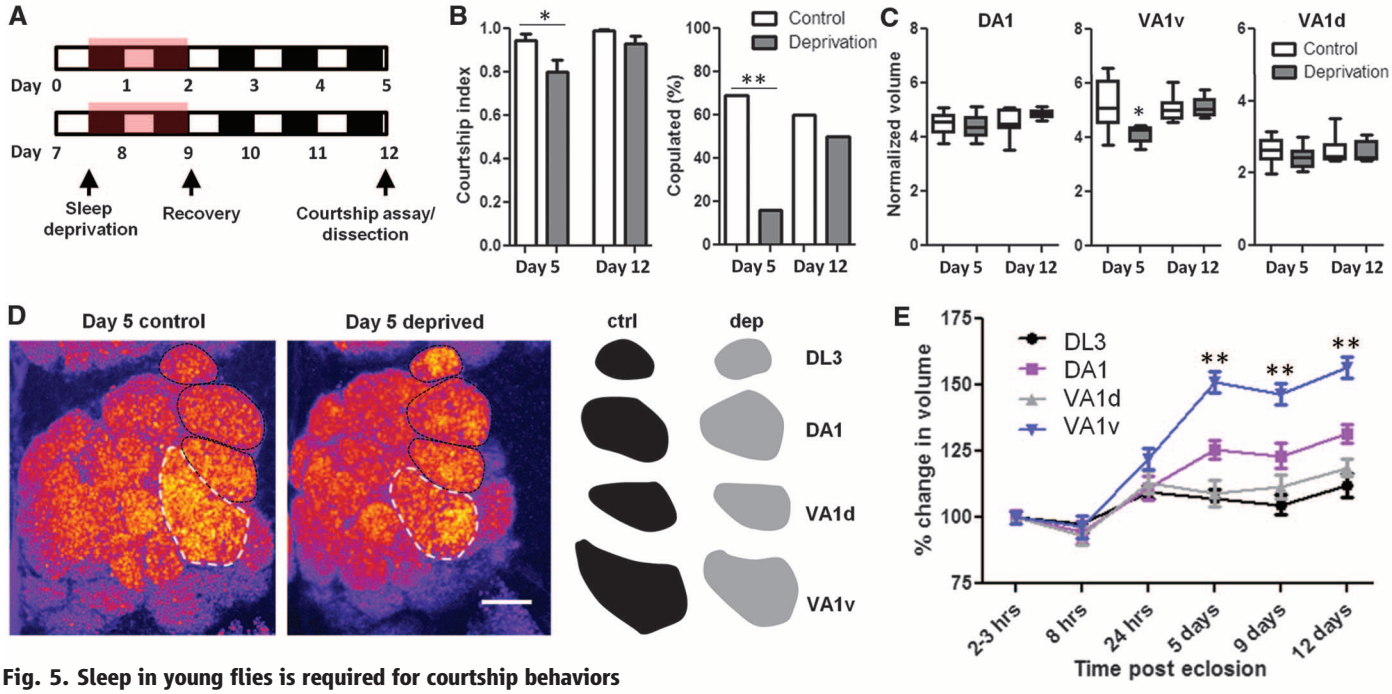

Fig. 5. Sleep in young flies is required for courtship behaviors and circuitry development. (**A**) Schematic of experimental approach. (**B**) Quantification of courtship index and copulation frequency (n = 14, 12, 15, and 12 flies for day-5 control, day-5 deprivation, day-12 control, and day-12 deprivation, respectively) in a 10-min assay using CS female virgin targets. (**C**) Quantification of olfactory glomerular volume normalized to DL3 (n = 11, 10, 10, and 9 flies for day-5 control, day-5 deprivation, day-12 control, and day-12 deprivation, respectively). (**D**) Representative images of the AL labeled with anti-nc82, pseudocolored "fire." White hashed outlines demarcate VA1v; black hashed lines demarcate DL3, DA1, and VA1d (from top to bottom). Right: Solid traces of each glomerulus in black (controls) and gray (deprived). Scale bar, 20 μm. (**E**) Quantification of the percentage growth of glomeruli (normalized to hour-2 to -3 values) at multiple developmental time points in *TH-GAL4>UAS-dTrpA1* males at 21°C (n = 11, 9, 12, 8, 11, and 10 flies for hour-2 to -3, hour-8, day-1, day-5, day-9, and day-12 respectively). (**F**) Representative images of the AL labeled with anti-nc82, pseudocolored "fire." White hashed outlines demarcate VA1v. Scale bar, 20 μm. $^{**}P < 0.001$, $^{*}P < 0.05$; one-way ANOVA with Tukey's post-hoc test [(B); courtship index, (C)]; Fischer's exact test [(B), copulation frequency]; and two-way ANOVA with post-hoc Bonferroni multiple comparisons (E).

using *TH-D4-GAL4>UAS-dTrpA1* resulted in sleep deprivation (fig. S8D), and after recovery days, we found a deficit in courtship measures and a specific reduction in VA1v volume (fig. S8, B and C); DA1 and VA1d volumes were unaffected. Together, these findings demonstrate that early developmental sleep deprivation affects a specific part of courtship-relevant circuitry and pinpoint a small group of TH^+ neurons that are sufficient for the effect.

We wondered why VA1v in particular would be affected by sleep deprivation. The volume reduction as compared to controls could result either from volume loss or failure of normal growth. To distinguish between these two possibilities, we charted the developmental time course of growth in the same four glomeruli in *TH-GAL4>UAS-dTrpa1* males. We used these flies to control for background effects on volumetric measures when comparing to preceding experiments. Flies were reared at 21°C, and dissections were performed at multiple time points after eclosion (Fig. 5E). All four glomeruli showed some degree of post-eclosion growth, although this was minimal in DL3 and VA1d (Fig. 5, E and F, and fig. S9, A and B). Both Fru^+ glomeruli underwent more extensive growth after eclosion, but VA1v grew significantly more than all other glomeruli (Fig. 5, E and F, and fig. S9, A and B). Thus, sleep deprivation impairs the developmental growth of VA1v, as opposed to inducing volume loss. VA1v normally undergoes the most rapid growth beginning ~8 hours after eclosion, which is the time when sleep deprivation began in experiments showing the long-lasting effect of deprivation on volume and courtship behaviors. Our data therefore suggest that sleep deprivation might be particularly deleterious to rapidly growing regions of the brain.

Discussion

The ubiquity among animals of increased sleep early in life suggests an important role for sleep during this period. Here we have defined a specific function for sleep in structural development of the brain. In addition, we identified a neural circuit controlling sleep in young flies. Sleep ontogeny in *Drosophila* is controlled by a developmental program: Dopaminergic neurons projecting to the dFSB are less active in young flies, leading to increased activity of this sleep-promoting region (fig. S10). It is possible that regulation of dopamine—a conserved arousal signal—also accounts for developmental changes in sleep in other species, perhaps even through specific circuits. Sudden infant death syndrome usually occurs early in infant life, and (in addition to environmental risk factors) abnormalities in sleep structure and arousal are thought to play a significant role (*40*, *41*). We suggest that the dysfunction of specific molecular signals or circuits could underlie pathological sleep/wake imbalances during mammalian development.

Courtship behaviors in *Drosophila* are innate and required for species propagation. Many studies have focused on the role of pheromone detection in this process (*42*). VA1v (also known as VA1lm) is the target of olfactory receptor neurons expressing Or47b (*43*, *44*) and confers responsiveness to odors from both male and female flies (*45*). A specific role for VA1v in male-female courtship has remained unclear (*46*), although genetic disruption of Or47b suggests a role in male localization of females (*47*), generally consistent with our finding that reduced size of VA1v correlates with courtship deficits. We cannot rule out the possibility that other regions of the nervous system involved in courtship are affected by early sleep deprivation as well. However, antennal lobe glomeruli are known to be highly plastic structures that exhibit volume and growth changes in response to external stimuli during specific periods of development (*38*, *39*). Post-eclosion experience-dependent glomerular plasticity could therefore be involved in encoding courtship encounters throughout life.

Sleep is involved in alterations of synaptic strength (*48*–*50*). Work in adolescent mice also suggests changes in dendritic spine number depending on the wake or sleep state, but only within a developmental period of heightened spine turnover (*51*). Whether ontogenetic sleep changes are required for synapse formation is not known. The antibody we used for volumetric glomerular measurements, anti-nc82, specifically recognizes the presynaptic active zone protein Bruchpilot, which exhibits homology to human presynaptic protein ELKS/CAST/ERC (*52*), and previous work has shown that glomerular volume correlates with synapse number (*53*). We propose a model whereby VA1v undergoes a period of rapid synapse addition in young flies, and we suggest that sleep is required for this process. Sleep disruption during this time affects VA1v and probably other regions with heightened rates of synaptogenesis. Many neuropsychiatric diseases are increasingly viewed as synaptic and developmental in origin (*54*), and sleep abnormalities are pervasive in psychiatric illness (*55*). Sleep during critical periods of development may therefore play an important role in diseases that manifest later in life.

References and Notes

1. H. P. Roffwarg, J. N. Muzio, W. C. Dement, *Science* **152**, 604–619 (1966).
2. D. Jouvet-Mounier, L. Astic, D. Lacote, *Dev. Psychobiol.* **2**, 216–239 (1969).
3. M. G. Frank, H. C. Heller, *Am. J. Physiol.* **272**, R1792–R1799 (1997).
4. P. J. Shaw, C. Cirelli, R. J. Greenspan, G. Tononi, *Science* **287**, 1834–1837 (2000).
5. L. M. O'Brien *et al.*, *Pediatrics* **114**, 44–49 (2004).
6. A. C. Halbower *et al.*, *PLOS Med.* **3**, e301 (2006).
7. M. Ednick *et al.*, *Sleep* **32**, 1449–1458 (2009).
8. M. G. Frank, *Prog. Brain Res.* **193**, 221–232 (2011).
9. J. C. Hendricks *et al.*, *Neuron* **25**, 129–138 (2000).
10. L. Seugnet, Y. Suzuki, J. M. Donlea, L. Gottschalk, P. J. Shaw, *Sleep* **34**, 137–146 (2011).
11. M. N. Wu, L. Kodama, Q. Liu, S. Liu, M. R. Driscoll, *Curr. Biol.* (2012).
12. F. N. Hamada *et al.*, *Nature* **454**, 217–220 (2008).
13. F. Friggi-Grelin *et al.*, *J. Neurobiol.* **54**, 618–627 (2003).
14. K. Kume, S. Kume, S. K. Park, J. Hirsh, F. R. Jackson, *J. Neurosci.* **25**, 7377–7384 (2005).
15. R. Andretic, B. van Swinderen, R. J. Greenspan, *Curr. Biol.* **15**, 1165–1175 (2005).
16. M. N. Wu, K. Koh, Z. Yue, W. J. Joiner, A. Sehgal, *Sleep* **31**, 465–472 (2008).
17. B. D. Pfeiffer, J. W. Truman, G. M. Rubin, *Proc. Natl. Acad. Sci. U.S.A.* **109**, 6626–6631 (2012).
18. T. Kitamoto, *J. Neurobiol.* **47**, 81–92 (2001).
19. W. J. Joiner, A. Crocker, B. H. White, A. Sehgal, *Nature* **441**, 757–760 (2006).
20. A. Crocker, M. Shahidullah, I. B. Levitan, A. Sehgal, *Neuron* **65**, 670–681 (2010).
21. S. Kumar, D. Chen, A. Sehgal, *Genes Dev.* **26**, 1224–1234 (2012).
22. A. K. Tanenhaus, J. Zhang, J. C. P. Yin, *PLOS ONE* **7**, e45130 (2012).
23. M. Sheng, M. A. Thompson, M. E. Greenberg, *Science* **252**, 1427–1430 (1991).
24. J. M. Donlea, M. S. Thimgan, Y. Suzuki, L. Gottschalk, P. J. Shaw, *Science* **332**, 1571–1576 (2011).
25. J. M. Donlea, D. Pimentel, G. Miesenböck, *Neuron* **81**, 860–872 (2014).
26. T. Ueno *et al.*, *Nat. Neurosci.* **15**, 1516–1523 (2012).
27. K. Masuyama, Y. Zhang, Y. Rao, J. W. Wang, *J. Neurogenet.* **26**, 89–102 (2012).
28. W. J. Kim, L. Y. Jan, Y. N. Jan, *Neuron* **80**, 1190–1205 (2013).
29. Y. Shang, L. C. Griffith, M. Rosbash, *Proc. Natl. Acad. Sci. U.S.A.* **105**, 19587–19594 (2008).
30. H. K. Inagaki *et al.*, *Cell* **148**, 583–595 (2012).
31. T. Osterwalder, K. S. Yoon, B. H. White, H. Keshishian, *Proc. Natl. Acad. Sci. U.S.A.* **98**, 12596–12601 (2001).
32. J. C. Hall, *Science* **264**, 1702–1714 (1994).
33. D. Yamamoto, M. Koganezawa, *Nat. Rev. Neurosci.* **14**, 681–692 (2013).
34. Y. Kondoh, K. Y. Kaneshiro, K. Kimura, D. Yamamoto, *Proc. Biol. Sci.* **270**, 1005–1013 (2003).
35. K.-I. Kimura, M. Ote, T. Tazawa, D. Yamamoto, *Nature* **438**, 229–233 (2005).
36. D. S. Manoli *et al.*, *Nature* **436**, 395–400 (2005).
37. P. Stockinger, D. Kvitsiani, S. Rotkopf, L. Tirián, B. J. Dickson, *Cell* **121**, 795–807 (2005).
38. S. Sachse *et al.*, *Neuron* **56**, 838–850 (2007).
39. J.-M. Devaud, A. Acebes, M. Ramaswami, A. Ferrús, *J. Neurobiol.* **56**, 13–23 (2003).
40. V. L. Schechtman, R. M. Harper, A. J. Wilson, D. P. Southall, *Pediatrics* **89**, 865–870 (1992).
41. R. M. Harper *et al.*, *Science* **213**, 1030–1032 (1981).
42. B. J. Dickson, *Science* **322**, 904–909 (2008).
43. A. Couto, M. Alenius, B. J. Dickson, *Curr. Biol.* **15**, 1535–1547 (2005).
44. E. Fishilevich, L. B. Vosshall, *Curr. Biol.* **15**, 1548–1553 (2005).
45. W. van der Goes van Naters, J. R. Carlson, *Curr. Biol.* **17**, 606–612 (2007).
46. L. Wang *et al.*, *Nat. Neurosci.* **14**, 757–762 (2011).
47. C. M. Root *et al.*, *Neuron* **59**, 311–321 (2008).
48. T. Abel, R. Havekes, J. M. Saletin, M. P. Walker, *Curr. Biol.* **23**, R774–R788 (2013).
49. D. Bushey, G. Tononi, C. Cirelli, *Science* **332**, 1576–1581 (2011).
50. M. G. Frank, N. P. Issa, M. P. Stryker, *Neuron* **30**, 275–287 (2001).
51. S. Maret, U. Faraguna, A. B. Nelson, C. Cirelli, G. Tononi, *Nat. Neurosci.* **14**, 1418–1420 (2011).
52. D. A. Wagh *et al.*, *Neuron* **49**, 833–844 (2006).
53. J.-M. Devaud, A. Acebes, A. Ferrús, *J. Neurosci.* **21**, 6274–6282 (2001).
54. H. Y. Zoghbi, *Science* **302**, 826–830 (2003).
55. D. J. Kupfer, *Biol. Psychiatry* **38**, 391–403 (1995).

Acknowledgments: We thank D. Raizen, T. Abel, M. Frank, and members of the Sehgal lab for helpful input and advice. This work was supported by grants T32HL07713 and R25MH060490 from the National Institutes of Health (M.S.K.) and the Howard Hughes Medical Institute (A.S.). M.S.K. and A.S. designed the experiments. M.S.K. and Z.Y. performed the research. M.S.K., Z.Y., and A.S. collected, analyzed, and interpreted the data. M.S.K., Z.Y., and A.S. wrote and edited the paper. The authors have no patents pending or financial conflicts to disclose.

Supplementary Materials

www.sciencemag.org/content/344/6181/269/suppl/DC1
Materials and Methods
Figs. S1 to S10
References (*56*–*61*)

8 January 2014; accepted 24 March 2014
10.1126/science.1250553

KOI-3278: A Self-Lensing Binary Star System

Ethan Kruse[1]* and Eric Agol[1]

Over 40% of Sun-like stars are bound in binary or multistar systems. Stellar remnants in edge-on binary systems can gravitationally magnify their companions, as predicted 40 years ago. By using data from the Kepler spacecraft, we report the detection of such a "self-lensing" system, in which a 5-hour pulse of 0.1% amplitude occurs every orbital period. The white dwarf stellar remnant and its Sun-like companion orbit one another every 88.18 days, a long period for a white dwarf–eclipsing binary. By modeling the pulse as gravitational magnification (microlensing) along with Kepler's laws and stellar models, we constrain the mass of the white dwarf to be ~63% of the mass of our Sun. Further study of this system, and any others discovered like it, will help to constrain the physics of white dwarfs and binary star evolution.

Einstein's general theory of relativity predicts that gravity can bend light and, consequently, that massive objects can distort and magnify more distant sources (*1*). This lensing effect provided one of the first confirmations of general relativity during a solar eclipse (*2*). Gravitational lensing has since become a widely used tool in astronomy to study galactic dark matter, exoplanets, clusters, quasars, cosmology, and more (*3*, *4*). One application has yet to be realized: In 1973, André Maeder predicted that binary star systems in which one star is a degenerate, compact object—a white dwarf, neutron star, or black hole—could cause repeated magnification of its companion star (instead of the standard eclipses) if the orbit happened to be viewed edge-on (*5*). The magnification of these self-lensing binary systems is small, typically a part in one thousand or less if the companion is Sun-like, and so it was not until high-precision stellar photometry was made possible with the Corot and Kepler spacecrafts that this could be detected (*6*, *7*). Stellar evolution models predict that about a dozen self-lensing binaries could be found by the Kepler spacecraft (*8*), but none have been discovered to date. A self-lensing binary system allows the measurement of the mass of the compact object, which is not true for most galaxy-scale microlensing events in which there is a degeneracy between the velocity, distance, and mass of the lensing object (*9*). Microlensing does affect several known white dwarfs in binaries in which the depth of eclipse is made slightly shallower (*10*–*14*) but does not result in brightening because occultation dominates over magnification at the short orbital periods of those systems.

Here, we report that Kepler Object of Interest 3278 (KOI-3278) (*15*, *16*), a term intended for planetary candidates, is instead a self-lensing binary composed of a white dwarf star orbiting a Sun-like star. The candidate planetary transit signal is actually the repeated occultation of the white dwarf as it passes behind its stellar companion. A search for other planets in this system with the Quasiperiodic Automated Transit Search algorithm (*17*) turned up a series of symmetric pulses, brightenings rather than dimmings, with a near-identical period and duration as the transit candidate but occurring almost half an orbital period later. All these properties can be explained by magnification of the Sun-like star as the white dwarf passes in front; 16 microlensing pulses were found, in addition to 16 occultations. The pulses and occultations are periodic and uniform in magnitude and duration (Fig. 1), which is consistent with a nearly circular, Keplerian orbit. Because there is no other phenomenon (that we know of) that can cause such a brief, symmetric, periodic brightening, we constructed a model for KOI-3278 composed of an eclipsing white dwarf and G dwarf (Sun-like star) binary (*18*).

Even without a full model, an estimate of the mass of the white dwarf, M_2, can be made directly from the light curve. The ratio of the fluence of the microlensing pulse, $F_{\rm pulse}$, to the stellar fluence over an orbital period, $F_{\rm tot}$, is given (*19*) by $F_{\rm pulse}/F_{\rm tot} = 5.4 \times 10^{-6}\sqrt{(1-b^2)}(M_2/M_\odot)(R_\odot/R_1)$, where R_1 is the radius of the G dwarf and b is the impact parameter (*20*). Because the duration of the pulse is 5 hours, the period is 88.18 days, and the magnification is 10^{-3}, we calculated $F_{\rm pulse}/F_{\rm tot}[1-(b/0.7)^2]^{-1/2} \approx 3.3 \times 10^{-6}$ and $M_2 \approx 0.6\,M_\odot$, which is a typical mass for a white dwarf star (*21*).

To jointly constrain the parameters of both stars, we fitted a full model simultaneously to the Kepler time-series photometry and the multiband photometry collected from other surveys (*18*). We modeled the light curve by using a Keplerian orbit with the gravitational lensing approximated as an inverted transit light curve, which is appropriate when the Einstein radius is small (*19*). We compared the Padova stellar evolution models (*22*) to the multiband photometry to constrain the properties of the G dwarf while accounting for extinction (A_V). Last, we used cooling models to constrain the age of the white dwarf (*23*).

Our model provides an accurate description of the data (Fig. 2) with a reduced χ^2 value of unity. From this model, we calculated the stellar parameters and the binary system's orbital properties (Table 1), with uncertainties derived from a Markov-chain Monte Carlo analysis (*18*). The model produced a white dwarf mass of $M_2 = 0.63\,M_\odot \pm 0.05\,M_\odot$, with a G dwarf companion of $M_1 = 1.04^{+0.03}_{-0.06}\,M_\odot, R_1 = 0.96^{+0.03}_{-0.05}\,R_\odot$, and effective temperature $T_{\rm eff,1} = 5568 \pm 39$ K: a star very similar to our Sun. Because the white dwarf, with its small size, is much fainter than the G dwarf, we cannot yet measure its temperature directly. However, given the measured mass from gravitational lensing, we inferred its size to be $R_2 =$

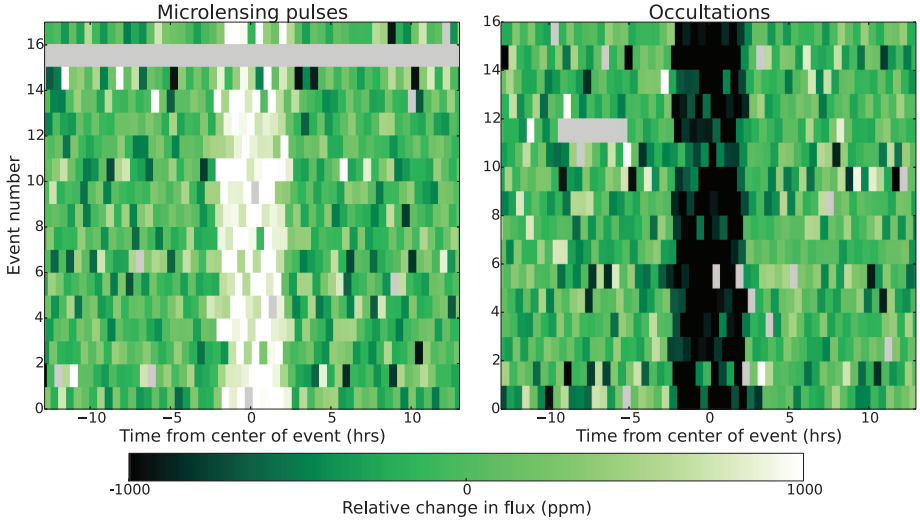

Fig. 1. Detrended flux versus time for all 16 microlensing pulses and 16 occultations in KOI-3278. Each row depicts the relative fluxes in 29.3-min Kepler cadences around an event. The rows are separated by the orbital period, $P = 88.18$ days. White represents brighter flux and black dimmer, whereas gray represents missing data or outliers that have been removed. ppm, parts per million.

[1]Department of Astronomy, University of Washington, Box 351580, Seattle, WA 98195, USA.

*Corresponding author. E-mail: eakruse@uw.edu

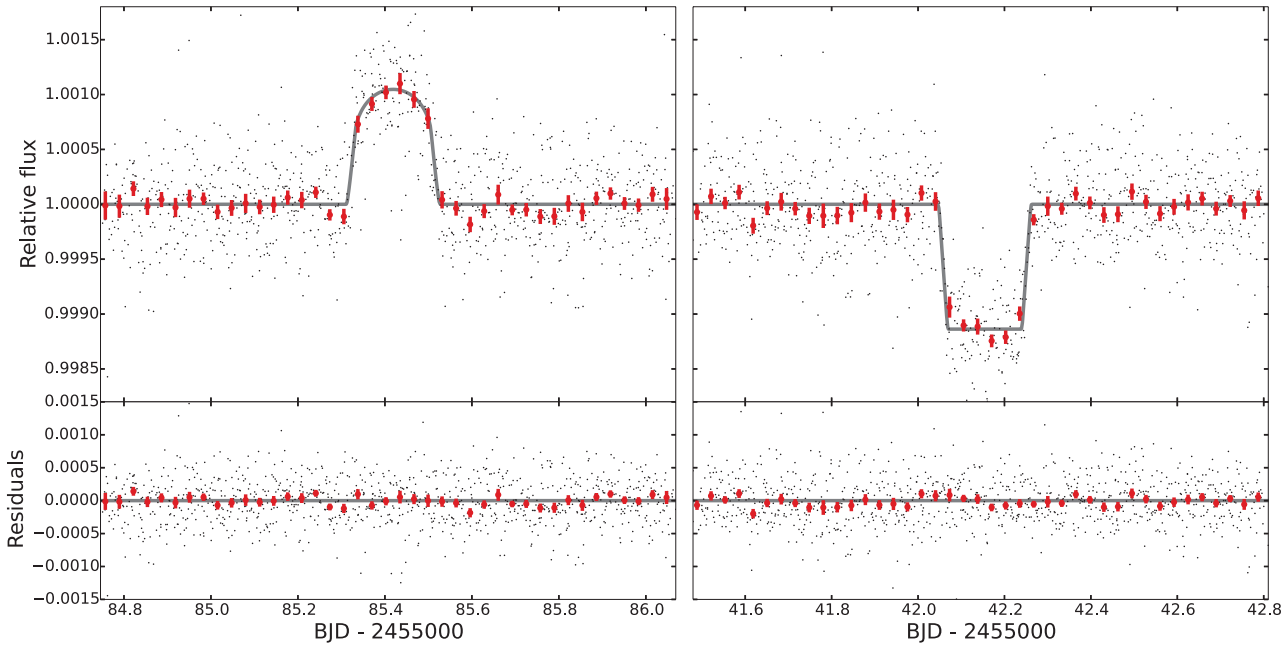

Fig. 2. Model fit to the data. Detrended and folded Kepler photometry of KOI-3278 presented as black points (all pulses and occultations have been aligned), overplotted with the best-fit model (gray line) for the microlensing pulse (**left**) and occultation (**right**). Red error bars show the mean of the folded data over a 45-min time scale. Bottom graphs show the residuals of the data with the best-fit model subtracted. BJD, barycentric Julian date.

0.0117 $R_\odot$ ± 0.0006 $R_\odot$ by using a mass-radius relation appropriate for carbon-oxygen white dwarfs. With a radius for the white dwarf, the measured occultation depth when it passes behind the G dwarf can be used to constrain the temperature of the white dwarf, which we found to be $T_{\mathrm{eff},2}$ = 10,000 ± 750 K; this temperature would give the white dwarf the bluish hue of an A star. The Einstein radius (R_E) is about twice the inferred size of the white dwarf, which allows lensing to dominate over occultation when the white dwarf passes in front. Gravitational lensing causes a distorted and magnified image of the G dwarf outside the Einstein ring in addition to a second inverted and reflected image of the G dwarf within the Einstein ring (Fig. 3); the inner image is partially occulted by the white dwarf's disk, reducing the observed magnification slightly.

Our model does not include the effect of star spots, but the Kepler G dwarf light curve displays their characteristic quasi-periodic fluctuations with a root mean square of 0.76%. We estimated that the spots would affect the derived stellar properties by less than a percent, smaller than the statistical errors in our model. Spot analysis revealed a G dwarf rotational period of P_{rot} = 12.5 ± 0.1 days. This short rotational period is expected for a G dwarf of only 0.89 ± 0.14 Gy (*18*). The white dwarf cooling time, t_{cool}, is 0.66 ± 0.06 Gy, which when added to the main sequence lifetime (t_2) of its progenitor with mass $M_{2,\mathrm{init}}$ gives a total age of the binary system of $t_1 = 1.6^{+0.9}_{-0.6}$ Gy; this age is marginally inconsistent (1.4σ) with the spin-down age of the G dwarf.

However, the G dwarf may have been spun up because of accretion of gas from the white dwarf progenitor. Because the white dwarf progenitor was previously a red giant, it should have enveloped the G dwarf during a common-envelope phase (*24*). The initial orbital period of the binary was likely several years long, and the period was likely shortened because of drag during the common-envelope phase. During this phase, the G dwarf accreted some gas from the red giant, increasing its mass by 10^{-3} to 10^{-2} $M_\odot$ and spinning the G dwarf up from the angular momentum contained in the accreted gas; this spin-up would have reset the age-spin relation, which could explain the slight age discrepancy.

KOI-3278 is the longest period eclipsing post-common-envelope binary found to date (fig. S7), and it is also one of the only examples of an eclipsing Sirius-like system—a binary composed of a noninteracting white dwarf and a Sun-like (or hotter) main-sequence star (*25*–*27*). As such, it will help to provide constraints on the physics of formation and evolution of short and intermediate period evolved binary stars, thereby improving our knowledge of the formation of accreting binaries and sources of gravitational waves. We expect that a few more self-lensing binaries will be found in the Kepler data at shorter orbital periods than KOI-3278. The magnification decreases down to periods of ≈16 days, making them more difficult to find; at even shorter periods, occultation by the white dwarf's disk wins out over the lensing, causing a shallower eclipse as in KOI-256 (*13*). Systems like KOI-3278 should not be a substantial source of false-positives for exoplanets;

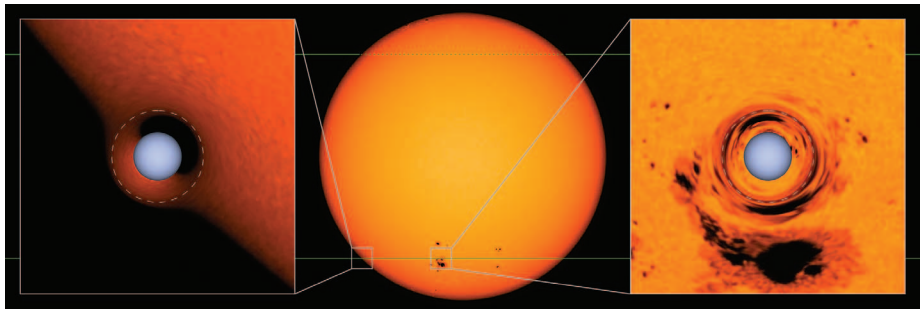

Fig. 3. Illustration of lensing magnification. (**Center**) The false-color disk of a G dwarf (using an actual image of the Sun from NASA/SDO HMI), in which the green line shows the trajectory of the white dwarf, with the dotted portion indicating where it passes behind the G dwarf. (**Left** and **right**) Close-ups of areas boxed in center show the lensed image of the G dwarf at two different times during the microlensing pulse; the white dwarf is the blue sphere. The white dashed line shows the Einstein ring of the white dwarf. The model that we fit to the data does not contain spots; however, the spots and granulation make the lensing distortion more apparent.

Table 1. Parameters of the KOI-3278 binary star system. More information can be found in the supplementary text. The median and 68.3% bounds are given for each parameter. g_1, surface gravity in cm/s^2. L_{WD}, luminosity of the white dwarf. e, eccentricity. ω, argument of periastron. a, semimajor axis. i, inclination. F_2/F_1 flux ratio between the white dwarf and G dwarf in the Kepler band. D, distance. σ_{sys}, systematic errors in the multiband photometry.

Variable	Value
G Dwarf	
M_1 ($M_\odot$)	$1.042^{+0.028}_{-0.058}$
R_1 ($R_\odot$)	$0.964^{+0.034}_{-0.054}$
$[Fe/H]_1$	$0.39^{+0.22}_{-0.22}$
t_1 (Gy)	$1.62^{+0.93}_{-0.55}$
$T_{eff,1}$ (K)	5568^{+40}_{-38}
$\log(g_1)$	$4.485^{+0.026}_{-0.020}$
White Dwarf	
$M_{2,init}$ ($M_\odot$)	$2.40^{+0.70}_{-0.533}$
M_2 ($M_\odot$)	$0.634^{+0.047}_{-0.055}$
$T_{eff,2}$ (K)	9960^{+700}_{-760}
R_2 ($R_\odot$)	$0.01166^{+0.00069}_{-0.00056}$
R_E ($R_\odot$)	$0.02305^{+0.00093}_{-0.00107}$
t_2 (Gy)	$0.96^{+0.90}_{-0.53}$
t_{cool} (Gy)	$0.663^{+0.065}_{-0.057}$
L_{WD} ($L_\odot$)	$0.00120^{+0.00024}_{-0.00023}$
Binary System	
P (days)	$88.18052^{+0.00025}_{-0.00027}$
t_0 (−2,455,000 BJD)	$85.4190^{+0.0023}_{-0.0023}$
$e\cos\omega$	$0.014713^{+0.000047}_{-0.000061}$
$e\sin\omega$	$0.000^{+0.049}_{-0.054}$
a (AU)	$0.4605^{+0.0064}_{-0.0103}$
a/R_1	$102.8^{+3.7}_{-2.4}$
b_0	$0.706^{+0.020}_{-0.025}$
i (deg)	$89.607^{+0.026}_{-0.020}$
F_2/F_1	$0.001127^{+0.000039}_{-0.000039}$
D (pc)	808^{+36}_{-49}
σ_{sys} (mags)	$0.0246^{+0.0127}_{-0.0078}$
K_1 (km/s)	$21.53^{+0.96}_{-0.98}$
π (milli–arc sec)	$1.237^{+0.079}_{-0.053}$
α_1 (milli–arc sec)	$0.2169^{+0.0076}_{-0.0072}$
A_V (mags)	$0.206^{+0.017}_{-0.016}$

only one was predicted to be found in the Kepler data with its magnification of ≈0.1% (*8*).

Follow-up observations should better constrain the parameters of the white dwarf star in KOI-3278, allowing a test of the mass-radius relation for white dwarfs (*28*, *29*). Once the Kepler field rises (it had set before we detected the microlensing signal), radial velocity observations should show a semi-amplitude K_1 of 21.5 km/s and a line-broadening of 4 km/s. High-resolution spectroscopy will also better constrain the atmospheric properties of the G dwarf; in particular, spectral abundance anomalies caused by accretion of nuclear-processed material from the white dwarf progenitor should be sought. Measurements of the occultation of the white dwarf in the ultraviolet (with the Hubble Space Telescope) should appear much deeper, as much as 60% in depth as opposed to the 0.1% occultation depth in the Kepler band, and will yield constraints on the radius and temperature of the white dwarf. High angular resolution imaging would allow for better constraints to be placed on the presence of a third star in the system (*18*). Last, parallax measurements (π) with the Gaia spacecraft (*30*) will improve the precision of the properties of the G dwarf; Gaia can also detect the reflex motion of the G dwarf α_1 as it orbits the center of mass with the white dwarf. This provides another means to detect systems like KOI-3278 with inclinations that do not show microlensing or occultation; there are likely 100 of these among the Kepler target stars alone, given the ~1% geometric lensing probability of KOI-3278.

References and Notes

1. A. Einstein, *Science* **84**, 506–507 (1936).
2. F. W. Dyson, A. S. Eddington, C. Davidson, *Philos. Trans. R. Soc. London Ser. A* **220**, 291–333 (1920).
3. J. Wambsganss, *Living Reviews in Relativity* **1**, 12 (1998).
4. P. Schneider, C. Kochanek, J. Wambsganss, *Gravitational Lensing: Strong, Weak and Micro* (Saas-Fee Advanced Course 33, Springer, Berlin, 2006).
5. A. Maeder, *Astron. Astrophys.* **26**, 215 (1973).
6. E. Agol, *Astrophys. J.* **579**, 430–436 (2002).
7. K. C. Sahu, R. L. Gilliland, *Astrophys. J.* **584**, 1042–1052 (2003).
8. A. J. Farmer, E. Agol, *Astrophys. J.* **592**, 1151–1155 (2003).
9. B. Paczyński, *Annu. Rev. Astron. Astrophys.* **34**, 419–459 (1996).
10. T. R. Marsh, *Mon. Not. R. Astron. Soc.* **324**, 547–552 (2001).
11. J. D. R. Steinfadt, D. L. Kaplan, A. Shporer, L. Bildsten, S. B. Howell, *Astrophys. J.* **716**, L146–L151 (2010).
12. J. F. Rowe *et al.*, *Astrophys. J.* **713**, L150–L154 (2010).
13. P. S. Muirhead *et al.*, *Astrophys. J.* **767**, 111 (2013).
14. D. L. Kaplan *et al.*, *Astrophys. J.* **780**, 167 (2014).
15. C. J. Burke *et al.*, *Astrophys. J. Suppl. Ser.* **210**, 19 (2014).
16. P. Tenenbaum *et al.*, *Astrophys. J. Suppl. Ser.* **211**, 6 (2014).
17. J. A. Carter, E. Agol, *Astrophys. J.* **765**, 132 (2013).
18. Materials and methods are available as supplementary materials on *Science* Online.
19. E. Agol, *Astrophys. J.* **594**, 449–455 (2003).
20. The impact parameter is the projected sky separation of the white dwarf and G dwarf at midpulse, in units of the radius of the G dwarf; we find a best-fit value of $b = 0.7$ based on the full model fit. This formula assumes a circular orbit, neglects limb-darkening, and neglects obscuration by the white dwarf; whereas these effects (although minor) are accounted for in our full model.
21. S. O. Kepler *et al.*, *Mon. Not. R. Astron. Soc.* **375**, 1315–1324 (2007).
22. A. Bressan *et al.*, *Mon. Not. R. Astron. Soc.* **427**, 127–145 (2012).
23. P. Bergeron *et al.*, *Astrophys. J.* **737**, 28 (2011).
24. N. Ivanova *et al.*, *Astron. Astrophys. Rev.* **21**, 59 (2013).
25. A. Rebassa-Mansergas *et al.*, *Mon. Not. R. Astron. Soc.* **423**, 320–327 (2012).
26. M. Zorotovic, M. R. Schreiber, *Astron. Astrophys.* **549**, A95 (2013).
27. J. B. Holberg, T. D. Oswalt, E. M. Sion, M. A. Barstow, M. R. Burleigh, *Mon. Not. R. Astron. Soc.* **435**, 2077–2091 (2013).
28. J. L. Provencal, H. L. Shipman, E. Hog, P. Thejll, *Astrophys. J.* **494**, 759–767 (1998).
29. S. G. Parsons *et al.*, *Mon. Not. R. Astron. Soc.* **420**, 3281–3297 (2012).
30. M. A. C. Perryman *et al.*, *Astron. Astrophys.* **369**, 339–363 (2001).

Acknowledgments: E.K. was funded by an NSF Graduate Student Research Fellowship. E.A. acknowledges funding by NSF Career grant AST 0645416; NASA Astrobiology Institute's Virtual Planetary Laboratory, supported by NASA under cooperative agreement NNH05ZDA001C; and NASA Origins of Solar Systems grant 12-OSS12-0011. Solar image courtesy of NASA/Solar Dynamics Observatory (SDO) and the Helioseismic and Magnetic Imager (HMI) science teams. The Kepler data presented in this paper were obtained from the Mikulski Archive for Space Telescopes (MAST). The code used for analysis is provided in a repository at https://github.com/ethankruse/koi3278. The authors welcome requests for additional information regarding the material presented in this paper.

Supplementary Materials

www.sciencemag.org/content/344/6181/275/suppl/DC1
Materials and Methods
Supplementary Text
Figs. S1 to S7
Table S1
References (*31*–*84*)

10 February 2014; accepted 25 March 2014
10.1126/science.1251999

An Earth-Sized Planet in the Habitable Zone of a Cool Star

Elisa V. Quintana,[1,2]* Thomas Barclay,[2,3] Sean N. Raymond,[4,5] Jason F. Rowe,[1,2] Emeline Bolmont,[4,5] Douglas A. Caldwell,[1,2] Steve B. Howell,[2] Stephen R. Kane,[6] Daniel Huber,[1,2] Justin R. Crepp,[7] Jack J. Lissauer,[2,8] David R. Ciardi,[9] Jeffrey L. Coughlin,[1,2] Mark E. Everett,[10] Christopher E. Henze,[2] Elliott Horch,[11] Howard Isaacson,[12] Eric B. Ford,[13,14] Fred C. Adams,[15,16] Martin Still,[3] Roger C. Hunter,[2] Billy Quarles,[2] Franck Selsis[4,5]

The quest for Earth-like planets is a major focus of current exoplanet research. Although planets that are Earth-sized and smaller have been detected, these planets reside in orbits that are too close to their host star to allow liquid water on their surfaces. We present the detection of Kepler-186f, a 1.11 ± 0.14 Earth-radius planet that is the outermost of five planets, all roughly Earth-sized, that transit a 0.47 ± 0.05 solar-radius star. The intensity and spectrum of the star's radiation place Kepler-186f in the stellar habitable zone, implying that if Kepler-186f has an Earth-like atmosphere and water at its surface, then some of this water is likely to be in liquid form.

In recent years, we have seen great progress in the search for planets that, like our own, are capable of harboring life. Dozens of known planets orbit within the habitable zone (HZ), the region around a star within which a planet can sustain liquid water on its surface (*1*–*4*). Most of these HZ planets are gas giants, but a few, such as Kepler-62f (*5*), are potentially rocky despite having a larger

radius than Earth. Hitherto, the detection of an Earth-sized planet in the HZ of a main-sequence star has remained elusive.

Low-mass stars are good targets in the search for habitable worlds. They are less luminous than the Sun, so their HZs are located closer in (*6*). The shorter orbital period and larger planet-to-star size ratio of a planet in the HZ of a cool star relative to planets orbiting in the HZ of solar-type stars allow for easier transit detections. M dwarfs, stars with 0.1 to 0.5 times the mass of the Sun ($M_\odot$), are very abundant, constituting about three quarters of all the main-sequence stars in our galaxy (*7*). They also evolve very slowly in luminosity, thus their HZs remain nearly constant for billions of years.

Kepler-186 (also known as KIC8120608 and KOI-571) is a main-sequence M1-type dwarf star with a temperature of 3788 ± 54 K and an iron abundance half that of the Sun [(*8*) and supplementary materials (SM) section 2]. The star was observed by the Kepler spacecraft at near-continuous 29.4-min intervals. The presence of four planets, designated Kepler-186b to Kepler-186e, all smaller than 1.5 Earth radius ($R_\oplus$), with orbital periods between 3.9 and 22.4 days, was confirmed with the first 2 years of data (*9*, *10*). The fifth planet candidate, Kepler-186f, which we discuss here, was detected with an additional year of data.

We compared the observed data to a five-planet model with limb-darkened transits (*9*, *11*), allowing for eccentric orbits to estimate the physical properties of Kepler-186f. We used an affine invariant Markov-chain Monte Carlo (MCMC) algorithm (*12*, *13*) to efficiently sample the model parameter posterior distribution. Kepler-186f has an orbital period of 129.9 days and a planet-to-star radius ratio of 0.021. The additional constraint on stellar density from the transit model allowed us to refine the stellar radius that was previously derived by modeling spectroscopic data. Interior models of cool main-sequence stars such as Kepler-186 show systematic differences from empirically measured stellar properties (*14*–*16*) (SM section 2). To account for discrepancies between the empirically measured radii and those derived from model isochrones at the measured temperature for Kepler-186, we have added a 10% uncertainty in quadrature to our stellar radius ($R_\star$) and mass estimate, yielding a final estimate of $R_\star$ = 0.472 ± 0.052 and a planet radius of 1.11 ± 0.14 $R_\oplus$ (Fig. 1 and table S2).

The Kepler-186 planets do not induce a detectable reflex motion on the host star or dynamically perturb each other so as to induce substantial non-Keplerian transit ephemerides, both of which can be used to help confirm the planetary nature of Kepler's planet candidates (*17*, *18*). Instead, we used a statistical approach to measure the confidence in the planetary interpretation of each candidate planet (*19*, *20*). We obtained follow-up high-contrast imaging observations using the Keck-II and Gemini-North telescopes (SM section 5) to restrict the parameter space of stellar magnitude/separation where a false-positive–inducing star could reside and mimic a planetary transit. No nearby sources were observed in either the Keck-II or Gemini data; the 5σ detection limit set the brightness of a false-positive star to be *K*p = 21.9 at 0.5″ from Kepler-186 and 19.5 at 0.2″, where *K*p is the apparent magnitude of a star in the Kepler bandpass.

The probability of finding a background eclipsing binary or planet-hosting star that could mimic a transit in the parameter space not excluded by observations is very low: 0.5% chance relative to the probability that we observe a planet

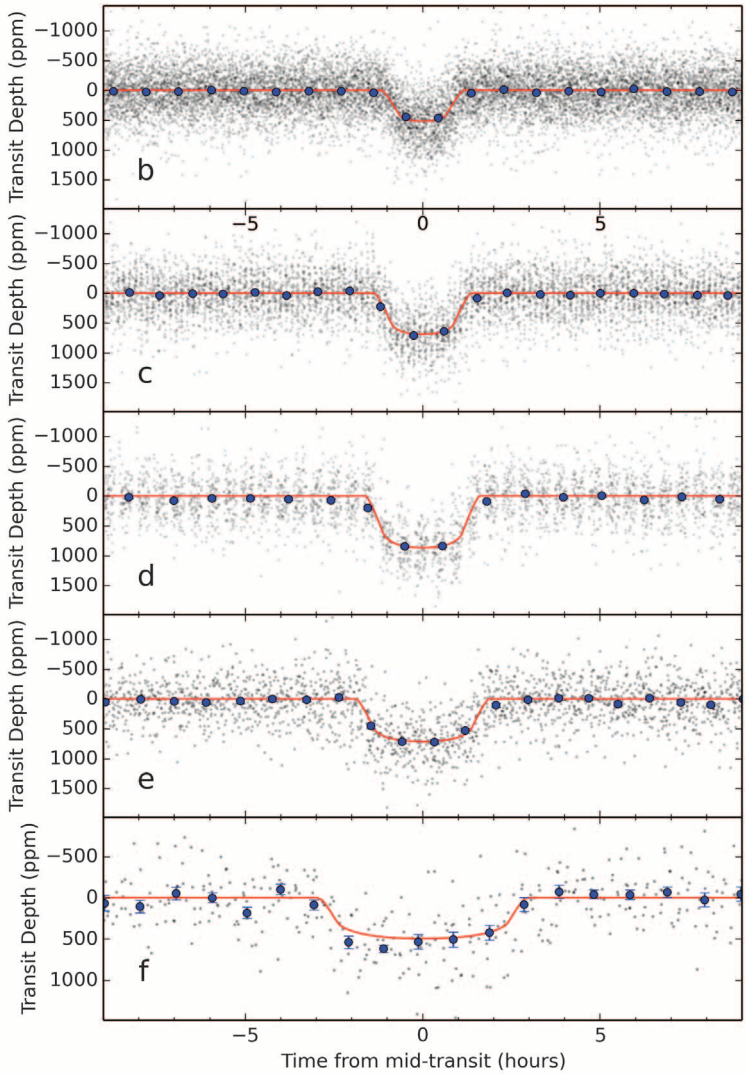

Fig. 1. The five transiting planet signals observed by Kepler, folded on the orbital periods of the respective planets. ppm, parts per million. The plots are ordered by ascending planet orbital periods. The black points show the observed data, and the blue points are the observed data binned in time with one point per phase-folded hour. The most probable transit model is shown in red. The incomplete phase coverage for Kepler-186d is a result of the orbital period of the planet having a value close to an integer multiple of the sampling.

[1]SETI Institute, 189 Bernardo Avenue, Suite 100, Mountain View, CA 94043, USA. [2]NASA Ames Research Center, Moffett Field, CA 94035, USA. [3]Bay Area Environmental Research Institute, 596 1st Street, West Sonoma, CA 95476, USA. [4]University of Bordeaux, Laboratoire d'Astrophysique de Bordeaux, UMR 5804, F-33270, Floirac, France. [5]CNRS, Laboratoire d'Astrophysique de Bordeaux, UMR 5804, F-33270, Floirac, France. [6]San Francisco State University, 1600 Holloway Avenue, San Francisco, CA 94132, USA. [7]University of Notre Dame, 225 Nieuwland Science Hall, Notre Dame, IN 46556, USA. [8]Department of Geological and Environmental Sciences, Stanford University, 450 Serra Mall, Building 320, Stanford, CA 94305, USA. [9]NASA Exoplanet Science Institute, California Institute of Technology, 770 South Wilson Avenue, Pasadena, CA 91125, USA. [10]National Optical Astronomy Observatory, 950 North Cherry Avenue, Tucson, AZ 85719, USA. [11]Southern Connecticut State University, New Haven, CT 06515, USA. [12]University of California, Berkeley, CA 94720, USA. [13]Center for Exoplanets and Habitable Worlds, 525 Davey Laboratory, The Pennsylvania State University, University Park, PA 16802, USA. [14]Department of Astronomy and Astrophysics, The Pennsylvania State University, 525 Davey Laboratory, University Park, PA 16802, USA. [15]Michigan Center for Theoretical Physics, Department of Physics, University of Michigan, Ann Arbor, MI 48109, USA. [16]Department of Astronomy, University of Michigan, Ann Arbor, MI 48109, USA.

*Corresponding author. E-mail: elisa.quintana@nasa.gov

orbiting the target. However, this does not account for the possibility that the planets orbit a fainter bound stellar companion to Kepler-186. Although we have no evidence of any binary companion to the target star, faint unresolved stellar companions to planet host stars do occur (*21*). We constrained the density of the host star from the transit model by assuming that all five planets orbit the same star. The 3σ upper bound of the marginalized probability density function of stellar density from our MCMC simulation is 11.2 g cm^{-3}. If Kepler-186 and a hypothetical companion coevolved, the lower limit on the stellar mass and brightness of a companion would be 0.39 $M_\odot$ and Kp = 15.1, respectively.

Given the distance to Kepler-186 of 151 ± 18 pc, a companion would have to be within a projected distance of 4.2 astronomical units (AU) from the target to avoid detection via our follow-up observations. However, a star closer than 1.4 AU from the primary would cause planets around the fainter star to become unstable (*22*). The probability of finding an interloping star with the specific parameters needed to masquerade as a transiting planet is very small relative to the a priori probability that the planets orbit Kepler-186 (<0.02%). Therefore, we are confident that all five planets orbit Kepler-186.

Although photometry alone does not yield planet masses, we used planetary thermal evolution models to constrain the composition of the Kepler-186 planets. These theories predict that the composition of planets with radii less than about 1.5 $R_\oplus$ is unlikely to be dominated by H/He gas envelopes (*23*). Although a thin H/He envelope around Kepler-186f cannot be entirely ruled out, the planet was probably vulnerable to photoevaporation early in the star's life, when extreme ultraviolet flux from the star was significantly higher. Hence, any H/He envelope that was accreted would probably have been stripped by hydrodynamic mass loss (*23*). Although Kepler-186f probably does not have a thick H_2-rich atmosphere, a degeneracy remains between the relative amounts of iron, silicate rock, and water, because the planet could hold on to all of these cosmically abundant constituents. Mass estimates for Kepler-186f can therefore range from 0.32 $M_\oplus$ if composed of pure water/ice to 3.77 $M_\oplus$ if the planet is pure iron, and an Earth-like composition (about 1/3 iron and 2/3 silicate rock) would give an intermediate mass of 1.44 $M_\oplus$ (table S3).

For Kepler-186, the conservative estimate of the HZ (i.e., likely narrower than the actual annulus of habitable distances) extends from 0.22 to 0.40 AU (*4*). The four inner planets are too hot to ever enter the HZ. Kepler-186f receives 32^{+6}_{-4}% of the intensity of stellar radiation (insolation) received by Earth from the Sun. Despite receiving less energy than Earth, Kepler-186f is within the HZ throughout its orbit (Fig. 2). It is difficult for an Earth-sized planet in the habitable zone of an M star to accrete and retain H_2O (*24*, *25*), but being in the outer portion of its star's HZ reduces these difficulties.

The high coplanarity of the planets' orbits (given by the fact that they all transit the star) suggests that they formed from a protoplanetary disk. The leading theories about the growth of planets include in situ accretion of local material in a disk (*26*, *27*), collisional growth of inward-migrating planetary embryos (*28*, *29*), or some combination thereof. We performed a suite of *n*-body simulations of late-stage in situ accretion from a disk of planetary embryos around a star like Kepler-186 (SM section 9). We found that a massive initial disk (>10 $M_\oplus$) of solid material with a very steep surface density profile is needed to form planets similar to those in the Kepler-186 system. Accretion disks with this much mass so close to their star (<0.4 AU) or with such steep surface density profiles, however, are not commonly observed (*30*), suggesting that the Kepler-186 planets either formed from material that underwent an early phase of inward migration while gas was still present in the disk (*31*) or were somehow perturbed inward after they formed. Regardless, all simulations produced at least one stable planet in between the orbits of planets e and f, in the range from 0.15 to 0.35 AU (fig. S5). The presence of a sixth planet orbiting between e and f is not excluded by the observations; if such a planet were to have a modest inclination of a few degrees with respect to the common plane of the other planets, we would not observe a transit.

Planets that orbit close to their star are subjected to tidal interactions that can drive the planets to an equilibrium rotational state, typically either a spin-orbit resonance or a pseudosynchronous-state in which the planet co-rotates with the star at its closest approach (*32*, *33*). The proximity of the inner four planets to Kepler-186 suggests that they are probably tidally locked. Kepler-186f, however, is at a large enough distance from the star that uncertainties in the tidal dissipation function preclude any determination of its rotation rate (*34*). Regardless, tidal locking (or pseudosynchronous rotation) does not preclude a planet from being habitable. The 5.6 $M_\oplus$ planet GJ 581d (*35*) probably rotates pseudosynchronously with its star and in addition receives a similar insolation (27%) as Kepler-186f. Detailed climate models have shown GJ 581d to be capable of having liquid water on its surface (*36*, *37*). Taken together, these considerations suggest that the newly discovered planet Kepler-186f is likely to have the properties required to maintain reservoirs of liquid water.

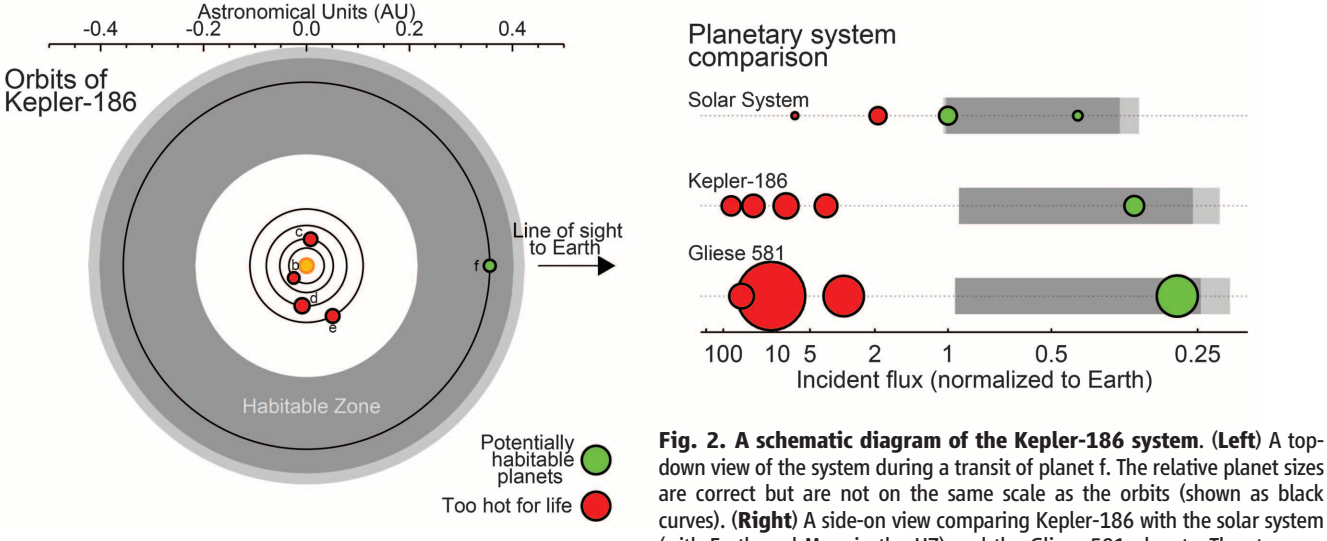

Fig. 2. A schematic diagram of the Kepler-186 system. (**Left**) A top-down view of the system during a transit of planet f. The relative planet sizes are correct but are not on the same scale as the orbits (shown as black curves). (**Right**) A side-on view comparing Kepler-186 with the solar system (with Earth and Mars in the HZ) and the Gliese 581 planets. The stars are located at the left edge of the plots. The dark gray regions represent conservative estimates of the HZ; the light gray regions are more-optimistic extensions of the HZ around each star (*3*, *4*). Kepler186f receives $0.32^{+0.06}_{-0.04}$ of the incident flux that Earth receives from the Sun. This puts Kepler-186f comfortably within the conservative HZ, which ranges from 0.25 to 0.88 of Earth's incident flux for this star. Kepler-186f receives a similar incident flux as Gliese 581d (*35*), which has been shown to be capable of hosting liquid water (*36*, *37*).

References and Notes

1. S. R. Kane, D. M. Gelino, *Publ. Astron. Soc. Pac.* **124**, 323–328 (2012).
2. J. F. Kasting, D. P. Whitmire, R. T. Reynolds, *Icarus* **101**, 108–128 (1993).
3. F. Selsis *et al.*, *Astron. Astrophys.* **476**, 1373–1387 (2007).
4. R. K. Kopparapu *et al.*, *Astrophys. J.* **765**, 131 (2013).
5. W. J. Borucki *et al.*, *Science* **340**, 587–590 (2013).
6. J. C. Tarter *et al.*, *Astrobiology* **7**, 30–65 (2007).
7. P. Kroupa, C. A. Tout, G. Gilmore, *Mon. Not. R. Astron. Soc.* **262**, 545–587 (1993).
8. P. S. Muirhead *et al.*, *Astrophys. J.* **750**, L37 (2012).
9. J. F. Rowe *et al.*, *Astrophys. J.* **784**, 45 (2014).
10. J. J. Lissauer *et al.*, *Astrophys. J.* **784**, 44 (2014).
11. K. Mandel, E. Agol, *Astrophys. J.* **580**, L171–L175 (2002).
12. J. Goodman, J. Weare, *Comm. App. Math. Comp. Sci.* **5**, 65–80 (2010).
13. D. Foreman-Mackey, D. Hogg, D. Lang, J. Goodman, *Publ. Astron. Soc. Pac.* **125**, 306–312 (2013).
14. M. Lopez-Morales, *Astrophys. J.* **660**, 732–739 (2007).
15. A. J. Bayless, J. A. Orosz, *Astrophys. J.* **651**, 1155–1165 (2006).
16. J. Irwin *et al.*, *Astrophys. J.* **701**, 1436–1449 (2009).
17. M. Mayor, D. Queloz, *Nature* **378**, 355–359 (1995).
18. M. J. Holman *et al.*, *Science* **330**, 51–54 (2010).
19. G. Torres, M. Konacki, D. Sasselov, S. Jha, *Astrophys. J.* **614**, 979–989 (2004).
20. T. Barclay *et al.*, *Astrophys. J.* **768**, 101 (2013).
21. J. Wang, J. Xie, T. Barclay, D. Fischer, *Astrophys. J.* **783**, 4 (2014).
22. E.-M. David, E. V. Quintana, M. Fatuzzo, F. C. Adams, *Publ. Astron. Soc. Pac.* **115**, 825–836 (2003).
23. E. D. Lopez, J. J. Fortney, N. Miller, *Astrophys. J.* **761**, 59 (2012).
24. J. J. Lissauer, *Astrophys. J.* **660**, L149–L152 (2007).
25. S. N. Raymond, J. Scalo, V. S. Meadows, *Astrophys. J.* **669**, 606–614 (2007).
26. S. N. Raymond, R. Barnes, A. M. Mandell, *Mon. Not. R. Astron. Soc.* **384**, 663–674 (2008).
27. E. Chiang, G. Laughlin, *Mon. Not. R. Astron. Soc.* **431**, 3444–3455 (2013).
28. C. Terquem, J. C. B. Papaloizou, *Astrophys. J.* **654**, 1110–1120 (2007).
29. C. Cossou, S. N. Raymond, A. Pierens, *IAU Symp.* **299**, 360–364 (2014).
30. S. M. Andrews, J. P. Williams, *Astrophys. J.* **671**, 1800–1812 (2007).
31. S. N. Raymond, C. Cossou, *Mon. Not. R. Astron. Soc.* (2014).
32. P. Hut, *Astron. Astrophys.* **99**, 126–140 (1981).
33. S. Ferraz-Mello, A. Rodriguez, H. Hussmann, *Celestial Mech. Dyn. Astron.* **101**, 171–201 (2008).
34. R. Heller, J. Leconte, R. Barnes, *Astron. Astrophys.* **528**, A27 (2011).
35. S. Udry *et al.*, *Astron. Astrophys.* **469**, L43–L47 (2007).
36. P. von Paris *et al.*, *Astron. Astrophys.* **522**, A23 (2010).
37. R. D. Wordsworth *et al.*, *Astrophys. J.* **733**, L48 (2011).

Acknowledgments: The authors working at NASA Ames thank the SETI Institute for hosting them during the U.S. government shutdown. E.V.Q. and J.F.R. acknowledge support from the Research Opportunities in Space and Earth Sciences Kepler Participating Scientist Program Grant NNX12AD21G. S.N.R.'s contribution was performed as part of the NASA Astrobiology Institute's Virtual Planetary Laboratory Lead Team, supported by NASA under cooperative agreement no. NNA13AA93A. D.H. acknowledges support by an appointment to the NASA Postdoctoral Program at the Ames Research Center, administered by Oak Ridge Associated Universities through a contract with NASA, and the Kepler Participating Scientist Program. The Center for Exoplanets and Habitable Worlds is supported by the Pennsylvania State University, the Eberly College of Science, and the Pennsylvania Space Grant Consortium. F.S. acknowledges support from the European Research Council (Starting Grant 209622: E3ARTHs). This paper includes data collected by the Kepler mission. Funding for the Kepler mission is provided by the NASA Science Mission directorate. This research also made use of NASA's Astrophysics Data System. Some of the data presented in this paper were obtained from the Mikulski Archive for Space Telescopes (MAST). The Space Telescope Science Institute is operated by the Association of Universities for Research in Astronomy, under NASA contract NAS5-26555. Support for MAST for non-Hubble Space Telescope data is provided by the NASA Office of Space Science via grant NNX13AC07G and by other grants and contracts. This research made use of the NASA Exoplanet Archive, which is operated by the California Institute of Technology, under contract with NASA under the Exoplanet Exploration Program. The Gemini Observatory is operated by the Association of Universities for Research in Astronomy, under a cooperative agreement with the National Science Foundation (NSF) on behalf of the Gemini partnership: NSF (United States), the National Research Council (Canada), the Comisión Nacional de Investigación Científica y Tecnológica (Chile), the Australian Research Council (Australia), the Ministério da Ciência, Tecnologia e Inovação (Brazil), and the Ministerio de Ciencia, Tecnología e Innovación Productiva (Argentina).

Supplementary Materials

www.sciencemag.org/content/344/6181/277/suppl/DC1
Materials and Methods
Figs. S1 to S7
Tables S1 and S2
References (*38*–*73*)

6 December 2013; accepted 12 March 2014
10.1126/science.1249403

Emergent Space-Time Supersymmetry at the Boundary of a Topological Phase

Tarun Grover,[1] D. N. Sheng,[2] Ashvin Vishwanath[3,4]*

In contrast to ordinary symmetries, supersymmetry (SUSY) interchanges bosons and fermions. Originally proposed as a symmetry of our universe, it still awaits experimental verification. Here, we theoretically show that SUSY emerges naturally in condensed matter systems known as topological superconductors. We argue that the quantum phase transitions at the boundary of topological superconductors in both two and three dimensions display SUSY when probed at long distances and times. Experimental consequences include exact relations between quantities measured in disparate experiments and, in some cases, exact knowledge of the universal critical exponents. The topological surface states themselves may be interpreted as arising from spontaneously broken SUSY, indicating a deep relation between topological phases and SUSY.

Since the 1970s, space-time "supersymmetry" (SUSY) has been actively pursued by particle physicists to attack the long-standing hierarchy problem of fundamental forces (*1*–*4*). Unlike any other symmetry, SUSY interchanges bosons and fermions and, when applied twice, generates translations of space and time, which ultimately leads to the conservation of momentum and energy (*3*). But despite sustained effort, SUSY has yet to be experimentally established in nature.

Here, we theoretically show that certain condensed matter systems display phenomena of emergent SUSY; that is, space-time SUSY naturally emerges as an accurate description of these systems at low energy and at long distances, although the microscopic ingredients are not supersymmetric. The physical systems we mainly consider are topological superconductors (TSCs) (*5*, *6*), in which pairs of fermions, which may be electrons or fermionic atoms such as helium-3, pair together in a special way. The resulting state has an energy gap to fermions in the bulk but gapless excitations at the surface. We consider the quantum phase transition at which the surface modes acquire a gap and establish emergent supersymmetry D = 1 + 1 and D = 2 + 1 dimensional surfaces (Fig. 1) by using a combination of numerical and analytical techniques (D denotes the space-time dimensionality).

The study of SUSY at a phase transition point was initiated in (*7*), where it was shown that the 1 + 1 dimensional tricritical Ising model, which can be accessed by tuning two parameters, is supersymmetric. A few other proposals that realize SUSY by fine-tuning two or more parameters have been made as well (*8*–*11*). Here, we require that SUSY be achievable by tuning only a single parameter, akin to a conventional quantum critical point (*12*). This is crucial for our results to be experimentally realizable. We also require that our theory has full space-time SUSY rather than only a limited "quantum-mechanical" SUSY (*13*). This automatically ensures translation invariance in space and time and will lead to experimental consequences, as we discuss below. Perhaps most interesting, in contrast to the strategy adopted in (*7*), our approach is not restricted to 1 + 1 dimensional theories.

There has been an explosion of activity in the field of topological phases since the discovery of $\mathbb{Z}_2$ topological insulators (TIs) (*14*–*17*). We will focus on a set of closely related phases, the time-reversal invariant TSCs (*5*, *6*), which include the well-known B-phase of superfluid helium-3 (*18*). These phases exist in both two and three spatial dimensions (*19*, *20*) and support Majorana modes at their boundary; the modes are protected by

[1]Kavli Institute for Theoretical Physics, University of California, Santa Barbara, CA 93106, USA. [2]Department of Physics and Astronomy, California State University, North Ridge, CA 91330, USA. [3]Department of Physics, University of California, Berkeley, CA 94720, USA. [4]Materials Science Division, Lawrence Berkeley National Laboratory, Berkeley, California 94720, USA.

*Corresponding author. E-mail: ashvinv@berkeley.edu

time-reversal symmetry from acquiring an energy gap. Spontaneous breaking of this symmetry provides a natural mechanism to gap them out. For example, electron-electron interactions at the surface could lead to magnetic order, which breaks time reversal symmetry. A natural question is how the surface modes evolve as the magnetic order sets in. We will see that space-time SUSY naturally emerges at the onset of magnetic order.

The D = 2 + 1 dimensional TSC, protected by the time-reversal symmetry, provides the simplest setting to address this question. Whereas the bulk of the superconductor is gapped, the boundary, a $D_{edge} = 1 + 1$ dimensional system, contains a pair of Majorana modes χ_R, χ_L that propagate in opposite directions. The aforementioned instability of the edge may be described by introducing an Ising field ϕ that changes sign under time reversal. The action is given by

$$S^{d+1} = \int d\tau\, d^d x \left[\frac{1}{2}\bar{\chi}\partial\!\!\!/\chi + \frac{1}{2}(\partial_\tau \phi)^2 + \frac{v_\phi^2}{2}(\nabla\phi)^2 + \frac{r}{2}\phi^2 + g\phi\bar{\chi}\chi + u\phi^4 \right] \quad (1)$$

with $d = 1$, $\chi = [\chi_R \chi_L]^T$, and we have used the conventional Dirac gamma matrices for the relativistic fermion $\chi \cdot v_\phi$ and u are, respectively, the velocity and self-interaction of ϕ; g is the coupling between the fermions and ϕ, whereas r is the tuning parameter for the transition. The symmetry-broken phase is characterized by $\phi \neq 0$, which leads to a mass gap $g\phi$ for the fermions.

The mode count in the action S is favorable for $\mathcal{N} = 1$ SUSY in D = 1 + 1 (*21*), with the bosons ϕ and Majorana fermions χ as superpartners. We now show that this is indeed the case by using a numerical simulation of a D = 1 + 1 lattice model that reproduces the action in Eq. 1 at low energies. The model is given by

$$H = -i\sum_j \left[1 - g\mu^z_{j+\frac{1}{2}}\right]\chi_j\,\chi_{j+1} + H_b$$

where

$$H_b = \sum_j [\mathcal{J}\mu^z_{j-1/2}\mu^z_{j+1/2} - h\mu^x_{j+1/2}] \quad (2)$$

Here, χ_j is a single Majorana fermion at site j, whereas the Ising spins $\mu^z_{j+1/2}$ sit on bond centers. When the transverse magnetic field $h \gg 1$, $\langle\mu^z\rangle = 0$ and lattice translation symmetry ensures that the Majorana fermions are gapless. As h decreases, at some point μ^z orders antiferromagnetically, leading to a mass gap for the fermions through the coupling g, reproducing the field theory in Eq. 1 at and near the critical point. $\mathcal{J}$ tunes the relative bare velocities between the boson and the fermion modes, similar to v_ϕ in Eq. 1.

We numerically simulate a spin version of Eq. 2 by using the density matrix renormalization group (DMRG) method (*22*).(Fig. 2). At larger h, a gapless phase is obtained that is separated by a critical line from a gapped ordered phase at small h. To characterize the critical theory, consider crossing the phase boundary along fixed g, say, $g = 0.5$, while monitoring the central charge c, which quantifies the amount of entanglement of a 1 + 1 – D critical system (Fig. 2B). At small h, c is almost equal to zero, which indicates a gapped phase. At $h > h_c \approx 1.62$, the central charge saturates at $c \approx 0.5$, indicating that the symmetry is restored and a gapless Majorana mode is present. At the transition, $h = h_c$, we find $c \approx 0.7$, which precisely corresponds to the SUSY tricritical Ising

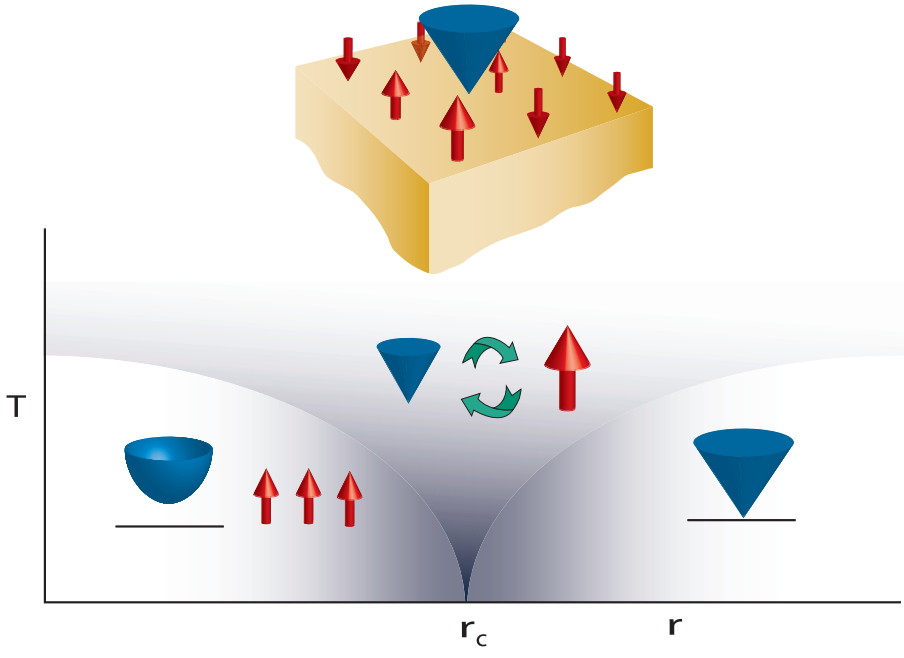

Fig. 1. Supersymmetry in a 3D TSC. Ising magnetic fluctuations (denoted by red arrows) at the boundary couple to the Majorana fermions (blue cone). When the tuning parameter $r < r_c$, the Ising spins are ordered, leading to a gap for the Majorana fermions. The critical point that separates the two sides is supersymmetric, where bosons (Ising order parameter) and Majorana fermions transform into each other.

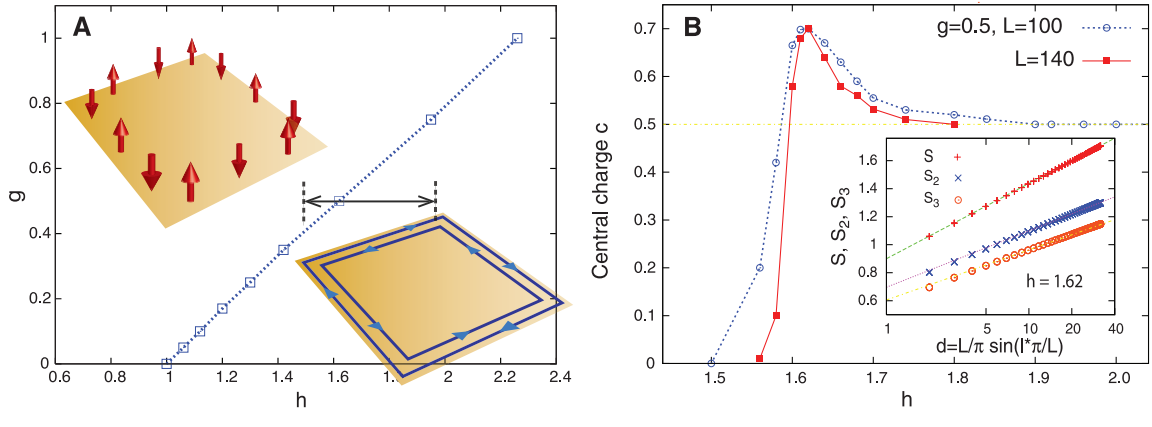

Fig. 2. Supersymmetry in a 2D TSC. (A) The phase diagram of the Hamiltonian H in Eq. 2, which realizes the Majorana edge coupled to Ising magnetic fluctuations in this system. At large h, the Ising spins disorder, and the counterpropagating Majorana modes (blue arrows) remain gapless. As h decreases, the ordering of Ising spins (red arrows) leads to a gap for the Majorana modes. **(B)** The region of the phase diagram indicated by the black arrows in (A). Plotted is the central charge c as a function of h for fixed $g = 0.5$, $\mathcal{J} = 1$. For $h > h_c$ (= 1.62), c equals 1/2, consistent with gapless Majorana modes; for $h < h_c$, c is 0, which indicates the gapped phase. At the critical point, c is 7/10, which corresponds to supersymmetric tricritical Ising point. (Inset) von Neumann entropy S and the Renyi entropies S_2,S_3 at the critical point, which were used to deduce the central charge. L is the system size, and **l** is the size of the entanglement subsystem.

theory (*7*). Note that we access this transition by tuning a single variable. Even when the parameter $\mathcal{J}$, which controls relative bare velocities of boson and fermion, is varied between $\mathcal{J} = 1$, and $\mathcal{J} = 4$, we obtain a second-order transition in the same universality class (*23*). We now turn to 3 + 1 dimensional TSCs, whose two-dimensional (2D) surface supports gapless Majorana fermions, protected by time-reversal symmetry. As advertised earlier, we study spontaneous breaking of time-reversal symmetry that gaps out the surface states. In the absence of numerics, we resort to an analytical calculation within a $D = 4 - \varepsilon$ expansion to unravel the nature of quantum criticality and argue that 2 + 1 dimensional SUSY arises here. The relevant action is again given by Eq. 1 with $d = 2$. At $r = 0$, this action has $\mathcal{N} = 1$ SUSY (*21*) in 2 + 1D only if one sets $u = g^2/2$ and $v_\phi = 1$. We ask whether SUSY emerges in the low energy limit as we tune to the quantum critical point, without enforcing these conditions microscopically. We find (*23*) that this is indeed the case: The terms that break SUSY are irrelevant at the critical point leading to a stable superconformal fixed point in the infrared. Additional support has recently emerged from a rather different, conformal bootstrap approach (*24*) that obtains the scaling dimension $\Delta\phi = 0.565$, which matches well with our ε expansion result, $\Delta\phi \approx \frac{1}{2} + \frac{\varepsilon}{14} = 0.571$.

To explore an experimental realization, consider a film of superfluid He_3-B, with surface perpendicular to the z direction and a magnetic field parallel to the surface. Despite breaking time-reversal symmetry, this does not introduce an energy gap (*24*, *25*) because of a symmetry $\mathcal{T}'$, that combines time reversal with 180° rotation about the z axis. However, the system can lower its energy by spontaneously breaking rotation symmetry and gapping the surface modes. Indeed, the order parameter of He_3-B includes a rotation matrix $\mathcal{R}(n, \varphi)$ that depends on an angle φ and a direction n. In the absence of a magnetic field, microscopic dipolar interactions pin the vector $n = \hat{z}$. However, if the n vector develops an in-plane component $n_\parallel$, it can break the protecting symmetry $\mathcal{T}'$. The energetic incentive for an in-plane component increases with the applied magnetic field, because the surface gap m is proportional to the field: $m \approx 2Hn_\parallel \sin\varphi/2$. Thus, for fields $0 \leq |H| < H_c$ we have a gapless symmetric state, whereas for $H_c < |H|$ spontaneous symmetry breaking occurs, leading to a gap for surface Majorana modes. In (*24*), the critical field was predicted to be $H_c = 30$ G, which is readily accessible. However, we note the challenges to realizing SUSY in this physical system (*23*). The low temperatures of the superfluid transition restricts the temperature window for experiments, and the bare boson and fermion velocities are expected to be rather different, with a ratio controlled by E_F/Δ.

We now discuss the possibility of emergent SUSY in 3D TIs. The surface states of these materials (*14*–*17*) consist of Dirac fermions at a chemical potential $\mu : H = \sum_{k_x, k_y} c^\dagger(k_x\sigma_y - k_y\sigma_x - \mu)c$.

Let us fine-tune μ to zero and consider the instability of these surface modes to an s-wave superconductor. This multicritical point can potentially be driven by intrinsic interactions and may also be realized by patterning the surface with a Josephson junction array. We restrict ourselves to particle-hole symmetric superconducting fluctuations. The effective near the transition is given by

$$S = \int d\tau\, d^2x \left[\overline{\psi}\partial\!\!\!/\psi + g(\phi\psi^T\varepsilon\psi + c.c.) + |\partial_\tau\phi|^2 + c^2|\vec{\nabla}\phi|^2 + r|\phi|^2 + u|\phi|^4\right] \quad (3)$$

where ϕ is the superconducting order parameter, the fermion field $\psi^T = [c_\uparrow\ c_\downarrow]$, and ε is the 2D antisymmetric tensor. g, r, and u have meaning analogous to Eq. 1, whereas c is the velocity of ϕ. The above action is known to flow to a $\mathcal{N} = 2$ superconformal fixed point (*26*, *27*).

Because SUSY rotates fermions into bosons, the universal critical exponents satisfy nontrivial relations between them, thus relating results from disparate experiments. In particular, the scaling dimensions Δ_χ,Δ_ϕ of χ,ϕ satisfy $\Delta_\chi = \Delta_\phi + 1/2$. In an electronic system, Δ_χ may be determined via tunneling experiments, whereas Δ_ϕ may be obtained from neutron scattering. As an example, consider the boundary of a 2D TSC, for which we showed that the transition lies in the tricritical Ising universality class. The exact critical exponents in this case are $\Delta_\chi = 0.70 = \Delta_\phi + \frac{1}{2}$. Similarly, at the boundary of 3D TSC, we find $\Delta_\chi = 1 + \frac{1}{14} = \Delta_\phi + \frac{1}{2}$ at order ε in the renormalization group. Lastly, in the case of 3D TI, because of the larger ($\mathcal{N} = 2$) SUSY, one can determine the scaling dimensions of the boson and Fermi fields exactly, with (*28*) $\Delta_\chi = 7/6 = \Delta_\phi + 1/2$. Another consequence of SUSY is that the velocity for the fermion and the boson at low energies become equal, despite the fact that their bare velocities will be generically different.

SUSY has nontrivial consequences for the proximate phases as well. At the TSC boundary in the time-reversal broken phase, SUSY implies that the masses of the fermion and the boson are equal to each other as one moves away from the critical point. Mathematically, m_ϕ and m_χ are equal to $\alpha(r - r_c)^\nu$, where r_c is the critical value of the tuning parameter, α is a constant, and, owing to SUSY, $\nu^{-1} = 2 - \Delta_\phi$.

Emergent SUSY also provides insight into the topological excitations on either side of the transition. First, consider the time-reversal invariant boundary of a TSC in either two or three spatial dimensions, which supports a gapless Majorana fermion. This is conventionally viewed as resulting from the topological band structure. However, a completely different viewpoint is obtained by realizing that the flow from SUSY critical point ($r = 0$) to a phase where ϕ is gapped ($r > 0$) corresponds to spontaneous breaking of SUSY. Because SUSY is a fermionic symmetry, this leads to the generation of a massless Majorana fermion, the "goldstino" mode (*23*, *29*, *30*), which precisely corresponds to the topologically protected Majorana fermion. Thus, one can model the boundary modes with a continuum model in the same dimension if SUSY is assumed, which serves to protect their gaplessness. We provide details of this phenomenon in (*23*).

The dichotomy between SUSY and topology runs deeper: It has robust, physical manifestation in the time-reversal broken phase as well. As discussed in (*23*) and hinted above, the SUSY is unbroken as the boson ϕ condenses, resulting in equal mass for ϕ and χ. It is well known that, in the symmetry broken boundary phase, topological defects—kinks in 1D and line domain walls in 2D—carry fermion modes on them (*31*). We interpret these also as Goldstino modes of a type of SUSY breaking. First consider kinks, which spontaneously break translational symmetry in 1D. Because of the deep connection between translation symmetry and SUSY, this ultimately leads to a spontaneous breaking of half of the SUSY (*23*, *32*, *33*). Thus, in addition to the coordinate of the domain wall, $\tilde{\phi}$, which can be viewed as a gapless 0 + 1 – D Goldstone boson of translation breaking, there is also a single Majorana Goldstino mode $\tilde{\chi}$ localized on the kink, which is the superpartner of $\tilde{\phi}$. The low-energy theory of the kink is $S_{\text{kink}} = \frac{1}{2}\int d\tau[(\partial_\tau\tilde{\phi})^2 + i\tilde{\chi}\partial_\tau\tilde{\chi}]$, which one might have anticipated independently on topological grounds (*31*). This argument also applies to TSCs coupled via Josephson junction discussed in (*34*).

The generalization to line domain walls at the time-reversal breaking boundary of 3D TSC is straightforward. The partial SUSY breaking leads to 1 + 1 – D chiral Majorana fermion $\tilde{\chi}$ propagating along the domain line; $\tilde{\chi}$ is a superpartner of the Goldstone mode $\tilde{\phi}$ associated with the translational symmetry breaking, $S_{\text{DW}} = \frac{1}{2}\int d\tau\, dx[(\partial_\tau\tilde{\phi})^2 + (\partial_x\tilde{\phi})^2 + i\tilde{\chi}(\partial_\tau + \partial_x)\tilde{\chi}]$. SUSY not only predicts the anticipated chiral Majorana fermions on the domain walls, it also predicts equal velocity for the superpartners $\tilde{\phi}$,$\tilde{\chi}$ and an exact "Fermi-Bose" degeneracy associated with the whole excitation spectra of the domain wall or kink. These predictions hold in the ordered phase close to the criticality. In general, we expect that the boundary modes in a topological phase can be thought of as Goldstinos unless the tuning parameter breaks SUSY explicitly; an example of the latter possibility is provided by the SUSY critical point in 3D TIs mentioned above.

References and Notes

1. J. L. Gervais, B. Sakita, *Nucl. Phys. B* **34**, 632–639 (1971).
2. J. Wess, B. Zumino, *Nucl. Phys. B* **70**, 39–50 (1974).
3. E. Noether, *Nachr. Konig. Gesellsch. Wiss Gottingen Math.-Phys. Kl.* **235** (1918).
4. S. Dimopoulos, H. Georgi, *Nucl. Phys. B* **193**, 150–162 (1981).
5. R. Roy, Topological superfluids with time reversal symmetry, http://arxiv.org/abs/0803.2868 (2008).
6. X.-L. Qi, T. L. Hughes, S. Raghu, S.-C. Zhang, *Phys. Rev. Lett.* **102**, 187001 (2009).
7. D. Friedan, Z. Qiu, S. Shenker, *Phys. Rev. Lett.* **52**, 1575–1578 (1984).

8. P. Fendley, K. Schoutens, J. de Boer, *Phys. Rev. Lett.* **90**, 120402 (2003).
9. Y. Yu, K. Yang, *Phys. Rev. Lett.* **105**, 150605 (2010).
10. L. Huijse, J. Halverson, P. Fendley, K. Schoutens, *Phys. Rev. Lett.* **101**, 146406 (2008).
11. B. Bauer, L. Huijse, E. Berg, M. Troyer, K. Schoutens, *Phys. Rev. B* **87**, 165145 (2013).
12. S. Sachdev, *Quantum Phase Transitions* (Cambridge Univ. Press, Cambridge, ed. 2, 2011).
13. Quantum mechanical SUSY corresponds to SUSY only in the time-direction; see, e.g., (*35*) and (*10*).
14. M. Z. Hasan, C. L. Kane, *Rev. Mod. Phys.* **82**, 3045–3067 (2010).
15. X. L. Qi, S. C. Zhang, *Rev. Mod. Phys.* **83**, 1057–1110 (2011).
16. M. König *et al*., *Science* **318**, 766–770 (2007).
17. D. Hsieh *et al*., *Nature* **452**, 970–974 (2008).
18. A. Leggett, *Rev. Mod. Phys.* **47**, 331–414 (1975).
19. A. P. Schnyder, S. Ryu, A. Furusaki, A. W. W. Ludwig, *Phys. Rev. B* **78**, 195125 (2008).
20. A. Kitaev, presentation to the L. D. Landau Memorial Conference "Advances in Theoretical Physics," Chernogolovka, Russia, 22 to 26 June 2008; http://landau100.itp.ac.ru/Talks/kitaev.pdf.
21. J. Wess, J. Bagger, *Supersymmetry and Supergravity* (Princeton Univ. Press, Princeton, NJ, 1992).
22. S. R. White, *Phys. Rev. Lett.* **69**, 2863–2866 (1992).
23. Supplementary materials are available on *Science* Online.
24. D. Bashkirov, Bootstrapping the $N = 1$ SCFT in three dimensions, http://arxiv.org/abs/1310.8255 (2013).
25. T. Mizushima, M. Sato, K. Machida, *Phys. Rev. Lett.* **109**, 165301 (2012).
26. L. Balents, M. P. A. Fisher, C. Nayak, *Int. J. Mod. Phys. B* **12**, 1033–1068 (1998).
27. S.-S. Lee, *Phys. Rev. B* **76**, 075103 (2007).
28. O. Aharony, A. Hanany, K. Intriligator, N. Seiberg, M. J. Strassler, *Nucl. Phys. B* **499**, 67–99 (1997).
29. A. Das, M. Kaku, *Phys. Rev. D Part. Fields* **18**, 4540–4544 (1978).
30. D. A. Kastor, E. J. Martinec, S. H. Shenker, *Nucl. Phys. B* **316**, 590–608 (1989).
31. J. C. Y. Teo, C. L. Kane, *Phys. Rev. B* **82**, 115120 (2010).
32. E. Witten, D. I. Olive, *Phys. Lett. B* **78**, 97–101 (1978).
33. M. Shifman, A. Vainshtein, M. Voloshin, *Phys. Rev. D Part. Fields* **59**, 045016 (1999).
34. A slightly different theory, which might also exhibit emergent SUSY, arises in the context of time-reversal breaking 1 + 1 – D topological superconductors coupled via a Josephson junction (*36*).
35. A. Lahiri, P. K. Roy, B. Baghi, *Int. J. Mod. Phys. A* **05**, 1383–1456 (1990).
36. E. Grosfeld, A. Stern, *Proc. Natl. Acad. Sci. U.S.A.* **108**, 11810–11814 (2011).

Acknowledgments: We thank M. Fisher, T. Mizushima, D. Huse, R. Mong, and S. Trivedi for discussions. This work is supported by Army Research Office Multidisciplinary University Research Initiative grant W911-NF-12-0461 and NSF Division of Materials Research grant 0645691 (A.V.) and by U.S. Department of Energy Office of Basic Energy Sciences under grant DE-FG02-06ER46305 (D.N.S.).

Supplementary Materials

www.sciencemag.org/content/344/6181/280/suppl/DC1
Supplementary Text
References (*37*–*39*)

8 November 2013; accepted 11 March 2014
Published online 3 April 2014;
10.1126/science.1248253

Strong Increase of T_c of Sr_2RuO_4 Under Both Tensile and Compressive Strain

Clifford W. Hicks,[1,2]* Daniel O. Brodsky,[1,2] Edward A. Yelland,[2,3] Alexandra S. Gibbs,[2,4] Jan A. N. Bruin,[2,5] Mark E. Barber,[1,2] Stephen D. Edkins,[2,6] Keigo Nishimura,[7] Shingo Yonezawa,[7] Yoshiteru Maeno,[7] Andrew P. Mackenzie[1,2]*

A sensitive probe of unconventional order is its response to a symmetry-breaking field. To probe the proposed $p_x \pm ip_y$ topological superconducting state of Sr_2RuO_4, we have constructed an apparatus capable of applying both compressive and tensile strains of up to 0.23%. Strains applied along ⟨100⟩ crystallographic directions yield a strong, strain-symmetric increase in the superconducting transition temperature T_c. ⟨110⟩ strains give a much weaker, mostly antisymmetric response. As well as advancing the understanding of the superconductivity of Sr_2RuO_4, our technique has potential applicability to a wide range of problems in solid-state physics.

The layered perovskite Sr_2RuO_4 is one of the most extensively studied unconventional superconductors (*1*–*4*). It has attracted particular attention because of the strong possibility that the pairing is spin-triplet, with an odd-parity, chiral orbital order parameter, $p_x \pm ip_y$. This would be a superconducting analog of superfluid ^{3}He, but with the key additional feature of being quasi–two-dimensional. This combination of properties, distinct among known superconductors, would, in principle, support topologically protected edge states and half-flux quantum vortices with Majorana zero modes (*5*, *6*). Thus, the study of the superconducting state of Sr_2RuO_4 is of fundamental interest.

The evidence for triplet pairing is strong (*7*, *8*), but definitive demonstration of the orbital order has proved more difficult (*9*). Some predictions of two-component chiral order have been observed in experiments, including time-reversal symmetry-breaking (*10*, *11*) and complex Josephson interferometry (*12*). However, chiral order is also expected to result in substantial edge currents (*13*), splitting of the transition in an in-plane magnetic field, and anisotropy in the upper critical field H_{c2} at temperatures near the transition temperature T_c (*14*). Despite experimental effort, none of these properties have been observed (*15*–*18*).

Because the existence of $p_x \pm ip_y$ order in Sr_2RuO_4 would have broad importance, further evaluation is necessary. Under the tetragonal symmetry of the Sr_2RuO_4 lattice, the two components p_x and p_y have the same transition temperatures. This degeneracy can be lifted by applying a symmetry-breaking field, with in-plane uniaxial strain an ideal choice: Based purely on symmetry considerations, a phase diagram of the form shown in Fig. 1A is expected for a strained $p_x \pm ip_y$ superconductor (*19*, *20*). If the transition temperature T_c is measured with a probe sensitive mainly to the upper transition, such as resistivity or susceptibility, then the observed T_c versus strain ε is expected to follow the solid line, showing a cusp at $\varepsilon = 0$, and a substantial symmetric response about zero (*21*, *22*).

Sr_2RuO_4 has consistently been found to be sensitive to uniaxial pressure: The 3-K phase, locally higher-T_c superconductivity that appears in Sr_2RuO_4-Ru eutectic samples (*23*), can be induced in pure Sr_2RuO_4 by uniaxial pressures (*24*, *25*). But the direction dependence of the uniaxial strain effect has not been resolved, and the higher-T_c superconductivity has not been induced homogeneously. Furthermore, the expected

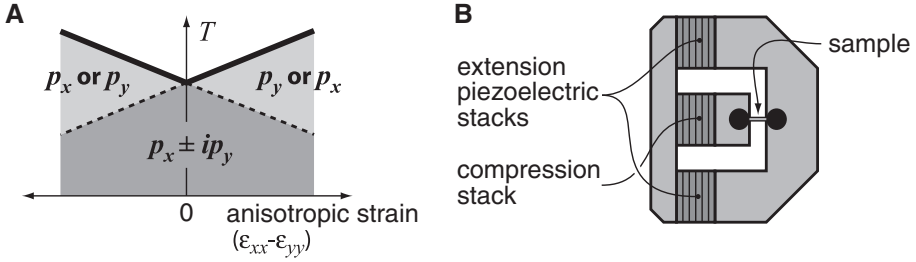

Fig. 1. Hypothesis and apparatus. (A) General phase diagram expected for $p_x \pm ip_y$ superconductivity in a tetragonal crystal subject to a small, volume-preserving, symmetry-breaking strain $\varepsilon_{xx} - \varepsilon_{yy}$. *T*, temperature. **(B)** Sketch of the uniaxial strain apparatus constructed to test this hypothesis.

[1]Max Planck Institute for Chemical Physics of Solids, Nöthnitzer Straße 40, 01187 Dresden, Germany. [2]Scottish Universities Physics Alliance (SUPA), School of Physics and Astronomy, North Haugh, University of St. Andrews, St. Andrews KY16 9SS, UK. [3]SUPA, School of Physics and Astronomy and Centre for Science at Extreme Conditions, University of Edinburgh, Mayfield Road, Edinburgh EH9 3JZ, UK. [4]Department of Physics, The University of Tokyo, 7-3-1 Hongo, Bunkyo-ku, Tokyo 113-0033, Japan. [5]High Field Magnet Laboratory, Radboud University Nijmegen, Toernooiveld 7, 6525 ED Nijmegen, Netherlands. [6]Laboratory of Solid State Physics, Department of Physics, Cornell University, Ithaca, NY 14853, USA. [7]Department of Physics, Graduate School of Science, Kyoto University, Kyoto 606-8502, Japan.

*Corresponding author. E-mail: hicks@cpfs.mpg.de (C.W.H.); mackenzie@cpfs.mpg.de (A.P.M.)

strain-symmetric response has not been probed because it requires applying both tensile and compressive stresses, a capability that has been lacking.

To address these issues, we constructed the apparatus sketched in Fig. 1B. More details can be found in (*26*), but the main features are as follows: (i) The sample is epoxied into place, and piezoelectric stacks are used to apply compression and extension; (ii) the stacks are arranged so that their thermal contraction does not, in principle, strain the sample; and (iii) "strain amplification," meaning that the stacks are longer than the sample, allowing larger strains to be applied to the sample than are achievable on the stacks. In addition, the sample is cut into a long, thin bar to obtain good strain homogeneity toward its center. The apparatus is compact and would be compatible with many cryogenic platforms; for our experiments, it was mounted in an adiabatic demagnetization refrigerator.

As with the piezoelectric-based technique of (*27*), it is mainly the sample strain, rather than stress, that is the controlled parameter. The pressure on the sample is the strain times the relevant elastic constant. The strain is monitored with a strain gauge mounted beneath the sample but not attached to it. A portion of the applied displacement (27%, on average, for the samples studied here) is taken up by deformation of the sample-mounting epoxy, so for each sample the actual sample strain was estimated by finite element analysis (*26*, *28*, *29*).

We measured T_c through ac magnetic susceptibility χ, using two concentric coils mounted on top of the sample. Measurement frequencies ranged from 59 to 369 Hz, and the excitation field from ~0.05 to ~0.5 G.

We used single-crystal samples grown by a floating-zone method (*1*). In Fig. 2, A and B, we show $\chi(T)$ for a sample with $T_c = 1.35$ K at zero strain, under compression (A) and tension (B) along a ⟨100⟩ crystal direction. Full superconducting transitions are seen at all strains, with minimal broadening. The extra structure observed at high strains is most likely an effect of strain inhomogeneity.

We measured four samples cut in a ⟨100⟩ direction and three in a ⟨110⟩ direction. The main features we report were reproduced across the entire sample set. The dependence of T_c on strains applied along ⟨100⟩ and ⟨110⟩ directions is shown in Fig. 2, C and D. There is some uncertainty in locating zero strain, but the data can be summarized thus: For ⟨100⟩ strain (ε_{100}), there is a large symmetric response about $\varepsilon_{100} = 0$, whereas the response to ⟨110⟩ strain (ε_{110}) is far weaker and mainly linear in ε. The proposed $p_x \pm ip_y$ superconductivity of Sr_2RuO_4 has often been modeled supposing an isotropic, cylindrical Fermi surface, but these data show that the tetragonal symmetry is hugely influential.

Neglecting *c*-axis strain, the applied strains can be resolved into isotropic dilatation ($\varepsilon_{xx} = \varepsilon_{yy}$) and volume-preserving anisotropic distortion ($\varepsilon_{xx} = -\varepsilon_{yy}$ for ε_{100}, and $\varepsilon_{xx} = \varepsilon_{yy} = 0$, $\varepsilon_{xy} \neq 0$ for ε_{110}) (*30*). The in-plane Poisson's ratio for Sr_2RuO_4 is ≈0.40 (*29*, *31*), so for both ε_{100} and ε_{110}, ~30% of the longitudinal strain is dilatation, and ~70% is volume-preserving distortion. Dilatation will, in general, give a ε-linear response for small strains about zero, but under tetragonal crystal symmetry the volume-preserving distortion must give a symmetric response. It seems clear that the dominant effect of ⟨110⟩ strains is through dilatation and of ⟨100⟩ strains through the volume-preserving distortion. Small variations about ⟨110⟩ have a large effect: A 2.5° change in the angle of cut increased the symmetric component of the response considerably, probably by mixing in a small ε_{100} component to the strain (fig. S3).

A key question is the lack of the expected cusp near zero strain. At $|\varepsilon_{100}| < 0.03\%$, $T_c(\varepsilon)$ and $dT_c/d\varepsilon$ are essentially flat, then T_c rises strongly at larger strains. Both of these features remain essentially unchanged when the excitation field is varied (fig. S4). As emphasized by the $dT_c/d\varepsilon$ data in Fig. 2E, the increase of T_c beyond 0.03% strain is quadratic in strain, not linear. The precise low-strain form of $T_c(\varepsilon_{100})$ may be affected by inhomogeneity and requires further investigation, but the strong increase in T_c at larger strains is unambiguous, and this is where we wish to focus our attention.

A quadratic form can result from strain-induced mixture of near-degenerate order parameters. The tetragonal crystal symmetry and strong response to ⟨100⟩ strain suggest s- and $d_{x^2-y^2}$-wave orders, but these would be in conflict with both triplet pairing and time-reversal symmetry breaking at T_c and, thus, are unlikely. Another possibility is that sketched in Fig. 3A: that Sr_2RuO_4 at $\varepsilon = 0$ does, in fact, have degenerate order parameters, but the cusp appears on top of a strong underlying strain response and is too small to be resolved in the present data.

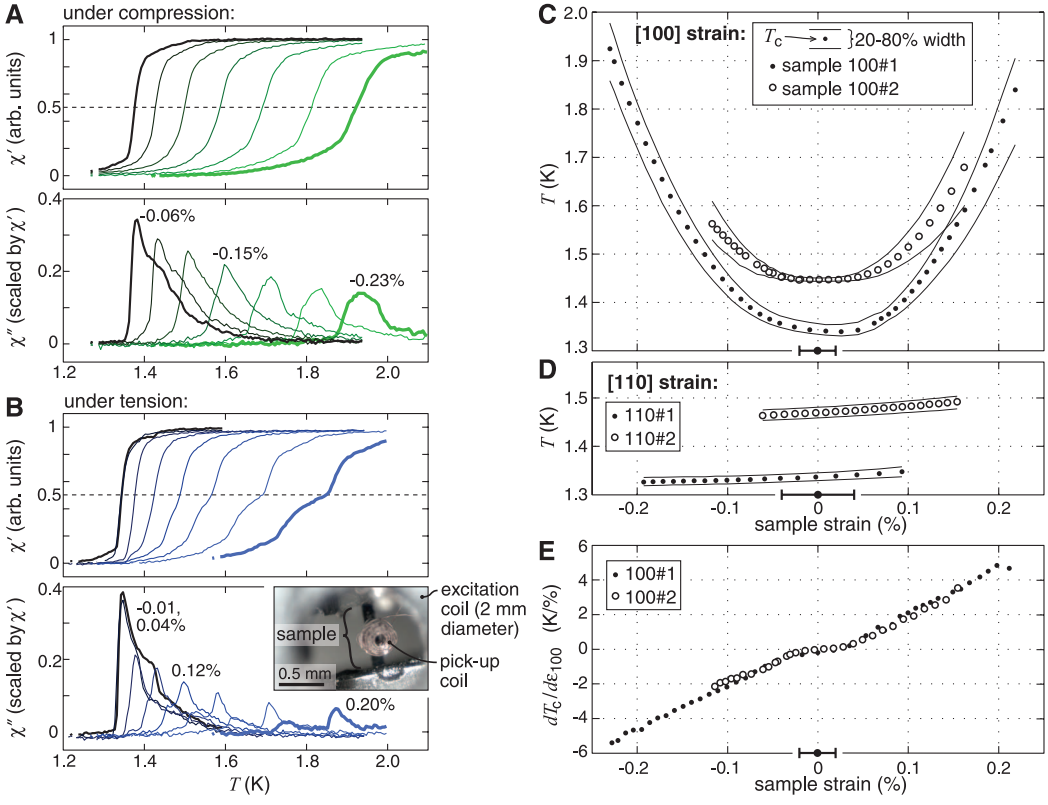

Fig. 2. Superconductivity of Sr_2RuO_4 under strain. (**A** and **B**) In-phase (χ') and out-of-phase (χ'') parts of the ac susceptibility, measured at 369 Hz on the ⟨100⟩-oriented sample shown in the inset of (B). Approximate strains for some curves are indicated. arb. units, arbitrary units. (**C**) T_c versus ⟨100⟩-oriented strain ε_{100} of two samples of Sr_2RuO_4, one with a zero-strain T_c of 1.35 K [for which the raw data are shown in (A) and (B)] and the other with 1.45 K. $\varepsilon > 0$ indicates tension. T_c is taken as the 50% point of χ', and the black lines are the 20 and 80% points, giving a measure of the transition width. The error bar on the horizontal axis indicates the error in locating $\varepsilon = 0$ (*29*). (**D**) T_c versus ⟨110⟩ strain ε_{110} for two further samples cut from the same crystals as in (C). The temperature scale is the same as in (C), highlighting the large difference in response between the two directions. (**E**) $dT_c/d\varepsilon$ for the data in (C).

To gain further insight, we used the Wien2k package (*32*) to calculate the electronic structure in the presence of strain; the Fermi surfaces for ε_{100} and $\varepsilon_{110} = \pm 0.5\%$ are shown in Fig. 3, B and C. For each strain, the lattice parameters were set according to the applied strain and the in- and out-of-plane Poisson's ratios. The Fermi surfaces are altered more dramatically by ⟨100⟩ than ⟨110⟩ strains, a result supported by ultrasound data: Above T_c, sound waves that generate *xx* and *yy* strains are damped much more than waves generating *xy* strains (*33*).

The shifting Fermi surfaces will alter T_c. With $p_x \pm ip_y$ order, a strong cusp is expected when the longitudinal and transverse responses to strain are very different. In Sr_2RuO_4, this occurs most clearly on the {100} sections of the γ sheet, near the van Hove points: Under ⟨100⟩ strains, the Fermi surface and, correspondingly, the density of states change rapidly and oppositely on the (100) and (010) sections. If the superconducting gap were dominated by these sections of Fermi surface, a large cusp would be expected. Based on our structure calculations, we estimate that $dT_c/d\varepsilon_{100}$ would jump by several kelvin per percent across the cusp (*29*), which would have been easily observable.

However, a large gap is not expected near the van Hove points: By symmetry, with p-wave order the gap must vanish at the van Hove points themselves. Some authors have proposed that the α and β sheets might have the largest gaps (*34*–*36*), in which case a weaker cusp is expected, which could have been obscured by a strong underlying response. Finally, $p_x \pm ip_y$ superconductivity may live dominantly on the {110} sections of the γ sheet (*37*, *38*), as indicated by field-angle–dependent specific heat data (*39*). In this case, a stronger cusp would be expected for ⟨110⟩ than ⟨100⟩ strains. But [110] strain changes the dispersions on the (110) and $(1\bar{1}0)$ sections of the γ sheet almost identically, so the cusp might be tiny. We estimate that $dT_c/d\varepsilon_{110}$ would change at the cusp by well under 0.1 K per percent (*29*), below the resolution of the present experiment.

Therefore, by our estimates our data still permit certain models of $p_x \pm ip_y$ order. The challenge for degenerate p-wave models is to explain simultaneously the apparent weakness of the cusp and the large nonlinear response to ⟨100⟩ strains. A natural hypothesis is that the superconductivity is strongly intertwined with the van Hove points (*40*), even if this is not where the gap is largest. This is a qualitative observation, however, and further theoretical effort would be very interesting.

Figure 3, B and C, illustrate a final point with implications far beyond the superconductivity of Sr_2RuO_4: The characteristic energy scale of a 0.5% change in strain is large—roughly that percentage of the bandwidth. For Sr_2RuO_4, a Zeeman splitting with an equivalent energy scale would require a magnetic field of hundreds of teslas. This method can produce these large changes with directional resolution and precise tunability, without introducing disorder and while leaving the upper surface of the sample open for spectroscopic probes such as angle-resolved photoemission (*41*, *42*), electron energy-loss spectroscopy, and scanning probe microscopy. We therefore believe that the technique we have developed opens the way to a host of new experiments across a wide range of materials.

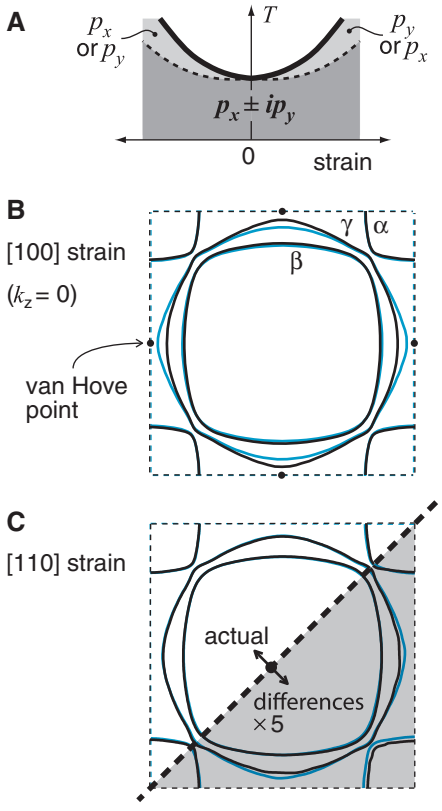

Fig. 3. Electronic structure under strain. (**A**) A possible phase diagram with a weak cusp and strong underlying response to strain. (**B** and **C**) Calculated Fermi surfaces (labeled α, β, and γ) at zero *z*-axis momentum under 0.5% compression (black) and tension (blue). The dashed lines are, for reference, the two-dimensional zone boundaries of the RuO_2 sheets. (B) [100] strain (along $\hat{\mathbf{x}}$); (C) [110] strain (along $\hat{\mathbf{x}} + \hat{\mathbf{y}}$). In the lower right (shaded) portion of (C) only, the surfaces have been distorted slightly to make the zone boundaries match, and differences between the surfaces have been exaggerated by a factor of 5.

References and Notes

1. Y. Maeno *et al.*, *Nature* **372**, 532–534 (1994).
2. A. P. Mackenzie, Y. Maeno, *Rev. Mod. Phys.* **75**, 657–712 (2003).
3. Y. Maeno, S. Kittaka, T. Nomura, S. Yonezawa, K. Ishida, *J. Phys. Soc. Jpn.* **81**, 011009 (2012).
4. C. Kallin, *Rep. Prog. Phys.* **75**, 042501 (2012).
5. D. A. Ivanov, *Phys. Rev. Lett.* **86**, 268–271 (2001).
6. J. Jang *et al.*, *Science* **331**, 186–188 (2011).
7. H. Murakawa *et al.*, *J. Phys. Soc. Jpn.* **76**, 024716 (2007) and references therein.
8. J. A. Duffy *et al.*, *Phys. Rev. Lett.* **85**, 5412–5415 (2000).
9. R. Jin *et al.*, *Phys. Rev. B* **59**, 4433–4438 (1999).
10. G. M. Luke *et al.*, *Nature* **394**, 558–561 (1998).
11. J. Xia, Y. Maeno, P. T. Beyersdorf, M. M. Fejer, A. Kapitulnik, *Phys. Rev. Lett.* **97**, 167002 (2006).
12. F. Kidwingira, J. D. Strand, D. J. Van Harlingen, Y. Maeno, *Science* **314**, 1267–1271 (2006).
13. M. Stone, R. Roy, *Phys. Rev. B* **69**, 184511 (2004).
14. D. F. Agterberg, *Phys. Rev. B* **64**, 052502 (2001).
15. C. W. Hicks *et al.*, *Phys. Rev. B* **81**, 214501 (2010).
16. J. R. Kirtley *et al.*, *Phys. Rev. B* **76**, 014526 (2007).
17. Z. Q. Mao, Y. Maeno, S. NishiZaki, T. Akima, T. Ishiguro, *Phys. Rev. Lett.* **84**, 991–994 (2000).
18. K. Deguchi, M. A. Tanatar, Z. Mao, T. Ishiguro, Y. Maeno, *J. Phys. Soc. Jpn.* **71**, 2839–2842 (2002).
19. M. Sigrist, K. Ueda, *Rev. Mod. Phys.* **63**, 239–311 (1991).
20. M. B. Walker, P. Contreras, *Phys. Rev. B* **66**, 214508 (2002).
21. In addition to $p_x \pm ip_y$, ground states of unstrained Sr_2RuO_4 that would yield cusps in T_c at $\varepsilon = 0$ include $d_{xz} \pm id_{yz}$ (*22*) and the nonchiral orders p_x and $p_x + p_y$.
22. I. Žutić, I. Mazin, *Phys. Rev. Lett.* **95**, 217004 (2005).
23. Y. Maeno *et al.*, *Phys. Rev. Lett.* **81**, 3765–3768 (1998).
24. S. Kittaka, H. Yaguchi, Y. Maeno, *J. Phys. Soc. Jpn.* **78**, 103705 (2009).
25. S. Kittaka, H. Taniguchi, S. Yonezawa, H. Yaguchi, Y. Maeno, *Phys. Rev. B* **81**, 180510 (2010).
26. C. W. Hicks, M. E. Barber, S. D. Edkins, D. O. Brodsky, A. P. Mackenzie, http://arxiv/abs/1403.4368.
27. J.-H. Chu, H.-H. Kuo, J. G. Analytis, I. R. Fisher, *Science* **337**, 710–712 (2012).
28. Strain, rather than stress, is the controlled parameter if the apparatus spring constant dominates the sample spring constant. The softest part of the apparatus is the sample-mounting epoxy. For all samples, the apparatus exceeded the sample spring constant, but not vastly, so finite element analysis of the sample and epoxy deformation was necessary.
29. More details on our methods and calculations can be found in the supplementary materials on *Science* Online.
30. We use ε_{100} and ε_{110} to denote the applied strains, implying simultaneous transverse strains following the Poisson's ratios, whereas ε_{ij} are defined as usual.
31. J. P. Paglione *et al.*, *Phys. Rev. B* **65**, 220506 (2002).
32. P. Blaha, K. Schwarz, G. K. H. Madsen, D. Kvasnicka, J. Luitz, *WIEN2k: An Augmented Plane Wave Plus Local Orbitals Program for Calculating Crystal Properties* (Karlheinz Schwarz, Techn. Universität Wien, Austria, 2001); ISBN 3-9501031-1-2.
33. C. Lupien *et al.*, *Phys. Rev. Lett.* **86**, 5986–5989 (2001).
34. T. Kuwabara, M. Ogata, *Phys. Rev. Lett.* **85**, 4586–4589 (2000).
35. K. Kuroki, M. Ogata, R. Arita, H. Aoki, *Phys. Rev. B* **63**, 060506 (2001).
36. S. Raghu, A. Kapitulnik, S. A. Kivelson, *Phys. Rev. Lett.* **105**, 136401 (2010).
37. T. Nomura, K. Yamada, *J. Phys. Soc. Jpn.* **71**, 404–407 (2002).
38. K. Miyake, O. Narikiyo, *Phys. Rev. Lett.* **83**, 1423–1426 (1999).
39. K. Deguchi, Z. Q. Mao, Y. Maeno, *J. Phys. Soc. Jpn.* **73**, 1313–1321 (2004).
40. Q. H. Wang *et al.*, *Europhys. Lett.* **104**, 17013 (2013).
41. Angle-resolved photoemission spectroscopy under uniaxial stress has been performed [see (*42*)].
42. M. Yi *et al.*, *Proc. Natl. Acad. Sci. U.S.A.* **108**, 6878–6883 (2011).

Acknowledgments: We acknowledge useful discussions with E. Berg, C. Hooley, A. Huxley, S. Kivelson, J. Sauls, and S. Simon. We thank the UK Engineering and Physical Sciences Research Council, the Max Planck Society, and the Royal Society for financial support. Work at Kyoto University was supported by a KAKENHI grant (no. 22103002) from the Ministry of Education, Culture, Sports, Science and Technology.

Supplementary Materials

www.sciencemag.org/content/344/6181/283/suppl/DC1
Materials and Methods
Supplementary Text
Figs. S1 to S7
References (*43*–*47*)

11 November 2013; accepted 24 March 2014
10.1126/science.1248292

Wafer-Scale Growth of Single-Crystal Monolayer Graphene on Reusable Hydrogen-Terminated Germanium

Jae-Hyun Lee,[1,2,3]* Eun Kyung Lee,[4]* Won-Jae Joo,[3,4]* Yamujin Jang,[2,3] Byung-Sung Kim,[1,3] Jae Young Lim,[1,3] Soon-Hyung Choi,[2,3] Sung Joon Ahn,[5] Joung Real Ahn,[1,5] Min-Ho Park,[2] Cheol-Woong Yang,[2] Byoung Lyong Choi,[4]† Sung-Woo Hwang,[3,4]† Dongmok Whang[1,2,3]†

The uniform growth of single-crystal graphene over wafer-scale areas remains a challenge in the commercial-level manufacturability of various electronic, photonic, mechanical, and other devices based on graphene. Here, we describe wafer-scale growth of wrinkle-free single-crystal monolayer graphene on silicon wafer using a hydrogen-terminated germanium buffer layer. The anisotropic twofold symmetry of the germanium (110) surface allowed unidirectional alignment of multiple seeds, which were merged to uniform single-crystal graphene with predefined orientation. Furthermore, the weak interaction between graphene and underlying hydrogen-terminated germanium surface enabled the facile etch-free dry transfer of graphene and the recycling of the germanium substrate for continual graphene growth.

The availability of high-quality, large, single-crystal Si wafers is fundamental to current Si-based electronics. Given that the potential advantages of graphene as a host material for various devices have been established, the primary requirement is cost-efficient, reliable, and high-throughput synthesis of single-crystal monolayer graphene over wafer-scale dimensions with methods compatible with current semiconductor technology. In addition, single-crystal graphene with a predefined orientation will allow various applications of graphene's orientation-dependent properties (*1*, *2*). Various methods for synthesizing large-area graphene monolayers have been reported, including the graphitization of silicon carbide surfaces (*3*, *4*) and catalytic chemical vapor deposition (CVD) on metals (*5*–*7*). In particular, CVD has been used to synthesize predominantly large-area monolayer graphene of excellent quality on polycrystalline copper foils (*5*) that can easily be transferred to other substrates. However, the large-scale synthetic graphene produced thus far are typically polycrystalline, consisting of many single-crystalline grains separated by defective grain boundaries that degrade their electrical and mechanical properties (*8*, *9*).

There are two possible approaches to catalytic growth of a single-crystal graphene layer over a solid substrate surface. The first approach involves growing a single grain to as large a size as possible from a single nucleation site. The growth of a centimeter-size single-crystal graphene domain from a single nucleus was recently demonstrated (*10*). However, this approach may not be practical for reproducible and high-throughput synthesis of wafer-scale single-crystal graphene. The second approach involves the catalytic and epitaxial growth of graphene on a single-crystal substrate. If initial multiple nucleation of the graphene seeds occurs but with perfect rotational alignment, the unidirectionally aligned seeds can grow and coalesce into a uniform single-crystal layer without grain boundary defects, even if the nucleation density is high (Fig. 1A and fig. S1) (*11*). The epitaxial graphene growth has been extensively investigated with various single-crystal substrates (*7*, *12*–*14*). However, wafer-scale single-crystal monolayer graphene has not yet been realized. Recent studies on the nucleation of graphene on a weakly interacting metal surface have demonstrated that the interaction between the metal surface and the graphene edge is responsible for the orientation determination of graphene seeds at the early stage of graphene growth (*15*). These results indicate that uniaxial and reversible binding of the seed edge on the catalytic surface is critical for the growth of single-crystal graphene from multiple nucleations.

If possible, a Si single-crystal wafer is an ideal substrate for the epitaxial graphene growth, because it is readily available up to 450 mm in diameter. However, the low carbon diffusivity on Si surface and the relatively high carbon solubility hamper the direct growth of high-quality monolayer graphene on Si (*16*). Instead of Si, we used a single-crystal Ge surface for the growth of single-crystal graphene, because of (i) its catalytic activity, which can lower the energy barriers for the catalytic decomposition of carbon precursor and thus can induce formation of graphitic carbon on the surface (*17*); (ii) the extremely low solubility of carbon in Ge even at its melting temperature ($<10^8$ atoms/cm^3) (*18*), enabling growth of complete monolayer graphene (*19*); (iii) the well-defined and anisotropic atomic arrangement of single-crystal Ge surface, enabling aligned growth of multiple seeds that can merge into single-crystal layer without producing grain boundaries; (iv) the availability of a large-area single-crystal surface via epitaxial Ge growth on Si wafers (*20*); and (v) the small difference in thermal expansion coefficients between Ge and graphene, suppressing intrinsic wrinkle formation (*21*, *22*).

For single-crystal graphene growth from the aligned seeds, we selected a Ge(110) substrate having anisotropic twofold in-plane surface symmetry. The graphene islands at the early stage of growth on H-terminated Ge(110) surface were uniaxially aligned along the [$\bar{1}$10] direction of the underlying Ge(110) surface (Fig. 1B) and then grown to form uniform monolayer graphene on an entire growth substrate (Fig. 1C and fig. S2). The single-crystal Ge layers were epitaxially grown on a Si(110) wafer (fig. S3), then highly uniform monolayer graphene was synthesized on the hydrogen-terminated Ge surfaces via a controlled low-pressure CVD by flowing a CH_4 gas (1 to 2% diluted in H_2) at 900° to 930°C (*11*). The chemisorption of H and C atoms on the Ge surface can be reversible at high temperature, enabling the catalytic growth of graphene on the H-terminated Ge surface (fig. S4). The highly symmetric C 1s core peak at a binding energy of 284.4 eV and the absence of Ge-C related peaks in the XPS spectra of the as-grown graphene on Ge surface imply that the carbon atoms in the graphene are fully sp^2-hybridized without a bonding interaction with the underlying Ge surface (fig. S5).

A high-resolution transmission electron microscopy (HR-TEM) image of the graphene reveals that well-defined monolayer graphene was formed without any noticeable structural defects (Fig. 1D). The overlaid selected area electron diffraction (SAED) patterns acquired from four different points separated from each other by ~2 μm illustrate that all of the points had the same crystallographic orientations, displaying a single-crystalline lattice structure of the graphene (Fig. 1D, inset). The cross-sectional TEM image in Fig. 1E also indicates that the as-grown graphene is monolayered. The low-energy electron diffraction (LEED) pattern of graphene grown on Ge(110) revealed six hexagonally arranged spots that correspond to single-crystal graphene (Fig. 2A). The positions of the LEED spots of graphene and the underlying Ge surface in Fig. 2A show that zigzag and armchair directions of graphene lattice are parallel to [001] and [$\bar{1}$10] directions of the Ge(110) facet, respectively (fig. S6). There were no satellite spots commonly observed for graphene epitaxially grown on a metal surface (*12*), suggesting the absence of interlayer bonding between graphene and the underlying Ge surface. We also investigated graphene growth on isotropic Ge(111) surface for comparative study. Growth on Ge(111) also produced monolayer graphene; however, the seed shapes are isotropic (fig. S7, A and B). Furthermore, the LEED

[1]SKKU Advanced Institute of Nanotechnology, Sungkyunkwan University (SKKU), Suwon 440-746, Korea. [2]School of Advanced Materials Science and Engineering, Sungkyunkwan University, Suwon 440-746, Korea. [3]Research Center for Time-Domain Nano-functional Devices, Samsung Advanced Institute of Technology, Yongin 449-712, Korea. [4]Nano Electronics Laboratory, Samsung Advanced Institute of Technology, Yongin 449-712, Korea. [5]Department of Physics, Sungkyunkwan University, Suwon 440-746, Korea.

*These authors contributed equally to this work.
†Corresponding author. E-mail: dwhang@skku.edu (D.W.); swnano.hwang@samsung.com (S.-W.H.); choibl@samsung.com (B.L.C.)

patterns (Fig. 2B) and TEM images (fig. S7) of graphene grown on Ge(111) indicate that the obtained graphene is polycrystalline with a weak domain orientation preference.

The Raman spectra of single-crystalline and polycrystalline graphene grown on Ge(110) and Ge(111) demonstrate that both materials are monolayer graphene (*23*); however, the integrated intensity ratio between D and G peaks [*I*(D)/*I*(G)] of the single-crystal graphene (<0.03) is substantially smaller than that of the polycrystalline graphene (~0.4) (Fig. 2C), suggesting the absence of the extended grain boundary defects in the single-crystal graphene on Ge(110) and its superior electrical properties. To evaluate the electrical characteristics of the single-crystalline and polycrystalline graphene, we fabricated back-gated graphene field-effect transistors (GFETs) on SiO_2/Si substrates by using two different types of graphenes grown on Ge(110) and Ge(111) (fig. S8) (*11*). Compared with the GFET based on Ge(111)-catalyzed polycrystalline graphene, the single-crystal graphene exhibits smaller sheet resistances at the Dirac point with a narrower distribution (Fig. 2D). The carrier mobilities extracted from the sheet resistance by using the simple Drude model for single-crystal graphene were 7250 ± 1390 $cm^2/V{\cdot}s$ (SD) with a maximum value of 10,620 $cm^2/V{\cdot}s$ (Fig. 2E), which are comparable to the values of previously reported metal-catalyzed single-domain graphene on Si/SiO_2 substrates (*10*, *24*). The carrier mobility of the Ge-catalyzed polycrystalline graphene (2570 ± 460 $cm^2/V{\cdot}s$) decreased because of grain boundary scattering. Considering that typical nucleation density of Ge-catalyzed graphene (~10 per μm^2) is considerably higher than the densities reported for metal-catalyzed graphene (<0.1 per μm^2), the mobilities from the graphene grown on Ge(111) are still reasonably high, which suggests good intergrain connectivity in the polycrystalline graphene (*8*). Both prebake of the CVD chamber under H_2 flow and excessive H_2 flow during the growth were necessary to prepare the single-crystal graphene without a substantial number of defects, indicating that even a trace amount of oxygen in the CVD chamber can affect the graphene growth results (fig. S9) (*11*).

These results demonstrate that the H-terminated Ge(110) surface is an ideal substrate for the catalytic growth of single-crystal graphene. The asymmetric twofold geometry of the Ge(110) surface and the anisotropic nature of the Ge-C covalent bonds dictate the perfect alignment of the edges

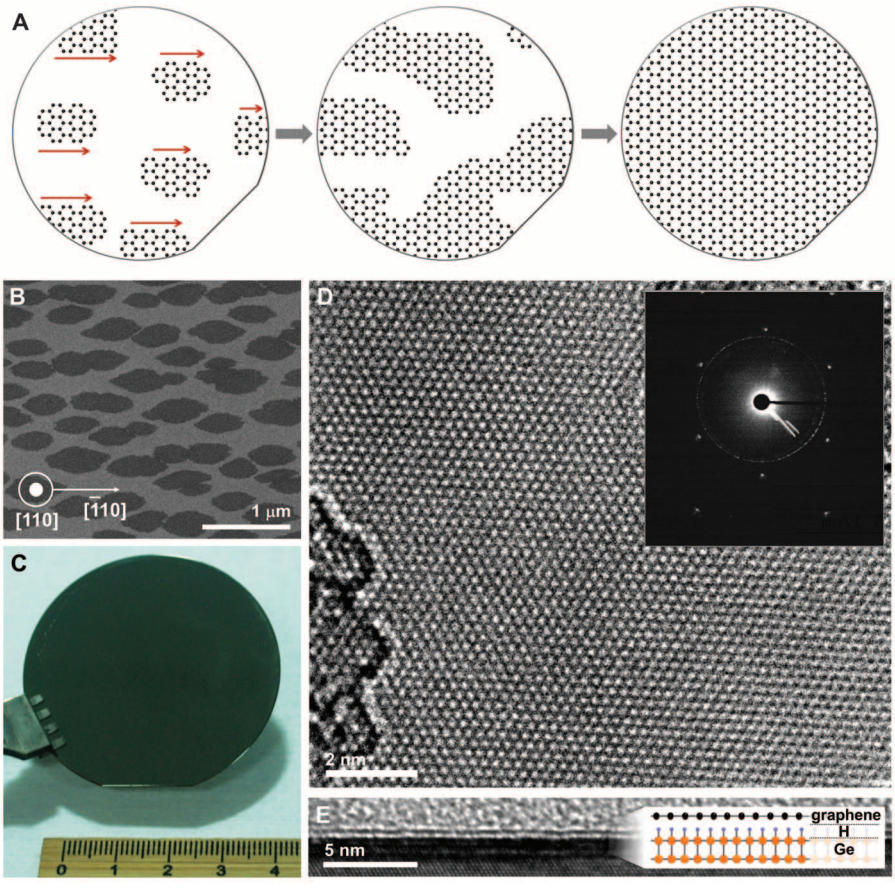

Fig. 1. Single-crystal monolayer graphene grown on a hydrogen-terminated Ge(110) surface. (**A**) A schematic illustration of catalytic growth of single-crystal monolayer graphene from unidirectionally aligned multiple seeds. (**B**) A typical SEM image of graphene seeds at the early stage of growth. (**C**) A photograph of graphene grown on a 5.08-cm Ge/Si (110) wafer. (**D**) A HR-TEM image of the single-crystal monolayer graphene. (Inset) Four overlaid SAED patterns, which were measured across the four different points. The distance between each point is ~2 μm. (**E**) A cross-sectional TEM image demonstrating that the as-grown graphene is monolayer. (Inset) A schematic illustration of the monolayer graphene grown on the H-terminated Ge surface.

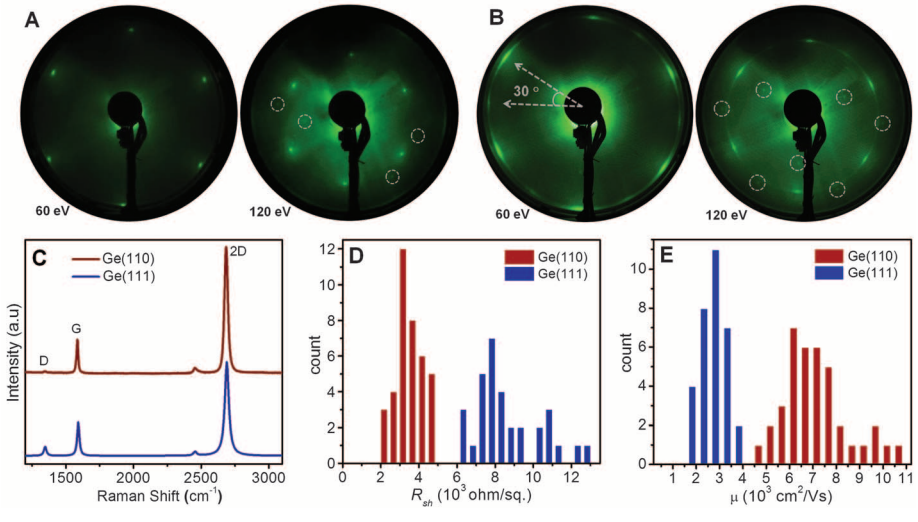

Fig. 2. Comparison of single-crystalline and polycrystalline graphene grown on H-terminated Ge(110) and Ge(111) surfaces. (**A**) LEED patterns of single-crystal graphene grown on a H-Ge (110) substrate at 60 and 120 eV. The diameter of the electron beam was ~1 mm. (**B**) LEED patterns of polycrystalline graphene grown on a H-Ge(111) substrate at 60 and 120 eV. Gray circles in (A) and (B) denote the diffraction spots resulting from the Ge(110) and the Ge(111) substrate, respectively. (**C**) Raman spectra of single-crystal and polycrystalline graphene grown on H-Ge(110) and H-Ge(111) surfaces under same growth conditions. a.u, arbitrary units. (**D**) The distribution of sheet resistance (R_{sh}) at the Dirac point. The carrier mobility μ near the Dirac point ($n = 3 \times 10^{11}$ per cm^2).

of graphene seeds at the early stage of growth (fig. S10), and such an orientation can be retained during further growth of the seeds to continuous single-crystal graphene layer because of the high barrier of graphene island rotation. When the edges of two adjacent graphene islands with same orientation approach each other before merging, atomic positions of the edges may not be well matched in our growth process. If the islands are tightly bound on the substrate surface, and thus the offset is not removed during coalesce of the islands, the positional displacement between the adjacent islands may form a nontilt grain boundary or extended line defect in spite of high formation energy of the extended defects in covalently bonded graphene (*25*). However, considering the pseudo–free-standing nature of the graphene islands on H-terminated Ge surface, the spontaneous formation of the extended grain-boundary defect during the growth of graphene on H-terminated Ge surface is highly unlikely. Figure 3 and fig. S2 show scanning electron microscopy (SEM) and TEM images of a typical edge front at which adjacent graphene islands are coalescing. In the reconstructed {1100} planes of the edge front (Fig. 3D), no discontinuous line was observed, indicating that adjacent islands are coalescing without grain boundary defects.

In addition to single crystallinity of graphene, wrinkle-free growth has been considered another challenge in graphene growth because the wrinkles cause scattering in the device characteristics and lead to inferior electrical properties (*26*). Wrinkles are known to be formed through thermal expansion mismatch because the underlying substrate contracts more than the graphene during postgrowth cooling, resulting in interlayer mechanical strain. However, as-grown graphene on a Ge substrate exhibited no wrinkles (fig. S11). We infer that the free-standing nature of graphene on the H-terminated surface and the relatively small difference in thermal expansion coefficient between the materials enabled the formation of flat graphene without wrinkles.

The extremely weak adhesion between graphene and the underlying substrate also allowed facile mechanical exfoliation of the graphene layer with few defects, regenerating the H-terminated Ge surface for further continual growth (figs. S12 and S13). Gold-coated graphene was easily exfoliated from the Ge surface, which shows that the binding energy between the graphene and the underlying Ge surface ($\gamma_{G\text{-}Ge}$) must be much less than 60 meV ($\gamma_{Au\text{-}G} \approx 60$ meV) (*27*). The merit of the mechanical exfoliation of monolayer graphene is apparent because catalytic single-crystal substrates are expensive to dispose and their chemical etchants are environmentally hazardous. Given research results that demonstrate the undesirable doping effect and physical damage on graphene caused by a wet transfer process, direct dry transfer without substrate etching appears even more favorable (*28*, *29*). Figure 4A shows an optical image of the graphene that was mechanically exfoliated and transferred on the SiO_2/Si substrate with 300-nm thermal oxide, indicating that the transferred graphene was a monolayer and wrinkle-free over the entire area. In addition, the Ge-catalyzed graphene exhibits transmittance of 97.64% at 550 nm (fig. S14), which agrees well with the ideal transmittance for monolayer graphene (*30*). Water contact angles of H-terminated Ge surface and Ge surface exposed after graphene delamination were almost identical (Fig. 4B and fig. S12), demonstrating the underlying Ge surface after graphene growth is hydrogen terminated. We repeated the growth and etch-free dry transfer five times with the same H-terminated Ge/Si substrate, and the transferred graphene was evaluated by using Raman spectra (Fig. 4C). The Raman spectra of each of the graphene are almost identical, demonstrating that the single-crystal Ge substrate can be reused multiple times for graphene growth without degradation. Thus, the repeated, orientation-controlled synthesis of single-crystal monolayer graphene on the entire surface of a Si wafer using an H-terminated Ge buffer layer, in combination with complementary metal-oxide semiconductor–compatible etch-free

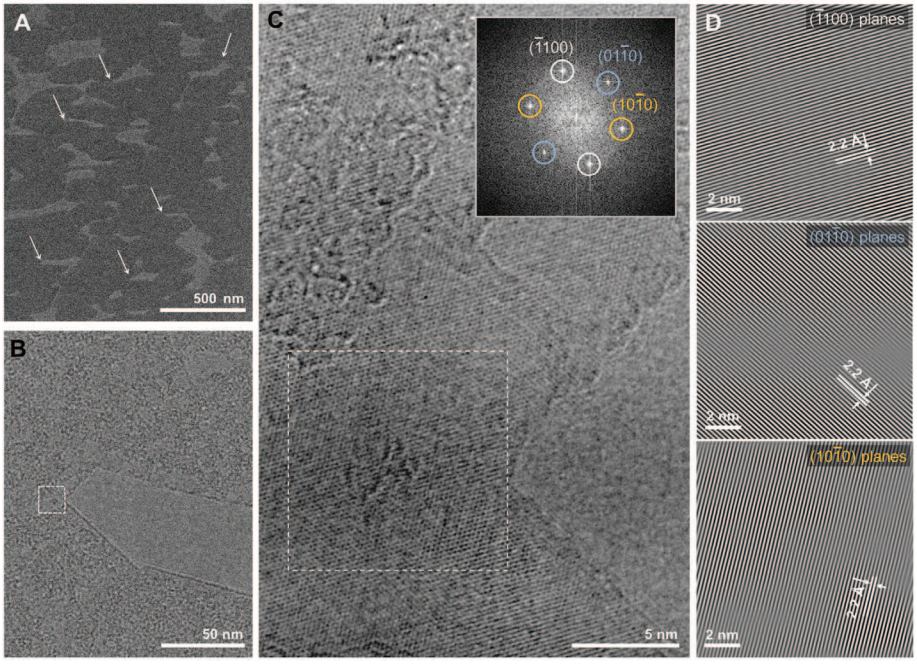

Fig. 3. A graphene edge where adjacent graphene islands are merging. (**A**) A SEM image of incompletely grown graphene on Ge(110). Arrows point out edge fronts at which adjacent islands are merging. (**B** and **C**) Bright-field TEM images of an edge front similar to the white arrows in (A). (C inset) A fast Fourier transform diffractogram taken from the region indicated by the dashed square in (B) and (C). (**D**) Three {1100} planes reconstructed from the three sets of diffraction spots in the (C) inset, showing no sign of grain boundary defects in the merged area.

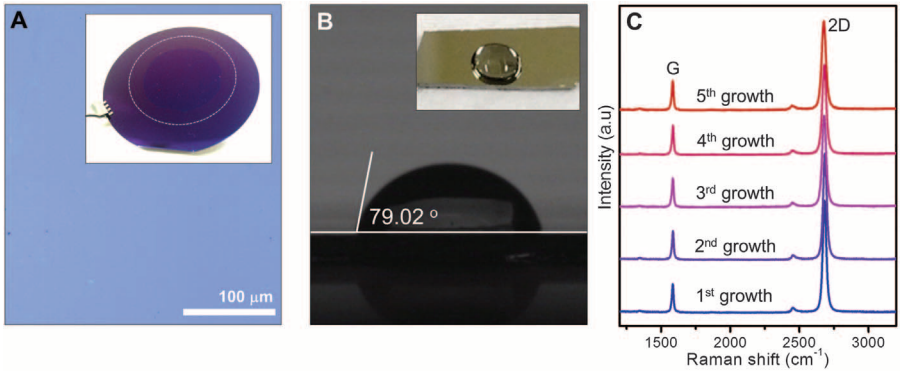

Fig. 4. Etch-free dry transfer and repeated growth of single-crystal graphene on the same Ge/Si wafer. (**A**) An optical image of graphene transferred onto a SiO_2/Si substrate with 300-nm thermal oxide. (Inset) A photograph of the 5.08-cm graphene transferred onto a 10.16-cm SiO_2/Si wafer. (**B**) Water droplet contact angle measurement on the H-terminated Ge surface exposed after mechanical peeling of the as-grown graphene. (Inset) A photograph of water droplet on the regenerated H-Ge surface. (**C**) Raman spectra of five different graphene layers grown by using the same Ge(110) substrates.

transfer processes, may open up commercial realization of various functional devices based on single-crystal graphene.

References and Notes

1. A. K. Singh, B. I. Yakobson, *Nano Lett.* **9**, 1540–1543 (2009).
2. C. Zhang, L. Chen, Z. Ma, *Phys. Rev. B* **77**, 241402 (2008).
3. K. V. Emtsev *et al.*, *Nat. Mater.* **8**, 203–207 (2009).
4. C. Berger *et al.*, *Science* **312**, 1191–1196 (2006).
5. X. Li *et al.*, *Science* **324**, 1312–1314 (2009).
6. K. S. Kim *et al.*, *Nature* **457**, 706–710 (2009).
7. N. C. Bartelt, K. F. McCarty, *MRS Bull.* **37**, 1158–1165 (2012).
8. A. W. Tsen *et al.*, *Science* **336**, 1143–1146 (2012).
9. Y. Wei *et al.*, *Nat. Mater.* **11**, 759–763 (2012).
10. Y. Hao *et al.*, *Science* **342**, 720–723 (2013).
11. Materials and methods are available as supplementary materials on *Science* Online.
12. P. W. Sutter, J.-I. Flege, E. A. Sutter, *Nat. Mater.* **7**, 406–411 (2008).
13. S. Nie, J. M. Wofford, N. C. Bartelt, O. D. Dubon, K. F. McCarty, *Phys. Rev. B* **84**, 155425 (2011).
14. Z. R. Robinson, P. Tyagi, T. R. Mowll, C. A. Ventrice Jr., J. B. Hannon, *Phys. Rev. B* **86**, 235413 (2012).
15. X. Zhang, Z. Xu, L. Hui, J. Xin, F. Ding, *J. Phys. Chem. Lett.* **3**, 2822–2827 (2012).
16. P. Thanh Trung *et al.*, *Appl. Phys. Lett.* **102**, 013118 (2013).
17. P. W. Loscutoff, S. F. Bent, *Annu. Rev. Phys. Chem.* **57**, 467–495 (2006).
18. R. I. Scace, G. A. Slack, *J. Chem. Phys.* **30**, 1551–1555 (1959).
19. G. Wang *et al.*, *Sci. Rep* **3**, 2465 (2013).
20. R. Lieten, S. Degroote, M. Leys, N. Posthuma, G. Borghs, *Appl. Phys. Lett.* **94**, 112113 (2009).
21. W. Bao *et al.*, *Nat. Nanotechnol.* **4**, 562–566 (2009).
22. D. F. Gibbons, *Phys. Rev.* **112**, 136–140 (1958).
23. A. C. Ferrari, J. Robertson, *Phys. Rev. B* **61**, 14095–14107 (2000).
24. L. Gao *et al.*, *Nat. Commun.* **3**, 699 (2012).
25. J. Lahiri, Y. Lin, P. Bozkurt, I. I. Oleynik, M. Batzill, *Nat. Nanotechnol.* **5**, 326–329 (2010).
26. W. Zhu *et al.*, *Nano Lett.* **12**, 3431–3436 (2012).
27. I. Hamada, M. Otani, *Phys. Rev. B* **82**, 153412 (2010).
28. J. Kim *et al.*, *Science* **342**, 833–836 (2013).
29. J. Kang, D. Shin, S. Bae, B. H. Hong, *Nanoscale* **4**, 5527–5537 (2012).
30. R. R. Nair *et al.*, *Science* **320**, 1308 (2008).

Acknowledgments: We are grateful to J.-H. Ahn, B. H. Hong, and Y. J. Song for helpful discussions. This work was supported by the National Research Foundation of Korea (NRF) grant funded by the Korean government (Ministry of Science, ICT, and Future Planning) (no. 2007-0054845). D.W. acknowledges support from the Basic Science Research Program through the NRF (no. 2009-0083540) and Samsung-SKKU graphene center.

Supplementary Materials

www.sciencemag.org/content/344/6181/286/suppl/DC1
Materials and Methods
Figs. S1 to S14
References (*31*–*33*)

14 February 2014; accepted 20 March 2014
Published online 3 April 2014;
10.1126/science.1252268

Ultimate Permeation Across Atomically Thin Porous Graphene

Kemal Celebi,[1]* Jakob Buchheim,[1]* Roman M. Wyss,[1] Amirhossein Droudian,[1] Patrick Gasser,[1] Ivan Shorubalko,[2] Jeong-Il Kye,[3] Changho Lee,[3] Hyung Gyu Park[1]†

A two-dimensional (2D) porous layer can make an ideal membrane for separation of chemical mixtures because its infinitesimal thickness promises ultimate permeation. Graphene—with great mechanical strength, chemical stability, and inherent impermeability—offers a unique 2D system with which to realize this membrane and study the mass transport, if perforated precisely. We report highly efficient mass transfer across physically perforated double-layer graphene, having up to a few million pores with narrowly distributed diameters between less than 10 nanometers and 1 micrometer. The measured transport rates are in agreement with predictions of 2D transport theories. Attributed to its atomic thicknesses, these porous graphene membranes show permeances of gas, liquid, and water vapor far in excess of those shown by finite-thickness membranes, highlighting the ultimate permeation these 2D membranes can provide.

Recent advances in graphene synthesis and processing (*1*–*3*) have enabled demonstrations of atomically thin two-dimensional (2D) membranes showing mechanical sturdiness and hermetic sealing (*4*, *5*). Initial attempts to endow mass permeability to the otherwise impermeable graphene have been based on formation of a single aperture (*6*) and randomly etched or defect-originated pores (*7*, *8*). However, the macroscopic quantification of mass transport through such 2D pores is extremely challenging because the task demands a large number of pores with controlled dimensions.

We have developed a facile and reliable method for making 2D membranes (Fig. 1, A to G). This process uses chemical vapor deposition (CVD) optimized to grow graphene with minimal defects and good grain connectivity in order to prevent undesirable crack formation (*9*). A clean transfer process places two layers of graphene consecutively onto a SiN_x frame punctured with 49 pores each of 4 μm in diameter (Fig. 1D), forming freestanding graphene layers that are thinner than 1 nm. This double transfer strengthens the freestanding graphene and keeps it from leakage through random defects (*10*, *11*). Cleanliness and quality of graphene are found to be crucial during this graphene transfer process because grain boundary defects, polymer residues, or dust particles can induce crack formation while perforating the graphene. Scanning electron microscope (SEM) images (Fig. 1E and fig. S1) support that our transfer process produces crack-free graphene over the length scale of the entire frame. The freestanding film of double-layer graphene remains impermeable to gases and water. Nanopores were then drilled with a focused ion beam (FIB) to produce porous membranes (Fig. 1, F and G). We used Ga-based FIB to perforate apertures between 14 nm and 1 μm in diameter and He-based FIB for <10-nm-pore drilling. Low exposure doses (5×10^{-6} to 5×10^{-5} pA/nm^2 for Ga^+ ions and 6×10^{-3} pA/nm^2 for He^+ ions) enabled fast and precise drilling, resulting in well-defined pore diameter distributions (Fig. 1, H to K).

The large number of pores (~10^3 to 10^6 per membrane) allows gas flows detectable with conventional mass flow meters. The membranes are mechanically sturdy enough to stand pressure differences of up to 2 bar (higher pressure not tested). N_2 flow shows linear pressure dependence (figs. S2 and S3), resulting in pressure-independent permeance. N_2 flux displays diameter dependence characterized by two asymptotic theories: free molecular transport (effusion) and modified Sampson's model (*12*, *13*) for small- and large-size apertures, respectively (Fig. 2A). For apertures smaller than 50 nm, the mean free path (λ) becomes larger than the aperture diameter (d), and the probability of having intermolecular collisions in the vicinity of the aperture decreases. Here, the transport enters the molecular flow regime featured by effusion for small apertures. Knudsen numbers (λ/d) for membranes (7.6 nm < d < 50 nm) are between 1 and 10, which is well within the molecular flow regime, and so the flow can be explained by the effusion mechanism, which is purely dependent on the probability of a molecule hitting the aperture. This can be quantified by the effusion flux, $Q_E = \overline{u}\Delta n/4 = \Delta P/\sqrt{2\pi m k_B T}$, where n is the gas number density, $\overline{u}$ is the mean molecular speed, P is the pressure, k_B is the Boltzmann constant, T is the temperature, and m is the molecular weight. As the pore diameter enlarges, more molecules interact with one another near the aperture, causing a transition from effusion to a more collective flow. However, collective flow models based on pore wall interactions (the Hagen-Poiseuille model) are not suitable to explain the flow behavior for atomically thin membranes. Such flows through an

[1]Nanoscience for Energy Technology and Sustainability, Department of Mechanical and Process Engineering, Eidgenössische Technische Hochschule (ETH) Zurich, Sonneggstrasse 3, CH-8092 Zürich, Switzerland. [2]Laboratory for Electronics/Metrology/Reliability, EMPA (Swiss Federal Laboratories for Materials Science and Technology), Überlandstrasse 129, CH-8600 Dübendorf, Switzerland. [3]Materials and Components R&D Laboratory, LG Electronics Advanced Research Institute, 38 Baumoe-ro, Seocho-gu, Seoul 137-724, Korea.

*These authors contributed equally to this work.
†To whom correspondence should be addressed: parkh@ethz.ch

transfer processes, may open up commercial realization of various functional devices based on single-crystal graphene.

References and Notes

1. A. K. Singh, B. I. Yakobson, *Nano Lett.* **9**, 1540–1543 (2009).
2. C. Zhang, L. Chen, Z. Ma, *Phys. Rev. B* **77**, 241402 (2008).
3. K. V. Emtsev *et al.*, *Nat. Mater.* **8**, 203–207 (2009).
4. C. Berger *et al.*, *Science* **312**, 1191–1196 (2006).
5. X. Li *et al.*, *Science* **324**, 1312–1314 (2009).
6. K. S. Kim *et al.*, *Nature* **457**, 706–710 (2009).
7. N. C. Bartelt, K. F. McCarty, *MRS Bull.* **37**, 1158–1165 (2012).
8. A. W. Tsen *et al.*, *Science* **336**, 1143–1146 (2012).
9. Y. Wei *et al.*, *Nat. Mater.* **11**, 759–763 (2012).
10. Y. Hao *et al.*, *Science* **342**, 720–723 (2013).
11. Materials and methods are available as supplementary materials on *Science* Online.
12. P. W. Sutter, J.-I. Flege, E. A. Sutter, *Nat. Mater.* **7**, 406–411 (2008).
13. S. Nie, J. M. Wofford, N. C. Bartelt, O. D. Dubon, K. F. McCarty, *Phys. Rev. B* **84**, 155425 (2011).
14. Z. R. Robinson, P. Tyagi, T. R. Mowll, C. A. Ventrice Jr., J. B. Hannon, *Phys. Rev. B* **86**, 235413 (2012).
15. X. Zhang, Z. Xu, L. Hui, J. Xin, F. Ding, *J. Phys. Chem. Lett.* **3**, 2822–2827 (2012).
16. P. Thanh Trung *et al.*, *Appl. Phys. Lett.* **102**, 013118 (2013).
17. P. W. Loscutoff, S. F. Bent, *Annu. Rev. Phys. Chem.* **57**, 467–495 (2006).
18. R. I. Scace, G. A. Slack, *J. Chem. Phys.* **30**, 1551–1555 (1959).
19. G. Wang *et al.*, *Sci. Rep* **3**, 2465 (2013).
20. R. Lieten, S. Degroote, M. Leys, N. Posthuma, G. Borghs, *Appl. Phys. Lett.* **94**, 112113 (2009).
21. W. Bao *et al.*, *Nat. Nanotechnol.* **4**, 562–566 (2009).
22. D. F. Gibbons, *Phys. Rev.* **112**, 136–140 (1958).
23. A. C. Ferrari, J. Robertson, *Phys. Rev. B* **61**, 14095–14107 (2000).
24. L. Gao *et al.*, *Nat. Commun.* **3**, 699 (2012).
25. J. Lahiri, Y. Lin, P. Bozkurt, I. I. Oleynik, M. Batzill, *Nat. Nanotechnol.* **5**, 326–329 (2010).
26. W. Zhu *et al.*, *Nano Lett.* **12**, 3431–3436 (2012).
27. I. Hamada, M. Otani, *Phys. Rev. B* **82**, 153412 (2010).
28. J. Kim *et al.*, *Science* **342**, 833–836 (2013).
29. J. Kang, D. Shin, S. Bae, B. H. Hong, *Nanoscale* **4**, 5527–5537 (2012).
30. R. R. Nair *et al.*, *Science* **320**, 1308 (2008).

Acknowledgments: We are grateful to J.-H. Ahn, B. H. Hong, and Y. J. Song for helpful discussions. This work was supported by the National Research Foundation of Korea (NRF) grant funded by the Korean government (Ministry of Science, ICT, and Future Planning) (no. 2007-0054845). D.W. acknowledges support from the Basic Science Research Program through the NRF (no. 2009-0083540) and Samsung-SKKU graphene center.

Supplementary Materials

www.sciencemag.org/content/344/6181/286/suppl/DC1
Materials and Methods
Figs. S1 to S14
References (*31*–*33*)

14 February 2014; accepted 20 March 2014
Published online 3 April 2014;
10.1126/science.1252268

Ultimate Permeation Across Atomically Thin Porous Graphene

Kemal Celebi,[1]* Jakob Buchheim,[1]* Roman M. Wyss,[1] Amirhossein Droudian,[1] Patrick Gasser,[1] Ivan Shorubalko,[2] Jeong-Il Kye,[3] Changho Lee,[3] Hyung Gyu Park[1]†

A two-dimensional (2D) porous layer can make an ideal membrane for separation of chemical mixtures because its infinitesimal thickness promises ultimate permeation. Graphene—with great mechanical strength, chemical stability, and inherent impermeability—offers a unique 2D system with which to realize this membrane and study the mass transport, if perforated precisely. We report highly efficient mass transfer across physically perforated double-layer graphene, having up to a few million pores with narrowly distributed diameters between less than 10 nanometers and 1 micrometer. The measured transport rates are in agreement with predictions of 2D transport theories. Attributed to its atomic thicknesses, these porous graphene membranes show permeances of gas, liquid, and water vapor far in excess of those shown by finite-thickness membranes, highlighting the ultimate permeation these 2D membranes can provide.

Recent advances in graphene synthesis and processing (*1*–*3*) have enabled demonstrations of atomically thin two-dimensional (2D) membranes showing mechanical sturdiness and hermetic sealing (*4*, *5*). Initial attempts to endow mass permeability to the otherwise impermeable graphene have been based on formation of a single aperture (*6*) and randomly etched or defect-originated pores (*7*, *8*). However, the macroscopic quantification of mass transport through such 2D pores is extremely challenging because the task demands a large number of pores with controlled dimensions.

We have developed a facile and reliable method for making 2D membranes (Fig. 1, A to G). This process uses chemical vapor deposition (CVD) optimized to grow graphene with minimal defects and good grain connectivity in order to prevent undesirable crack formation (*9*). A clean transfer process places two layers of graphene consecutively onto a SiN_x frame punctured with 49 pores each of 4 μm in diameter (Fig. 1D), forming freestanding graphene layers that are thinner than 1 nm. This double transfer strengthens the freestanding graphene and keeps it from leakage through random defects (*10*, *11*). Cleanliness and quality of graphene are found to be crucial during this graphene transfer process because grain boundary defects, polymer residues, or dust particles can induce crack formation while perforating the graphene. Scanning electron microscope (SEM) images (Fig. 1E and fig. S1) support that our transfer process produces crack-free graphene over the length scale of the entire frame. The freestanding film of double-layer graphene remains impermeable to gases and water. Nanopores were then drilled with a focused ion beam (FIB) to produce porous membranes (Fig. 1, F and G). We used Ga-based FIB to perforate apertures between 14 nm and 1 μm in diameter and He-based FIB for <10-nm-pore drilling. Low exposure doses (5×10^{-6} to 5×10^{-5} pA/nm^2 for Ga^+ ions and 6×10^{-3} pA/nm^2 for He^+ ions) enabled fast and precise drilling, resulting in well-defined pore diameter distributions (Fig. 1, H to K).

The large number of pores (~10^3 to 10^6 per membrane) allows gas flows detectable with conventional mass flow meters. The membranes are mechanically sturdy enough to stand pressure differences of up to 2 bar (higher pressure not tested). N_2 flow shows linear pressure dependence (figs. S2 and S3), resulting in pressure-independent permeance. N_2 flux displays diameter dependence characterized by two asymptotic theories: free molecular transport (effusion) and modified Sampson's model (*12*, *13*) for small- and large-size apertures, respectively (Fig. 2A). For apertures smaller than 50 nm, the mean free path (λ) becomes larger than the aperture diameter (d), and the probability of having intermolecular collisions in the vicinity of the aperture decreases. Here, the transport enters the molecular flow regime featured by effusion for small apertures. Knudsen numbers (λ/d) for membranes (7.6 nm < d < 50 nm) are between 1 and 10, which is well within the molecular flow regime, and so the flow can be explained by the effusion mechanism, which is purely dependent on the probability of a molecule hitting the aperture. This can be quantified by the effusion flux, $Q_E = \overline{u}\Delta n/4 = \Delta P/\sqrt{2\pi m k_B T}$, where n is the gas number density, $\overline{u}$ is the mean molecular speed, P is the pressure, k_B is the Boltzmann constant, T is the temperature, and m is the molecular weight. As the pore diameter enlarges, more molecules interact with one another near the aperture, causing a transition from effusion to a more collective flow. However, collective flow models based on pore wall interactions (the Hagen-Poiseuille model) are not suitable to explain the flow behavior for atomically thin membranes. Such flows through an

[1]Nanoscience for Energy Technology and Sustainability, Department of Mechanical and Process Engineering, Eidgenössische Technische Hochschule (ETH) Zurich, Sonneggstrasse 3, CH-8092 Zürich, Switzerland. [2]Laboratory for Electronics/Metrology/Reliability, EMPA (Swiss Federal Laboratories for Materials Science and Technology), Überlandstrasse 129, CH-8600 Dübendorf, Switzerland. [3]Materials and Components R&D Laboratory, LG Electronics Advanced Research Institute, 38 Baumoe-ro, Seocho-gu, Seoul 137-724, Korea.

*These authors contributed equally to this work.
†To whom correspondence should be addressed: parkh@ethz.ch

array of infinitely thin orifices can be modeled by a modified Sampson's formula (*12*, *13*)

$$Q_S = \frac{1}{6\mu}\frac{\sum_i d_i^3}{\sum_i \pi d_i^2}\Delta P(1 + 0.894\kappa^{3/2}) \quad (1)$$

where Q_S is the orifice flux, d_i is the diameter of aperture i on the graphene, μ is the dynamic viscosity of the gas species, and κ is the porosity based on the graphene area. The narrow pore diameter distributions allow us to predict that Q_S is linearly correlated with the diameter. Indeed, the permeance asymptotically approaches the Q_S prediction as the diameter gets larger than the mean free path (λ) (Fig. 2A). A more comprehensive quantification of gas permeance can be performed with respect to the Knudsen number (Kn = λ/*d*). The gas permeances for different pore size and gas variations are shown collectively in Fig. 2B, spanning a Kn range of 0.03 to 15. Here, the permeances are normalized by the effusion prediction for the corresponding species. For gas diffusion in a long capillary, it is known that there exists a minimum in the flux-Kn diagram at Kn of $O(1)$, stemming from molecule-wall interaction and drift-to-diffusion shift (*14*–*16*). However, investigators have observed no such minimum for relatively short capillaries that limit this interaction. Indeed, the gas permeation data of our extremely thin membrane confirms the omission of Knudsen's minimum, which underscores that Knudsen's minimum is primarily the result of the molecule-wall interaction. In the absence of the continuous radial confinement of gas transport, the effusion sets the asymptote in both the transition and molecular flow regimes, thus eliminating any minimum in the permeance.

Because effusion is directly proportional to the average thermal speed of the molecules, it is expected that the effusive permeance would be directly proportional with $m^{-1/2}$ following Graham's law of effusion. Moreover, when the flow deviates from the effusive to collective behavior, gas viscosity also scales with $m^{1/2}$, leading to the same mass scaling. These predictions are confirmed in

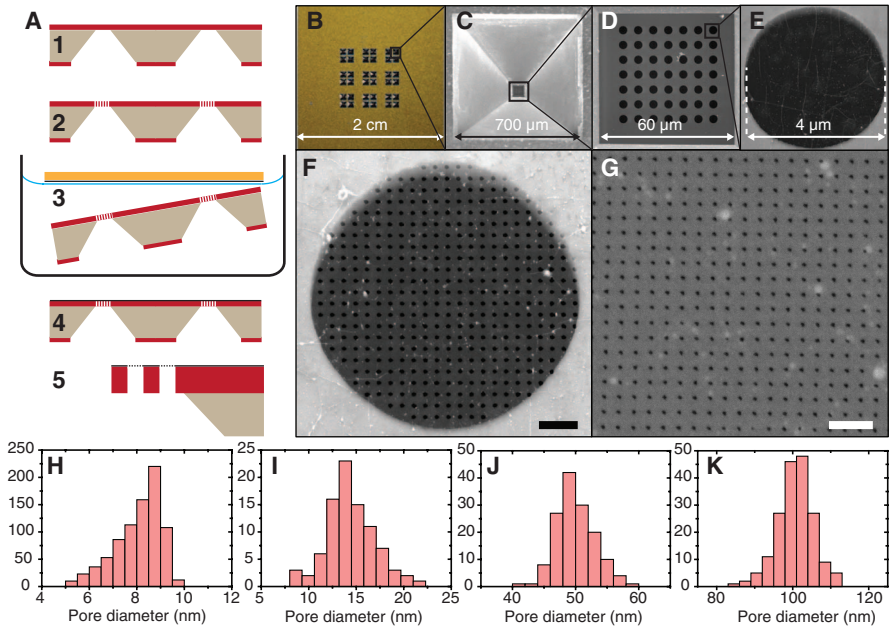

Fig. 1. Membrane fabrication and diameter distribution. (**A**) Schematic of the porous graphene fabrication process. Step 1: freestanding SiN_x membrane formation (by means of KOH etching). Step 2: microscale pore formation through the SiN_x membrane (by means of photolithography and reactive ion etching). Step 3: graphene transfer. Step 4: graphene surface cleanup. Step 5: physical perforation of graphene (by means of Ga- and He-based FIB drilling). (**B**) Photograph (bottom view) of a full membrane structure. (**C**) Bottom view SEM image of the SiN_x membrane. (**D** to **G**) Top view SEM images of (D) porous freestanding SiN_x window before graphene transfer, (E) freestanding graphene transferred on one of the 4-μm-wide SiN_x open pores, (F) 50-nm-wide apertures FIB-drilled on the freestanding graphene (Ga FIB) (scale bar, 500 nm), and (G) 7.6-nm-wide apertures perforated in the similar way (He FIB) (scale bar, 100 nm). (**H** to **K**) Aperture size distributions of the (H) 7.6-nm-, (I) 16-nm-, (J) 50-nm-, and (K) 100-nm-perforated graphene membranes.

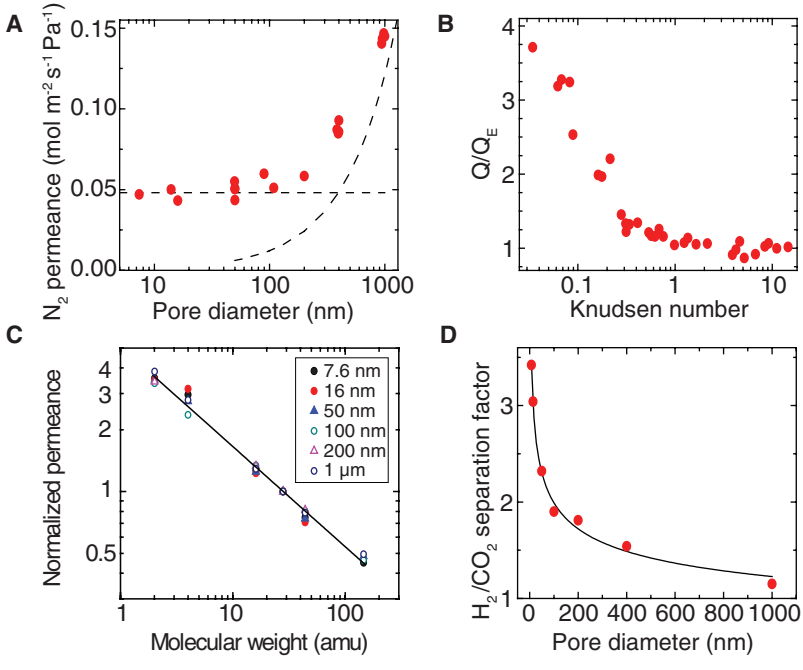

Fig. 2. Characterization of gas transport through the membranes. (**A**) N_2 permeance per pore through different-diameter apertures (red circles) in comparison with predictions of the free molecular flow (effusion) theory (horizontal dashed line) and the modified Sampson's model (dashed curve). (**B**) Permeance normalized with the free molecular flow prediction versus Knudsen number, with the Knudsen minimum undetected. (**C**) Gas permselectivity (defined as the permeances of H_2, He, CH_4, N_2, CO_2, or SF_6 normalized by N_2 permeance) for graphene membranes with different pore diameters (7.6 to 1000 nm) presented with respect to molecular weight. The solid line represents a power-law fit of the data, showing an exponent of −0.49, indicating an inverse square root mass dependence. (**D**) H_2/CO_2 gas separation factors versus pore diameter. The permeate composition was determined with mass spectroscopy for calculation of the separation factors. The solid line is drawn for visual guidance.

Fig. 2C for all pore diameters, showing a permselectivity proportional to $m^{-1/2}$. The origin of gas separation lies in the absence of linear momentum transfer between different molecular species (*17*). When intermolecular collisions exist during the permeation, the linear momentum is transferred from lighter molecules to heavier ones, causing a collective flow, thus reducing the separation. For single-component gas flows, there is no such momentum transfer even if there are molecular collisions, but when a gas mixture is permeating through graphene pores, these collisions must be eliminated. Therefore, apertures with diameters smaller than λ can have better separation efficiencies.

Selectivity for gas mixtures deviates from the permselectivity estimation for single gas permeance comparison. We measured mixed gas selectivity under cross flow conditions (fig. S4A). Gas mixtures with well-defined compositions were partially permeated through each graphene membrane, and the permeate gas compositions were determined by means of mass spectroscopy. The separation factor is defined as

$$\alpha = \frac{\gamma_1/\gamma_2}{\varphi_1/\varphi_2} \quad (2)$$

where α is the separation factor and γ_i and φ_i denote the mole fractions of species i in the permeate and the feed sides, respectively. The pore size dependence of α is shown in Fig. 2D for equally mixed H_2 and CO_2 gases. As predicted, the smallest pores can separate the best, close to the theoretical maximum predicted by the effusion theory for H_2/CO_2 ($\alpha_{max} = 4.69$), whereas a clear decay in α is seen as the diameter increases, approaching the no-separation limit. This approach is correlated with the increased role of the collective flow, as explained above. The separation factor as we measured does not change much over the molar ratios of the feed mixture (fig. S4B).

Our atomically thin graphene membranes also permeated water and vapor at rates in excess of the conventional ultrafiltration and transpiration membranes, respectively. Onset of the water permeation is unfavorable for the membrane if only one side is wet because of capillarity, provided that the continuum theory holds true. Assuming that a mean free path for liquids can be comparable with the molecule's own sizes, we took the water molecule size (~0.3 nm) as the displacement between molecular interactions and compared it with the pore aperture diameters. The equivalent Kn for water lies well below 0.01, placing the transport in the continuum flow regime. Therefore, it is not surprising that even a few bars of applied pressure could not initiate water flows because the capillary force at the graphene opening is high enough to equilibrate the driving pressure. On the contrary, water vapor permeated easily. Our measurements (fig. S5), based on the upright cup method (*18*), yielded many-orders-of-magnitude-higher water vapor transmission rate in comparison with that of breathable textiles (*19*). In order to eliminate the air-water-graphene interface and instigate water flow, we connected water from both sides of the membrane by prewetting the permeate side (micropit). This prewetting process helped initiate water permeation through the membrane even at a slight pressure difference of 250 mbar. After initial flow stabilization for ~5 min, a constant rate of water permeation through the membrane was established (fig. S6). The measured water permeance for the 50-nm pore membranes is five- to sevenfold higher than for conventional ultrafiltration membranes. We attribute these enhancements in water and vapor transport to the atomic thickness and the hydrophobic nature of graphene.

Our observed water flux is on the order of magnitude comparable with a theoretical prediction (Eq. 1) that accounts for the effect of water entrance to an infinitesimally thin porous membrane (Fig. 3) (*13*). The major obstacle in the data acquisition is that graphene could peel off during the water flux measurement (*20*). The water flow funneled toward graphene pores could shear off the stripped graphene from the membrane area and eventually break the membrane. To suppress membrane disintegration, we cut and glued the edge of the active membrane area to the underlying SiN_x support by means of direct Pt deposition using FIB (Fig. 3, inset). The Pt enclosure successfully protected the membranes from peeling.

Permeance and selectivity provide a figure of merit for membrane performance in practical applications. As shown in Fig. 4A, the gas permeance of the porous graphene membrane is orders of magnitude superior to other polymeric (*21*), inorganic (*22*–*24*), graphene oxide (*10*, *11*), and composite membranes. The selectivity is comparable with some conventional polymer or carbon molecular sieve (CMS) membranes (*25*–*27*). For certain applications, permeance becomes more crucial than selectivity, in which large amounts of gases with comparable molar ratios are separated (for example, CO_2 removal

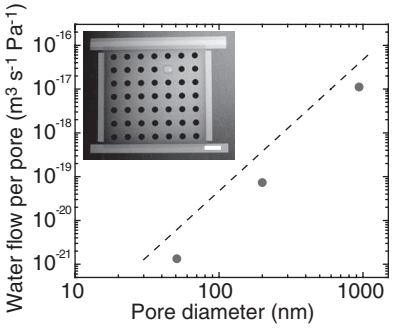

Fig. 3. Water permeation data. Water flow rates per graphene pore for three graphene membranes with different pore sizes, in comparison with the modified Sampson's model prediction (dashed line). (*Inset*) SEM image of the Pt enclosure surrounding the entire membrane area to prevent membrane disintegration (scale bar, 10 μm).

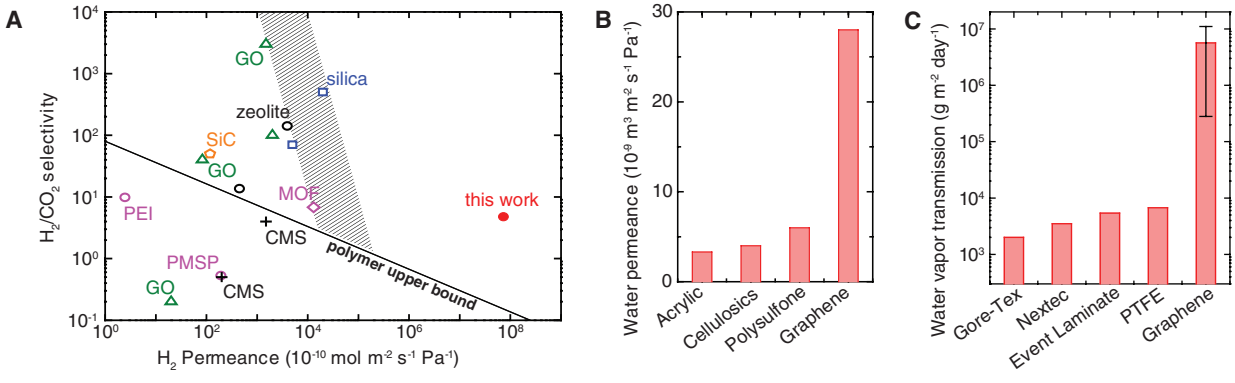

Fig. 4. Membrane figures of merit and comparisons. (**A**) Comparison of H_2/CO_2 gas-separation performances of the porous graphene membranes (7.6-nm pore diameter, with 4.0% porosity) and other membranes: graphene oxide (GO) (*10*, *11*), poly(1-trimethylsilyl-1-propyne) (PMSP) (*25*), polyetherimide (PEI) (*26*) carbon molecular sieve (CMS) (*27*), zeolite (*22*, *23*), silica (*24*), metal-organic framework (MOF) (*34*), and SiC (*35*). (**B**) Water permeance values for porous graphene (50-nm pores, with 4.7% porosity) and other ultrafiltration membranes [acrylic (*31*, *32*), cellulosics, and polysulfone (*31*, *33*)]. (**C**) Comparison of water vapor transmission rate for porous graphene membranes (five 400-nm-pore membrane samples, with porosity ranging from 3.6 to 11.5%) and waterproof-yet-breathable textile membranes [data taken from (*18*, *19*)]. All porous graphene permeance values are based on the total graphene membrane area.

from natural gas) (*28*, *29*). Effusion-based selectivity is also important for separation of gases with large mass differences, such as removal of high carbons from natural gas, flavor selection, and organic solvent separation (*30*).

Our porous graphene membranes also permeate water several times faster than do ultrafiltration membranes such as acrylic (*31*, *32*), cellulosics, and polysulfone (*31*, *33*), reducing the pressure requirements proportionally (Fig. 4B). Despite this high water permeance, when air is present on the other side of the graphene we have not observed any water flow, even up to a few bars of pressure difference. Our porous graphene membrane thus might be an efficient waterproof membrane material, while being highly breathable owing to observed ultrahigh vapor permeances. Indeed, the comparison of the water vapor transmission rate of our graphene membranes with commercial waterproof membranes (*18*, *19*) confirms up to 4 orders of enhancement in breathability (Fig. 4C).

We have engineered large-scale physical perforation of free-standing graphene having controlled pore sizes ranging from <10 nm to 1 μm. Such membranes enable quantitative analysis of mass transport phenomena, such as atmospheric pressure effusion, through atomically thin apertures, revealing distinct effusive, transition, and collective flow regimes. Orders-of-magnitude enhancements are observed for gas, water, and water vapor permeances, compared with the state-of-the-art membranes.

References and Notes

1. X. Li *et al.*, *Science* **324**, 1312–1314 (2009).
2. K. S. Kim *et al.*, *Nature* **457**, 706–710 (2009).
3. K. S. Novoselov *et al.*, *Science* **306**, 666–669 (2004).
4. J. S. Bunch *et al.*, *Nano Lett.* **8**, 2458–2462 (2008).
5. V. Berry, *Carbon* **62**, 1–10 (2013).
6. S. Garaj *et al.*, *Nature* **467**, 190–193 (2010).
7. S. P. Koenig, L. Wang, J. Pellegrino, J. S. Bunch, *Nat. Nanotechnol.* **7**, 728–732 (2012).
8. S. C. O'Hern *et al.*, *ACS Nano* **6**, 10130–10138 (2012).
9. K. Celebi *et al.*, *Nano Lett.* **13**, 967–974 (2013).
10. H. W. Kim *et al.*, *Science* **342**, 91–95 (2013).
11. H. Li *et al.*, *Science* **342**, 95–98 (2013).
12. R. A. Sampson, *Philos. Trans. R. Soc. London A* **182**, 449–518 (1891).
13. K.-K. Tio, S. S. Sadhal, *Appl. Sci. Res.* **52**, 1–20 (1994).
14. M. Knudsen, *Ann. Phys.* **333**, 75–130 (1909).
15. N. Dongari, A. Sharma, F. Durst, *Microfluid. Nanofluid.* **6**, 679 (2009).
16. L. Lund, A. Berman, *J. Appl. Phys.* **37**, 2489 (1966).
17. R. D. Present, A. J. Debethune, *Phys. Rev.* **75**, 1050–1057 (1949).
18. A. Gugliuzza, E. Drioli, *J. Membr. Sci.* **446**, 350–375 (2013).
19. S. A. Brewer, *Rec. Pat. Mat. Sci.* **4**, 1 (2011).
20. T. Yoon, J. H. Mun, B. J. Cho, T.-S. Kim, *Nanoscale* **6**, 151–156 (2013).
21. L. M. Robeson, *J. Membr. Sci.* **320**, 390–400 (2008).
22. Y. Li, F. Liang, H. Bux, W. Yang, J. Caro, *J. Membr. Sci.* **354**, 48–54 (2010).
23. Z. Tang, J. Dong, T. M. Nenoff, *Langmuir* **25**, 4848–4852 (2009).
24. R. M. de Vos, H. Verweij, *Science* **279**, 1710–1711 (1998).
25. K. Nagai, A. Higuchi, T. Nakagawa, *J. Polym. Sci. B* **33**, 289–298 (1995).
26. M. E. Rezac, B. Schöberl, *J. Membr. Sci.* **156**, 211–222 (1999).
27. D. Shekhawat, D. R. Luebke, H. W. Pennline, "A review of carbon dioxide selective membranes: A topical report," Report DOE/NETL 2003/1200 (U.S. Department of Energy, National Energy Technology Laboratory, Pittsburgh, PA, 2003).
28. W. J. Koros, R. Mahajan, *J. Membr. Sci.* **175**, 181–196 (2000).
29. P. Bernardo, E. Drioli, G. Golemme, *Ind. Eng. Chem. Res.* **48**, 4638–4663 (2009).
30. B. Freeman, Y. Yampolskii, I. Pinnau, *Materials Science of Membranes for Gas and Vapor Separation* (Wiley, New York, 2006).
31. A. Mehta, A. L. Zydney, *J. Membr. Sci.* **249**, 245–249 (2005).
32. R. Shukla, M. Balakrishnan, G. P. Agarwal, *Bioseparation* **9**, 7–19 (2000).
33. S. Nakatsuka, A. S. Michaels, *J. Membr. Sci.* **69**, 189–211 (1992).
34. H. Guo, G. Zhu, I. J. Hewitt, S. Qiu, *J. Am. Chem. Soc.* **131**, 1646–1647 (2009).
35. B. Elyassi, M. Sahimi, T. T. Tsotsis, *J. Membr. Sci.* **288**, 290–297 (2007).

Acknowledgments: We appreciate the support from Binnig Rohrer Nanotechnology Center of ETH Zurich and IBM Zurich. J.B. and H.G.P. thank Swiss National Science Foundation for financial support (200021–137964). This work was partially supported by LG Electronics Advanced Research Institute, for which K.C., R.M.W. and H.G.P. are grateful. I.S. is thankful to Swiss National Science Foundation for support in equipment procurement (REquip 206021_133823). H.G.P. appreciates P. Jenny at ETH Zurich for his discussion on Knudsen's minimum. J. Patscheider and L. Bernard at Laboratory for Nanoscale Materials Science of EMPA (Swiss Federal Laboratories for Materials Science and Technology), Switzerland, performed x-ray photoelectron spectroscopy and time-of-flight secondary ion mass spectrometry analyses, and C. Bae and H. Shin at the Department of Energy Science of Sungkyunkwan University, Korea, took high-resolution transmission electron microscope images, for which we are grateful.

Supplementary Materials

www.sciencemag.org/content/344/6181/289/suppl/DC1
Materials and Methods
Figs. S1 to S11
References (*36*–*45*)

28 November 2013; accepted 20 March 2014
10.1126/science.1249097

Missing Gas-Phase Source of HONO Inferred from Zeppelin Measurements in the Troposphere

Xin Li,[1]* Franz Rohrer,[1]* Andreas Hofzumahaus,[1] Theo Brauers,[1]† Rolf Häseler,[1] Birger Bohn,[1] Sebastian Broch,[1] Hendrik Fuchs,[1] Sebastian Gomm,[1] Frank Holland,[1] Julia Jäger,[1] Jennifer Kaiser,[2] Frank N. Keutsch,[2] Insa Lohse,[1] Keding Lu,[1]‡ Ralf Tillmann,[1] Robert Wegener,[1] Glenn M. Wolfe,[2]§ Thomas F. Mentel,[1] Astrid Kiendler-Scharr,[1] Andreas Wahner[1]

Gaseous nitrous acid (HONO) is an important precursor of tropospheric hydroxyl radicals (OH). OH is responsible for atmospheric self-cleansing and controls the concentrations of greenhouse gases like methane and ozone. Due to lack of measurements, vertical distributions of HONO and its sources in the troposphere remain unclear. Here, we present a set of observations of HONO and its budget made onboard a Zeppelin airship. In a sunlit layer separated from Earth's surface processes by temperature inversion, we found high HONO concentrations providing evidence for a strong gas-phase source of HONO consuming nitrogen oxides and potentially hydrogen oxide radicals. The observed properties of this production process suggest that the generally assumed impact of HONO on the abundance of OH in the troposphere is substantially overestimated.

The self-cleansing capacity of the atmosphere is largely dependent on the concentration level of OH (*1*). Because of the complexity of its chemistry, the mechanism forming and recycling OH is not fully understood (*2*). Since its atmospheric detection in the 1970s (*3*), HONO has been thought to be a major precursor of OH, contributing up to 80% of OH formation in the troposphere (*4*–*8*). During daytime, the atmospheric HONO lifetime is determined mainly (≥95%) by photodissociation (R1) into OH and nitrogen monoxide (NO) and to a small extent (≤5%) by its reaction with OH (R2) to form nitrogen dioxide (NO_2) and water (H_2O).

$$HONO + h\nu \rightarrow OH + NO \quad (320\ nm < \lambda < 400\ nm) \quad (R1)$$

$$HONO + OH \rightarrow NO_2 + H_2O \quad (R2)$$

The reverse reaction of R1 is the only important gas-phase reaction known to produce HONO.

$$OH + NO + M \rightarrow HONO + M \qquad M = N_2, O_2, \ldots \quad (R3)$$

Daytime concentrations of HONO measured during ground-based field measurements were typically 5 to 10 times as large as the values calculated from reactions R1 to R3 (*5*, *9*–*12*), indicating the existence of an additional HONO source on the order of 0.1 to 2 parts per billion (ppb) hour^{-1}. Laboratory and field studies suggest that (i) additional daytime HONO production is most likely due to heterogeneous reactions on various surfaces

[1]Institut für Energie-und Klimaforschung: Troposphäre (IEK-8), Forschungszentrum Jülich, Jülich, Germany. [2]Department of Chemistry, University of Wisconsin–Madison, Madison, WI, USA.

*Corresponding author. E-mail: f.rohrer@fz-juelich.de (F.R.), x.li@fz-juelich.de (X.L.)
†Deceased.
‡Present address: College of Environmental Sciences and Engineering, Peking University, Beijing, China.
§Present address: Joint Center for Earth Systems Technology, University of Maryland Baltimore County, Baltimore, MD, USA, and Atmospheric Chemistry and Dynamics Laboratory, NASA Goddard Space Flight Center, Greenbelt, MD, USA.

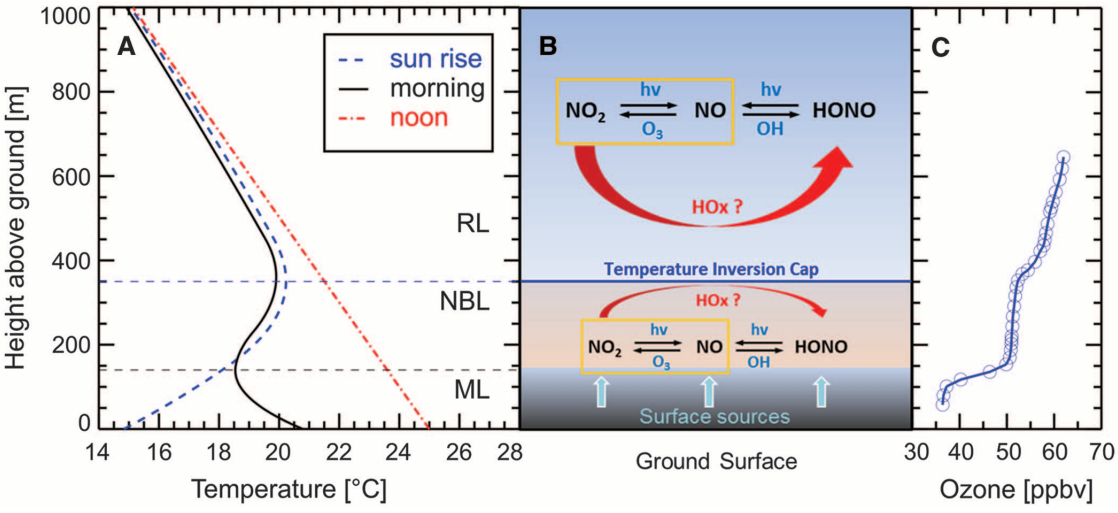

Fig. 1. Break-up of the nocturnal boundary layer during morning hours. (**A**) Conceptual representation of the vertical structure of temperature in the atmosphere up to 1 km height above ground. Blue, black, and red lines represent the situation at sunrise, during the morning, and around noon, respectively. Each day after sunset, Earth's surface cools due to thermal radiative emission. Because air temperature does not cool as fast, a positive vertical temperature gradient evolves typically in a 300-m height range. This is called temperature inversion. As a result, the PBL is divided into two sublayers, i.e., the NBL and the RL. At sunrise, these processes are reversed. The sun heats up the surface over the course of several hours, leading to the formation of a turbulent ML. Shortly before noon, this heating process has increased the surface temperature enough so that a negative temperature gradient is preserved throughout the PBL. After that, the ML, NBL, and RL become well mixed. (**B**) HONO formation pathways in different sublayers of the PBL. (**C**) Observed O_3 vertical profile around sunrise (i.e., 5:03 UTC) on 12 July 2012 at San Pietro Capofiume, Italy.

close to the ground—e.g., on snowpacks (*13*), on soils (*14*–*16*), and on forest canopies (*17*)—whereas (ii) reactions of excited NO_2 with H_2O (*18*), photolysis of orthonitrophenols (*19*), and reactions on aerosol surfaces (*20*, *21*) make only moderate contributions to daytime HONO formation. The overall affect of the proposed HONO sources in the troposphere remains widely unknown, however, due to the lack of measurements of HONO and its sources and sinks at higher altitudes above Earth's surface. During recent HONO gradient studies, unexpected high HONO concentrations [15 to 200 parts per trillion (ppt)] were observed for higher altitudes (300 to 1000 m) above ground (*12*, *22*, *23*). No strong HONO gradient was found for daytime periods when convective mixing in the atmosphere was masking the true point of origin of any HONO source. Therefore, the question arises whether the proposed HONO sources can explain the elevated HONO concentrations at higher altitudes in the troposphere.

The vertical structure of the troposphere, which influences the HONO distribution, is determined by thermal processes and wind shear. (In the following, we discuss only thermal processes because the Zeppelin flights gave no indication of a substantial influence of wind shear on the observations of trace species. This finding is certainly biased by flight restrictions of the Zeppelin at large wind speeds.) The lowest 1 to 2 km of the atmosphere is called planetary boundary layer (PBL). During afternoon hours, the PBL is well mixed throughout by convective turbulence, which is driven by solar heating of Earth's surface. In the night, the PBL develops sublayers (*24*), as a result of cooling of the surface, that even outlive for several hours the renewed surface heating after sunrise. The resulting evolution of air temperatures during morning hours is shown in Fig. 1A. A temperature inversion separates the

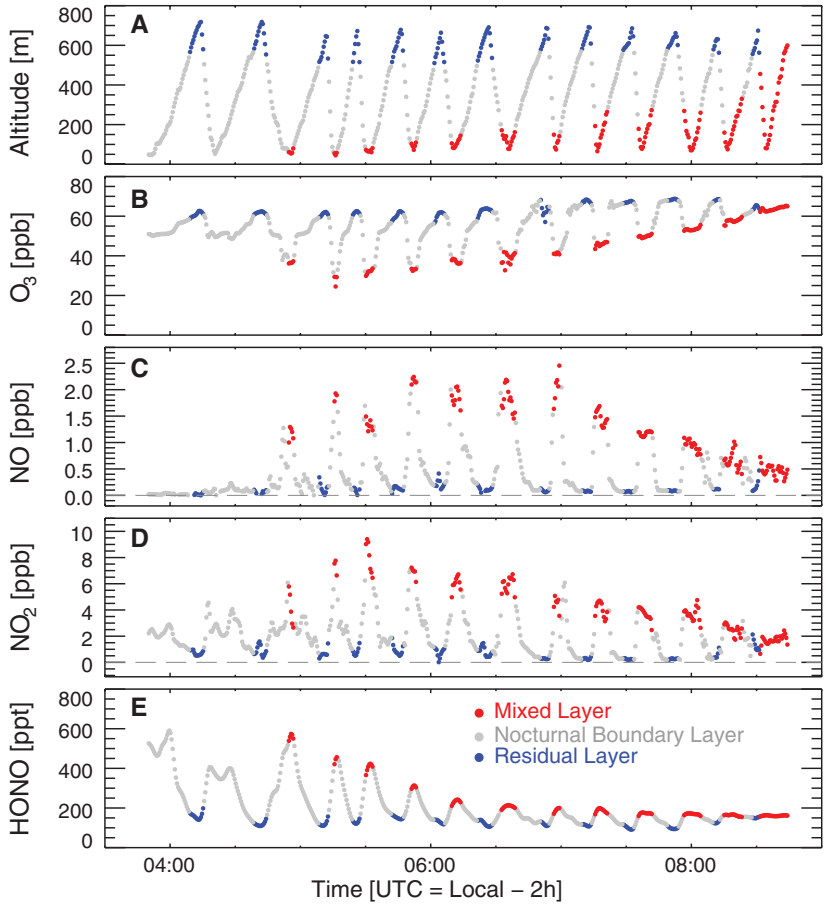

Fig. 2. Observations during profile flights on 12 July 2012 at San Pietro Capofiume, Italy. The flight altitude is shown in (**A**). (**B** to **E**) display observed O_3, NO, NO_2, and HONO concentrations at different altitudes. The data shown here are averaged or interpolated to the time step of the HONO measurements (30 s). The blue, gray, and red dots represent observations in the RL, NBL, and ML, respectively, as indicated by the measured O_3 concentrations. The onset of the development of the ML above 50 m is characterized by the steep drop of O_3 concentration in the NBL around 5:00 UTC, which is caused by deposition and reaction with freshly emitted NO (Fig. 2C) at the surface.

nocturnal boundary layer (NBL) from the residual layer (RL) above almost until noon. This inversion restricts vertical mixing of air constituents, as indicated by a measured O_3 profile (Fig. 1C), and isolates the RL from influences of Earth's surface (like deposition or titration by NO in case of O_3) as long as the temperature inversion is maintained. Thus, for several hours during each morning, the RL offers the unique opportunity to study photochemical processes—for example, those of HONO—undisturbed by emission or deposition processes near the surface.

The airship Zeppelin "New Technology" (NT) is an ideal platform to investigate the chemistry and dynamics of the PBL. During the PEGASOS (Pan-European Gas Aerosol Climate Interaction Study) 2012 field campaign in the Po Valley in Northern Italy, we performed vertical-profile measurements of trace gases (including HONO, NO, OH, and O_3), aerosols, photolysis frequencies, and meteorological parameters in the lower troposphere (see supplementary materials for details). The layered structure of the PBL was always clearly seen in the vertical distributions of the observed trace gases and temperatures—for example, on 12 July 2012 at San Pietro Capofiume (Fig. 2 and figs. S2 and S3). In this case, the concentration of O_3 remained essentially constant in the RL during the whole morning flight, whereas in the mixed layer (ML) it was influenced by processes at the surface such as deposition or titration by NO emitted at ground. With increasing irradiation, the surface temperature and height of the ML increased. The incorporation of air from the NBL leads to a rise in O_3 inside the ML. During the growth of the ML, the NBL acts as a buffer zone between ML and RL. O_3 concentrations in the RL remain stable and higher than in the NBL and ML. This implies that the RL is decoupled from the ML and is not influenced by emissions or deposition at Earth's surface. Complete mixing of the three layers is indicated by the disappearance of the vertical O_3 gradient (after 8:15 UTC).

During this flight, HONO concentrations in the RL remained nearly constant (150 ppt) while the RL stayed decoupled from the ML (Fig. 2D). Higher HONO concentrations were observed in the ML (200 to 600 ppt) due to the well-known accumulation of HONO via slow, nighttime NO_2 conversion at the surface (*3*, *4*). With increasing solar radiation, HONO concentrations in the ML started to decrease, but they remained stable in the RL. Analogous to O_3, the concentration difference of HONO between the three layers vanished when the ML had fully developed. The decrease of HONO in the ML after sunrise is well known (*3*) and caused by photolysis (R1). The observation that HONO in the RL was not depleted by photolysis, but rather stayed constant, is unexpected and implies the existence of a compensating HONO source after sunrise. HONO undepleted by photolysis was also found during our former observations onboard Zeppelin (*22*) and during airborne measurements in the United States (*23*).

This result is supported quantitatively by box-model simulations of HONO in the RL (see the supplementary materials for details). The calculated concentrations show the expected depletion by photolysis and reach a level smaller by a factor of 30 than the experimental data (Fig. 3A). When we include an additional HONO source in the model with a source strength S_{HONO} proportional to the photolysis frequency of HONO, J_{HONO}, we find good agreement between modeled and measured HONO concentrations (Fig. 3A). The required source strength (up to 0.7 ppb $hour^{-1}$) and its apparent light dependence are consistent with findings from ground-based field studies (*5*, *6*, *10*, *11*, *17*). However, in contrast to mixed-layer studies, we can exclude heterogeneous reactions at the ground as the missing HONO source in the RL. Furthermore, our estimates demonstrate that the aerosol and NO_2 abundances are not expected to allow a substantial heterogeneous NO_2 to HONO conversion given the measured aerosol surface-area density ($S_a \leq 1.8 \times 10^{-6}$ cm^2 cm^{-3}) and NO_2 concentration (≤500 ppt) in the RL. If such a conversion dominates the HONO production in the RL, S_{HONO} should depend on NO_2 concentration, aerosol S_a, and relative humidity (RH) (*25*). However, given the observed almost-constant aerosol surface area, RH = 60%, and decreasing NO_2 concentrations (500 to 200 ppt) before 8:00 UTC in the RL (fig. S4), such dependences cannot be expected. Based on the measured values of S_a and NO_2 concentration, the NO_2 to HONO conversion would require a conversion coefficient for NO_2 of 0.02, which is 2 to 4 orders of magnitude larger than reported values (10^{-6} to 10^{-4}) (*20*, *21*, *25*, *26*). Thus, our observations point to an unknown gas-phase source of HONO in the RL.

This unknown HONO source seems to dominate the overall HONO formation throughout

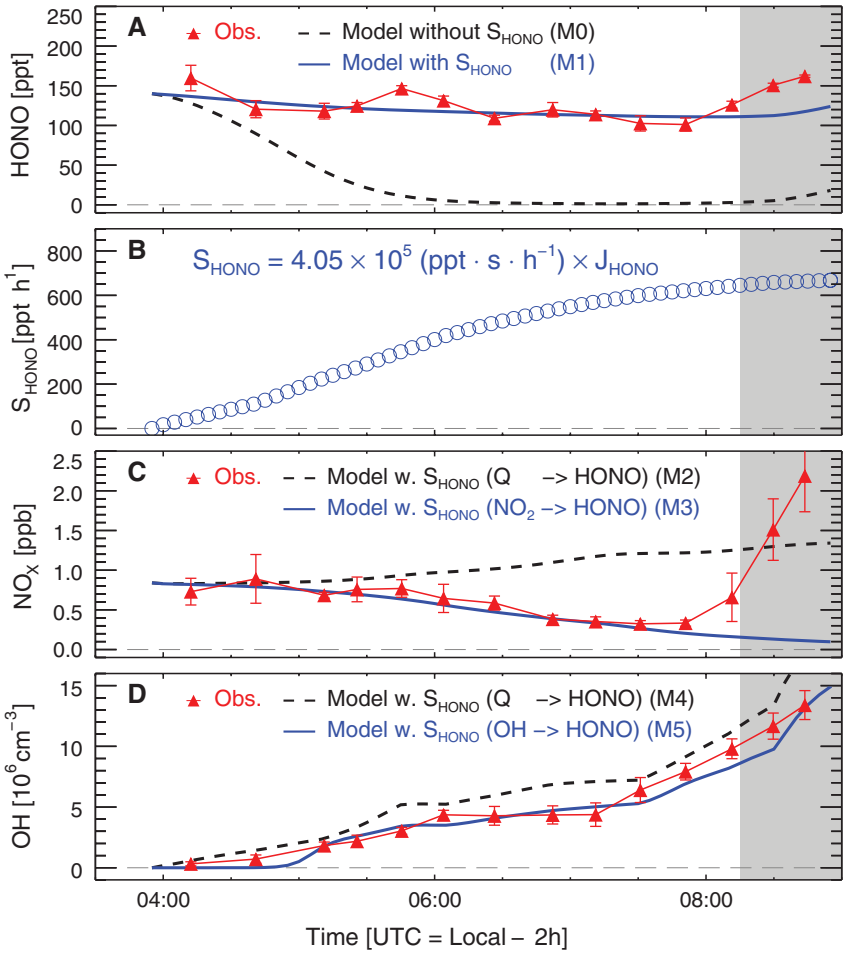

Fig. 3. Results of box model simulations for the residual layer on 12 July 2012 at San Pietro Capofiume, Italy. The red triangles represent the observed average concentrations in the residual layer for each encounter of the RL, the error bars the corresponding ±1 SDs. The gray shaded area highlights the time period when the PBL is well mixed. (**A**) HONO simulations without (M0) and with (M1) an assumed additional HONO source having the strength S_{HONO} shown in (**B**). (**C**) NO_X simulations assuming an external (M2: reservoir Q → HONO) or internal (M3: NO_2 → HONO) HONO source having the strength S_{HONO}. OH is prescribed by measured data. (**D**) OH simulations assuming an external (M4: reservoir Q → HONO) or internal (M3: OH → HONO) HONO source having the strength S_{HONO}. NO_X is prescribed by measured data. The model scenarios M0 to M5 are described in table S3 in the supplementary materials.

the PBL for daylight conditions. The measured HONO data (Fig. 3A) at the altitude of the previously existing RL show a slight increase of about 25% after the PBL becomes completely mixed (after 8:15 UTC). The increase is most likely caused by formation of HONO at the ground, which is vertically distributed by turbulence. Accordingly, we estimate the contribution of surface processes to the HONO formation in the PBL in this region to be around 25%; most HONO is produced by the unknown gas-phase source. Based on airborne HONO measurements in the PBL above a forest in Michigan, USA, similar findings were reported (*23*) with an estimated contribution of surface sources between 16 and 27% to the overall concentration of HONO.

The increase of S_{HONO} after sunrise (Fig. 3B) could be caused by photolysis of a precursor directly producing HONO, or it could indicate a reaction of light-dependent precursors producing HONO with a rate scaling (accidentally) with J_{HONO}. Furthermore, the HONO source could be either a process that consumes NO_X and/or HO_X (internal source) or a reaction releasing HONO without consumption of NO_X or HO_X [external source, e.g., photolysis of nitrite/nitrate aerosols (*17*) or photolysis of orthonitrophenol (*19*)]. Following reaction R1, an external HONO source would lead to an increase of ambient NO_X and OH under daylight conditions. If the observed HONO concentration is approximated by introducing an appropriate external HONO source (Fig. 3B), the model significantly overestimates the observed NO_X concentrations when HONO photolysis becomes effective (Fig. 3C, M2, after 06:00 UTC). The use of an internal source, however, can consistently reproduce measured HONO and NO_X as long as the RL remains isolated (Fig. 3C, M3). For OH, an external source leads to a small (30%) overprediction of the OH observations (Fig. 3D, M4). This discrepancy is not significant, if the accuracy (14%) of the measurement and the estimated model error (30%) are taken into account. If we assume an internal source consuming OH (or HO_2) for the production of HONO, the model result becomes almost equal to the measurements (Fig. 3D, M5). Thus, the sensitivity tests point to an internal source that requires NO_X and possibly HO_X.

As a hypothesis, we assume that HONO is formed in the reaction between a HO_X and a NO_X species without direct involvement of light. For this reason, we have calculated the rates of known reactions of HO_X with NO_X (fig. S12). The homogeneous reaction between NO_2, H_2O, and NH_3 is speculated to be important for conditions with high NH_3 concentration (30 ppb to 100 parts per million) (*27*). Such high NH_3 concentrations are not likely for the investigated RL in this study, so this process is not included in our considerations. Only the HO_2 + NO and HO_2 + NO_2 reactions have sufficiently fast turnover rates with the potential to balance the observed HONO loss rate (J_{HONO} × [HONO]). The well-studied HO_2 + NO reaction does not have a known pathway producing HONO. On the other hand, the reaction HO_2 + NO_2 has been postulated as a HONO source since the 1970s (*28*). Only a few laboratory experiments were performed investigating the HO_2 + NO_2 reaction products (table S5). These studies are conclusive in terms of negligible HONO yields under dry conditions which, however, certainly does not represent the lower troposphere. It is known that ~30% of HO_2 is present as a $HO_2 \cdot H_2O$ complex (*29*) in the lower troposphere, which has a different chemical behavior than HO_2. $HO_2 \cdot H_2O$ can react 3 to 4 times faster with NO_2 than HO_2 (*30*), but the products of this reaction were not measured. If we add in the model (i) the known equilibrium between HO_2 and $HO_2 \cdot H_2O$ and (ii) the reaction of $HO_2 \cdot H_2O$ with NO_2 as measured (*30*), and further assume that the reaction converts NO_2 to HONO with a yield of 100%, then the model (M6) reproduces the observed HONO, NO_X, OH, and HO_2 within experimental uncertainties (Fig. 4). The assumed mechanism is therefore consistent with the inferred daytime source of HONO.

Relatively high and constant HONO concentrations in the sunlit RL were observed during all Zeppelin flights of the PEGASOS 2012 field campaign in Italy (table S2 and figs. S13 to S15). The inferred daytime gas-phase source of HONO in the RL is of importance for the whole PBL and complicates the understanding of HONO chemistry in the mixed layer. More field and laboratory research is clearly required to understand all the relevant processes forming HONO in the troposphere. Our study suggests that the traditional understanding of the impact of HONO on tropospheric chemistry may need revision. If the missing gas-phase HONO source consumes HO_X in addition to the confirmed consumption of NO_X, then HONO photolysis would result in a cycle with zero net production of these species. That would imply that the photolysis of HONO as a primary source of tropospheric OH, which is thought

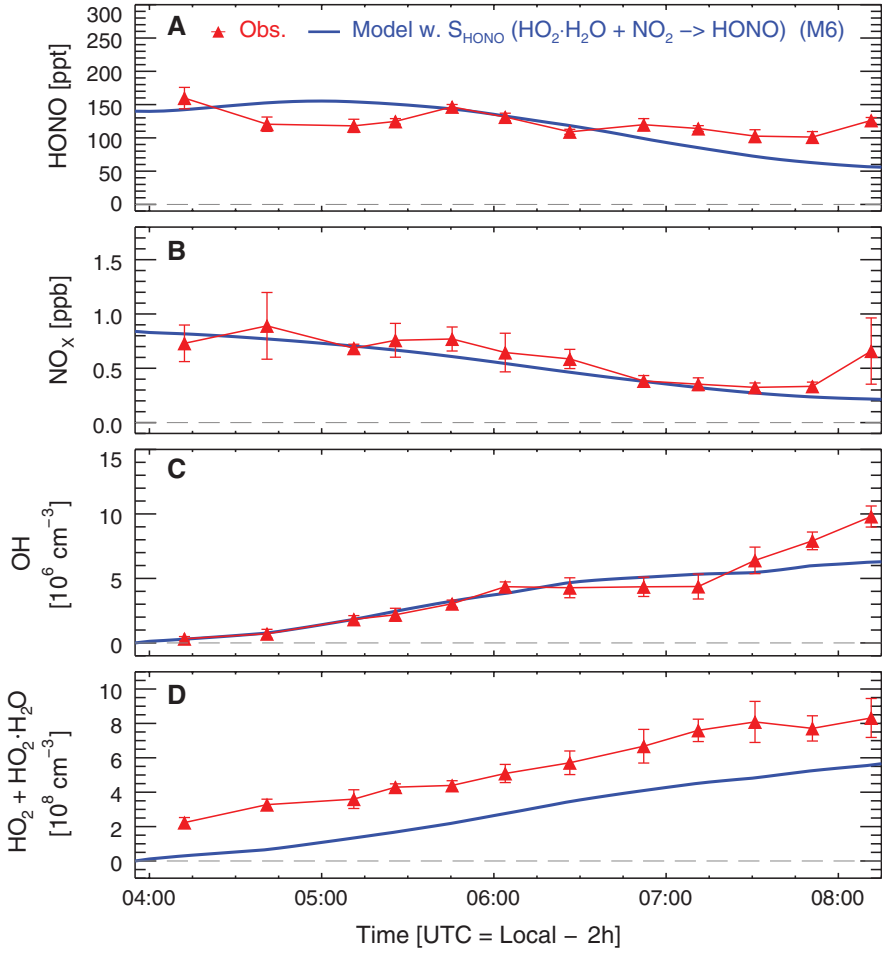

Fig. 4. Observed and calculated concentrations in the residual layer for 12 July 2012 at San Pietro Capofiume, Italy. (**A** to **D**) The red triangles represent the observed average concentrations in the residual layer for each encounter of the RL, the error bars the corresponding ±1 SDs. Accuracies of the experimental data are given in table S1. The constant difference between model and measurement results in (D) can be explained by the uncertainty of the offset correction of the measured HO_2 data (see supplementary materials). The blue line in each panel represents model results under the assumption of additional HONO production (S_{HONO}) by the reaction between the $HO_2 \cdot H_2O$ complex and NO_2 (model scenario M6).

(*4*–*6*, *8*) to contribute up to 80% to the primary OH formation in the continental PBL, is generally overestimated.

References and Notes

1. B. J. Finlayson-Pitts, J. N. Pitts, *Chemistry of the Upper and Lower Atmosphere: Theory, Experiments and Applications* (Academic Press, San Diego, 2000), first ed.
2. A. Hofzumahaus *et al.*, *Science* **324**, 1702–1704 (2009).
3. U. Platt, D. Perner, G. W. Harris, A. M. Winer, J. N. Pitts Jr., *Nature* **285**, 312–314 (1980).
4. B. Alicke *et al.*, *J. Geophys. Res.* **108**, (D4), 8247 (2003).
5. J. Kleffmann *et al.*, *Geophys. Res. Lett.* **32**, L05818 (2005).
6. K. Acker *et al.*, *Geophys. Res. Lett.* **33**, L02809 (2006).
7. P. S. Monks *et al.*, *Atmos. Environ.* **43**, 5268–5350 (2009).
8. Y. F. Elshorbany *et al.*, *Atmos. Environ.* **44**, 5383–5394 (2010).
9. A. Neftel, A. Blatter, R. Hesterberg, T. Staffelbach, *Atmos. Environ.* **30**, 3017–3025 (1996).
10. M. Sörgel *et al.*, *Atmos. Chem. Phys.* **11**, 10433–10447 (2011).
11. X. Li *et al.*, *Atmos. Chem. Phys.* **12**, 1497–1513 (2012).
12. K. W. Wong *et al.*, *Atmos. Chem. Phys.* **12**, 635–652 (2012).
13. X. Zhou *et al.*, *Geophys. Res. Lett.* **28**, 4087–4090 (2001).
14. K. Stemmler, M. Ammann, C. Donders, J. Kleffmann, C. George, *Nature* **440**, 195–198 (2006).
15. H. Su *et al.*, *Science* **333**, 1616–1618 (2011).
16. R. Oswald *et al.*, *Science* **341**, 1233–1235 (2013).
17. X. Zhou *et al.*, *Nat. Geosci.* **4**, 440–443 (2011).
18. S. Li, J. Matthews, A. Sinha, *Science* **319**, 1657–1660 (2008).
19. I. Bejan *et al.*, *Phys. Chem. Chem. Phys.* **8**, 2028–2035 (2006).
20. M. Ammann *et al.*, *Nature* **395**, 157–160 (1998).
21. K. Stemmler *et al.*, *Atmos. Chem. Phys.* **7**, 4237–4248 (2007).
22. R. Häseler, T. Brauers, F. Holland, A. Wahner, *Atmos. Meas. Tech. Discuss.* **2**, 2027–2054 (2009).
23. N. Zhang *et al.*, *Geophys. Res. Lett.* **36**, L15820 (2009).
24. R. B. Stull, *An Introduction to Boundary Layer Meteorology* (Kluwer Academic Publishers, 1988).
25. R. Bröske, J. Kleffmann, P. Wiesen, *Atmos. Chem. Phys.* **3**, 469–474 (2003).
26. M. Ndour *et al.*, *Geophys. Res. Lett.* **35**, L05812 (2008).
27. B. Zhang, F.-M. Tao, *Chem. Phys. Lett.* **489**, 143–147 (2010).
28. R. Simonaitis, J. Heicklen, *J. Phys. Chem.* **78**, 653–657 (1974).
29. S. Aloisio, J. S. Francisco, *J. Phys. Chem. A* **104**, 6212–6217 (2000).
30. S. P. Sander, M. E. Peterson, *J. Phys. Chem.* **88**, 1566–1571 (1984).

Acknowledgments: This work is within the PEGASOS project, which is funded by the European Commission under the Framework Programme 7 (FP7-ENV-2010-265148). We gratefully acknowledge the efforts that the Zeppelin NT pilots and ground crews made to this work. We also acknowledge Zeppelin Luftschifftechnik (ZLT) and Deutsche Zeppelin Reederei (DZR) for their cooperation. J.J., R.W., I.L., and B.B. thank Deutsche Forschungsgemeinschaft for funding from the priority program HALO (WE-4384/2-2 and BO1580/4-1). J.K., G.M.W., and F.N.K. thank M. Cazorla for helping with the calibration of the HCHO measurements and NDF-AGS (1051338) and Forschungszentrum Jülich for support. Our colleague Dr. Theo Brauers, sadly, passed away on 21 February 2014. We would like to take this opportunity to express our sincere appreciation for his excellent work.

Supplementary Materials

www.sciencemag.org/content/344/6181/292/suppl/DC1
Materials and Methods
Figs. S1 to S13
Tables S1 to S6
References (*31*–*53*)

26 November 2013; accepted 25 March 2014
10.1126/science.1248999

Assemblage Time Series Reveal Biodiversity Change but Not Systematic Loss

Maria Dornelas,[1]* Nicholas J. Gotelli,[2] Brian McGill,[3] Hideyasu Shimadzu,[1,4] Faye Moyes,[1] Caya Sievers,[1] Anne E. Magurran[1]

The extent to which biodiversity change in local assemblages contributes to global biodiversity loss is poorly understood. We analyzed 100 time series from biomes across Earth to ask how diversity within assemblages is changing through time. We quantified patterns of temporal α diversity, measured as change in local diversity, and temporal β diversity, measured as change in community composition. Contrary to our expectations, we did not detect systematic loss of α diversity. However, community composition changed systematically through time, in excess of predictions from null models. Heterogeneous rates of environmental change, species range shifts associated with climate change, and biotic homogenization may explain the different patterns of temporal α and β diversity. Monitoring and understanding change in species composition should be a conservation priority.

Habitat destruction, pollution, and overharvesting, as well as climate change and invasive species, have led to conspicuous reductions in biological diversity (*1*). Globally, increasing numbers of species are under threat (*2*), populations of vulnerable taxa are declining (*3*), and ecosystem function is changing as a result (*4*). Although these large-scale patterns emerge from processes that are based on local community structure, as yet there is no comprehensive analysis of how temporal change in ecological assemblages contributes to this global picture. Because the implementation of conservation and management decisions is typically at the scale of local to regional ecosystems (*5*, *6*), knowledge of biodiversity change within assemblages is essential to inform policy. A comparative analysis of change across taxa, biomes, and geographic regions also provides insights into the mechanisms involved. Here, we use a definition of biodiversity that includes components of species richness, composition, and relative abundance of species. We use standardized biodiversity monitoring of assemblages over years and decades to assess global patterns of temporal change in species diversity.

We quantified change in biodiversity through time by two measures: temporal trends in α diversity and temporal β diversity (*7*). Temporal α diversity is a measure of diversity within a sample. It can be measured as species richness or with related diversity metrics that take species abundances into account. To measure temporal change in α diversity, we calculated, for each time series, the slope of the long-term relationship between diversity and time. Typically, β diversity is used to compare the composition of different communities in space, but it can also be used to compare the composition of a single community through time. Temporal β diversity (temporal turnover) quantifies differences in species composition between two (or more) samples separated in time. Temporal turnover can be measured with metrics of similarity to track changes in species identities (and sometimes their abundances) through time, either by comparing adjacent sampling periods or with reference to a single baseline sample or time period. Because turnover metrics incorporate shifts in species composition, they potentially provide a more sensitive indicator of community change (*8*) than does α diversity.

Given widespread evidence of habitat change (*9*), abnormally high extinction rates (*10*), and documented declines of many species (*2*, *3*), we predicted that most assemblages would exhibit a decrease in α diversity through time, although the pattern and extent of change may differ among taxonomic groups, climatic regions, and marine or terrestrial realms and with spatial scale (*11*). For example, there is no evidence of consistent loss of biodiversity among terrestrial plants (*12*). Similarly, as a consequence of long-term changes in species composition, we expected increases in temporal β diversity measured relative to an early baseline sample.

To quantify biodiversity change, we gathered all data sets we could find that met a priori quality criteria (*13*) for standardized, long-term quantitative sampling. This collection includes more than 6.1 million species occurrence records from 100 individual time series. There are 35,613 species represented, encompassing mammals, birds, fish, invertebrates, and plants. The geographical distribution of study locations is global, and includes marine, freshwater, and terrestrial biomes, extending from the polar regions to the tropics in

[1]Centre for Biological Diversity and Scottish Oceans Institute, School of Biology, University of St. Andrews, St. Andrews, Fife KY16 9TH, UK. [2]Department of Biology, University of Vermont, Burlington, VT 05405, USA. [3]School of Biology and Ecology, Sustainability Solutions Initiative, University of Maine, Orono, ME 04469, USA. [4]Department of Mathematics, Keio University, 3-14-1 Hiyoshi Kohoku, Yokohama 223-8522, Japan.
*Corresponding author. E-mail: maadd@st-andrews.ac.uk

both hemispheres (Fig. 1). The collective time interval represented by these data is from 1874 to the present, although most data series are concentrated in the past 40 years (Fig. 2). (See table S1 for a full description of the data sets used in the analysis and their sources.) We measured temporal α diversity with 10 metrics, including species richness, and temporal β diversity with four metrics, including the Jaccard similarity index. A strength of our analysis is that we calculate all metrics from the original data, rather than relying on published summary statistics, and thus are able to standardize sampling effort within each time series. Details of statistical standardization of data sets, choice of α diversity metrics, and null distributions for β diversity metrics based on Markov chain Monte Carlo (MCMC) methods and neutral model analyses are described in (*13*).

Surprisingly, we did not detect a consistent negative trend in species richness (Fig. 2A) or in any of the other metrics of α diversity (fig. S1). The overall slope (estimated by allowing each study to have a different intercept, but constraining all studies to have the same slope) is statistically indistinguishable from zero (Fig. 2). However, not all data sets have constant species richness. In a mixed model in which both the

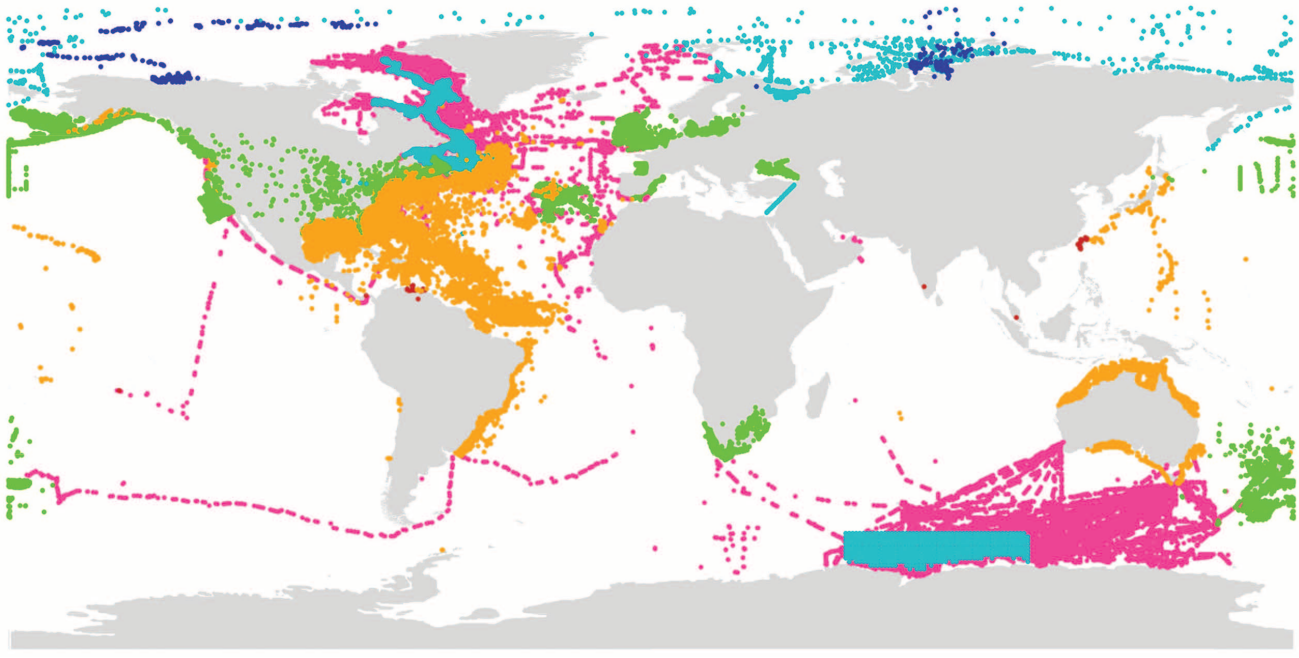

Fig. 1. Distribution of the survey sites included in our analysis. Data sets are color-coded to reflect their climatic region: pink, global; royal blue, polar; turquoise, polar-temperate; green, temperate; gold, temperate-tropical; red, tropical. See table S1 for details and sources of the data sets.

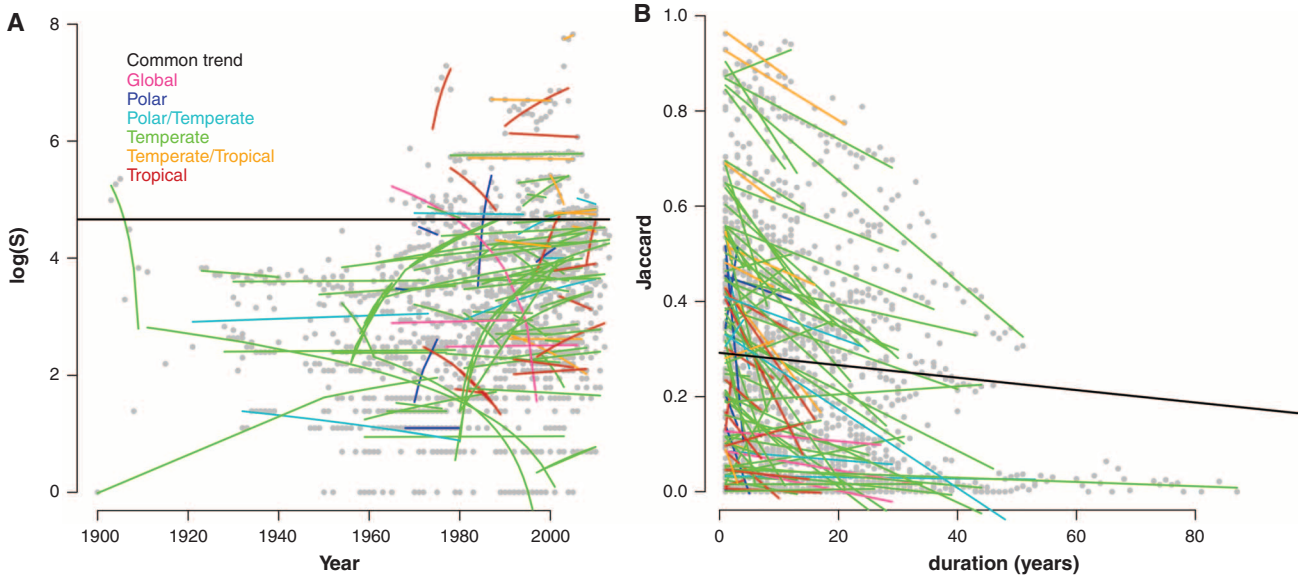

Fig. 2. Temporal change in α diversity and temporal β diversity. (**A** and **B**) Temporal change in species richness (A) and species composition (B) as measured by Jaccard similarity between each sample and the first sample in the time series. Data points are represented by gray circles and models fitted by solid lines. The black line corresponds to a model in which a single slope, but different intercepts, were fitted to all the time series, and is represented here with the mean intercept. The colored lines correspond to a model where each time series had a different slope and intercept. Color coding corresponds to Fig. 1. Figure S10 presents a similar analysis for a different approach to rarefaction.

slope and the intercept are allowed to vary for each time series, slopes for species richness differ among assemblages, but do not exhibit systematic deviations. The variation cancels out because there are approximately equal numbers of negative and positive slopes (41 and 59, respectively), and the distribution of slopes is centered around zero, with the majority of slopes being statistically very close to zero (65 of 100 time series; Fig. 3A). This pattern was also observed for short-term changes rather than long-term linear trends: Of 1557 measurements of species richness in two consecutive times, 629 (40%) increased, 624 (40%) decreased, and 304 (20%) did not change (fig. S2). Collectively, these analyses reveal local variation in temporal α diversity but no evidence for a consistent or even an average negative trend.

The variability in slopes of α diversity could be explained by spatial, temporal, and biological attributes of each of the time series. However, for all measures of α diversity, slope is not a significant function of total species richness, extent of the spatial distribution of samples, starting date, or duration of the time series (figs. S3 and S4). Average slopes estimated for the marine and terrestrial time series are not significantly different from zero (fig. S5). Time series for terrestrial plants exhibit, on average, a positive slope for species richness, in contrast to Vellend *et al*. (*12*), who found no consistent change. There are no significant patterns for other taxonomic groups. An analysis of slopes by climatic regions reveals that temperate time series have a significantly positive trend, and time series sampled at a global scale show a significantly negative trend (fig. S5). Tropical time series also have a negative slope, but it is not significantly different from zero.

In contrast to species richness and other measures of α diversity, species temporal turnover as measured by the Jaccard similarity index and other measures of β diversity (fig. S6) exhibits consistent long-term changes (Figs. 2B and 3B). Specifically, community similarity measured as Jaccard's index between an ensuing year and the first year of sampling (the time-series baseline) decreases in 79 out of 100 the time series, with a slope of −0.01 on average. Because Jaccard's similarity is bounded between 0 and 1, a 0.01 slope means change in community composition per decade of 10% of the species (Fig. 2B). This result is robust if the last census point is used as the baseline (fig. S7). A model with constant overall slope and different intercept for each time series (and with the time axis rescaled relative to each time-series baseline) is also negative. Turnover slopes are therefore almost uniformly negative, which is indicative of systematic change in community composition since the initial census point.

Even in a stochastic time series, some degree of turnover is to be expected because of temporal autocorrelation. However, the patterns of turnover in these time series are more pronounced and negative than what would be expected from simple temporal autocorrelation. Specifically, MCMC simulations of species-specific extinction and colonization produce slopes in turnover of –0.000013 on average, with confidence intervals straddling zero, and an approximately 50-50 distribution of positive and negative slopes (*13*) (fig. S8). Similarly, neutral model simulations incorporating species abundance show change in similarity two orders of magnitude lower than we observed (*13*) (fig. S9). The decrease in community similarity observed in our analysis is therefore not a simple consequence of drift and autocorrelation caused by a colonization-extinction Markov model or by a model of neutral dynamics.

These time series collectively exhibit no systematic change in temporal α diversity, although temperate assemblages show, on average, a positive trend in α diversity, whereas at the global scale we detected a negative trend. Moreover, across all climatic regions, realms, and taxonomic groups, temporal β diversity is increasing relative to the baseline (initial) sample. There are several reasons why α diversity may remain constant while temporal β diversity is consistently increasing.

One potential driver is that intensification of trade and transport, combined with the rapid increase in invasions of exotic taxa, is leading to the homogenization of species composition at local scales (*14*). Although homogenization may lead to a global loss of species, α diversity at local scales may stay constant or even increase as invaders replace residents and β diversity changes through time (*11*). This was the mechanism that Elton highlighted when he first voiced concerns about global biodiversity loss (*15*). Additional forces that might contribute to these contrasting patterns of α and β diversity include poleward shifts in geographic ranges as species respond to climate change (*16*). Moreover, contemporary habitat destruction and species loss is higher in tropical versus temperate regions (*9*), which is consistent with assessments of change in temporal α diversity in terrestrial plants (*12*) and population trends of vertebrates (*17*).

Our results suggest that local and regional assemblages are experiencing a substitution of their taxa, rather than systematic loss. This outcome may in part reflect the fact that most of the available data are from the past 40 years, which highlights concerns over the problem of a "shifting baseline" in diversity monitoring (*18*). Nonetheless, we show that at these temporal and spatial scales there is no evidence of consistent or accelerating

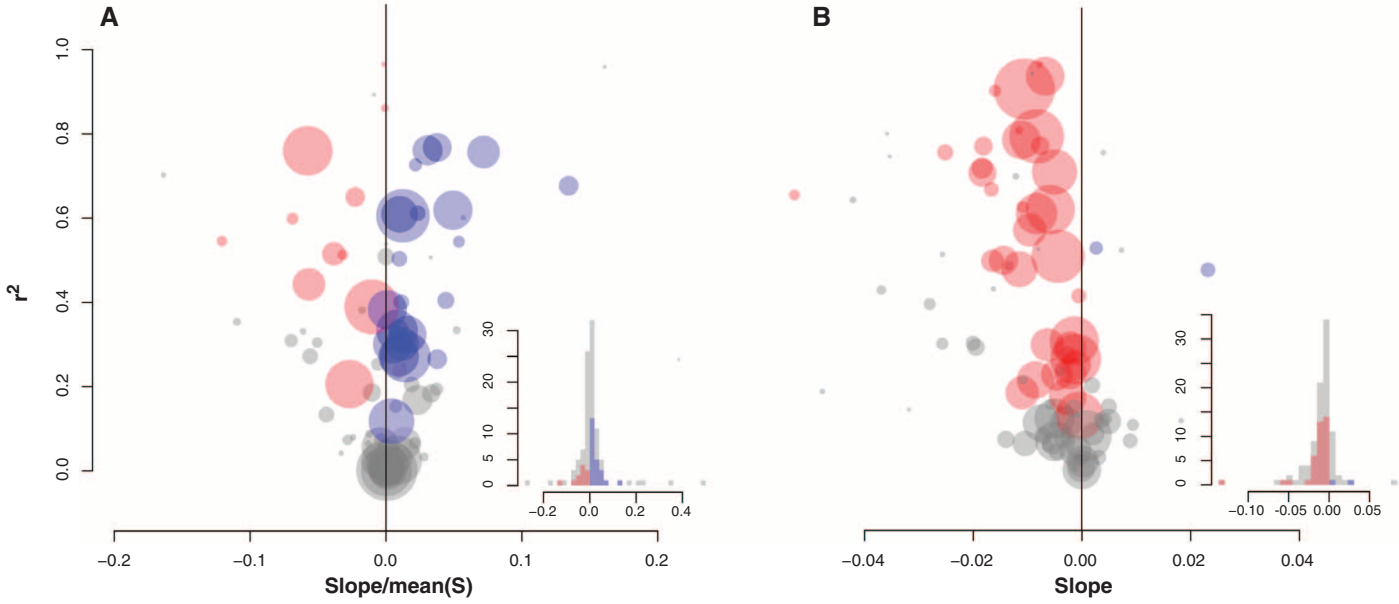

Fig. 3. Trends in α diversity and temporal β diversity. (**A** and **B**) Slope estimate distributions for species richness (A) and Jaccard similarity (B). Slope estimates (horizontal axis), coefficient of determination r^2 (vertical axis), and number of data points in time series (bubble size) are shown for each of the data sets. Bubbles are color-coded as blue (positive slope), red (negative slope), and gray (nonsignificantly different from 0) (*13*).

loss of α diversity. Most important, changes in species composition usually do not result in a substitution of like with like, and can lead to the development of novel ecosystems (*19*). For example, disturbed coral reefs can be replaced by assemblages dominated by macroalgae (*20*) or different coral species (*21*); these novel marine assemblages may not necessarily deliver the same ecosystem services (such as fisheries, tourism, and coastal protection) that were provided by the original coral reef (*22*).

Our core result—that assemblages are undergoing biodiversity change but not systematic biodiversity loss (Figs. 2 and 3)—does not negate previous findings that many taxa are at risk, or that key habitats and ecosystems are under grave threat. Neither is it inconsistent with an unfolding mass extinction, which occurs at a global scale and over a much longer temporal scale. The changing composition of communities that we document may be driven by many factors, including ongoing climate change and the expanding distributions of invasive and anthrophilic species. The absence of systematic change in temporal α diversity we report here is not a cause for complacency, but rather highlights the need to address changes in assemblage composition, which have been widespread over at least the past 40 years. Robust analyses that acknowledge the complexity and heterogeneity of outcomes at different locations and scales provide the strongest case for policy action. There is a need to expand the focus of research and planning from biodiversity loss to biodiversity change.

References and Notes

1. Millennium Ecosystem Assessment, *Ecosystems and Human Well-being: Synthesis* (2006); www.millenniumassessment.org/documents/document.356.aspx.pdf.
2. S. H. M. Butchart *et al.*, *Philos. Trans. R. Soc. London Ser. B* **360**, 255–268 (2005).
3. J. Loh *et al.*, *Philos. Trans. R. Soc London Ser. B* **360**, 289–295 (2005).
4. B. J. Cardinale *et al.*, *Nature* **486**, 59–67 (2012).
5. B. F. Erasmus, S. Freitag, K. J. Gaston, B. H. Erasmus, A. S. van Jaarsveld, *Proc. R. Soc. London Ser. B* **266**, 315–319 (1999).
6. S. Ferrier *et al.*, *Bioscience* **54**, 1101–1109 (2004).
7. R. H. Whittaker, *Ecol. Monogr.* **30**, 279–338 (1960).
8. A. E. Magurran, P. A. Henderson, *Philos. Trans. R. Soc. London Ser. B* **365**, 3611–3620 (2010).
9. E. C. Ellis *et al.*, *Proc. Natl. Acad. Sci. U.S.A.* **110**, 7978–7985 (2013).
10. A. D. Barnosky *et al.*, *Nature* **471**, 51–57 (2011).
11. D. F. Sax, S. D. Gaines, *Trends Ecol. Evol.* **18**, 561–566 (2003).
12. M. Vellend *et al.*, *Proc. Natl. Acad. Sci. U.S.A.* **110**, 19456–19459 (2013).
13. See supplementary materials on *Science* Online.
14. F. J. Rahel, *Annu. Rev. Ecol. Syst.* **33**, 291–315 (2002).
15. C. S. Elton, *The Ecology of Invasion by Animals and Plants* (Univ. of Chicago Press, Chicago, 1958).
16. C. Parmesan, *Annu. Rev. Ecol. Evol. Syst.* **37**, 637–669 (2006).
17. B. Collen *et al.*, *Conserv. Biol.* **23**, 317–327 (2009).
18. D. Pauly, *Trends Ecol. Evol.* **10**, 430 (1995).
19. R. J. Hobbs *et al.*, *Glob. Ecol. Biogeogr.* **15**, 1–7 (2006).
20. T. P. Hughes, *Science* **265**, 1547–1551 (1994).
21. J. M. Pandolfi, S. R. Connolly, D. J. Marshall, A. L. Cohen, *Science* **333**, 418–422 (2011).
22. N. A. J. Graham, J. E. Cinner, A. V. Norström, M. Nyström, *Curr. Opin. Environ. Sustain.* **7**, 9–14 (2014).

Acknowledgments: Supported by the European Research Council (BioTIME 250189), the Scottish Funding Council (MASTS, grant reference HR09011) (M.D.), and the Royal Society (A.E.M.). We are grateful to all the data providers for making data publicly available and to their funders: Belspo (Belgian Science Policy); NSF; NOAA Marine Fisheries Service (grant NA11NMF4540174); Fisheries and Oceans Canada; Government of Nunavut, Nunavut Wildlife Management Board, Nunavut Tunngavik Inc., and Nunavut Emerging Fisheries Fund; Makivik Corporation; Smithsonian Institution; Atherton Seidell Grant Program; grants BSR-8811902, DEB 9411973, DEB 0080538, DEB 0218039, DEB 0620910, and DEB 0963447 from NSF to the Institute for Tropical Ecosystem Studies, University of Puerto Rico, and to the International Institute of Tropical Forestry, U.S. Forest Service, as part of the Luquillo Long-Term Ecological Research Program; University of Puerto Rico; NSF's Long-Term Ecological Research program and Fishery Administration Agency; Council of Agriculture, Taiwan; Azores Fisheries Observer Program; and the Center of the Institute of Marine Research (IMAR) of the University of the Azores. In addition, data were provided by the H. J. Andrews Experimental Forest research program, funded by NSF's Long-Term Ecological Research Program (DEB 08-23380), P. Henderson (Pisces Conservation), U.S. Forest Service Pacific Northwest Research Station, and Oregon State University. Cruise data were collected through the logistical efforts of the Australian Antarctic Division and approved by the Australian Antarctic Research Advisory Committee (projects 2208 and 2953), the Australian Antarctic Data Centre of the Australian Antarctic Division, Tasmania. We are also grateful to the databases that compile these data: OBIS, Ecological Data Wiki, DATRAS, and LTER. Finally, we thank O. Mendivil-Ramos for advice on database design, L. Antão, and M. Barbosa and three anonymous referees for comments on earlier versions of the manuscript. The rarefied time series used in our analysis are included as Databases S1 and S2.

Supplementary Materials

www.sciencemag.org/content/344/6181/296/suppl/DC1
Materials and Methods
Figs. S1 to S10
Table S1
Databases S1 and S2
References (*23–160*)

13 November 2013; accepted 18 March 2014
10.1126/science.1248484

Structural Basis for Assembly and Function of a Heterodimeric Plant Immune Receptor

Simon J. Williams,[1]*† Kee Hoon Sohn,[2,6]*† Li Wan,[1]* Maud Bernoux,[3]* Panagiotis F. Sarris,[2] Cecile Segonzac,[2,6] Thomas Ve,[1] Yan Ma,[2] Simon B. Saucet,[2] Daniel J. Ericsson,[1]‡ Lachlan W. Casey,[1] Thierry Lonhienne,[1] Donald J. Winzor,[1] Xiaoxiao Zhang,[1] Anne Coerdt,[4] Jane E. Parker,[4] Peter N. Dodds,[3] Bostjan Kobe,[1,5]† Jonathan D. G. Jones[2]†

Cytoplasmic plant immune receptors recognize specific pathogen effector proteins and initiate effector-triggered immunity. In *Arabidopsis*, the immune receptors RPS4 and RRS1 are both required to activate defense to three different pathogens. We show that RPS4 and RRS1 physically associate. Crystal structures of the N-terminal Toll–interleukin-1 receptor/resistance (TIR) domains of RPS4 and RRS1, individually and as a heterodimeric complex (respectively at 2.05, 1.75, and 2.65 angstrom resolution), reveal a conserved TIR/TIR interaction interface. We show that TIR domain heterodimerization is required to form a functional RRS1/RPS4 effector recognition complex. The RPS4 TIR domain activates effector-independent defense, which is inhibited by the RRS1 TIR domain through the heterodimerization interface. Thus, RPS4 and RRS1 function as a receptor complex in which the two components play distinct roles in recognition and signaling.

Plant immune receptors contain nucleotide-binding and leucine-rich repeat domains and resemble mammalian nucleotide-binding oligomerization domain (NOD)–like receptor (NLR) proteins (*1*). During infection, plant NLR proteins activate effector-triggered immunity upon recognition of corresponding pathogen effectors (*2*, *3*). NLR protein activation of defense mechanisms is adenosine triphosphate dependent, causes defense gene induction, and often culminates in the hypersensitive cell death response (hereafter referred to as cell death) (*4–6*).

In some cases, plant and animal NLRs function in pairs to mediate immune recognition (*7*). For instance, both *RPS4* (resistance to *Pseudomonas syringae* 4) and *RRS1* (resistance to *Ralstonia solanacearum* 1) NLRs are required in *Arabidopsis* to recognize bacterial effectors AvrRps4 from *P. syringae* pv. *pisi* and PopP2 from *R. solanacearum* and also the fungal pathogen *Colletotrichum higginsianum* (*8*, *9*). Several NLR gene pairs in rice also function cooperatively to provide resistance to the fungus *Magnaporthe oryzae* (*10–14*). Similarly,

[1]School of Chemistry and Molecular Biosciences and Australian Infectious Diseases Research Centre, University of Queensland, Brisbane, QLD 4072, Australia. [2]The Sainsbury Laboratory, John Innes Centre, Norwich Research Park, Norwich, NR4 7UH, UK. [3]Commonwealth Scientific and Industrial Research Organisation Plant Industry, Canberra, ACT 2601, Australia. [4]Max-Planck Institute for Plant Breeding Research, Department of Plant-Microbe Interactions, Carl-von-Linné-Weg 10, D-50829 Cologne, Germany. [5]Division of Chemistry and Structural Biology, Institute for Molecular Bioscience, University of Queensland, Brisbane, QLD 4072, Australia. [6]Bioprotection Research Centre, Institute of Agriculture and Environment, Massey University, Private Bag 11222, Palmerston North, 4442, New Zealand.

*These authors contributed equally to this work.
†Corresponding author. E-mail: b.kobe@uq.edu.au (B.K.); jonathan.jones@sainsbury-laboratory.ac.uk (J.D.G.J.); s.williams8@uq.edu.au (S.J.W.); k.sohn@massey.ac.nz (K.H.S.)
‡Present address: Macromolecular Crystallography, Australian Synchrotron, 800 Blackburn Road, Clayton, Victoria 3168, Australia.

in mammals, the NLR protein NLRC4 acts with either the NLRs NAIP5/6 or NAIP2 to activate defense after recognition of flagellin or bacterial type III secretion rod protein PrgJ, respectively (*15*). Cooperative activity of immune receptor pairs is thus common in both plants and animals and might operate by evolutionarily conserved mechanisms (*16*). To address the underlying processes, we investigated how interaction between *Arabidopsis* RPS4 and RRS1 mediates recognition of their corresponding effectors. PopP2, a *Yersinia* YopJ effector family member, is an acetyltransferase that directly interacts with RRS1 in the plant nucleus (*17*, *18*). AvrRps4 is processed in the plant cell, and its C-terminal domain triggers RRS1/RPS4-dependent immunity (*19*). No direct interaction between AvrRps4 and RRS1 has yet been demonstrated.

RPS4 and RRS1 both carry a Toll–interleukin-1 receptor/resistance protein (TIR) domain at their N termini. Homo- and heterotypic interactions between TIR domains are implicated in Toll-like receptor signaling pathways in animals, mediating interactions between Toll-like receptors and intracellular TIR domain–containing adaptors to regulate immune signaling and gene expression (*20*, *21*). For several plant TIR-NLR proteins, including RPS4, expression of the TIR domain alone can activate effector-independent defense (*22*), and for the TIR domain of the flax (*Linum*

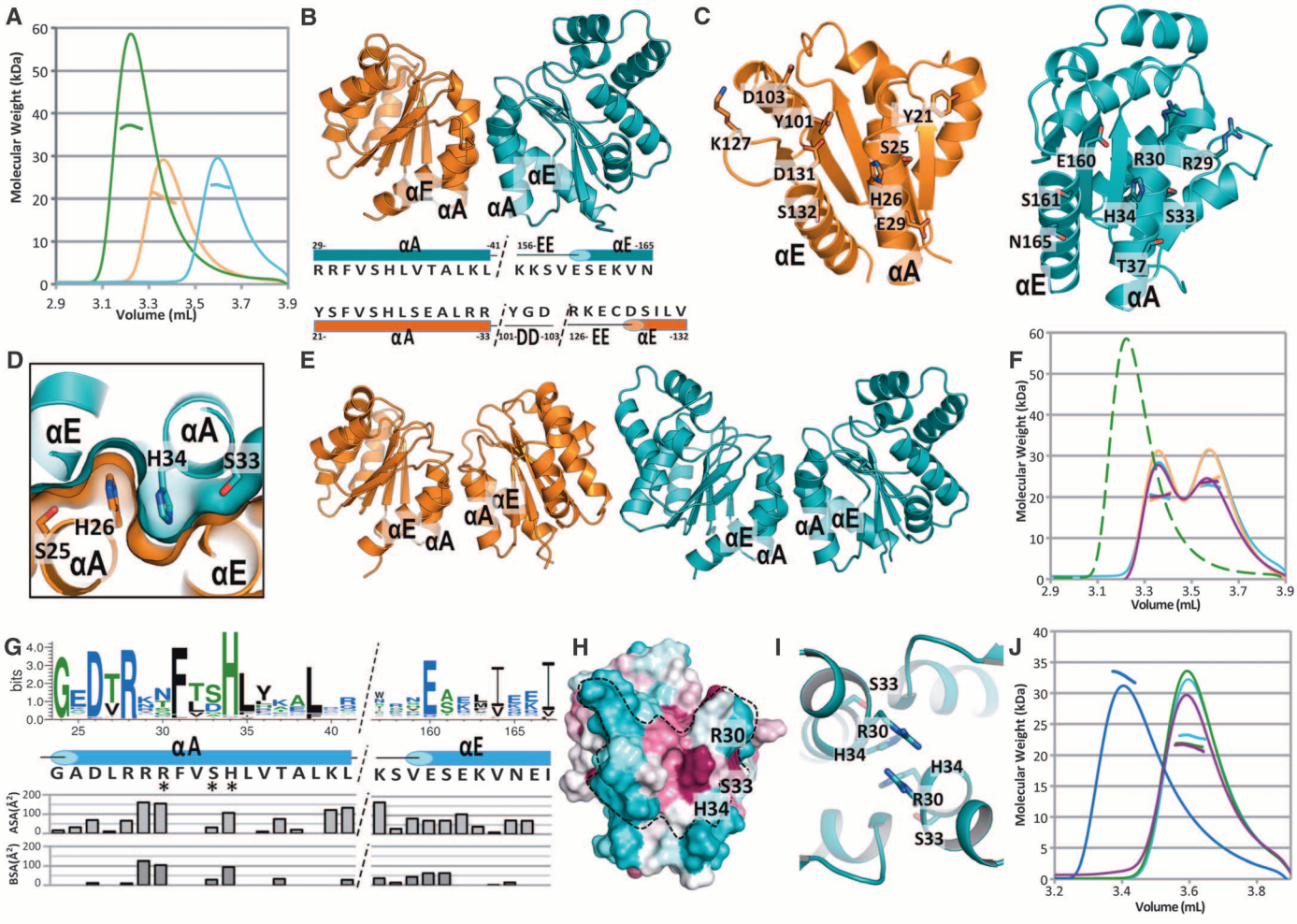

Fig. 1. A conserved TIR/TIR domain interaction interface is involved in hetero- and homo-dimerization between RPS4 and RRS1 TIR domains. (**A**) SEC-MALS analysis of RPS4TIR, RRS1TIR, and RPS4TIR + RRS1TIR complex. Green, orange, and teal lines indicate the trace from the refractive index detector (arbitrary units) during SEC of RPS4TIR/RRS1TIR, RRS1TIR, and RPS4TIR, respectively. Solid lines (equivalent coloring) under the peak correspond to the averaged molecular weight (*y* axis) distributions across the peak as determined by MALS. (**B**) Crystal structure of the RRS1TIR (orange) and RPS4TIR (teal) heterodimer shown in cartoon representation. The domains form a pseudo-symmetrical dimer with major interactions involving the αA and αE helices of both monomers. Residues contributing to the interface are displayed in the amino acid sequence with secondary structure elements and residue numbers labeled (below). (**C**) The heterodimerization interface facing the plane of the page. RRS1 and RPS4 rotated −90° and 90°, respectively, around the vertical axis compared to (B), and buried residues are displayed as sticks. (**D**) The position of serine and histidine residues within the heterodimerization interface. (**E**) A common interface observed in the crystal packing of RRS1TIR (orange) and RPS4TIR (teal) structures. (**F**) Solution properties of SH mutants as measured by SEC-MALS, with traces, units, and calculations represented as for (A). RPS4TIR H34A + RRS1TIR, teal; RPS4TIR + RRS1TIR H26A, orange; RPS4TIR S33A + RRS1TIR S25A, purple. Broken green line represents the refractive index trace of RPS4TIR/RRS1TIR as in (A). (**G**) Sequence logo (WebLogo 3.3) from a multiple sequence alignment generated by the program ConSurf (*34*) using 150 unique plant TIR domain sequences (20 to 40% identity to RPS4TIR). Sequence and secondary structure elements of RPS4 are shown below the logo. Asterisks on the sequence represent residues mutated in Fig. 1. Graphs represent residue accessible surface area (ASA) and buried surface area (BSA) within the RPS4TIR structure (Å^2), calculated by PISA (*35*). (**H**) Surface representation of RPS4TIR with coloring by sequence conservation from (G). Cyan and purple corresponds to variable and conserved regions, respectively. Broken black line represents the BSA in the homodimer. (**I**) Structure of RPS4TIR focusing on the common interface, with labeled residues in stick representation. (**J**) Solution properties of RPS4TIR mutants measured by SEC-MALS, with traces, units, and calculations represented as for (A). RPS4TIR, teal; H34A, green; S33A, purple; R30A, blue.

usitatissimum) NLR protein L6, homodimerization is involved in defense signaling (*23*).

We first investigated whether RPS4 and RRS1 TIR domains interact. Using yeast two-hybrid assays (Y2H), we found that although TIR domains of RPS4 and RRS1 self-associate weakly, they interact more strongly with each other and do not interact with L6 or RPP5 TIR domains (fig. S1). We transiently coexpressed RPS4 and RRS1 TIR domains with C-terminal hemagglutinin (HA) or green fluorescent protein (GFP) tags in *Nicotiana benthamiana* leaves, and coimmunoprecipitation also showed that they weakly self-associate but interact more strongly with each other (fig. S1). The RPS4 TIR (residues 10 to 178, RPS4TIR) and RRS1 TIR (residues 6 to 153, RRS1TIR) domains were then expressed in *Escherichia coli* and purified to homogeneity (see the supplementary materials). RRS1TIR interacts in glutathione *S*-transferase pull-down assays with RPS4TIR but not with TIR domains from NLR proteins N and L6 (*N. tabacum* and flax, respectively) (fig. S1). Size-exclusion chromatography (SEC) coupled with multiangle light scattering (MALS), as well as small-angle x-ray scattering (SAXS) experiments measured a molecular weight of ~37 kD (Fig. 1A and fig. S2) for the RPS4TIR and RRS1TIR complex, consistent with the formation of a heterodimer. The binding affinity between RRS1TIR with RPS4TIR was estimated to be ~435 nM by isothermal titration calorimetry analysis, which also confirmed a 1:1 binding stoichiometry (fig. S3). By SEC-MALS, the averaged molecular weights of RPS4TIR and RRS1TIR alone were 23 kD and 20 kD (Fig. 1A), respectively, higher than the theoretical monomeric molecular weights of ~20 kD and ~17 kD, and consistent with weak self-association. Thus, the TIR domains of RPS4 and RRS1 form a stable and specific heterodimer but also can self-associate.

To better understand homo- and heterodimerization of RPS4 and RRS1 TIR domains, we crystallized (*24*) and solved the structures of RPS4TIR and RRS1TIR individually (Fig. 1, B to E, and fig. S4). Covalently linking the protein chains of RPS4TIR and RRS1TIR through a five-residue linker (designated RRS1/RPS4TIR) enabled cocrystallization. The structures of RPS4TIR, RRS1TIR, and RRS1/RPS4TIR were determined at 2.05, 1.75, and 2.65 Å resolution, respectively

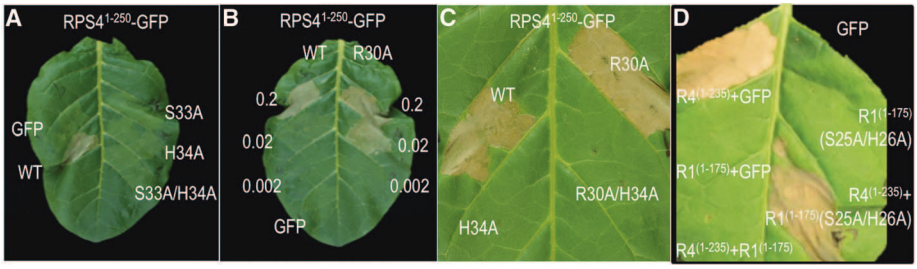

Fig. 2. RPS4 TIR domain–induced cell-death signaling is dependent on the conserved TIR/TIR domain interface. (**A**) Mutations in the SH motif abolish RPS4 TIR domain–induced hypersensitive response (HR). (**B**) The R30A mutation enhances HR-inducing activity of RPS4 TIR domain. (**C**) The H34A mutation abolishes RPS4$^{(1-250)}$ TIR domain (R30A)–induced HR. (**D**) RRS1 TIR domain (R1) suppresses RPS4$^{(1-235)}$ TIR domain (R4)–induced HR. Mutations in the SH motif of RRS1 TIR domain abolish the suppression activity. Agroinfiltration assays were performed in 4- to 5-week-old *N. tabacum* leaves, and images were taken at 2 to 5 days after infiltration. The superscripted numbers in (B) indicate inoculum densities (A_{600}) of *Agrobacteria*.

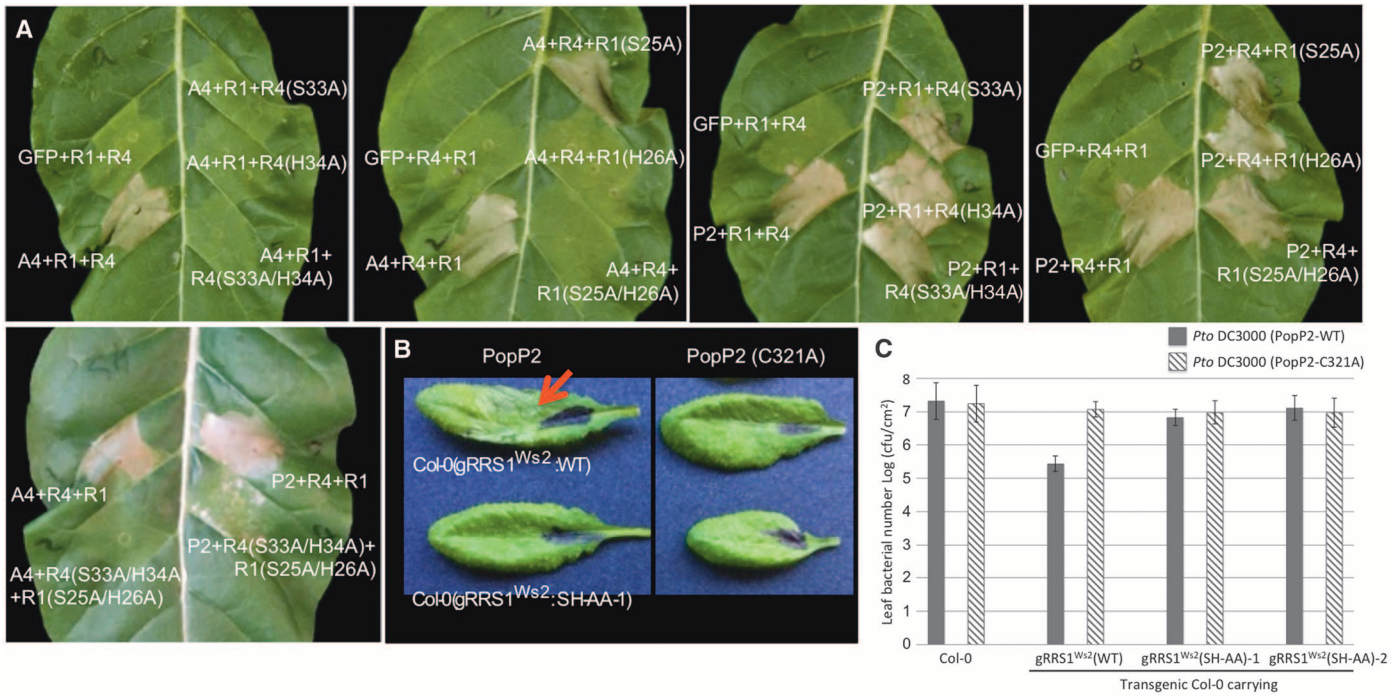

Fig. 3. Mutations that disrupt the RRS1/RPS4 TIR domain dimer abolish the recognition of AvrRps4 and PopP2. (**A**) The SH motif of RPS4 (R4) and RRS1 (R1) is fully or partially required for recognition of AvrRps4 (A4) or PopP2 (P2), respectively, in *N. tabacum* agroinfiltration assays. The indicated C-terminally epitope-tagged RRS1 (Flag), RPS4 (HA), AvrRps4 (GFP), and PopP2 (GFP) proteins were transiently expressed in *N. tabacum* leaf cells using agroinfiltration. The images were taken at 3 dpi. (**B**) PopP2-triggered HR is abolished by mutations in the SH motif in the transgenic *Arabidopsis* (Col-0) line carrying *gRRS1^{Ws2}*. PopP2 variants were delivered from Pf0-1(T3S) into leaves of 5-week-old *Arabidopsis* plants. PopP2^{C321A} represents a catalytic inactive mutant of PopP2 that is not recognized by a resistant RRS1 allele (*18*). Red arrow indicates HR induced by PopP2. The images were taken at 22 hours after infiltration. This experiment was repeated twice. (**C**) Transgenically expressed *gRRS1^{Ws2}* carrying SH-AA mutation does not confer resistance to *Pto* DC3000 (*PopP2*). PopP2 variants were delivered from *Pto* DC3000 and the bacterial colonies were recovered at 4 dpi.

(table S1). The RPS4TIR globular fold comprises a five-stranded parallel β sheet (βA to βE) surrounded by five α-helical regions (αA to αE). In RRS1TIR, the αD-helical region consists of only one helix, in contrast to three observed in RPS4TIR, AtTIR (TIR domain-containing protein AT1G72930 from *A. thaliana*) (*25*), and L6 TIR domains (*23*), consistent with a 22–amino acid deletion in RRS1 (fig. S4).

In the RRS1/RPS4TIR crystal, the largest heterodimeric interface involves residues within the αA and αE helices and EE loops of RPS4TIR and RRS1TIR and the DD loop of RRS1TIR (Fig. 1B). This interface is observed twice within the asymmetric unit of the RRS1/RPS4TIR crystal, which consists of two chains of the linked proteins (fig. S5). Surface-exposed residues in RPS4TIR and RRS1TIR contribute to a combined total buried surface area of ~1300 $Å^2$ in the heterodimer (Fig. 1C), containing a network of side-chain/side-chain and backbone/side-chain hydrogen bonds (fig. S6). The core of the interface is stabilized by a stacking interaction between histidine residues RPS4 His^{34} and RRS1 His^{26} (Fig. 1D). In both proteins, a conserved serine that precedes the histidine within the αA helix forms backbone hydrogen-bonding interactions with a conserved serine in the αE helix of the interacting protein (fig. S6). The adjacent serine and histidine residues (the SH motif) provide complementary stacking and hydrogen-bonding interactions that stabilize the heterodimer (Fig. 1D).

SAXS data were collected on both the RRS1TIR/RPS4TIR heterodimer and the linked (RRS1/RPS4TIR) construct, and scattering profiles suggested that their behavior in solution was similar (fig. S7). Furthermore, the calculated scattering of the crystallographic dimer was consistent with data from the heterodimer (fig. S7). Thus, the linked RRS1/RPS4TIR protein resembles the heterodimer in solution.

An identical interface to that observed in the RRS1/RPS4TIR heterodimer is also present in the crystal structures of RRS1TIR and RPS4TIR alone (Fig. 1E). The SH motif again forms stacking and hydrogen-bonding interactions; however, the RRS1/RPS4 TIR domain heterodimer interface involves amino acids that are more complementary (fig. S8). This common interface involves different regions of the TIR domain compared to the proposed L6 dimerization interface (*23*), but an identical interface is observed in the crystal packing of the AtTIR (*25*) (fig. S9). A multiple sequence alignment of plant TIR domains highlights the conservation of the residues corresponding to Ser^{33} and His^{34} in RPS4 (Fig. 1G). Mapping of this sequence conservation onto the surface of RPS4TIR reveals a patch with the conserved His residue in its center (Fig. 1H).

To investigate the role of specific amino acids in RPS4 and RRS1 TIR domain homo- and heterodimerization, we generated mutations in the interface. In Y2H assays, mutation of residues within the dimeric interface prevents RRS1/RPS4 TIR domain interaction (fig. S10). By SEC-MALS, the most significant effect on heterodimerization is caused by alanine substitutions of the SH motif (Fig. 1F and fig. S11). Single-residue mutations of the RPS4TIR H34A or RRS1TIR H26A and a double mutation of RPS4TIR S33A/RRS1TIR S25A completely destabilized the TIR/TIR domain heterodimer (Fig. 1F). No interaction could be detected between RRS1TIR and RPS4TIR H34A by isothermal titration calorimetry analysis (fig. S3). Mutation of the SH motif in RPS4 also prevents self-association interactions in Y2H assays (fig. S10). Although weak self-association of wild-type RPS4TIR is observed by SEC-MALS, the S33A and H34A mutants run as monomers (Fig. 1J). Close inspection of the RPS4 TIR domain homodimer interface suggested that the arginine at position 30 likely destabilizes homomeric interactions (Fig. 1I). Mutation of this arginine to an alanine (R30A) results in stronger self-association of RPS4TIR by SEC-MALS (measured ~33 kD) and Y2H assays (Fig. 1J and fig. S10). Sedimentation equilibrium experiments using analytical ultracentrifugation demonstrated that at 15 μM, RPS4TIR R30A completely dimerized, whereas wild-type RPS4TIR formed an equilibrating mixture of monomer and dimer, with an estimated dimerization constant of 13,000 M^{-1} (K_d ~77 μM), further corroborating SEC-MALS experiments (fig. S12). Dimerization of RPS4 R30A was only observed when the His^{34} was maintained (fig. S13).

The TIR domain–containing N-terminal region of $RPS4^{(1-236)}$ activates effector-independent cell death in tobacco (*22*, *26*); this was completely abolished by the S33A, H34A, and S33A/H34A mutations (Fig. 2A and fig. S14). We performed

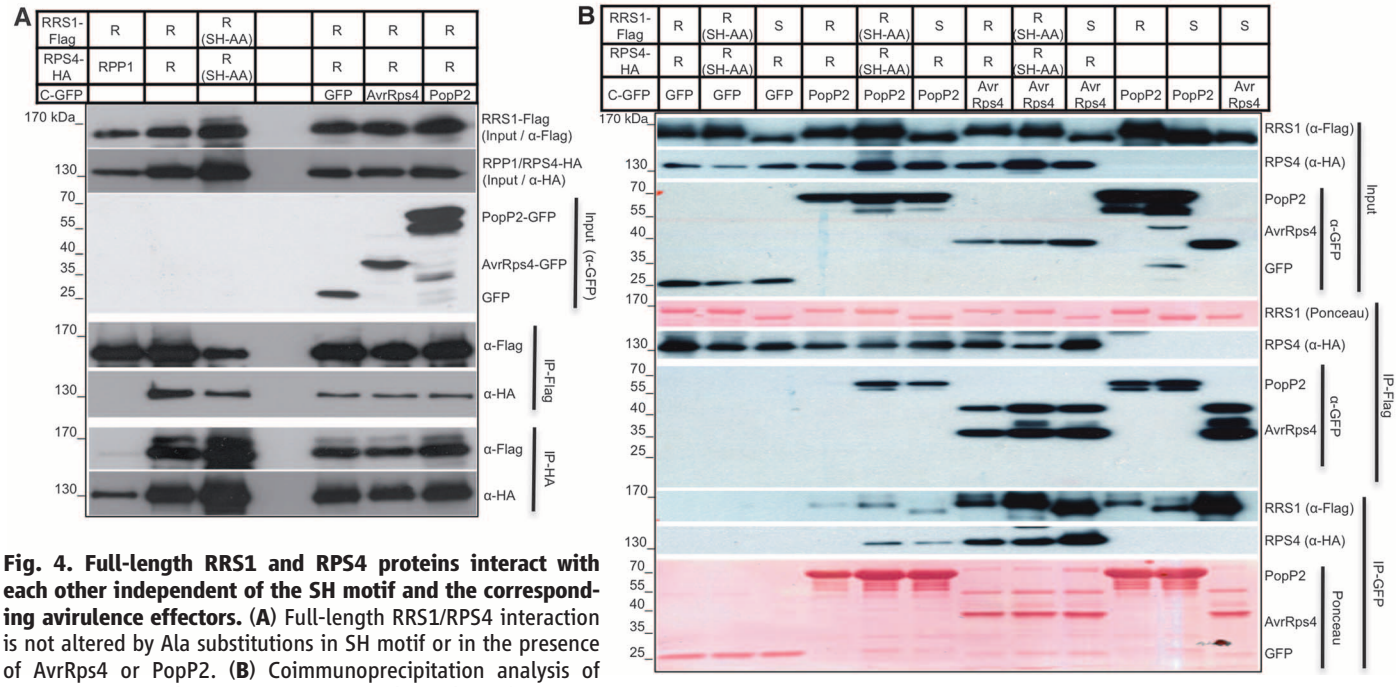

Fig. 4. Full-length RRS1 and RPS4 proteins interact with each other independent of the SH motif and the corresponding avirulence effectors. (**A**) Full-length RRS1/RPS4 interaction is not altered by Ala substitutions in SH motif or in the presence of AvrRps4 or PopP2. (**B**) Coimmunoprecipitation analysis of RRS1 variants and AvrRps4 or PopP2. The indicated proteins were transiently expressed in *N. benthamiana* leaf cells by agroinfiltration. Total protein extracts were used for coimmunoprecipitation and immunoblot analyzes. R and S indicate resistant and susceptible alleles, in Ws2 and Col-0, respectively, for RRS1. Mutations in the SH motif (SH-AA) have been introduced in RRS1 (Ws-2) and RPS4 (No-0) resistant alleles.

agroinfiltration of serially diluted RPS4 TIR domain and R30A variants in *N. tabacum* leaves. A stronger cell death was induced by the R30A variant than the wild-type protein at 0.02 inoculum density (A_{600}) (Fig. 2B and fig. S14), and the R30A/H34A double mutant was unable to induce cell-death (Fig. 2C), suggesting that homodimerization of RPS4 TIR domain is required for cell death signaling.

Transient expression of RRS1 TIR domain does not cause cell death in *N. tabacum* (Fig. 2D and fig. S14). However, coexpression of RRS1 TIR domain suppressed RPS4 TIR domain-induced cell death, whereas the S25A/H26A loss-of-heterodimerization variant of RRS1 TIR domain did not (Fig. 2D and fig. S14). Because the heterodimeric interaction between RPS4 and RRS1 TIR domains is stronger than homomeric interactions, this suggests that the heterodimer is inactive in signaling and outcompetes the formation of the active RPS4 TIR domain homodimer.

To determine whether the SH motif and TIR/TIR domain heterodimerization are required for effector-triggered immunity, we coexpressed full-length RRS1 and RPS4 with AvrRps4 or PopP2 effectors (or controls) in *N. tabacum* by agroinfiltration (Fig. 3A). Mutations of the conserved histidine and serine/histidine (SH-AA double mutant) in either RPS4 or RRS1 abolished AvrRps4-triggered RRS1/RPS4-dependent cell death. Although these mutations in the individual proteins had little effect on cell death triggered by PopP2, reduced PopP2-triggered immunity was observed when SH-AA mutants of both RPS4 and RRS1 were coexpressed (Fig. 3A). In susceptible *Arabidopsis* (Col-0), transgenically expressed wild-type but not SH-AA mutant RRS1-Ws-2 confers recognition of PopP2 (Fig. 3, B and C, and fig. S15), demonstrating that TIR domain heterodimerization is required to form a functional complex to recognize AvrRps4 and PopP2.

To investigate whether RRS1 and RPS4 proteins interact in planta, we transiently expressed RPS4-HA and RRS1-Flag tag variants, with or without AvrRps4-GFP or PopP2-GFP, in *N. benthamiana* leaves (Fig. 4). The *Arabidopsis* TIR-NLR protein RPP1 (resistance to *Peronospora parasitica* 1) provided a negative control. RPS4-HA, but not RPP1-HA, coimmunoprecipitate with RRS1-Flag (Fig. 4A). SH motif mutations in RPS4 and/or RRS1 TIR domains do not abolish RRS1/RPS4 interactions, suggesting that other domains also contribute to the interaction.

RRS1/RPS4 interaction is independent of the effectors (Fig. 4A). For AvrL567/L6, ATR1/RPP1, and AvrM/M (*23*, *27*, *28*), effector/NLR interaction correlates with activation of defense. However, PopP2 interacts in the nucleus with both susceptible (Col-0) and resistant (Nd-1) forms of RRS1 (*17*). Several other resistant accessions (Ws-2 and No-0) were reported (*9*, *29*). Both RRS1 (Col-0) and RRS1 (Ws-2) coimmunoprecipitate with PopP2 in *N. benthamiana* (Fig. 4B). However, the interactions between PopP2 and RRS1 or RRS1 + RPS4 were stronger in combinations that do not activate defense [RRS1 (Col-0), RRS1 SH-mutant, PopP2 inactive mutant, or in the absence of RPS4] (Fig. 4B and fig. S16).

AvrRps4 also interacts strongly with RRS1 in the presence or absence of RPS4, and the interaction between RRS1 and AvrRps4 is not affected by an RRS1 SH-AA mutation (Fig. 4B).

Mutations in the P-loop motif of many NLR proteins disturb nucleotide binding and abolish function (*4*). The RPS4 NB domain P-loop mutation (K242A) abolished recognition of AvrRps4 and PopP2 in transient assays in *N. tabacum* without affecting protein accumulation (figs. S17 and S18). By contrast, an RRS1 P-loop mutation (K185A) did not attenuate AvrRps4 or PopP2-triggered cell death (fig. S18).

Because TIR/TIR domain interactions have previously been difficult to define structurally (*30*), our data may have broad implications for understanding TIR domain function across phyla. Current models of plant NLR protein activation imply that effector perception leads to considerable domain reorganization and formation of oligomeric forms (*31*). Rather than effector-induced disassociation of RRS1 and RPS4 proteins, rearrangements within a preformed RRS1/RPS4 complex, culminating in stabilization of an RPS4 TIR domain homodimer, likely distinguish the preactivation complex from its activated state. Domains in RRS1 and RPS4 other than the TIR domain are also likely to hold or bring the complex together and mediate its effector-dependent reconfiguration. Nucleotide-binding or exchange by RPS4, but not RRS1, is required for a functional NLR resistance complex. Thus AvrRps4 or PopP2 recognition is accomplished by an RRS1/RPS4 complex, distinct from indirect recognition of effectors by other plant NLR proteins (*32*, *33*). We propose that upon effector binding, defense activation requires the release of RPS4 TIR domain inhibition by the RRS1 TIR domain, allowing formation of a signaling-competent RPS4 TIR domain homodimer (fig. S19).

References and Notes

1. J. L. Dangl, D. M. Horvath, B. J. Staskawicz, *Science* **341**, 746–751 (2013).
2. P. N. Dodds *et al.*, *Proc. Natl. Acad. Sci. U.S.A.* **103**, 8888–8893 (2006).
3. J. D. G. Jones, J. L. Dangl, *Nature* **444**, 323–329 (2006).
4. F. L. Takken, M. Albrecht, W. I. Tameling, *Curr. Opin. Plant Biol.* **9**, 383–390 (2006).
5. S. J. Williams *et al.*, *Mol. Plant Microbe Interact.* **24**, 897–906 (2011).
6. J. T. Greenberg, *Annu. Rev. Plant Physiol. Plant Mol. Biol.* **48**, 525–545 (1997).
7. T. K. Eitas, J. L. Dangl, *Curr. Opin. Plant Biol.* **13**, 472–477 (2010).
8. D. Birker *et al.*, *Plant J.* **60**, 602–613 (2009).
9. M. Narusaka *et al.*, *Plant J.* **60**, 218–226 (2009).
10. I. Ashikawa *et al.*, *Genetics* **180**, 2267–2276 (2008).
11. S. Cesari *et al.*, *Plant Cell* **25**, 1463–1481 (2013).
12. S.-K. Lee *et al.*, *Genetics* **181**, 1627–1638 (2009).
13. Y. Okuyama *et al.*, *Plant J.* **66**, 467–479 (2011).
14. B. Yuan *et al.*, *Theor. Appl. Genet.* **122**, 1017–1028 (2011).
15. E. M. Kofoed, R. E. Vance, *Nature* **477**, 592–595 (2011).
16. J. von Moltke, J. S. Ayres, E. M. Kofoed, J. Chavarría-Smith, R. E. Vance, *Annu. Rev. Immunol.* **31**, 73–106 (2013).
17. L. Deslandes *et al.*, *Proc. Natl. Acad. Sci. U.S.A.* **100**, 8024–8029 (2003).
18. C. Tasset *et al.*, *PLOS Pathog.* **6**, e1001202 (2010).
19. K. H. Sohn, Y. Zhang, J. D. G. Jones, *Plant J.* **57**, 1079–1091 (2009).
20. K. Takeda, S. Akira, *Int. Immunol.* **17**, 1–14 (2005).
21. T. Ve, N. J. Gay, A. Mansell, B. Kobe, S. Kellie, *Curr. Drug Targets* **13**, 1360–1374 (2012).
22. M. R. Swiderski, D. Birker, J. D. G. Jones, *Mol. Plant Microbe Interact.* **22**, 157–165 (2009).
23. M. Bernoux *et al.*, *Cell Host Microbe* **9**, 200–211 (2011).
24. L. Wan *et al.*, *Acta Crystallogr. Sect. F Struct. Biol. Cryst. Commun.* **69**, 1275–1280 (2013).
25. S. L. Chan, T. Mukasa, E. Santelli, L. Y. Low, J. Pascual, *Protein Sci.* **19**, 155–161 (2010).
26. Y. Zhang, S. Dorey, M. Swiderski, J. D. Jones, *Plant J.* **40**, 213–224 (2004).
27. K. V. Krasileva, D. Dahlbeck, B. J. Staskawicz, *Plant Cell* **22**, 2444–2458 (2010).
28. T. Ve *et al.*, *Proc. Natl. Acad. Sci. U.S.A.* **110**, 17594–17599 (2013).
29. Y. Noutoshi *et al.*, *Plant J.* **43**, 873–888 (2005).
30. E. Valkov *et al.*, *Proc. Natl. Acad. Sci. U.S.A.* **108**, 14879–14884 (2011).
31. F. L. Takken, A. Goverse, *Curr. Opin. Plant Biol.* **15**, 375–384 (2012).
32. M. J. Axtell, B. J. Staskawicz, *Cell* **112**, 369–377 (2003).
33. D. Mackey, Y. Belkhadir, J. M. Alonso, J. R. Ecker, J. L. Dangl, *Cell* **112**, 379–389 (2003).
34. H. Ashkenazy, E. Erez, E. Martz, T. Pupko, N. Ben-Tal, *Nucleic Acids Res.* **38**, (Web Server), W529–W533 (2010).
35. E. Krissinel, K. Henrick, *J. Mol. Biol.* **372**, 774–797 (2007).

Acknowledgments: This research was supported by the Australian Research Council (ARC) Discovery Project (DP120100685), by Rural Development Administration (Korea) Project PJ007850201006, and by the Gatsby Foundation (United Kingdom). M.B. was a recipient of an ARC Discovery Early Career Award (DE130101292). A.C. is an International Max-Planck Research School Ph.D. student. B.K. is a National Health and Medical Research Council Research Fellow (1003325). P.F.S is supported by the European Commission FP7-PEOPLE-2011-Intra-European Fellowships (299621). The x-ray diffraction and small-angle scattering data collection was undertaken on the Micro Crystallography and Small- and Wide-Angle X-Ray Scattering beamlines at the Australian Synchrotron. We thank the Australian Synchrotron beamline scientists for help with x-ray data collection, and we acknowledge the use of the University of Queensland Remote Operation Crystallization and X-ray Diffraction Facility (UQ ROCX). We thank R. Counago for valuable help and suggestions, K. Newell and J. Rajamony for providing excellent technical assistance, Icon Genetics and S. Marillonnet for early access to vectors, and J. Ellis and S. Cesari for critical reading of the manuscript. The coordinate and structure factor data for RPS4TIR, RRS1TIR, and RRS1/RPS4TIR have been deposited to the Protein Data Bank (PDB) with PDB IDs 4c6r, 4c6s, and 4c6t, respectively.

Supplementary Materials

www.sciencemag.org/content/344/6181/299/suppl/DC1
Materials and Methods
Supplementary Text
Figs. S1 to S19
Table S1
References (*36*–*64*)

18 October 2013; accepted 12 March 2014
10.1126/science.1247357

Crystal Structure of a Claudin Provides Insight into the Architecture of Tight Junctions

Hiroshi Suzuki,[1]* Tomohiro Nishizawa,[2,3]* Kazutoshi Tani,[1]* Yuji Yamazaki,[4]† Atsushi Tamura,[4] Ryuichiro Ishitani,[2,3] Naoshi Dohmae,[3] Sachiko Tsukita,[4] Osamu Nureki,[2,3]‡ Yoshinori Fujiyoshi[1,5]‡

Tight junctions are cell-cell adhesion structures in epithelial cell sheets that surround organ compartments in multicellular organisms and regulate the permeation of ions through the intercellular space. Claudins are the major constituents of tight junctions and form strands that mediate cell adhesion and function as paracellular barriers. We report the structure of mammalian claudin-15 at a resolution of 2.4 angstroms. The structure reveals a characteristic β-sheet fold comprising two extracellular segments, which is anchored to a transmembrane four-helix bundle by a consensus motif. Our analyses suggest potential paracellular pathways with distinctive charges on the extracellular surface, providing insight into the molecular basis of ion homeostasis across tight junctions.

Multicellular organisms comprise many organ compartments that are separated from their external environments by epithelial cell sheets. The movement of ions and solutes through the epithelia is regulated by the barrier function of the sheets, and its proper regulation is important for homeostasis and organism survival (*1*). Ions are transported through the epithelial sheet by two routes: the transcellular pathway through membrane transporters and channels, and the paracellular pathway through the intercellular spaces. Ion transport through the paracellular pathway is restricted by an intercellular seal that is formed by specific junctional complexes, termed tight junctions (TJs), which circumscribe the apical-most part of the epithelial cells and completely occlude the intercellular space between the plasma membranes of adjacent cells (*2*). Physiological studies indicate that TJs not only serve as barriers, but also provide paracellular channels that are selectively permeable to ions and small molecules in a charge- and size-specific manner (*3*, *4*).

TJs are multimolecular complexes in which various transmembrane and cytoplasmic proteins constitute a network of continuous intramembrane particle strands or fibrils, called TJ strands (*5*, *6*). The backbone of the TJ strands is formed by a group of membrane proteins called claudins (*7*–*9*), a multigene family in humans comprising 27 members with tissue-specific expression patterns (*10*). Mutations in claudin genes cause many inherited human disorders involving the disruption of ionic balance in body compartments, such as familial hypomagnesemia (*11*), neonatal sclerosing cholangitis (*12*), and autosomal recessive deafness (*13*). Claudin-1 also plays a role in hepatitis C virus entry (*14*) and is thus a potential pharmaceutical target. Members of the claudin family share a structural topology of four putative transmembrane (TM) segments, a large extracellular loop containing a consensus sequence motif, and a second shorter extracellular loop (*15*). Claudins facilitate cell adhesion by head-to-head interactions between claudins in adjacent cell membranes and polymerize by side-by-side interactions within the same cell membrane. Mutational and chimeric analyses indicate that the two extracellular loops are crucial for the formation of paracellular barriers and pores for solutes and are thought to determine the permeability characteristics of TJs (*16*, *17*). Although high-resolution structures have been determined for various membrane channels involved in transmembrane ion and solute transport (*18*–*20*), structural information on claudins has remained elusive.

To gain insight into the TJ architecture, we expressed various claudin subtypes in Sf9 insect cells and assessed their capacity to form TJ-like strands (*21*). Mouse claudin-15 (mCldn15) could be expressed in large quantities and formed prominent TJ-like strands in the plasma membrane in contact regions between adjacent cells (fig. S1). For crystallization, 33 residues at the C terminus were truncated, and the membrane-proximal cysteines were substituted with alanines to avoid heterogeneous palmitoyl modification. The modified mCldn15 construct was expressed, purified with maltose neopentyl glycol detergent, and crystallized in lipidic cubic phase (LCP). High-resolution diffraction data were obtained from the crystals with a microfocused x-ray beam (*22*), and the structure was determined at 2.4 Å resolution using selenomethionine (SeMet)–labeled derivatives by the multiple anomalous dispersion (MAD) method (table S1 and fig. S2, A and B). Crystals of mCldn15 belong to the *C2* space group and contain one claudin monomer per asymmetric unit (fig. S3, A and B).

The TM segments of mCldn15 (TM1 to TM4) form a typical left-handed four-helix bundle, and large portions of the two extracellular segments form a prominent β-sheet structure (Fig. 1, A to C). Except for the longer TM3, the length of the TM helices is consistent with the thickness of a lipid bilayer. The TM region contains many residues with small side chains, such as Gly and Ala, ensuring tight packing of the helices. Mutations

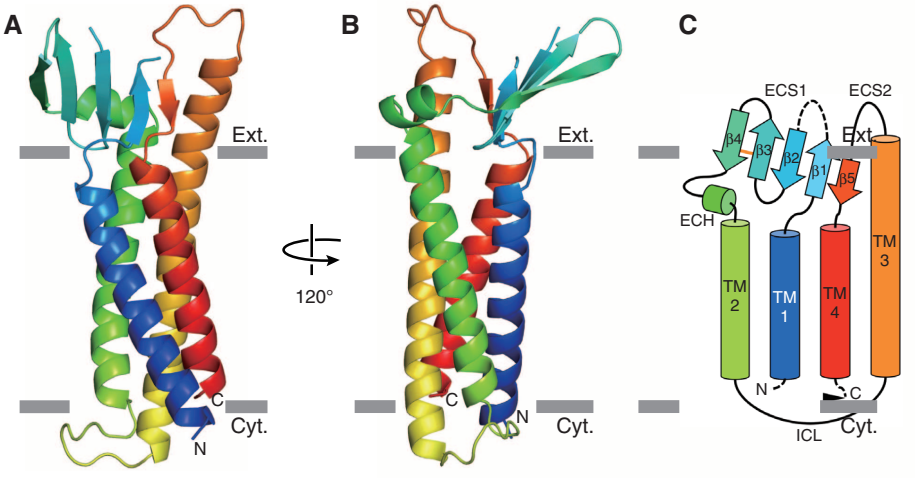

Fig. 1. Overall structure of the mCldn15 protomer. (**A** and **B**) Structure of monomeric mCldn15 in ribbon representation viewed parallel to the membrane. The color changes gradually from the N terminus (blue) to the C terminus (red). Gray bars suggest boundaries of outer (Ext.) and inner (Cyt.) leaflets of the lipid bilayer. (**C**) Secondary structure diagram of mCldn15. The orange line represents a disulfide bond; dashed lines indicate disordered regions. An arrowhead indicates the truncation site for crystallization.

[1]Cellular and Structural Physiology Institute, Nagoya University, Chikusa, Nagoya 464-8601, Japan. [2]Department of Biophysics and Biochemistry, Graduate School of Science, University of Tokyo, Bunkyo, Tokyo 113-0032, Japan. [3]Global Research Cluster, RIKEN, Wako, Saitama 351-0198, Japan. [4]Laboratory of Biological Science, Graduate School of Frontier Biosciences and Graduate School of Medicine, Osaka University, Suita, Osaka 565-0871, Japan. [5]Department of Basic Medicinal Sciences, Graduate School of Pharmaceutical Sciences, Nagoya University, Chikusa, Nagoya 464-8601, Japan.

*These authors contributed equally to this work.
†Present address: Department of Molecular and Cell Biology, University of California, Berkeley, CA 94720, USA.
‡Corresponding author. E-mail: nureki@bs.s.u-tokyo.ac.jp (O.N.); yoshi@cespi.nagoya-u.ac.jp (Y.F.)

at these residues might cause human disease (*11*, *13*) by destabilizing the helical bundle (fig. S4). The β-sheet domain extends from the membrane surface and comprises five β strands (β1 to β5), four contributed by the first extracellular segment (ECS1) and one by the second extracellular segment (ECS2). The loop region (residues 34 to 41) between β1 and β2 is structurally disordered (Fig. 1C and Fig. 2A). At the end of ECS1, the β4 strand connects to a short extracellular helix (ECH) that connects to TM2 after a sharp bend. The cytoplasmic loop (ICL) between TM2 and TM3 is clearly resolved, but the cytoplasmic C-terminal region is disordered. TM3 extends from the extracellular membrane surface and the loop that connects to TM4 forms a β strand that is part of the β-sheet domain. The five β strands adopt an antiparallel arrangement and gradually twist along the axis parallel to the membrane plane. The β-sheet structure is further stabilized by a disulfide bond between cysteine residues at β3 and β4 (Cys^{52} and Cys^{62}, respectively; Fig. 2A). The two cysteine residues are conserved among all members of the claudin family as part of a consensus W-GLW-C-C motif, in which the Gly is substituted with Asn in mammalian claudin-10b and claudin-15 (figs. S5 and S6). It has been suggested that an intramolecular disulfide bridge between these cysteines is necessary for proper claudin function (*4*, *23*).

The residues of the conserved W-LW sequence (Trp^{29}, Leu^{48}, and Trp^{49}) are located adjacent to each other close to the extracellular membrane surface (Fig. 2A) and are embedded in a crevice formed by the top of the four-helix bundle (Fig. 1B). The first Trp residue in the motif, Trp^{29}, extends from β1 into the helix bundle, whereas Leu^{48} and Trp^{49} protrude from the tip of the β2-β3 loop and appear to be exposed to the lipid environment. An electron density that could be assigned as a monoolein lipid was located near Trp^{49} (fig. S7A). These motif residues are likely associated with the extracellular membrane surface to serve as a "hydrophobic anchor" for the β-sheet domain. This is supported by the low temperature factors of the atoms in the membrane-proximal region of the β-sheet domain and the gradual increase in the values toward the open edge (fig. S8). The β-sheet domain and the following ECH region are further stabilized by the conserved Arg^{79} residue that extends from the intramembrane part of TM2 (Fig. 2B). The guanidinium group of Arg^{79} forms hydrogen bonds with the main-chain carbonyl groups of Leu^{48} and Phe^{65}, and the ECH is held over the membrane plane, running almost perpendicular to TM2, to which it connects through the Ser^{72}-Gly^{73} hinge residues (fig. S7B). Although these two residues are not conserved, the corresponding hinge regions often contain a glycine or proline residue (fig. S5). The kink between the ECH and the top of TM2 is thus likely conserved in the claudin family. Homology modeling of other family members indicates that the conformation of the four-helix bundle and ECH regions is well conserved, although there are slight structural variations in the distal edges

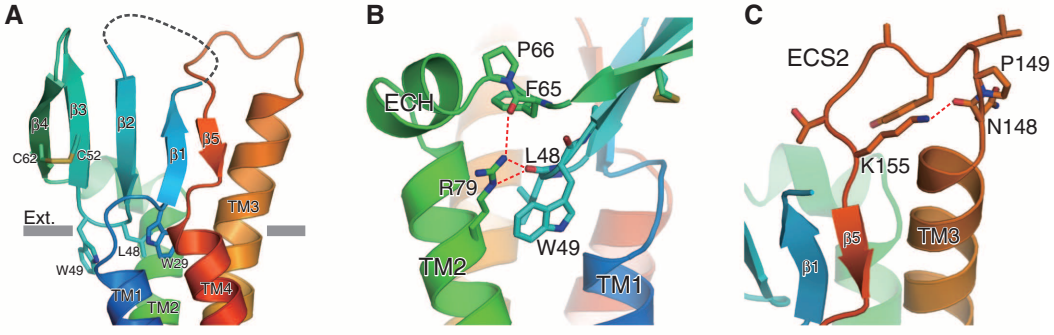

Fig. 2. Residues conserved in claudin family members. (**A**) Close-up view of the extracellular domains and hydrophobic anchors. Side chains of residues in the consensus sequences are labeled and shown in stick representation. (**B**) Close-up view around conserved residue Arg^{79}. Main-chain carbonyl groups and side chains involved in interactions with Arg^{79} are shown in stick representation. (**C**) Close-up view of ECS2. Side chains in the loop region are shown in stick representation. Red dashed lines indicate hydrogen bonds. Amino acid abbreviations: C, Cys; F, Phe; K, Lys; L, Leu; N, Asn; P, Pro; R, Arg; W, Trp.

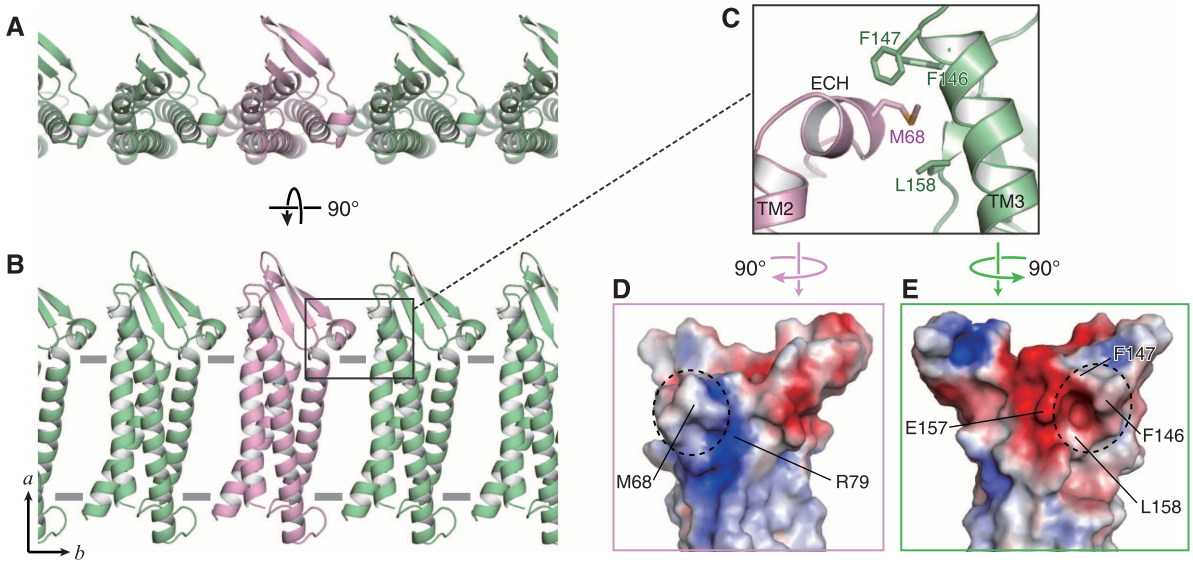

Fig. 3. Linear alignment of mCldn15 protomers. (**A** and **B**) Ribbon representation of a single row of mCldn15 protomers aligned along the *b* axis of the crystal, viewed from the extracellular side (A) and parallel to the membrane (B). One protomer is colored pink. (**C**) Close-up view of lateral interaction sites. Critical residues for the interaction are shown in stick representation (E, Glu; M, Met). (**D** and **E**) Electrostatic potential surfaces of the lateral interfaces of the pink protomer (D) and green protomer (E) shown in (C), contoured from −2 *kT/e* (red) to +2 *kT/e* (blue), viewed parallel to the *b* axis. Dashed circles indicate the complementary hydrophobic protrusion and pocket.

of the β sheet in ECS1 and the loop region in ECS2 (fig. S9A).

The ECS2 loop structure starts with a highly conserved proline residue (Pro^{149}) that forms a hydrogen bond between its main-chain carbonyl and a conserved positively charged residue (Lys^{155} in mCldn15; Fig. 2C). The loop region in ECS2 forms an unstructured turn that connects to the β5 strand, which is part of the β-sheet domain. Such a lariat-like conformation should be relatively flexible and thus useful to keep the less-conserved residues in the loop exposed to the extracellular space. The sequence between the β1 and β2 strands in ECS1 is similarly diverse, and it includes the disordered loop in our structure. Therefore, we defined the loop regions with poorly conserved sequences as variable regions V1 and V2 in ECS1 and ECS2, respectively (figs. S5 and S9, B and C). The V1 and V2 regions located at the extracellular half could be involved in homotypic and heterotypic head-to-head interactions with subtype-specific compatibility.

In the crystal lattice, the mCldn15 protomers form a linear polymer (Fig. 3, A and B, and figs. S3 and S10). The tandem intermolecular interactions in this direction are mediated by specific regions between adjacent extracellular domains. In particular, a conserved hydrophobic residue (Met^{68} in mCldn15) protrudes from ECH in one protomer and snugly fits into a hydrophobic pocket formed by conserved residues in TM3 and ECS2 (Phe^{146}, Phe^{147}, and Leu^{158}) of the adjacent protomer (Fig. 3C). The two contact surfaces have complementary electrostatic potentials and are on opposite sides of the protomer (Fig. 3, D and E), allowing for the formation of a linear polymer. Freeze-fracture electron microscopy of cells expressing claudin-15 showed TJ-like strands in the plasma membranes, which were not observed when the key residues (Met^{68}, Phe^{146}, and Phe^{147}) were mutated to charged or small residues (fig. S11, A to C), whereas constructs with mutations of Met^{68} to bulky hydrophobic residues retained the ability to form TJ-like strands (fig. S11, D and E). These results support the idea that the linear alignment of mCldn15 protomers observed in the LCP crystals might be representative of linear claudin polymers that form in TJs.

Depending on the claudin subtypes that constitute the TJ strands, TJs either form a strict barrier against paracellular diffusion of solutes or include paracellular ion channels with distinct charge selectivity (*4*). The charge selectivity for ion permeation through TJs is determined by specific residues in the C-terminal half of the first extracellular domain (*17*, *24*, *25*). In the structure of mCldn15, a typical channel-forming claudin (*26*, *27*), all of the charged residues extend away from the β-sheet surface (Fig. 4A). The negatively charged residues Asp^{55} and Asp^{64} (Glu^{64} in human claudin-15), mutations of which reverse the ion charge selectivity (*28*), locate to one edge of the β-sheet domain. In addition to these residues, Trp^{63} in mCldn15 is at the position in which claudin-2 and claudin-4 have essential charged residues for their TJ functions (*28*, *29*). The distribution of the electrostatic potential at the extracellular surface of mCldn15 shows that half of the distal part of the β-sheet domain forms a negatively charged "palm" (Fig. 4B). Homology models indicate that the cation-selective TJ protein claudin-2 has a similarly negatively charged palm surface, whereas the anion-selective TJ protein claudin-10a has a positively charged surface (Fig. 4, C and D, and fig. S9A). Thus, the groove in the palm region between the β3-β4 strands and ECH likely lines the paracellular ion pathway, thereby contributing to its ion selectivity.

Further studies are needed to unveil how claudins assemble into strand-like polymers to restrict the intercellular spaces and how the charged residues in the extracellular surfaces line the paracellular pathways. Our crystal structure of a claudin protein, a building block of TJ strands, will advance our molecular understanding of paracellular barriers between epithelial cells in multicellular organisms.

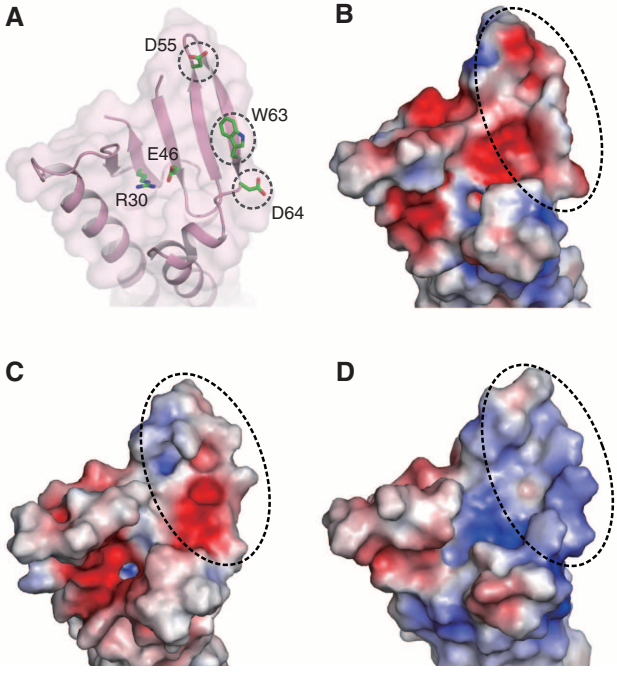

Fig. 4. Charge distribution of the extracellular surface. (**A**) Ribbon diagram and surface representation (transparent) of the extracellular domains. Charged residues and Trp^{63} in ECS1 are shown in stick representation and labeled (D, Asp). Dashed circles indicate the positions of residues that affect the charge-selective properties of claudins. (**B**) Electrostatic potential surface of the extracellular domains viewed as in (A), contoured from −2 *kT/e* (red) to +2 *kT/e* (blue). Dashed oval indicates the β3-β4 region, where residues important for charge selectivity are located. (**C** and **D**) Mapping of the electrostatic potential surfaces generated from the homology models of different claudin subtypes [claudin-2 in (C); claudin-10a in (D)], viewed as in (B).

References and Notes

1. D. W. Powell, *Am. J. Physiol.* **241**, G275–G288 (1981).
2. E. E. Schneeberger, R. D. Lynch, *Am. J. Physiol.* **262**, L647–L661 (1992).
3. V. W. Tang, D. A. Goodenough, *Biophys. J.* **84**, 1660–1673 (2003).
4. C. M. Van Itallie, J. M. Anderson, *Annu. Rev. Physiol.* **68**, 403–429 (2006).
5. L. A. Staehelin, *J. Cell Sci.* **13**, 763–786 (1973).
6. E. E. Schneeberger, R. D. Lynch, *Am. J. Physiol. Cell Physiol.* **286**, C1213–C1228 (2004).
7. M. Furuse, K. Fujita, T. Hiiragi, K. Fujimoto, S. Tsukita, *J. Cell Biol.* **141**, 1539–1550 (1998).
8. M. Furuse, H. Sasaki, K. Fujimoto, S. Tsukita, *J. Cell Biol.* **143**, 391–401 (1998).
9. S. Tsukita, M. Furuse, M. Itoh, *Nat. Rev. Mol. Cell Biol.* **2**, 285–293 (2001).
10. K. Mineta *et al.*, *FEBS Lett.* **585**, 606–612 (2011).
11. D. B. Simon *et al.*, *Science* **285**, 103–106 (1999).
12. S. Hadj-Rabia *et al.*, *Gastroenterology* **127**, 1386–1390 (2004).
13. E. R. Wilcox *et al.*, *Cell* **104**, 165–172 (2001).
14. M. J. Evans *et al.*, *Nature* **446**, 801–805 (2007).
15. D. Günzel, A. S. L. Yu, *Physiol. Rev.* **93**, 525–569 (2013).
16. M. Furuse, S. Tsukita, *Trends Cell Biol.* **16**, 181–188 (2006).
17. S. Angelow, R. Ahlstrom, A. S. L. Yu, *Am. J. Physiol. Renal Physiol.* **295**, F867–F876 (2008).
18. B. Hille, *Ion Channels of Excitable Membranes* (Sinauer Associates, Sunderland, MA, ed. 3, 2001).
19. G. E. Schulz, *Curr. Opin. Struct. Biol.* **10**, 443–447 (2000).
20. S. H. White, *Nature* **459**, 344–346 (2009).
21. See supplementary materials on *Science* Online.
22. K. Hirata *et al.*, *AIP Conf. Proc.* **1234**, 901–904 (2010).
23. J. Li, S. Angelow, A. Linge, M. Zhuo, A. S. L. Yu, *Am. J. Physiol. Cell Physiol.* **305**, C190–C196 (2013).
24. J. M. Anderson, C. M. Van Itallie, *Cold Spring Harb. Perspect. Biol.* **1**, a002584 (2009).
25. S. M. Krug *et al.*, *Ann. N.Y. Acad. Sci.* **1257**, 20–28 (2012).
26. A. Tamura *et al.*, *Gastroenterology* **140**, 913–923 (2011).
27. M. Wada, A. Tamura, N. Takahashi, S. Tsukita, *Gastroenterology* **144**, 369–380 (2013).
28. O. R. Colegio, C. M. Van Itallie, H. J. McCrea, C. Rahner, J. M. Anderson, *Am. J. Physiol. Cell Physiol.* **283**, C142–C147 (2002).
29. A. S. L. Yu *et al.*, *J. Gen. Physiol.* **133**, 111–127 (2009).

Acknowledgments: We thank M. Uji for technical support, T. Suzuki for mass spectrometry, T. Imasaki and Y. Takagi for sharing their unpublished protocol for SeMet incorporation and their technical advice, the beamline staff members at BL32XU of SPring-8 (Hyogo, Japan) for technical help during data collection, and T. Walz for critical reading of the manuscript. Supported by Grants-in-Aid for Scientific Research (S) (22227004, Y.F.; 24227004, O.N.) and (A) (S.T.), Grants-in-Aid

for Scientific Research on Innovative Areas (S.T.), Grants-in-Aid for Young Scientists (B) (K.T.), and Platform for Drug Discovery, Information, and Structural Life Science from the Ministry of Education, Culture, Sports, Science and Technology of Japan; and the Japan New Energy and Industrial Technology Development Organization (NEDO) and the National Institute of Biomedical Innovation (Y.F.). H.S., Y.Y., and A.T. screened claudin genes; H.S. performed protein expression, purification, and electron microscopic studies; T.N. crystallized the mCldn15 protein in lipidic cubic phase, collected and processed diffraction data, and solved and refined the structure; K.T. analyzed the structure; R.I. assisted with x-ray data collection and structure determination; N.D. performed mass spectrometric analyses; H.S., T.N., K.T., S.T., O.N., and Y.F. wrote the manuscript; and S.T., O.N., and Y.F. supervised the research. The authors declare no competing financial interests. Coordinates and structure factors have been deposited in the Protein Data Bank under accession number 4P79.

Supplementary Materials
www.sciencemag.org/content/344/6181/304/suppl/DC1
Materials and Methods
Table S1
Figs. S1 to S11
References (*30*–*47*)

15 November 2013; accepted 26 March 2014
10.1126/science.1248571

The Structural Basis of Pathogenic Subgenomic Flavivirus RNA (sfRNA) Production

Erich G. Chapman,[1,2] David A. Costantino,[1,2] Jennifer L. Rabe,[1] Stephanie L. Moon,[3] Jeffrey Wilusz,[3] Jay C. Nix,[4] Jeffrey S. Kieft[1,2]*

Flaviviruses are emerging human pathogens and worldwide health threats. During infection, pathogenic subgenomic flaviviral RNAs (sfRNAs) are produced by resisting degradation by the 5′→3′ host cell exonuclease Xrn1 through an unknown RNA structure-based mechanism. Here, we present the crystal structure of a complete Xrn1-resistant flaviviral RNA, which contains interwoven pseudoknots within a compact structure that depends on highly conserved nucleotides. The RNA's three-dimensional topology creates a ringlike conformation, with the 5′ end of the resistant structure passing through the ring from one side of the fold to the other. Disruption of this structure prevents formation of sfRNA during flaviviral infection. Thus, sfRNA formation results from an RNA fold that interacts directly with Xrn1, presenting the enzyme with a structure that confounds its helicase activity.

Flaviviruses (FVs, including Dengue, West Nile, Yellow Fever, Japanese Encephalitis, and others) are single-stranded positive-sense RNA viruses and emerging worldwide human health threats (*1*–*3*). During infection by arthropod-borne FVs, not only is the viral genomic RNA (gRNA) replicated, but specific 300- to 500-nucleotide-long subgenomic flaviviral RNAs (sfRNAs) also accumulate (*4*–*9*). These sfRNAs relate directly to disease, being essential for FV pathogenicity in fetal mice and for cytopathicity in cultured cells (*5*), through several proposed mechanisms (*10*–*13*). sfRNAs are produced through incomplete degradation of viral gRNA by the 5′→3′ host-cell exonuclease Xrn1 (*14*), which halts at defined locations within the gRNA's 3′ untranslated region (3′UTR), forming sfRNAs (fig. S1A) (*5*). Biochemical studies suggest that independently folded RNA structures are responsible for this programmed Xrn1 resistance (*15*–*17*); however, the structure-based mechanism remains unknown.

Xrn1 resistance is conferred by discrete RNA sequences conserved across FVs that we refer to as Xrn1-resistant RNAs (xrRNAs) (*15*). Alignment of putative xrRNA sequences (fig. S1B) suggests a shared structure that includes a three-way junction surrounded by conserved nucleotides and the potential to form a pseudoknot (Fig. 1A) (*5*, *16*, *17*). To identify xrRNAs suitable for structural studies, we used a previously validated assay using purified Xrn1 from *Kluyveromyces lactis* to test the Xrn1 resistance of putative xrRNAs from different arthropod-borne FVs (*15*); all were resistant in vitro (fig. S1C). The sequence alignments and functional data suggest that the structure of any one FV xrRNA is representative of all; therefore, we determined the structure of a functional xrRNA from Murray Valley Encephalitis (MVE) Virus (Fig. 1, B and C) to 2.5 Å resolution using x-ray crystallography (fig. S2). The RNA adopts a compact structure with helices P1 and P2 stacked coaxially and helix P3 at an acute angle relative to P1 (Fig. 1D), which is consistent with other RNA three-way junctions of this class (fig. S3) (*18*). Helices P1 and P3 form a ringlike structure defined by nucleotides 33 to 49, which comprise a continuous loop that resides entirely on one side of the structure. The 5′ end of the xrRNA passes directly through the center of the ring, crossing from one side of the structure to the other (fig. S4). The ringlike side of the xrRNA that Xrn1 encounters as it approaches in a 5′→3′ direction (the "front") is concave, with the phosphate backbone defining the rim of the concavity, the major groove as the inner surface, and the RNA that the enzyme must pull into the active site emerging from the center (Fig. 1D). In the crystal structure, the putative RNA pseudoknot is not formed, but the relevant bases are in a conformation where they can readily pair; this would allow the P4-L*4* hairpin to stack under helix P3. The structure shows that the pseudoknot is not essential for folding of the three-way junction, formation of the ring, or placement of the 5′ end through the ring; however, it does enhance resistance (fig S5, A and B). Stem-loop P4-L4 does not interact with the rest of the xrRNA and can be removed without compromising Xrn1 resistance (fig. S5C) (*15*). Upon encountering the xrRNA, Xrn1 must pull the 5′ end of the RNA through the ring. Rather than simply unwinding a prototypical RNA helix, unfolding this xrRNA requires that Xrn1 essentially turn the structure inside out (Fig. 2A). In contrast, the virally encoded RNA-dependent RNA polymerase approaching from the 3′ end during (–) strand synthesis would not encounter this impediment, suggesting that the three-dimensional topology confers the characteristic of unidirectional resistance.

The three-helix junction is the core of the xrRNA structure but is not independently folded; its structure depends on interactions with the 5′ end (Fig. 2B and fig S7, A to C). Specifically, C5 base-pairs with G46, and this pair stacks on a platform formed by intrastrand pairing of U47 with the Hoogsteen face of A49 (Fig. 2B). This stacking diverts the RNA chain to the space between P1 and P3, where U4 makes a base triple in the major groove of the A24-U38 pair; all three of these nucleotides are absolutely conserved. This interaction holds P1 and P3 together in a conformation further stabilized by inner-sphere coordination of a magnesium ion by the phosphates of C5 and A6 (fig. S7D). The next-most 5′ nucleotide, G3, forms a Watson-Crick (WC) base pair with junction nucleotide C40. Disruption of this base pair by mutation of either base (G3C and C40G) abolished the ability of the MVE RNA to resist Xrn1 degradation (Fig. 2C). The double mutant (G3C+C40G), designed to restore the base pairing, did not restore resistance. This is likely due to the formation of incorrect but stable structure induced by mutation, precluding restoration of proper base-pairing interactions in the double mutant (the C40G mutant could form a C-G pair with C22 that G3C cannot compete with). An additional intramolecular interaction involves U2, which was mutated to a G in the crystallized RNA. Nucleotide A41 in the three-way junction is poised to form a Watson-Crick pair with U2 in the wild-type (WT) sequence, and there is covariation between these positions (fig. S1, B and D). Together, this suggests the U2-A41 pair naturally forms; however, the structure folds

[1]Department of Biochemistry and Molecular Genetics, School of Medicine, University of Colorado Denver, Aurora, CO 80045, USA. [2]Howard Hughes Medical Institute, School of Medicine, University of Colorado Denver, Aurora, CO 80045, USA. [3]Department of Microbiology, Immunology and Pathology, Colorado State University, Fort Collins, CO 80523, USA. [4]Molecular Biology Consortium, Advanced Light Source, Lawrence Berkeley National Laboratory, Berkeley, CA 94720, USA.

*Corresponding author. E-mail: jeffrey.kieft@ucdenver.edu

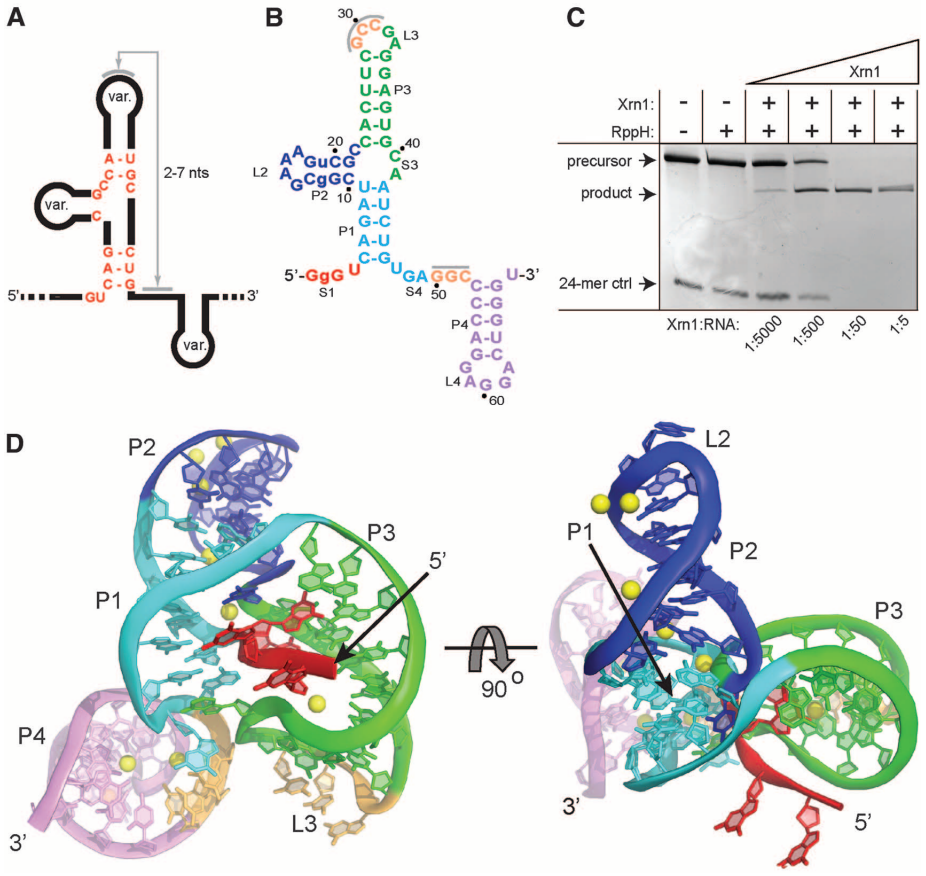

Fig. 1. Crystal structure of an xrRNA. (**A**) Conserved secondary structure and sequence (red) of xrRNAs. "Var." indicates elements of variable size and sequence. (**B**) Crystallized RNA sequence from MVE. Lower-case nucleotides were altered from wild type. The U2G mutation was made to increase transcription yields, but neither this nor the other mutation affected function (C). Gray bars indicate a putative pseudoknot interaction. (**C**) Gel demonstrating Xrn1 resistance by the crystallized RNA, using an assay with Xrn1 from *K. lactis* that was validated in a previous publication (*15*). The precursor is the crystallized RNA with a 30-nt 5′ leader. A 24-oligomer monophosphorylated RNA was included as a control for Xrn1 activity. Under these conditions, each Xrn1 molecule processes multiple copies of the xrRNA, and there is no in-trans protection of the 24-oligomer. This does not preclude a role for sfRNA as a transient Xrn1 inhibitor during infection (*11*, *15*). (**D**) Two views of the structure, colored to match (B). Yellow indicates Mg^{2+} ions.

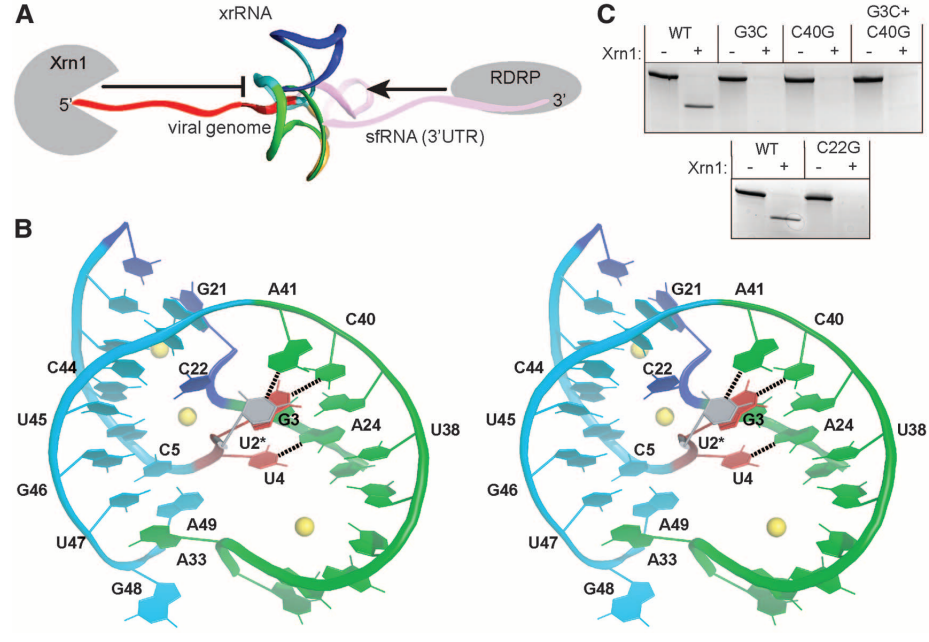

Fig. 2. Formation and importance of the junction and ring structures. (**A**) Structure (backbone ribbon) placed in context with upstream and downstream RNA and enzymes that approach from each side (not to scale). (**B**) Stereo view of the P1-P3 ring and 5′ end of the xrRNA, colored to match (A) and Fig. 1D. U2, which was mutated to a G, is shown modeled in position in gray. Base pairs between the 5′ nucleotides and P3 are shown with dashed lines. (**C**) Xrn1 resistance assays of mutant RNAs based on these interactions (mutant sequences are provided in fig. S6A).

and resists Xrn1 even when it is not present. The only nucleotide in the three-way junction that does not make base pair interactions with the 5′ end of the RNA is C22, which makes hydrogen bonds with U43, C44, and perhaps U45 through phosphates, nucleobase functional groups, and C22's 2′-hydroxyl (fig. S7E). Mutation of conserved C22 (C22G) eliminates Xrn1 resistance in vitro by the crystallized MVE RNA (Fig. 2C), by xrRNAs from Dengue, and from the Kunjin strain of West Nile Virus (WNV_{KUN}; a proven model for FV infection) and also disrupts sfRNA production during WNV_{KUN} infection (*15*).

The U2-A41 and G3-C40 base pairs comprise a second, previously unidentified pseudoknot in the xrRNA structure between S1 and S3 that is interwoven with the S4-L3 pseudoknot (fig. S8). Within the structure, these pseudoknot interactions couple the junction conformation with positioning of the 5′ end of the xrRNA through

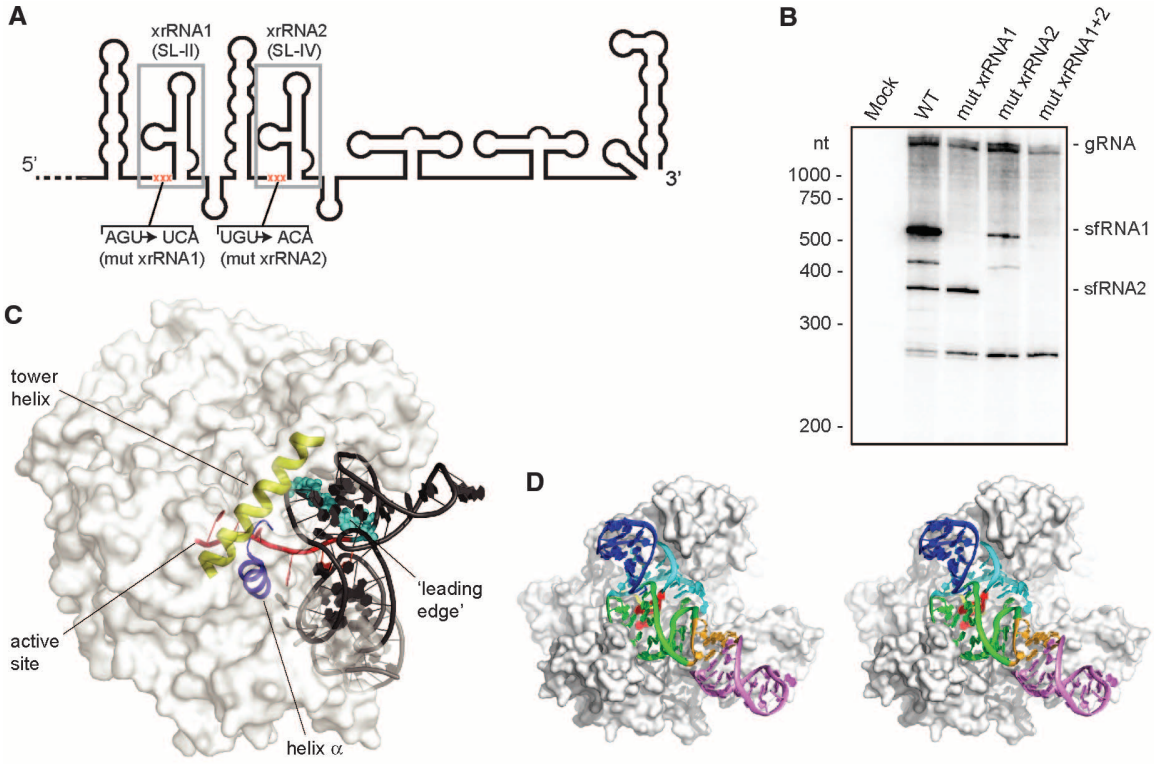

Fig. 3. Importance of the structure during infection and proposed mechanism of resistance. (**A**) Secondary structure cartoon of the 3′UTR from WNV_{KUN}. Two xrRNAs are boxed in gray, and the location of mutations is shown in red. (**B**) Northern blot analysis of total RNA isolated from human cells infected with the wild type and mutant WNV_{KUN} (mutant sequences are provided in fig. S6B). The location of molecular weight markers and the identity of sfRNA species are indicated to the left and right of the blot, respectively. (**C**) Model xrRNA structure on *D. melanogaster* Xrn1 (white surface) (fig. S9). The tower helix (yellow) and helix α (blue) involved in helicase activity, the active site, the RNA entering the active site (red), and leading edge of the helix to be unwound (light blue) are shown. (**D**) Stereo view of model showing how the xrRNA fits in a cleft in Xrn1's surface.

the P1/P3 ring. To test the importance of these structural features during infection, we disrupted the three 5′-most nucleotides in two xrRNA structures in WNV_{KUN} (Fig. 3A and fig. S6B) and monitored sfRNA production during infection in human cells by these viruses. WT virus produces multiple sfRNAs; the two largest, sfRNA1 and sfRNA2, are produced by Xrn resistance of xrRNA1 and xrRNA2, respectively (Fig. 3B). Mutation of xrRNA1 (mut xrRNA1) (fig. S6B) eliminated sfRNA1 production, mutation of xrRNA2 (mut xrRNA2) (fig. S6B) eliminated sfRNA2 production [mut xrRNA2 also decreased sfRNA1 production as has been reported previously (*15*)], and a double mutant (mut xrRNA1+2) (fig. S6B) eliminated both sfRNA1 and sfRNA2, indicating the 5′ end-junction interaction is essential for sfRNA formation during infection. The P1/P3 ring is closed on the side opposite the junction by extrusion and stacking of A33 on the U47-A49 platform at the base of P1 (Fig. 2B). Although folding of the 5′ end with the junction is sufficient to form the ring, we propose that closing of the S4-L3 pseudoknot provides the final "latch" that fully stabilizes the conformation (fig. S5A). Consistent with this, chemical probing suggests that the S4-L3 pseudoknot is conformationally dynamic or transiently formed and that the structure of the three-way junction, the 5′ end, and the pseudoknot are coupled (*15*).

We mapped the 5′ terminus of the RNA product resulting from resistance to a point 2 nucleotides upstream of the 5′ end of the RNA we crystallized (fig. S9A), which is consistent with studies of other xrRNAs (*4*, *5*, *15*, *17*). Using the structure of Xrn1 from *Drosophila melanogaster* bound to a substrate analog (*19*), we modeled the xrRNA structure in position with the last nucleotide to be processed in the Xrn1 active site (Fig. 3, C and D, and fig. S9, B to D). When the enzyme halts, the xrRNA directly contacts Xrn1's surface, positioned in a cleft, with its ring structure braced over the entry to the active site and conserved nucleotides in position to contact the protein (fig. S1D). The Xrn1-xrRNA contacts may further stabilize the xrRNA fold or prevent conformational changes hypothesized to be important for helicase activity. It is proposed that Xrn1's helicase activity is conferred by Brownian motion and the enzyme's "tower helix" and "helix α," which interact and unwind with the leading edge of an RNA duplex as it is pulled into the cleft over the active site (*19*). The model shows that the xrRNA structure is braced against the enzyme, holding the leading edge of the relevant RNA duplex behind the concave ring structure and away from these helices, suggesting a mechanism for RNA structure-driven Xrn1 resistance and, by extension, sfRNA production.

References and Notes

1. S. Bhatt *et al.*, *Nature* **496**, 504–507 (2013).
2. J. S. Mackenzie, D. J. Gubler, L. R. Petersen, *Nat. Med.* **10** (suppl.), S98–S109 (2004).
3. D. Normile, *Science* **342**, 415 (2013).
4. K. C. Lin, H. L. Chang, R. Y. Chang, *J. Virol.* **78**, 5133–5138 (2004).
5. G. P. Pijlman *et al.*, *Cell Host Microbe* **4**, 579–591 (2008).
6. G. Wengler, G. Wengler, H. J. Gross, *Virology* **89**, 423–437 (1978).
7. C. W. Naeve, D. W. Trent, *J. Virol.* **25**, 535–545 (1978).
8. H. Takeda, A. Oya, K. Hashimoto, T. Yasuda, M. A. Yamada, *J. Gen. Virol.* **38**, 281–291 (1978).
9. N. Urosevic, M. van Maanen, J. P. Mansfield, J. S. Mackenzie, G. R. Shellam, *J. Gen. Virol.* **78**, 23–29 (1997).
10. A. Schuessler *et al.*, *J. Virol.* **86**, 5708–5718 (2012).
11. S. L. Moon *et al.*, *RNA* **18**, 2029–2040 (2012).
12. E. Schnettler *et al.*, *J. Virol.* **86**, 13486–13500 (2012).
13. J. A. Roby, G. P. Pijlman, J. Wilusz, A. A. Khromykh, *Viruses* **6**, 404–427 (2014).
14. C. I. Jones, M. V. Zabolotskaya, S. F. Newbury, *Wiley Interdiscip. Rev. RNA* **3**, 455–468 (2012).
15. E. G. Chapman, S. L. Moon, J. Wilusz, J. S. Kieft, *eLife* (2014).
16. A. Funk *et al.*, *J. Virol.* **84**, 11407–11417 (2010).
17. P. A. Silva, C. F. Pereira, T. J. Dalebout, W. J. Spaan, P. J. Bredenbeek, *J. Virol.* **84**, 11395–11406 (2010).
18. A. Lescoute, E. Westhof, *RNA* **12**, 83–93 (2006).
19. M. Jinek, S. M. Coyle, J. A. Doudna, *Mol. Cell* **41**, 600–608 (2011).

Acknowledgments: We thank the members of the Kieft Lab for discussions and A. Ferré-d'Amaré, M. Johnston, and R. Batey for critical reading of this

manuscript. The University of Colorado Denver X-ray Facility is supported by University of Colorado Cancer Center Support Grant P30CA046934. J.S.K. is an Early Career Scientist of the Howard Hughes Medical Institute. J.W. was supported by a NIH award through the Rocky Mountain Regional Center of Excellence, U54 AI-065357. Coordinates and structure factors have been deposited with Protein Data Bank accession code 4PQV.

Supplementary Materials
www.sciencemag.org/content/344/6181/307/suppl/DC1
Materials and Methods
Figs. S1 to S9
Table S1
References

15 January 2014; accepted 24 March 2014
10.1126/science.1250897

The STAT3-Binding Long Noncoding RNA lnc-DC Controls Human Dendritic Cell Differentiation

Pin Wang,[1,2] Yiquan Xue,[1] Yanmei Han,[1] Li Lin,[2] Cong Wu,[3] Sheng Xu,[1] Zhengping Jiang,[1] Junfang Xu,[3] Qiuyan Liu,[1] Xuetao Cao[1,2,3]*

Long noncoding RNAs (lncRNAs) play important roles in diverse biological processes; however, few have been identified that regulate immune cell differentiation and function. Here, we identified lnc-DC, which was exclusively expressed in human conventional dendritic cells (DCs). Knockdown of lnc-DC impaired DC differentiation from human monocytes in vitro and from mouse bone marrow cells in vivo and reduced capacity of DCs to stimulate T cell activation. lnc-DC mediated these effects by activating the transcription factor STAT3 (signal transducer and activator of transcription 3). lnc-DC bound directly to STAT3 in the cytoplasm, which promoted STAT3 phosphorylation on tyrosine-705 by preventing STAT3 binding to and dephosphorylation by SHP1. Our work identifies a lncRNA that regulates DC differentiation and also broadens the known mechanisms of lncRNA action.

The mammalian genome transcribes numerous long noncoding RNAs (lncRNAs), and only some of them have been functionally characterized (*1*). Although a number of lncRNA molecules have been reported to play crucial roles in diverse processes and diseases (*2*–*4*), only a few examples of lncRNAs that regulate the immune system have been described (*5*–*7*).

Dendritic cells (DCs) are the most potent antigen-presenting cells in mammalian immune systems; their differentiation and function influences the outcome of innate and adaptive immune response (*8*). Although several transcription factors (*9*, *10*) and cytokines (*11*) have been identified as playing critical roles in the generation and homeostasis of DC populations, whether noncoding RNA, especially lncRNAs, play a role in DC differentiation and function is largely unknown.

Unlike the well-established mechanism of microRNA action, which is based on seed sequence base-pairing (*12*, *13*), lncRNAs' mode of action remains to be fully understood (*14*). A few lncRNAs exert their functions through interacting with heteronuclear proteins or chromatin modification complexes in the nucleus (*15*–*18*), whereas others are reported to affect mRNA stability or translation in the cytoplasm (*19*–*21*). Whether there are other unknown functional modes for lncRNAs is unclear.

To identify lncRNAs involved in DC differentiation and function, we utilized the well-accepted model of human DC differentiation from peripheral blood monocytes (*22*) and conducted transcriptome microarray analysis (Fig. 1A) and RNA sequencing (RNA-seq) (Fig. 1B). Both methods identified a modestly conserved intergenic lncRNA

[1]National Key Laboratory of Medical Immunology and Institute of Immunology, Second Military Medical University, Shanghai 200433, China. [2]National Key Laboratory of Molecular Biology and Department of Immunology, Institute of Basic Medical Sciences, Chinese Academy of Medical Sciences, Beijing 100005, China. [3]Institute of Immunology, Zhejiang University School of Medicine, Hangzhou 310058, China.

*Corresponding author. E-mail: caoxt@immunol.org

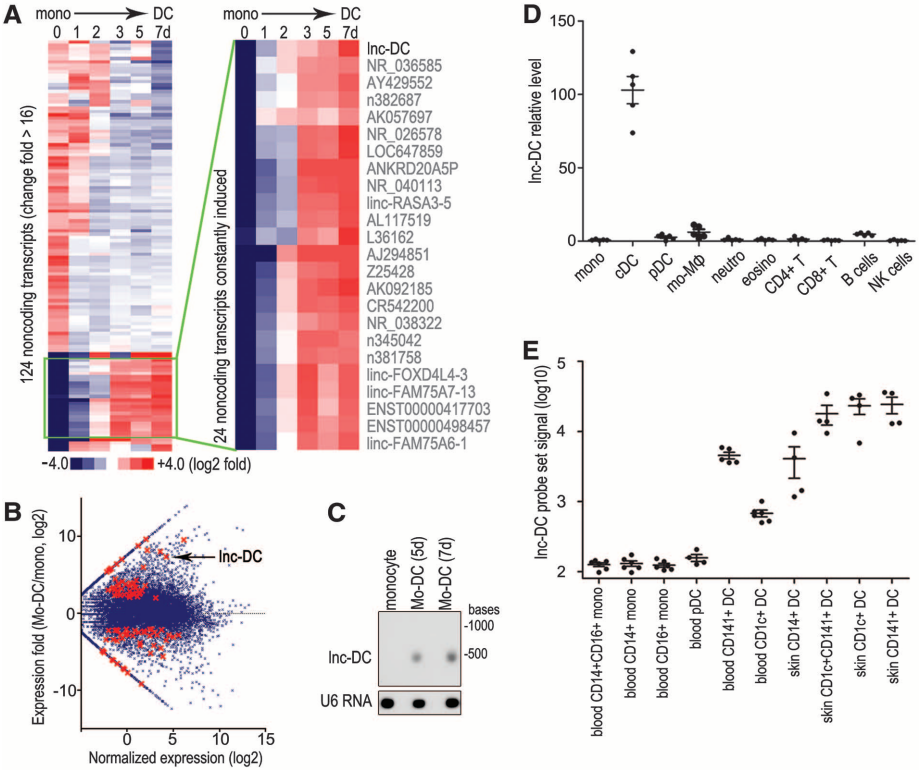

Fig. 1. lnc-DC is highly expressed in human cDC subsets. (A) The cluster heat map shows lncRNAs with expression change fold >16 from microarray data ($P < 0.05$). **(B)** Ratio of gene expression in Mo-DC to monocytes (vertical axis) and average expression of genes in Mo-DC versus that in monocytes (horizontal axis), presented as a Bland-Altman plot of our RNA-seq analysis. Highlighted in red are 99 lncRNAs with significant changes in expression (fold > 4, false discovery rate < 0.05). **(C)** Northern blotting of lnc-DC in monocytes and Mo-DC. U6 RNA serves as a loading control. Unless noted otherwise, all results in this and other figures were representative of at least three independent experiments. **(D)** qPCR detection of lnc-DC in immune cell subsets sorted from human peripheral blood. Data are normalized to glyceraldehyde-3-phosphate dehydrogenase (GAPDH) expression and monocytes (mono), which are set to a value of 1. NK cells, natural killer cells. **(E)** lnc-DC expression levels (signal intensity of probe set ILMN_3200140) in distinct DC/mono subsets of human blood and skin from GSE35457 data.

(Gene symbol LOC645638) (fig. S1), which was robustly induced in the process of human DC differentiation from monocytes (referred to as lnc-DC hereafter). Northern blot confirmed its high expression in monocyte-derived DCs (Mo-DCs) (Fig. 1C). Detection in sorted DC populations and other immunocytes from human peripheral blood revealed that lnc-DC was exclusively expressed in $Lin^{-}MHC\text{-}II^{+}CD11c^{+}$ conventional DC (cDCs) (Fig. 1D). Furthermore, transcriptome microarray analysis of distinct DC subsets sorted from human skin and blood (*23*) confirmed that lnc-DC was specifically expressed in all of these cDC subsets (Fig. 1E). RNA-seq data from the ENCODE project (*24*) also showed low or absent lnc-DC expression in human blood $CD20^{+}$ B cells, $CD14^{+}$ monocytes, mobilized $CD34^{+}$ hematopoietic progenitor cells, and the human embryonic stem cell line H1 (fig. S2). Thus, lnc-DC is exclusively expressed in cDCs of the hematopoietic system and may be a specific marker of cDCs (fig. S3).

We identified two transcript variants of lnc-DC in Mo-DCs [417 and 397 nucleotides (nt)] (fig. S4A), of which the 417-nt variant was expressed more highly (fig. S4B). Like most intergenic lncRNAs, lnc-DC had polyA tail and 5′ cap structure (fig. S5A) but was without coding capacity (fig. S5B).

Because the expression of lnc-DC in cDCs was both specific and stable, we investigated whether this was the result of epigenetic changes that occurred during DC differentiation. We performed

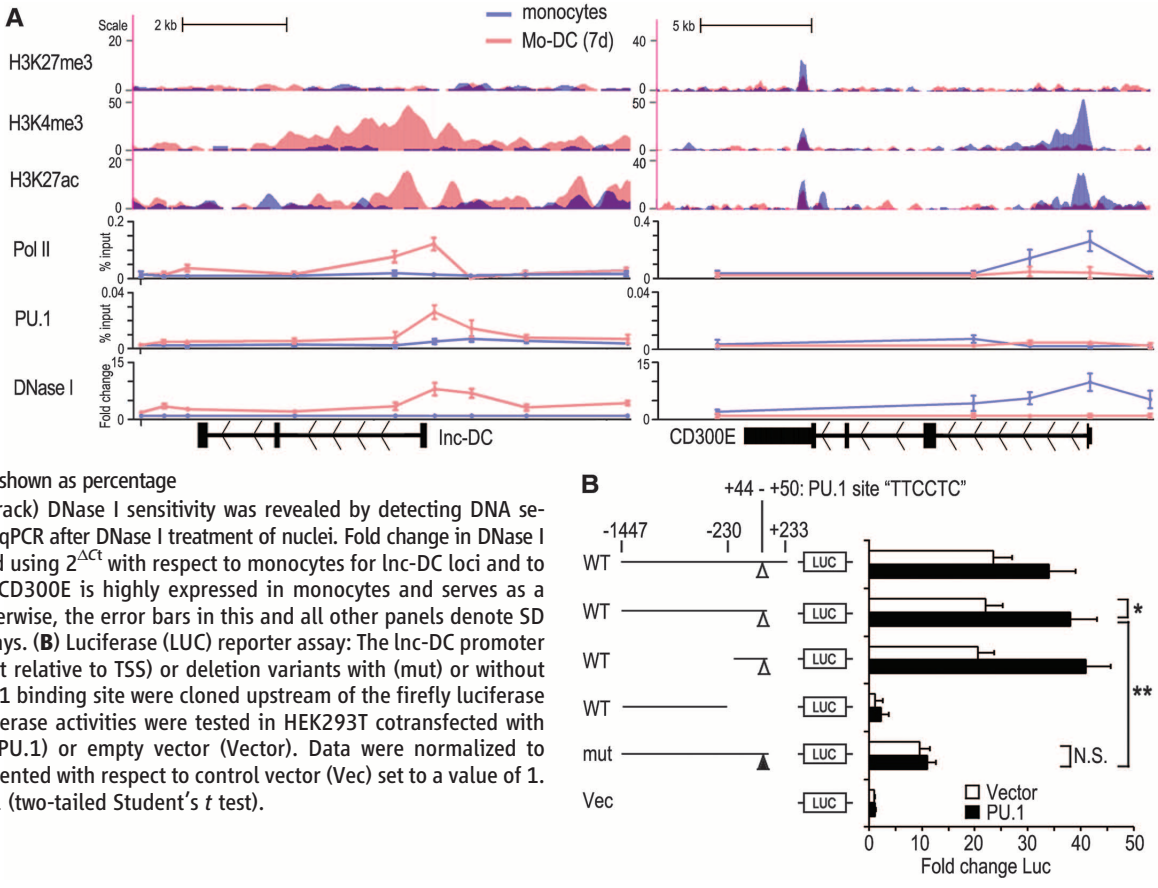

Fig. 2. The exclusive expression of lnc-DC in DC is attributed to acquired active histone modifications, accessible chromatin structures, and PU.1 binding at the promoter region. (**A**) (Upper three tracks) Indicated histone modifications were analyzed by ChIP-seq, and data are shown as reads density around lnc-DC loci. (Middle two tracks) PU.1 and Pol II occupancy were analyzed by multisite ChIP-qPCR. Normalized data are shown as percentage of input control. (Lower track) DNase I sensitivity was revealed by detecting DNA sequence integrality through qPCR after DNase I treatment of nuclei. Fold change in DNase I sensitivity was determined using $2^{\Delta Ct}$ with respect to monocytes for lnc-DC loci and to Mo-DC for CD300E loci. CD300E is highly expressed in monocytes and serves as a control. Unless noted otherwise, the error bars in this and all other panels denote SD ($n \geq 3$ replicates). 7d, 7 days. (**B**) Luciferase (LUC) reporter assay: The lnc-DC promoter region (−1447 to +233 nt relative to TSS) or deletion variants with (mut) or without (WT) mutations in the PU.1 binding site were cloned upstream of the firefly luciferase coding region. Their luciferase activities were tested in HEK293T cotransfected with PU.1 expression vector (PU.1) or empty vector (Vector). Data were normalized to renilla luciferase and presented with respect to control vector (Vec) set to a value of 1. $^{*}P < 0.05$ and $^{**}P < 0.01$ (two-tailed Student's *t* test).

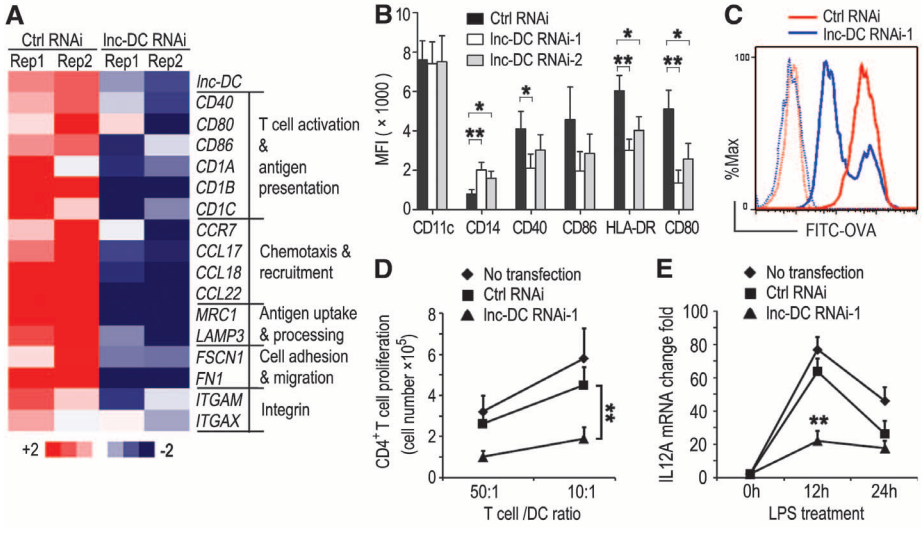

Fig. 3. Knockdown of lnc-DC impairs DC differentiation and function. (**A**) Indicated gene expression levels from our transcriptome microarray analysis in cells after 7 days of DC culture from monocytes with lentivirus-mediated lnc-DC RNAi or its control. (**B**) Flow cytometry of indicated surface markers of cells as in (A). Data are mean fluorescence intensity (MFI) ± SD, × 1000; $n = 3$. (**C**) Uptake of fluorescein isothiocyanate–ovalbumin (FITC-OVA) was measured by flow cytometry in cells after 5 days of DC culture from monocytes with lnc-DC RNAi or its control. Dashed lines represent 4°C controls. (**D**) $CD4^{+}$ T cell proliferation as measured by cell numbers after 5 days of coculture with allogeneic Mo-DC or cells with lnc-DC knockdown. (**E**) Quantitative RT-PCR of human IL-12A in cells stimulated with LPS (300 ng/ml) for the indicated time after 5 days of DC culture from monocytes with or without lnc-DC knockdown. $^{*}P < 0.05$ and $^{**}P < 0.01$ (two-tailed Student's *t* test).

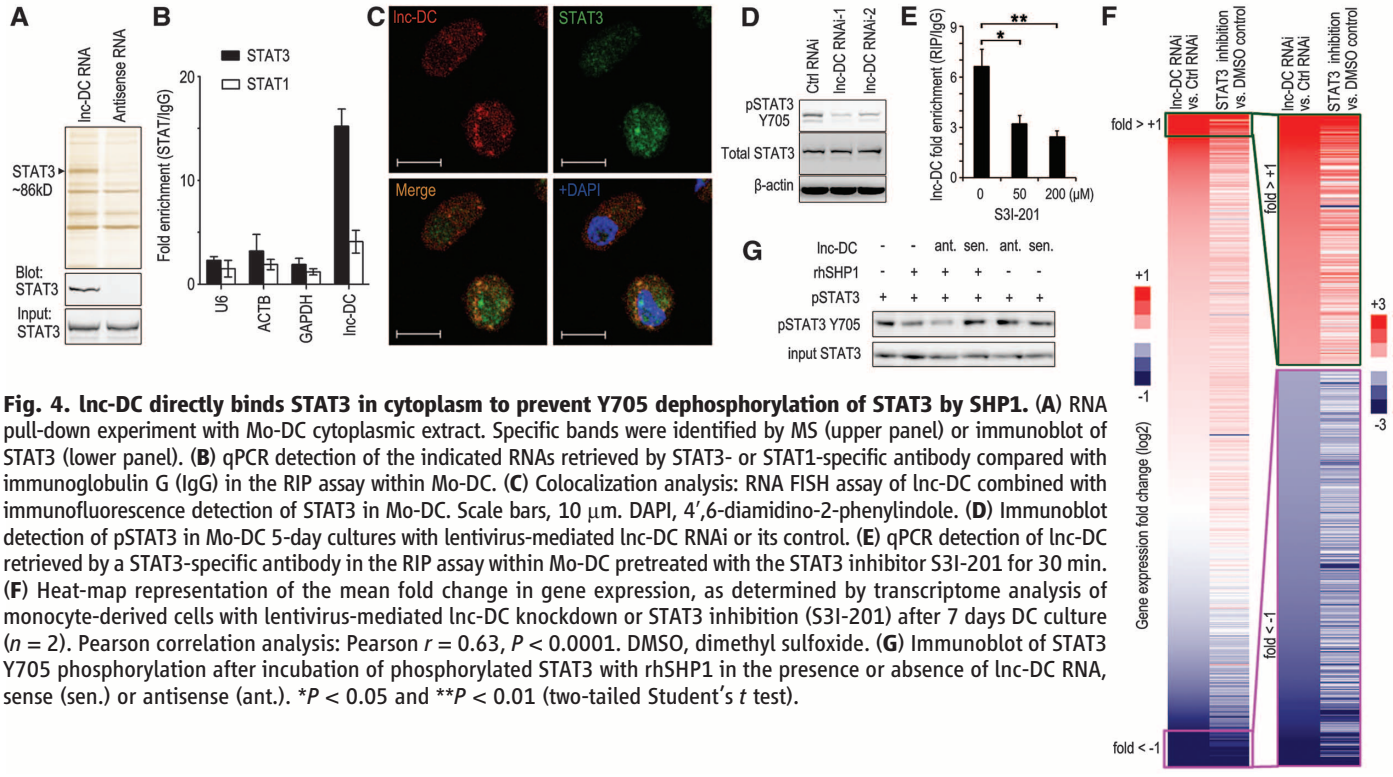

Fig. 4. lnc-DC directly binds STAT3 in cytoplasm to prevent Y705 dephosphorylation of STAT3 by SHP1. (**A**) RNA pull-down experiment with Mo-DC cytoplasmic extract. Specific bands were identified by MS (upper panel) or immunoblot of STAT3 (lower panel). (**B**) qPCR detection of the indicated RNAs retrieved by STAT3- or STAT1-specific antibody compared with immunoglobulin G (IgG) in the RIP assay within Mo-DC. (**C**) Colocalization analysis: RNA FISH assay of lnc-DC combined with immunofluorescence detection of STAT3 in Mo-DC. Scale bars, 10 μm. DAPI, 4′,6-diamidino-2-phenylindole. (**D**) Immunoblot detection of pSTAT3 in Mo-DC 5-day cultures with lentivirus-mediated lnc-DC RNAi or its control. (**E**) qPCR detection of lnc-DC retrieved by a STAT3-specific antibody in the RIP assay within Mo-DC pretreated with the STAT3 inhibitor S3I-201 for 30 min. (**F**) Heat-map representation of the mean fold change in gene expression, as determined by transcriptome analysis of monocyte-derived cells with lentivirus-mediated lnc-DC knockdown or STAT3 inhibition (S3I-201) after 7 days DC culture ($n = 2$). Pearson correlation analysis: Pearson $r = 0.63$, $P < 0.0001$. DMSO, dimethyl sulfoxide. (**G**) Immunoblot of STAT3 Y705 phosphorylation after incubation of phosphorylated STAT3 with rhSHP1 in the presence or absence of lnc-DC RNA, sense (sen.) or antisense (ant.). $*P < 0.05$ and $**P < 0.01$ (two-tailed Student's t test).

chromatin immunoprecipitation sequencing (ChIP-seq) and multisite ChIP–quantitative polymerase chain reaction (qPCR) to examine the major histone modifications and RNA polymerase II (Pol II) occupancy in monocytes and Mo-DC (Fig. 2A). We found high occupancy of Pol II around the lnc-DC transcription start site (TSS) in Mo-DCs (Fig. 2A, Pol II track), consistent with its high expression. Histone H3–lysine-4 trimethylation (H3K4me3) and histone H3–lysine-27 acetylation (H3K27ac), two histone modifications that positively regulate transcription, were markedly enhanced in Mo-DCs around the TSS (Fig. 2A). Accordingly, chromatin accessibility as measured by deoxyribonuclease (DNase) I sensitivity increased in Mo-DCs near the TSS (Fig. 2A), suggesting that an open chromatin structure formed during DC differentiation, probably due to H3K4me3 and H3K27ac modification. In contrast, our data from monocyte-derived macrophages (Mo-MΦ) (fig. S6) and ENCODE (Encyclopedia of DNA Elements) project data of other immunocytes (fig. S7) suggested that chromatin structures on lnc-DC loci in these cells were maintained in a compact state, and H3K4me3 and H3K27ac were mainly at low levels. On the basis of these results, we propose that the accessible chromatin structure and active histone modifications on lnc-DC loci contribute to the specific expression seen in human cDCs.

In the lnc-DC promoter region, we found a canonical binding motif (+44 to +50 nt relative to TSS) for the transcription factor PU.1, which is a key regulator of DC differentiation (*10*, *25*). ChIP-qPCR confirmed PU.1 binding to this region in Mo-DC (Fig. 2A, PU.1 track), indicating that PU.1 is involved in lnc-DC transcription. The lnc-DC promoter regions with or without PU.1 motif mutation were then cloned upstream of the firefly luciferase coding region (Fig. 2B, left). Luciferase expression was high only when the wild-type PU.1 motif was present and could be further enhanced by PU.1 overexpression (Fig. 2B, right). These results suggest that PU.1 directs lnc-DC expression in human cDCs.

To investigate the role of lnc-DC in human DCs, we used lentivirus-mediated RNA interference (RNAi) to knockdown lnc-DC during Mo-DC differentiation. lnc-DC knockdown resulted in a considerable change in gene expression (664 coding genes changed, fold > 2, $P < 0.05$; fig. S8) and many DC function–related genes were down-regulated (Fig. 3A). Analysis of protein expression by flow cytometry confirmed the microarray data, and we found that CD40, CD80, CD86, and HLA-DR (molecules important for T cell activation) were down-regulated, whereas the monocyte marker CD14 was up-regulated by lnc-DC knockdown (Fig. 3B). Functionally, we found that lnc-DC knockdown impaired antigen uptake by Mo-DC (Fig. 3C) and also impaired their ability to induce allogeneic $CD4^+$ T cell proliferation (Fig. 3D) and cytokine production (fig. S9). Overexpression of lnc-DC had the opposite effect (fig. S10). Production of the cytokine interleukin (IL)–12 upon lipopolysaccharide (LPS) stimulation was attenuated by lnc-DC knockdown (Fig. 3E and fig. S11A), whereas IL-10 was unaffected (fig. S11B). Knockdown of lnc-DC did not affect cell viability (fig. S12). These data indicate that lnc-DC is essential for optimal human DC differentiation from monocytes and DC function. Knockdown of the mouse lnc-DC ortholog (Gene symbol 1100001G20Rik) in bone marrow cells resulted in impaired mouse DC differentiation in vitro (fig. S13, A and B) and in vivo (fig. S13C). Taken together, our data suggest that lnc-DC is vital for DC differentiation in both human and mice.

We next sought to determine the underlying molecular mechanism by which lnc-DC regulated DC differentiation. Because knockdown of lnc-DC had no effect on the expression of its nearby coding genes (fig. S14), we excluded the possibility that lnc-DC acts by influencing its nearby genes in cis. RNA fluorescent in situ hybridization (FISH) and reverse transcription (RT)–PCR of nuclear and cytoplasmic fractions (fig. S15) suggested that lnc-DC was located in the cytoplasm. Two mechanisms have been reported for cytoplasmic lncRNA action: (i) sequestration of microRNA to restore mRNA translation as a competing endogenous RNA (*19*, *20*) or (ii) action through an ALU element to promote STAU1-mediated mRNA decay (*21*). However, RNA immunoprecipitation (RIP) revealed that lnc-DC was not associated with the AGO2 protein, a key component of the microRNA-containing RISC complex (fig. S16), and bioinformatics analysis indicated there was no ALU element in the lnc-DC sequence. Therefore, it seemed that cytoplasmic lnc-DC might exert its function in a previously unknown manner.

We next performed pull-down assays with biotinylated lnc-DC, followed by mass spectrometry (MS) to search for potential lnc-DC–interacting proteins. STAT3 (signal transducer and activator

of transcription 3), a transcription factor that regulates DC differentiation (*9*), was identified as a lnc-DC–associated protein, and this was confirmed by independent immunoblot (Fig. 4A). RIP further verified the specificity of this interaction (Fig. 4B). Moreover, RNA FISH followed by immunofluorescence showed lnc-DC colocalized with STAT3 in the cytoplasm but not the nucleus of DCs (Fig. 4C), indicating that lnc-DC may regulate cytoplasmic STAT3 activity. Analysis of lnc-DC truncation mutants revealed that the 3′-end segment of lnc-DC (nucleotides 265 to 417) was sufficient to bind STAT3 (fig. S17A). RNA folding analyses (*26*) of this 3′ region indicated a stable stem-loop structure (fig. S17B), which might provide the necessary spatial conformation for the interaction. RIP (fig. S18A), biotin-RNA pull-down assay (fig. S18B), and confocal analysis (fig. S18C) with full-length or truncated STAT3 demonstrated that the C terminus of STAT3 (residues 583 to 770) interacted with lnc-DC. Because this portion contains Tyr^{705} (Y705), whose phosphorylation is crucial for STAT3 activation and nuclear translocation (*27*), we wondered whether the binding of lnc-DC affects STAT3 phosphorylation status. Immunoblotting revealed that STAT3 Y705 phosphorylation was reduced by lnc-DC knockdown in Mo-DC and mouse bone marrow cells (Fig. 4D and fig. S13D), and subsequent STAT3 nuclear translocation was decreased (fig. S19A). Ectopic expression of lnc-DC enhanced STAT3 luciferase reporter activity in human embryonic kidney 293 T cells (HEK293T cells) (fig. S19B) and STAT3 Y705 phosphorylation in THP1 cells (fig. S19C). Furthermore, our protein posttranslational modification analysis of STAT3 revealed that only Y705 phosphorylation was enhanced by lnc-DC (fig. S20 and table S1). These data suggest that cytoplasmic lnc-DC promotes STAT3 signaling.

The pharmacological inhibitor of STAT3, S3I-201, which targets the C-terminal structure of STAT3 (*28*), could attenuate lnc-DC interaction with STAT3 in a dose-dependent manner (Fig. 4E). Furthermore, transcriptome microarray analysis revealed that treatment of Mo-DC with S3I-201 resulted in similar effects on gene expression as seen with lnc-DC knockdown (Fig. 4F). Many known STAT3 target genes were affected by lnc-DC knockdown (fig. S21). Functionally, administration of STAT3 inhibitors impaired Mo-DC differentiation from monocytes and attenuated DC function in a manner similar to lnc-DC knockdown (fig. S22). Thus, we propose that lnc-DC promotes DC differentiation through STAT3 signaling.

Mass spectrometric analysis of STAT3-interacting proteins affected by lnc-DC led us to focus on SHP1 (fig. S23A), a protein tyrosine phosphatase and an important negative regulator of cellular signaling pathways, including Jak/STAT signaling. Coimmunoprecipitation confirmed that knockdown of lnc-DC promoted the association of SHP1 with STAT3 in Mo-DC (fig. S23, B and C), and overexpression of lnc-DC attenuated SHP1-STAT3 interaction in HEK293T cells (fig. S23, D and E). Furthermore, an in vitro phosphatase assay with recombinant human protein SHP1 showed that lnc-DC, but not the antisense control RNA, protected STAT3 from Y705 dephosphorylation by SHP1 (Fig. 4G). Taken together, our results demonstrate that, during DC differentiation, lnc-DC promotes STAT3 signaling by interacting with the C terminus of STAT3 to prevent dephosphorylation of STAT3 Y705 by SHP1 (fig. S24).

Our work suggests that lncRNAs can affect cellular differentiation and function by directly interacting with signaling molecules in the cytoplasm and regulating their posttranslational modification. Whether other cytoplasmic lncRNAs perform their functions in a manner similar to lnc-DC is currently unclear. lnc-DC, as a specific regulator of DC differentiation and function, may have potential relevance to clinical diseases involving DC dysfunction and may aid the design of DC vaccines with more potency to activate T cell responses.

References and Notes

1. P. Johnsson, L. Lipovich, D. Grandér, K. V. Morris, *Biochim. Biophys. Acta* **1840**, 1063–1071 (2014).
2. O. Wapinski, H. Y. Chang, *Trends Cell Biol.* **21**, 354–361 (2011).
3. M. Sauvageau *et al.*, *eLife* **2**, e01749 (2013).
4. J. L. Rinn, H. Y. Chang, *Annu. Rev. Biochem.* **81**, 145–166 (2012).
5. Z. Li *et al.*, *Proc. Natl. Acad. Sci. U.S.A.* **111**, 1002–1007 (2014).
6. S. Carpenter *et al.*, *Science* **341**, 789–792 (2013).
7. G. Hu *et al.*, *Nat. Immunol.* **14**, 1190–1198 (2013).
8. P. Guermonprez *et al.*, *Nat. Med.* **19**, 730–738 (2013).
9. Y. Laouar, T. Welte, X. Y. Fu, R. A. Flavell, *Immunity* **19**, 903–912 (2003).
10. S. Carotta *et al.*, *Immunity* **32**, 628–641 (2010).
11. M. Merad, P. Sathe, J. Helft, J. Miller, A. Mortha, *Annu. Rev. Immunol.* **31**, 563–604 (2013).
12. L. A. O'Neill, F. J. Sheedy, C. E. McCoy, *Nat. Rev. Immunol.* **11**, 163–175 (2011).
13. M. S. Ebert, P. A. Sharp, *Cell* **149**, 515–524 (2012).
14. T. R. Mercer, J. S. Mattick, *Nat. Struct. Mol. Biol.* **20**, 300–307 (2013).
15. K. V. Morris, S. Santoso, A. M. Turner, C. Pastori, P. G. Hawkins, *PLOS Genet.* **4**, e1000258 (2008).
16. P. Johnsson *et al.*, *Nat. Struct. Mol. Biol.* **20**, 440–446 (2013).
17. M. Huarte *et al.*, *Cell* **142**, 409–419 (2010).
18. U. A. Ørom *et al.*, *Cell* **143**, 46–58 (2010).
19. M. Cesana *et al.*, *Cell* **147**, 358–369 (2011).
20. Y. Tay *et al.*, *Cell* **147**, 344–357 (2011).
21. C. Gong, L. E. Maquat, *Nature* **470**, 284–288 (2011).
22. See supplementary materials and methods on *Science* Online.
23. M. Haniffa *et al.*, *Immunity* **37**, 60–73 (2012).
24. S. Djebali *et al.*, *Nature* **489**, 101–108 (2012).
25. A. Guerriero, P. B. Langmuir, L. M. Spain, E. W. Scott, *Blood* **95**, 879–885 (2000).
26. A. R. Gruber, R. Lorenz, S. H. Bernhart, R. Neuböck, I. L. Hofacker, *Nucleic Acids Res.* **36** (suppl. 2), W70–W74 (2008).
27. J. J. O'Shea, R. Plenge, *Immunity* **36**, 542–550 (2012).
28. K. Siddiquee *et al.*, *Proc. Natl. Acad. Sci. U.S.A.* **104**, 7391–7396 (2007).

Acknowledgments: We thank M. Jin and P. Ma for technical assistance; W. Ge, P. Zhang, and X. Xu for helpful discussions; and Q. Li of Genminix Informatics for bioinformatics assistance. The data presented in this paper are tabulated in the main paper and in the supplementary materials. Our transcriptome microarray data and RNA-seq data are deposited in Gene Expression Omnibus (GEO) under the accession nos. GSE54143 and GSE54401, respectively, and our ChIP-seq data are deposited in GEO under the accession no. GSE43036. This work is supported by grants from the National Key Basic Research Program of China (2013CB530502) and the National Natural Science Foundation of China (31390431, 81230074, and 81123006). X.C. and P.W. designed the experiments; P.W., Y.X., Y.H., L.L., C.W., S.X., Z.J., J.X., and Q.L. performed the experiments; X.C. and P.W. analyzed data and wrote the paper; and X.C. was responsible for research supervision, coordination, and strategy. We declare no competing financial interests.

Supplementary Materials

www.sciencemag.org/content/344/6181/310/suppl/DC1
Materials and Methods
Figs. S1 to S24
Tables S1
References (*29*–*38*)

28 January 2014; accepted 26 March 2014
10.1126/science.1251456

Enhancing Depression Mechanisms in Midbrain Dopamine Neurons Achieves Homeostatic Resilience

Allyson K. Friedman,[1] Jessica J. Walsh,[1,2] Barbara Juarez,[1,2] Stacy M. Ku,[1,2] Dipesh Chaudhury,[1] Jing Wang,[3] Xianting Li,[3] David M. Dietz,[4] Nina Pan,[3] Vincent F. Vialou,[4] Rachael L. Neve,[5] Zhenyu Yue,[3,4] Ming-Hu Han[1,4]*

Typical therapies try to reverse pathogenic mechanisms. Here, we describe treatment effects achieved by enhancing depression-causing mechanisms in ventral tegmental area (VTA) dopamine (DA) neurons. In a social defeat stress model of depression, depressed (susceptible) mice display hyperactivity of VTA DA neurons, caused by an up-regulated hyperpolarization-activated current (I_h). Mice resilient to social defeat stress, however, exhibit stable normal firing of these neurons. Unexpectedly, resilient mice had an even larger I_h, which was observed in parallel with increased potassium (K^+) channel currents. Experimentally further enhancing I_h or optogenetically increasing the hyperactivity of VTA DA neurons in susceptible mice completely reversed depression-related behaviors, an antidepressant effect achieved through resilience-like, projection-specific homeostatic plasticity. These results indicate a potential therapeutic path of promoting natural resilience for depression treatment.

Resilience is the brain's capacity to cope with environmental stress and to achieve stable psychological functioning in response to prolonged stress (*1*–*3*). Multiple psychological techniques are used to promote resilience to stress. Specifically, active coping strategies, in

which qualities or perceptions of stressors are reassessed, as opposed to avoidant coping, have proven to promote behavioral adaptability and achieve psychological resilience (*4*, *5*). To understand the neurobiological mechanisms underlying stress resilience, tremendous efforts have been made to investigate the genetic, molecular, and developmental aspects of this phenomenon (*1*, *3*, *6*, *7*). Despite many advances, the neurophysiological processes determining the brain's ability to cope with stress are still poorly understood.

Multiple lines of evidence implicate dysregulation in the brain's reward neural circuit in depression (*1*, *8*–*11*). In a well-established chronic social defeat model of depression, susceptible and resilient phenotypes have been successfully segregated after a 10-day social defeat paradigm (*1*, *9*, *12*, *13*). Multiple depressive symptoms in susceptible mice have been causally linked to hyperactivity of ventral tegmental area (VTA) dopamine (DA) neurons (*1*, *9*, *12*). Optogenetic activation of these neurons promotes susceptible phenotype, whereas optogenetic reduction of the hyperactivity reverses depression-related behaviors (*9*). This increase in VTA DA neuron firing in susceptible mice is known to be intrinsically induced by up-regulation of hyperpolarization-activated cation channel–mediated current (I_h), an excitatory driving force in VTA DA neurons (*12*, *14*, *15*). Pharmacological reduction of the increased I_h in susceptible mice reverses depression-related symptoms (*12*). Chronic antidepressant fluoxetine treatment normalizes the hyperactivity and decreases I_h in these neurons (*12*). These observations suggest that hyperactivity and increased excitatory I_h in VTA DA neurons are both pathophysiological adaptations underlying the susceptible phenotype.

To understand the neurophysiological mechanisms of the resilient phenotype after chronic social stress, we used tyrosine hydroxylase–driven green fluorescent protein (TH-GFP) transgenic mice to visualize and reliably record from VTA DA neurons (fig. S1A). TH-GFP mice that undergo chronic social defeat stress reliably separate into either susceptible or resilient phenotypes on the basis of social interaction ratios (fig. S1, B and C) (*1*, *9*, *12*, *13*). Susceptible TH-GFP mice showed social avoidance, spending significantly less time in the interaction zone, whereas resilient mice spent a significant amount of time with the social target, similar to the time spent by control mice (fig. S1, D to G). Susceptible mice also display other depression-related anhedonic behaviors (fig. S1H) (*1*, *7*). We confirmed pathophysiological hyperactivity in the GFP-visualized DA neurons of susceptible TH-GFP mice (fig. S1I), whereas the pacemaker firing pattern was the same in the three groups. Overall, the resilient TH-GFP mice exhibited a stable control level firing of VTA DA neurons and appeared not to have undergone any pathogenic changes at cellular and behavioral levels in response to chronic social defeat stress (fig. S1, D to I, and fig. S2).

We next investigated whether the pathophysiological increase in I_h current is normalized in resilient mice. We performed whole-cell voltage-clamp recordings in GFP^+ VTA DA neurons in brain slices from control, susceptible, and resilient TH-GFP mice. In accordance with previous findings (*12*), I_h was increased in susceptible mice (Fig. 1A). However, unexpectedly, rather than a normalization of the I_h levels in resilient mice, the resilient phenotype showed an even larger significant increase in I_h when compared with susceptible and control mice (Fig. 1A). This was surprising and unanticipated because an increase in I_h was viewed as a stress-induced, pathological ion mechanism in susceptible mice.

To understand how VTA DA neurons in resilient mice maintain a level of firing similar to that of control mice with this extremely larger I_h, we focused on K^+ channels, an inhibitory driving force that was up-regulated selectively in the resilient subgroup in a previous microarray analysis (*1*). The VTA DA neurons of resilient mice, which displayed a further enhanced I_h, simultaneously exhibited significantly increased K^+ channel–mediated peak and sustained currents (Fig. 1B), which implicate multiple K^+ channel types mediating this increase in K^+ currents.

To investigate a possible benefit of resilient mice recruiting these extra channel functions, we measured intrinsic excitabilities of VTA DA neurons in the three groups. In response to a series of current injections, we observed an increase in spike number in susceptible mice and, inversely, a reduction in spike number in resilient mice, as compared with control mice (Fig. 1C). This suggests that the reestablished status of VTA DA neurons in resilient mice is more stable and less vulnerable to perturbations than that of controls.

The up-regulation of I_h in VTA DA neurons of resilient mice may be driving the neuronal firing extremely high and triggering a self-tuning K^+ current mechanism to bring the extreme firing back to control (fig. S3). This in turn normalizes the depressive behaviors. To determine whether enhancing I_h current in susceptible mice can trigger this hypothesized homeostatic plasticity observed in the resilient mice, we pharmacologically increased I_h through in vivo infusion of an I_h potentiator, lamotrigine, into the VTA of TH-GFP susceptible mice. Lamotrigine is known to enhance I_h (*16*) and is clinically used as a mood stabilizer to treat the depressed phase of bipolar disorder with uncertain mechanisms (*17*). In brain slices, bath application of lamotrigine increased I_h and the firing rate of VTA DA neurons (fig. S4). Consistently, a single in vivo infusion into the VTA of susceptible mice increased social avoidance (fig. S5). To determine whether repeated enhancement of this current can induce a homeostatic compensatory response, we performed repeated 5-day local infusions of lamotrigine (0.1 μg) into the VTA of susceptible TH-GFP mice (Fig. 1, D and E, and fig. S6A), because it is known that 4 to 5 days is sufficient to induce stable changes in social behaviors (*18*). After 5 days of local infusion, we observed a profound reversal of social avoidance, with more time spent interacting with a social target (Fig. 1F) and reduced time in the corner zone (fig. S6B), without adverse effects on locomotion (fig. S6C). The defeat-induced deficit in sucrose preference was also significantly reversed after repeated lamotrigine infusion (Fig. 1G), which indicated an overall resilient, antidepressant effect, without affecting the behaviors in either control or resilient mice (fig. S7 and S8).

Consistent with the behavioral antidepressant effect, the hyperactivity of VTA DA neurons in susceptible mice was normalized after I_h potentiation via lamotrigine (Fig. 1H). To examine the ionic mechanisms that underlie this promotion of resilience, we determined the effects of repeated lamotrigine infusion on I_h and K^+ currents. We observed a marked increase in I_h (Fig. 1I) and a compensatory increase in K^+ currents (Fig. 1J), a phenomenon not observed at lower doses (fig. S9). Consistently, these ionic changes induced a reduction in DA neuron excitability in the lamotrigine-treated animals (Fig. 1K), as compared with vehicle-treated controls. These data describe a possible mechanism of lamotrigine's mood-stabilizing efficacy.

Although one of the actions of lamotrigine is known to increase I_h current, lamotrigine has other effects on neurons, such as blockade of sodium channels (*19*). To specifically assess the role enhanced I_h has in VTA DA neurons, we selectively overexpressed hyperpolarization-activated and cyclic nucleotide–gated channel 2 (HCN2), a channel isoform that mediates I_h current (*20*). We used a combination of TH-Cre mice and Cre-inducible loxP-STOP-loxP herpes simplex virus with enhanced yellow fluorescent protein (HSV-LS1L-HCN2-eYFP) and HSV-LS1L-eYFP as control. The HSV vectors allow for the rapid expression of HCN2 over 5 days (*18*). The Cre-inducible vectors were injected bilaterally into the VTA of TH-Cre transgenic mice to ensure specific expression in DA neurons (Fig. 2, A and B). Functional validation 24 hours after injection successfully showed an increase in I_h (Fig. 2C) and corresponding increase in firing (Fig. 2D). Next, we injected HSV-LS1L-HCN2-eYFP or HSV-LS1L-eYFP into the VTA of susceptible TH-Cre mice and carried out the behavioral and electrophysiological measurements 4 to 6 days after viral injection (Fig. 2, E and F). Overexpression of HCN2 in the VTA DA neurons of susceptible mice resulted in a reversal of social avoidance (Fig. 2G and fig. S10A) and other depressive behaviors (Fig. 2, H and I), with no affect on locomotion (fig. S10B).

[1]Department of Pharmacology and Systems Therapeutics, Icahn School of Medicine at Mount Sinai, New York, NY 10029, USA. [2]Neuroscience Program, Graduate School of Biomedical Sciences, Icahn School of Medicine at Mount Sinai, New York, NY 10029, USA. [3]Department of Neurology, Icahn School of Medicine at Mount Sinai, New York, NY 10029, USA. [4]Department of Neuroscience and Friedman Brain Institute, Icahn School of Medicine at Mount Sinai, New York, NY 10029, USA. [5]McGovern Institute for Brain Research, Massachusetts Institute of Technology, Cambridge, MA 02139, USA.

*Corresponding author. E-mail: ming-hu.han@mssm.edu

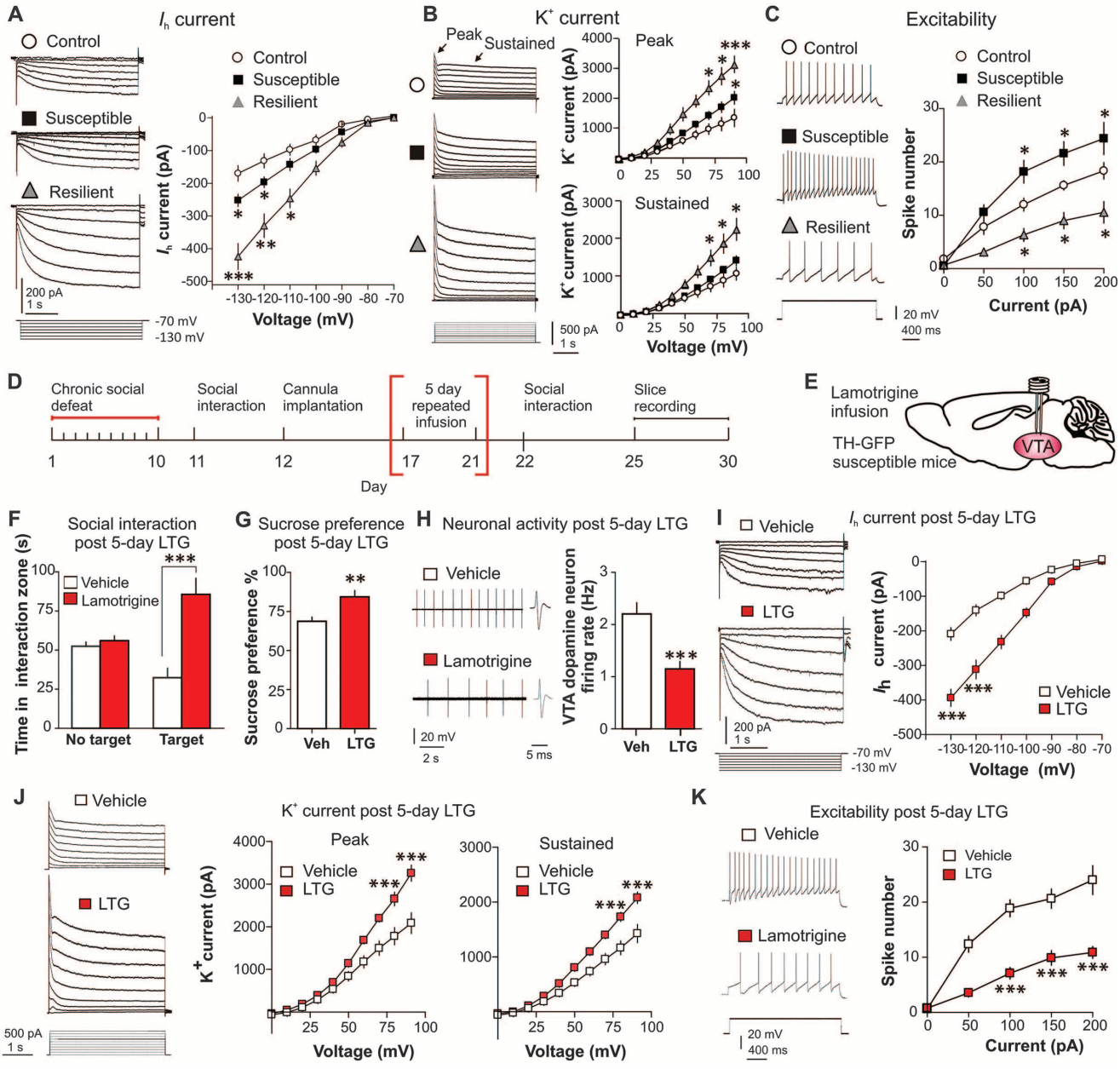

Fig. 1. The resilient phenotype shows dramatically increased I_h and K^+ channel currents in VTA DA neurons, and repeated infusion of I_h potentiator lamotrigine to the VTA of susceptible mice achieves antidepressant effects by inducing resilience-like homeostatic plasticity. (**A**) I_h sample traces and statistical data for control (open circles), susceptible (filled black squares), and resilient (filled gray triangles) mice. At −130 mV, $F_{(2,47)} = 19.19$, $P < 0.0001$; at −120 mV, $F_{(2,62)} = 17.69$, $P < 0.001$; $n = 12$ to 22 cells from 8 to 10 mice per group. Post hoc analysis at −130 mV shows a significant increase in I_h in susceptible mice ($t_{32} = 2.65$, $P < 0.05$) and an even significantly larger I_h increase in the resilient subgroup ($t_{24} = 5.24$, $P < 0.001$) compared with the control. (**B**) Sample traces and statistical data of isolated K^+ channel–mediated currents recorded from VTA DA neurons show that resilient mice have significantly increased peak and sustained phases of K^+ currents. At +90 mV, $F_{(2,58)} = 15.129$, $P < 0.001$; $n =$ 14 to 23 cells from 9 to 10 mice per group. Post hoc analysis shows a slight increase in peak K^+ currents in susceptible mice ($t_{41} = 2.62$, $P < 0.05$) and a larger increase in the resilient subgroup ($t_{36} = 5.25$, $P < 0.001$) compared with the control. (**C**) Susceptible mice display increased DA neuron excitability, whereas resilient mice display a reduction, after incremental steps in current injections (50, 100, 150, and 200 pA) compared with controls [at 100 pA: $F_{(2,28)} = 12.00$, $P <$ 0.001; at 150 pA $F_{(2,28)} = 12.66$, $P < 0.001$; and at 200 pA $F_{(2,25)} = 8.86$, $P <$ 0.001]. Post hoc analysis of susceptible and resilient compared with control mice for 100 and 150 and 200 pA currents at $P < 0.05$ ($n = 8$ to 12 cells from 7 to 8 mice per group). (**D** and **E**) Experimental timeline and schematic. (**F**) Five days of 4-min daily bilateral infusions of lamotrigine (LTG, 0.1 μg) or vehicle into the VTA reversed social avoidance ($t_{18} = 5.79$, $P < 0.001$; $n = 10$) and (**G**) sucrose preference ($t_{18} = 3.25$, $P < 0.01$; $n = 10$). (**H**) Sample traces and statistical data of VTA DA neuron firing in susceptible mice after repeated infusion of vehicle compared with lamotrigine infusions ($t_{32} = 4.10$, $P < 0.001$; $n = 17$ cells from 7 to 9 mice per group). (**I**) Sample traces and statistical data of I_h in susceptible mice after repeated infusion of vehicle (open squares) or lamotrigine (filled red squares) (at −130 mV: $t_{13} = 6.99$, $P < 0.0001$; at −120 mV: $t_{13} = 5.88$, $P < 0.0001$; $n = 7$ to 8 cells from 6 to 8 mice per group). (**J**) Sample traces and statistical data of K^+ currents in susceptible mice after repeated infusion of vehicle or lamotrigine: peak (at +20 mV: $t_{19} = 5.03$, $P < 0.001$; at +10 mV: $t_{19} = 5.92$, $P < 0.001$) and sustained (at +20 mV: $t_{19} = 5.95$, $P < 0.001$; at +10 mV: $t_{19} = 6.81$, $P < 0.001$; $n = 10$ to 11 cells from 7 to 9 mice per group). (**K**) Sample traces obtained at 100 pA current injection and statistical data of decreased excitability in susceptible mice infused with lamotrigine compared with vehicle (at 100 pA: $t_{15} = 6.41$, $P < 0.0001$; at 150 pA: $t_{15} = 4.93$, $P < 0.001$; at 200 pA: $t_{15} = 4.56$, $P < 0.001$; $n = 8$ to 9 cells from 7 to 9 mice per group). Error bars, ±SEM. *$P < 0.05$, **$P < 0.01$, ***$P < 0.001$.

After DA neuron–specific expression of HCN2 in susceptible mice, a robust reduction in hyperactivity was found in HCN2-expressing DA neurons, as compared with eYFP control neurons (Fig. 2J). We observed a significant increase in I_h current in HCN2-expressing cells (Fig. 2K), and in conjunction, we observed a significant increase in the K^+ currents (Fig. 2L), resulting in an overall reduction in excitability of these neurons (Fig. 2M).

Whereas excessively potentiating I_h resulted in a homeostatic up-regulation of K^+ channel function in VTA DA neurons of susceptible mice, this K^+ current compensation may be caused directly by the hyperactivity induced by I_h potentiation. In primary neuronal cultures, excessive hyperactivity can induce homeostatic up-regulation of K^+ channel–mediated current (*21*). We thus asked whether direct excessive activation of VTA DA neurons in susceptible mice could induce a functional K^+ channel counteraction that would normalize

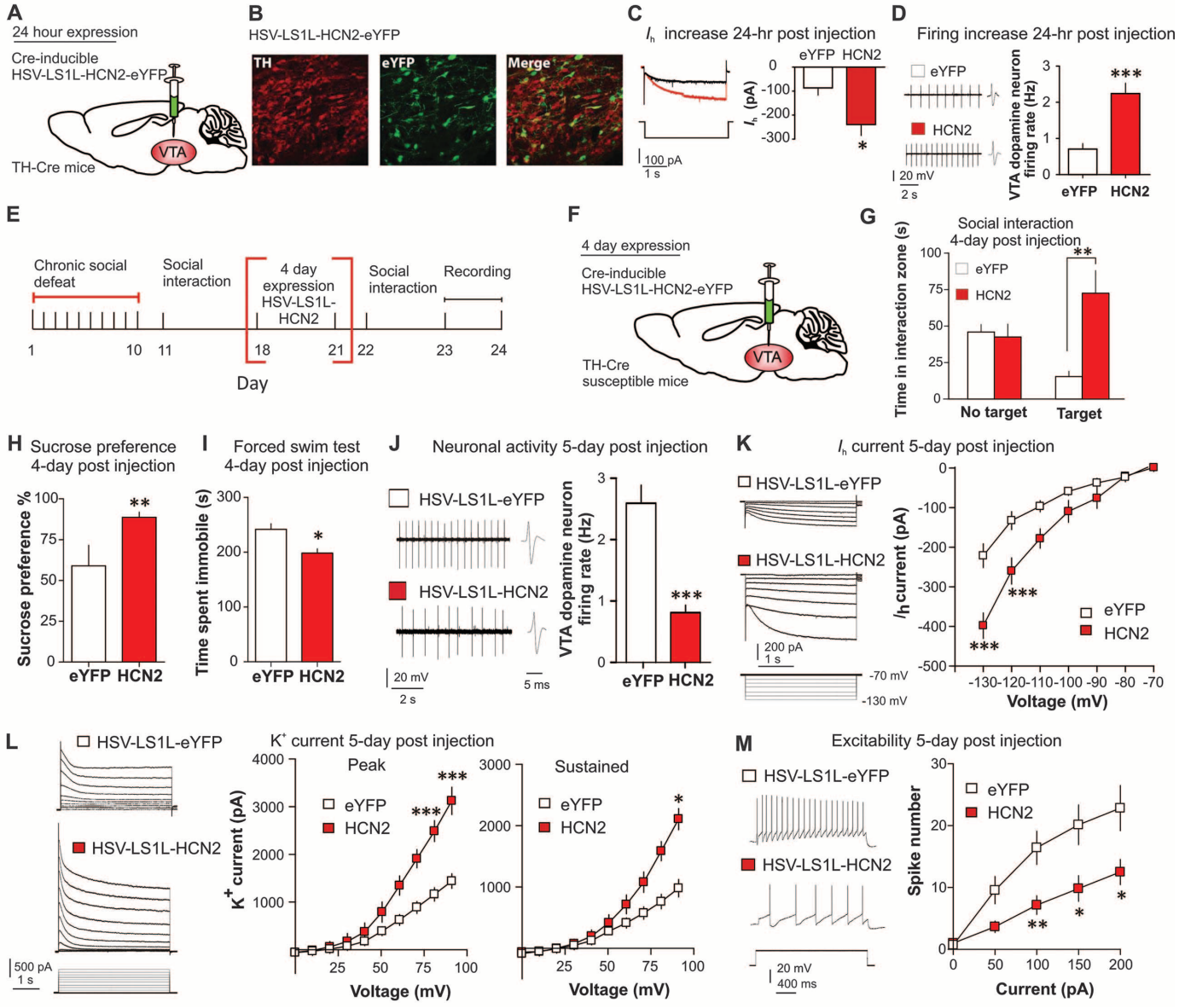

Fig. 2. DA neuron–specific overexpression of HCN2 channel induces an antidepressant behavioral effect and triggers a homeostatic response via an increase in compensatory K^+ currents. (**A**) Cre-inducible HSV-LS1L-HCN2-eYFP injection into the VTA of TH-Cre mice. (**B**) Confocal image showing colocalization (merge) of Cre-induced HCN2 (eYFP) expression in VTA DA neurons (TH) of TH-Cre mice. Quantification shows that HCN2-expressing TH^+ cells were 47 ± 4% of total TH^+ neurons in the VTA, and there was no expression of HCN2 in TH^- neurons (2 to 3 sections per mouse; $n = 4$). Scale bar, 100 μm; green, eYFP; red, TH. (**C**) Virally expressed HCN2 significantly increases I_h ($t_{13} = 2.73$, $P < 0.05$; $n = 7$ to 8 cells from each group, 3 mice per group) and (**D**) firing rate ($t_{25} = 6.86$, $P < 0.0001$; $n = 13$ to 14 cells from 4 mice per group) in VTA DA neurons as compared with control (eYFP) 24 hours after injection. (**E** and **F**) Experimental timeline and schematic. Behavioral effects of susceptible mice expressing HSV-LS1L-HCN2-eYFP or control HSV-LS1L-eYFP in DA neurons of the VTA on (**G**) social interaction test ($t_{22} = 3.72$, $P < 0.01$; $n = 12$); (**H**) sucrose preference test ($t_{18} = 3.40$, $P < 0.01$; $n = 10$); and (**I**) immobility time during forced swim test ($t_{18} = 2.87$, $P < 0.05$; $n = 10$). (**J** to **L**) Neuronal effects of 6 days of expression of HSV-LS1L-HCN2-eYFP (filled red squares) compared with HSV-LS1L-eYFP (open squares) in DA neurons of the VTA in susceptible mice on (J) firing rate ($t_{19} = 5.48$, $P < 0.0001$; $n = 10$ to 11); (K) I_h measurements (at –130 mV: $t_{22} = 4.51$, $P < 0.001$; at –120 mV: $t_{18} = 3.25$, $P < 0.005$); and (L) K^+ currents (–70 mV to +20 mV/10 mV step): peak (at +20 mV: $t_{16} = 5.70$, $P < 0.001$; at +10 mV: $t_{16} = 5.28$, $P < 0.001$); sustained (at +20 mV: $t_{16} = 2.480$, $P < 0.05$). (**M**) Sample traces at 100 pA current injection and statistical data of decreased excitability in susceptible mice expressing HCN2 compared with eYFP control (at 100 pA: $t_{12} = 3.21$, $P < 0.01$; at 150 pA: $t_{12} = 2.73$, $P < 0.05$; at 200 pA: $t_{12} = 2.54$, $P < 0.05$; $n = 7$ cells from 6 to 7 mice per group). Error bars, ±SEM. *$P < 0.05$, **$P < 0.01$, ***$P < 0.001$.

the hyperactivity of these neurons and depression-related behaviors. We examined social interaction behaviors and the channel functions after repeated optogenetic activation of VTA DA neurons in susceptible mice—further increasing the hyperactivity in susceptible mice. We injected Cre-inducible adenovirus-associated channelrhodopsin-2 (AAV-DIO-ChR2-eYFP) or control vector (AAV-DIO-eYFP) into the VTA of susceptible TH-Cre mice to selectively express ChR2 in VTA DA neurons (Fig. 3, A to C) (*9*, *22*, *23*). Bilateral implantable optic fibers were placed above the VTA (fig. S11A) for blue light photostimulation (five pulses, 20 Hz/10-s period) (Fig. 3, D and E) of DA neurons in susceptible mice, mimicking a validated in vivo firing pattern (*9*, *12*, *23*, *24*). After 5 days of 20-min photostimulation, susceptible mice with viral expression of ChR2 showed reduced social avoidance (Fig. 3F and fig. S11B) and reduced depressive behaviors (Fig. 3, G and H), without adverse effects on locomotion (fig. S11C). Excessive optogenetic activation of VTA DA neurons in susceptible mice reduced firing rate (Fig. 3I) and increased K^+ currents (Fig. 3J) in the ChR2-infected neurons, without altering I_h (fig. S11D). Consistent with the ionic alterations, we found a reduction in excitability of the ChR2-infected neurons (Fig. 3K).

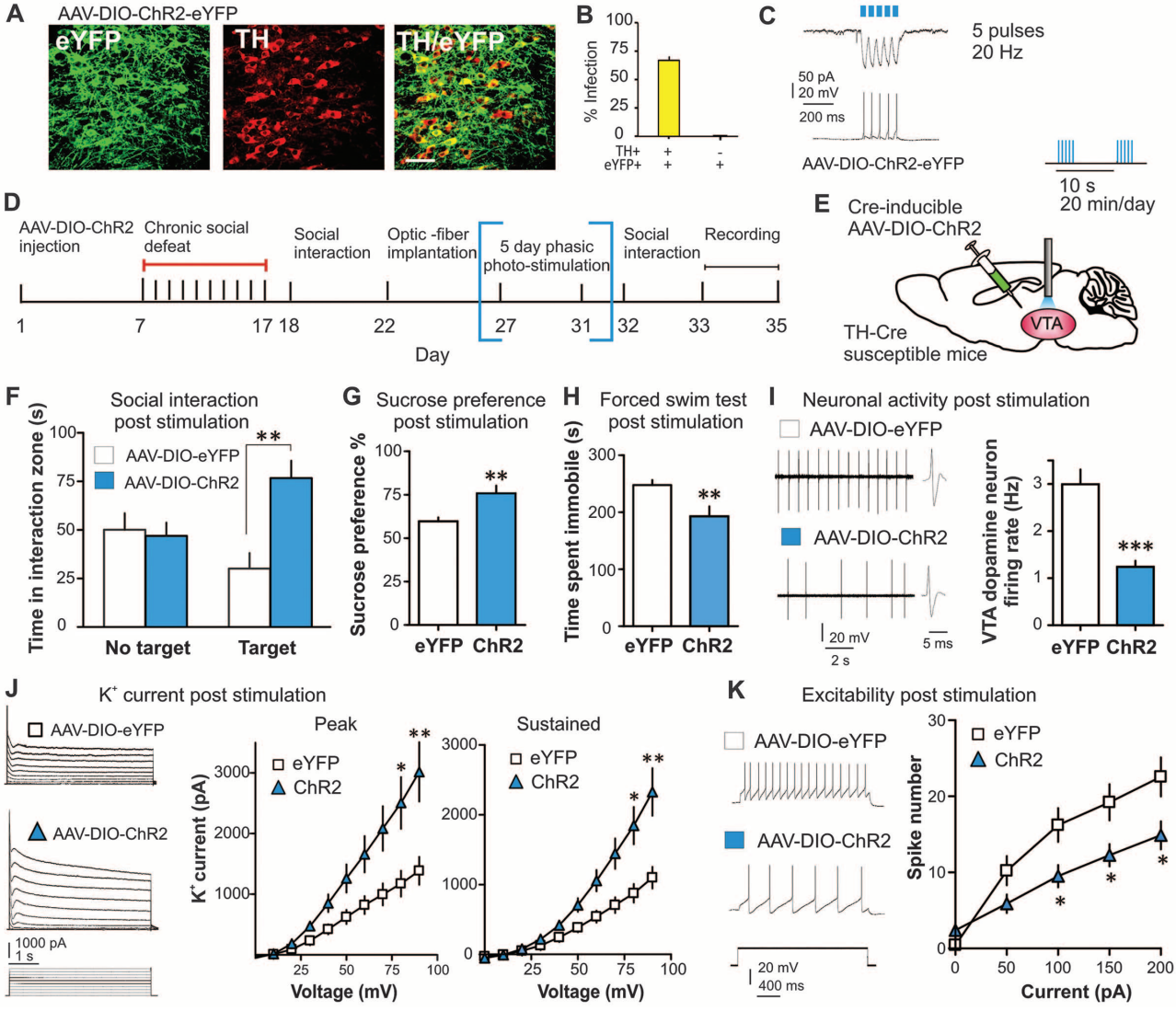

Fig. 3. Repeated optogenetic stimulation of VTA DA neurons normalizes the depressed phenotype and induces a significant compensation in K^+ currents. (**A**) Cell type–specific AAV-DIO-ChR2-eYFP expression (green) in VTA DA neurons (red) of TH-Cre mice. Scale bar, 100 μm. (**B**) Quantification shows that ChR2-expressing TH^+ cells are 67 ± 4% of total TH^+ neurons in the VTA, and there was no expression of ChR2 in TH^- neurons (n = 2 to 3 sections per mouse; n = 5 animals). (**C**) Voltage-clamp (upper trace) and current-clamp (lower trace) recordings from DA neurons in VTA slices. Five short bursts (20 Hz, 40 ms) of blue light (470 nm) induce temporally precise inward photocurrents and corresponding action potentials. (**D**) Experimental timeline. (**E**) Localization of bilateral viral injection and optic-fiber implantation used for in vivo delivery of blue light in susceptible TH-Cre mice. Phasic light pulses (470 nm, 20 Hz, five pulses/10 s) were delivered 20 min a day for five consecutive days. (**F**) After 5 days (20 min/day) of phasic stimulation of DA neurons, susceptible animals expressing ChR2 have increased social interaction (t_{22} = 3.59, P < 0.01; n = 12); (**G**) increased sucrose preference (t_{20} = 3.25, P < 0.01; n = 11); and (**H**) decreased immobility time during forced swim test (t_{18} = 2.89, P < 0.01; n = 10). (**I**) Sample traces and statistical data of VTA DA neuron firing in susceptible mice after chronic excessive activation (t_{23} = 6.25, P < 0.001; 12 to 13 cells from 6 mice per group). (**J**) Sample traces and statistical data of K^+ currents recorded from VTA DA neurons in brain slices from eYFP and ChR2-expressing neurons. Excessive optical activation of VTA DA neurons significantly increased the peak (at +20 mV: t_{19} = 3.08, P < 0.01; at +10 mV: t_{19} = 2.83, P < 0.05; at 0 mV) and sustained (at +20 mV: t_{19} = 3.53, P < 0.01; +10 mV: t_{19} = 3.18, P < 0.05) phases of K^+ currents. (**K**) Sample traces at 100 pA current injection and statistical data of decreased excitability in susceptible mice expressing ChR2 compared with eYFP (at 100 pA: t_{15} = 2.47, P < 0.05; at 150 pA: t_{15} = 2.41, P < 0.05; at 200 pA: t_{15} = 2.32, P < 0.05; n = 8 to 9 cells from 6 to 8 mice per group). Error bars, ±SEM. *P < 0.05, **P < 0.01, ***P < 0.001.

Recent studies show that VTA DA neurons are heterogeneous (*9*, *11*, *25*, *26*). For instance, VTA DA neurons projecting to nucleus accumbens (NAc) exhibit a large I_h, whereas medial prefrontal cortex (mPFC)–projecting VTA DA neurons have a small I_h (*26*). Utilizing retrograde tracers, we found that I_h alterations in response to chronic social defeat occur specifically in NAc-projecting VTA neurons but not in mPFC-projecting VTA neurons (Fig. 4, A and H, and figs. S12A and S13A). Note that the homeostatic plasticity that occurs in response to projection-specific HCN2 overexpression and repeated optogenetic stimulation is unique to the VTA-NAc projection (Fig. 4, B to G, and fig. S12). A different form of plasticity occurred in VTA-mPFC neurons: To our surprise, HCN2 overexpression had no effects on behavior, firing, I_h, and K^+ currents (Fig. 4, I to K, and fig. S13, B to G), whereas repeated optogenetic stimulation reversed social avoidance accompanied by a firing increase and a K^+ current decrease, the physiological changes opposite to those seen in VTA-NAc neurons (Fig. 4, L to N, and fig. S13, H to L).

Self-tuning adaptation of neuronal activity as a homeostatic plasticity concept was first described in primary neuronal culture (*27*) and further observed in in vivo animal models (*28*, *29*). Evidence shows that homeostatic plasticity plays a fundamental role in stabilizing neuronal activity in response to excessive perturbations under both physiological (*30*, *31*) and disease (*32*) conditions. We observed that resilient mice displayed enhanced I_h current in VTA DA neurons and simultaneously exhibited up-regulated inhibitory K^+ currents. Based on this unexpected observation, we tested the hypothesis that the resilience phenotype achieves its stable behavioral functioning through homeostatic plasticity and that this homeostatic adaptation can be established therapeutically in susceptible mice. Using pharmacological, viral, and optogenetic approaches, we found that enhancement of I_h or excessive activation of VTA DA neurons triggered self-tuning compensation of K^+ currents and functionally normalized the firing of these hyperactive neurons in susceptible animals, a homeostatic plasticity seen in VTA-NAc projections, but not in the VTA-mPFC pathway. Once the homeostatic balance is established naturally or experimentally in VTA DA neurons, these neurons are more stable, as indicated by their reduced response to physiological perturbation. Our findings advance the understanding of homeostatic plasticity in a behaviorally relevant in vivo disease

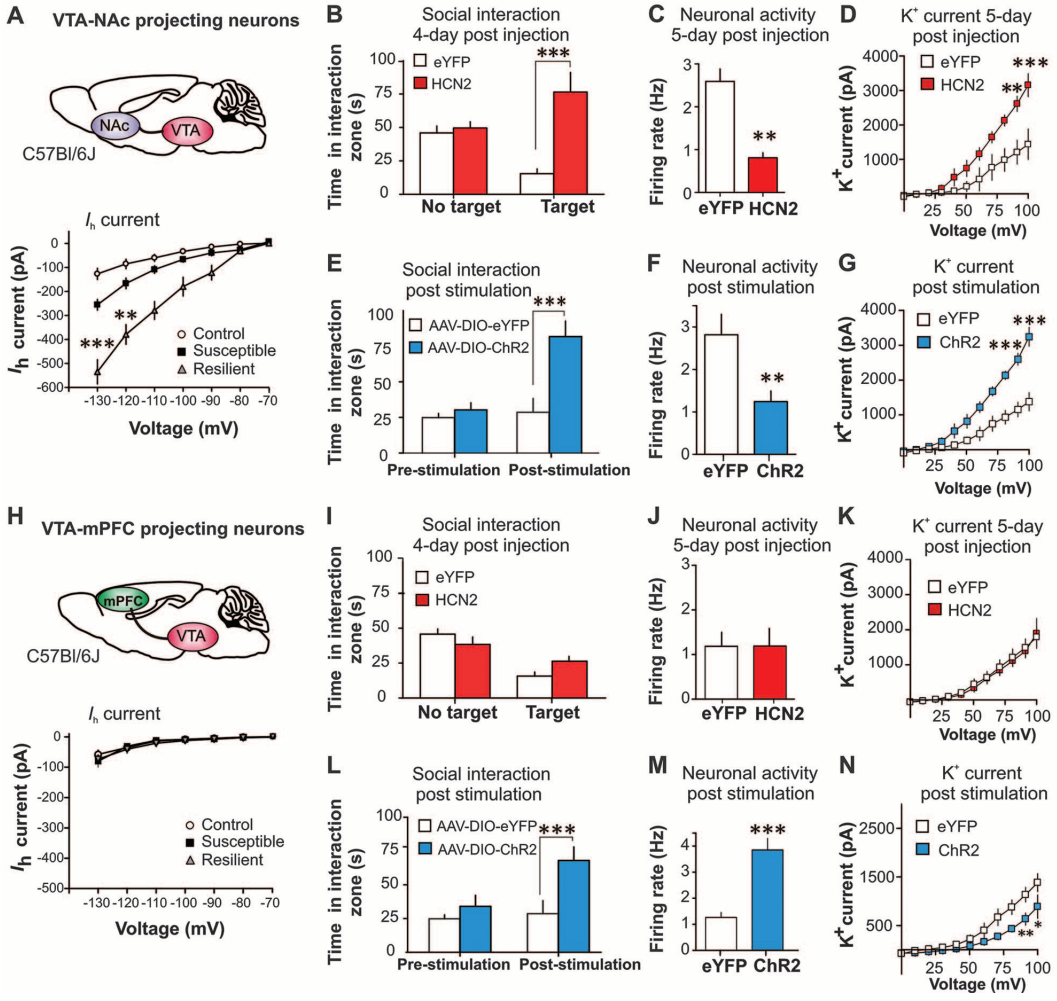

Fig. 4. The observed homeostatic plasticity is specific in the I_h-presenting VTA-NAc projection. (**A**) Statistical data of I_h in NAc-projecting VTA (VTA-NAc) neurons in control, susceptible and resilient mice. At −130 mV, $F_{(2,22)} = 39.27$, $P < 0.0001$; at −120 mV, $F_{(2,22)} = 27.78$, $P < 0.0001$; $n = 7$ to 10 cells from 6 to 7 mice per group. Post hoc analysis at −130 shows a significant increase in I_h in susceptible mice ($t_{16} = 3.98$, $P < 0.01$) and an even significantly larger I_h increase in the resilient subgroup ($t_{13} = 7.71$, $P < 0.001$), compared with the control group. (**B**) Susceptible mice expressing HCN2 in VTA-NAc neurons show an increase in social interaction ($t_{13} = 4.81$, $P < 0.001$; $n = 7$ to 8) and (**C**) a decrease in the firing rate of VTA-NAc neurons ($t_{22} = 3.31$, $P < 0.01$; $n = 11$ to 13 cells from 6 mice per group) compared with eYFP. (**D**) K^+ currents: peak (at +20 mV: $t_{12} = 4.47$, $P < 0.001$; at +10 mV: $t_{12} = 4.33$, $P < 0.01$; $n = 7$ cells from 6 mice per group). (**E**) After 5 days (20 min/day) of optical phasic stimulation of VTA-NAc neurons, susceptible animals expressing ChR2 have increased social interaction ($t_{18} = 4.24$, $P < 0.001$, $n = 10$) and (**F**) a decrease in the firing of VTA-NAc neurons expressing ChR2 ($t_{19} = 3.44$, $P < 0.01$, $n = 10$ to 11 cell from 5 to 6 mice per group). (**G**) K^+ currents are significantly increased in ChR2-expressing neurons: peak (at +20 mV: $t_{12} = 4.70$, $P < 0.001$; at +10 mV: $t_{12} = 4.82$, $P < 0.001$; $n = 7$ cells from 6 mice per group). (**H**) Statistical data of I_h in mPFC-projecting VTA (VTA-mPFC) neurons in control, susceptible, and resilient mice. At −130 mV, $F_{(2,38)} = 0.69$, $P = 0.51$; $n = 9$ to 11 cells from 5 to 6 mice per group. Susceptible mice expressing HCN2 or control eYFP in VTA-mPFC show no change in (**I**) social interaction ($t_{18} = 1.65$, $P = 0.12$; $n = 10$); (**J**) firing rate of VTA-mPFC neurons ($t_{24} = 0.34$, $P = 0.74$; $n = 13$ cells, 5 to 6 mice per group); and (**K**) K^+ currents of VTA-mPFC neurons: peak (at +20 mV: $t_{14} = 0.12$, $P = 0.90$; at +10 mV: $t_{14} = 0.85$, $P = 0.41$; $n = 8$ cells from 6 mice per group). After 5 days (20 min/day) of optical phasic stimulation of VTA-mPFC neurons, susceptible animals expressing ChR2 have increased (**L**) social interaction ($t_{18} = 4.07$, $P < 0.001$, $n = 10$) and (**M**) an increase in the firing of VTA-mPFC neurons ($t_{24} = 5.11$, $P < 0.0001$, $n = 12$ to 14 cell/group, 6 mice per group). (**N**) K^+ currents are significantly decreased after chronic activation: peak (at +20 mV: $t_{14} = 2.26$, $P < 0.05$; at +10 mV: $t_{14} = 3.20$, $P < 0.01$; $n = 8$ cells, 6 mice per group). Error bars, ±SEM. *$P <$ 0.05, **$P < 0.01$, ***$P < 0.001$.

model of depression and provide further insight into the stabilized physiological underpinnings of natural resilience.

Although homeostatic plasticity describes much of our current findings, the counterintuitive process by which ionic, cellular, and behavioral alterations are achieved and its close similarity to natural stress-resilience remains surprising. Recently, cell type–specific and neural circuit–probing optogenetic approaches have assisted in unraveling multiple unforeseen functions of the brain's reward DA neurons (*9*, *11*, *22*, *23*, *26*, *33*). By revealing a previously uncharacterized ionic mechanism of intrinsic homeostatic plasticity, we are bringing new insight to the complex functions of these neurons. Notably, the experimentally induced homeostatic plasticity in VTA-NAc–projecting neurons is triggered by enhancing stress-activated I_h current and stress-induced neuronal hyperactivity. Therefore, rather than reversing the underlying disruption or pathological mechanisms, the stress-activated pathogenic changes can be beneficially used to achieve treatment efficacy (fig. S14). It is interesting that reversing pathological adaptations rapidly induces antidepressant effects (*9*, *11*), whereas chronic manipulations are needed to promote active resilient mechanisms and to achieve treatment efficacy. Overall, our findings not only unravel a critical self-stabilizing capacity of midbrain DA neurons in the brain's reward circuit, but also identify a conceptually different therapeutic strategy of promoting natural resilience. This may provide useful information for the development of naturally acting antidepressants.

References and Notes

1. V. Krishnan *et al.*, *Cell* **131**, 391–404 (2007).
2. A. Feder, E. J. Nestler, D. S. Charney, *Nat. Rev. Neurosci.* **10**, 446–457 (2009).
3. S. J. Russo, J. W. Murrough, M. H. Han, D. S. Charney, E. J. Nestler, *Nat. Neurosci.* **15**, 1475–1484 (2012).
4. S. Kumar, G. Feldman, A. Hayes, *Cognit. Ther. Res.* **32**, 734–744 (2008).
5. T. A. Carey, *Clin. Psychol. Rev.* **31**, 236–248 (2011).
6. S. M. Southwick, D. S. Charney, *Science* **338**, 79–82 (2012).
7. V. Vialou *et al.*, *Nat. Neurosci.* **13**, 745–752 (2010).
8. E. J. Nestler, W. A. Carlezon Jr., *Biol. Psychiatry* **59**, 1151–1159 (2006).
9. D. Chaudhury *et al.*, *Nature* **493**, 532–536 (2013).
10. O. Berton *et al.*, *Science* **311**, 864–868 (2006).
11. K. M. Tye *et al.*, *Nature* **493**, 537–541 (2013).
12. J.-L. Cao *et al.*, *J. Neurosci.* **30**, 16453–16458 (2010).
13. S. A. Golden, H. E. Covington 3rd, O. Berton, S. J. Russo, *Nat. Protoc.* **6**, 1183–1191 (2011).
14. M. J. Wanat, F. W. Hopf, G. D. Stuber, P. E. M. Phillips, A. Bonci, *J. Physiol.* **586**, 2157–2170 (2008).
15. H. Neuhoff, A. Neu, B. Liss, J. Roeper, *J. Neurosci.* **22**, 1290–1302 (2002).
16. N. P. Poolos, M. Migliore, D. Johnston, *Nat. Neurosci.* **5**, 767–774 (2002).
17. M. A. Frye, *N. Engl. J. Med.* **364**, 51–59 (2011).
18. M. B. Wilkinson *et al.*, *J. Neurosci.* **31**, 9084–9092 (2011).
19. Y. Nakatani, H. Masuko, T. Amano, *J. Pharmacol. Sci.* **123**, 203–206 (2013).
20. M. Biel, C. Wahl-Schott, S. Michalakis, X. Zong, *Physiol. Rev.* **89**, 847–885 (2009).
21. J. Zhang, M. S. Shapiro, *Neuron* **76**, 1133–1146 (2012).
22. H. C. Tsai *et al.*, *Science* **324**, 1080–1084 (2009).
23. J. J. Walsh *et al.*, *Nat. Neurosci.* **17**, 27–29 (2014).
24. J. W. Koo *et al.*, *Science* **338**, 124–128 (2012).
25. E. B. Margolis, J. M. Mitchell, J. Ishikawa, G. O. Hjelmstad, H. L. Fields, *J. Neurosci.* **28**, 8908–8913 (2008).
26. S. Lammel *et al.*, *Neuron* **57**, 760–773 (2008).
27. G. Turrigiano, L. F. Abbott, E. Marder, *Science* **264**, 974–977 (1994).
28. G. Turrigiano, *Annu. Rev. Neurosci.* **34**, 89–103 (2011).
29. A. Maffei, K. Nataraj, S. B. Nelson, G. G. Turrigiano, *Nature* **443**, 81–84 (2006).
30. A. Destexhe, E. Marder, *Nature* **431**, 789–795 (2004).
31. K. Whalley, *Nat. Rev. Neurosci.* **14**, 820–821 (2013).
32. D. K. Dickman, G. W. Davis, *Science* **326**, 1127–1130 (2009).
33. S. Lammel *et al.*, *Nature* **491**, 212–217 (2012).

Acknowledgments: We thank E. J. Nestler for his continuing support of this work. We also thank S. J. Russo, H. P. Xu, J. L. Cao, F. Henn, and E. J. Nestler for their helpful discussion and G. R. Tibbs and P. A. Goldstein from Weill Cornell Medical College for providing the HCN2 plasmid. This work was supported by the National Institute of Mental Health (R01 MH092306: S.M.K., D.C., M.-H.H.), National Research Service Award (F31 MH095425 to J.J.W.; T32 MH 087004 to B.J.; F32 MH096464 to A.K.F.), and Johnson & Johnson–International Mental Health Research Organization (IMHRO) Rising Star Translational Research Award (M.-H.H.).

Supplementary Materials

www.sciencemag.org/content/344/6181/313/suppl/DC1
Materials and Methods
Figs. S1 to S14
References (*34*)

3 December 2013; accepted 26 March 2014
10.1126/science.1249240

Distinct Profiles of Myelin Distribution Along Single Axons of Pyramidal Neurons in the Neocortex

Giulio Srubek Tomassy,[1] Daniel R. Berger,[2,3] Hsu-Hsin Chen,[1] Narayanan Kasthuri,[2] Kenneth J. Hayworth,[2] Alessandro Vercelli,[4] H. Sebastian Seung,[3]* Jeff W. Lichtman,[2] Paola Arlotta[1]†

Myelin is a defining feature of the vertebrate nervous system. Variability in the thickness of the myelin envelope is a structural feature affecting the conduction of neuronal signals. Conversely, the distribution of myelinated tracts along the length of axons has been assumed to be uniform. Here, we traced high-throughput electron microscopy reconstructions of single axons of pyramidal neurons in the mouse neocortex and built high-resolution maps of myelination. We find that individual neurons have distinct longitudinal distribution of myelin. Neurons in the superficial layers displayed the most diversified profiles, including a new pattern where myelinated segments are interspersed with long, unmyelinated tracts. Our data indicate that the profile of longitudinal distribution of myelin is an integral feature of neuronal identity and may have evolved as a strategy to modulate long-distance communication in the neocortex.

Myelin plays critical roles in enabling complex neuronal function, including learning and cognition, and abnormal myelination is associated with neurological disorders and mental illnesses (*1*, *2*). Given the importance of myelin for network behavior, realistic models of structure-function relations in the central nervous system (CNS) must be built in consideration of myelin structure and distribution as fundamental elements. Among all myelinated axons, the thickness of the myelin sheath varies greatly, and it is a major determinant of the speed of impulse propagation (*1*). However, structural features other than myelin thickness have the potential to contribute to establishing and modulating conduction velocity and network behavior. In particular, the alternating sequence of nodes and internodes along each axon could affect conduction speed.

High-resolution maps of myelin distribution along individual axons are not currently available. Furthermore, it is not known whether different neurons are endowed with signature patterns of longitudinal myelination. This analysis has been hampered by the technical difficulty of tracing single, long, winding axons through the complex milieu of the CNS, a task that requires electron microscopy (EM) serial reconstructions of large volumes of tissue. Fortunately, however, large EM data sets that allow analysis of myelin are beginning to be available (*3*, *4*). Here, using the neocortex as a prominent model of neuronal diversity, we traced the distribution of myelin along a large set of individual pyramidal neuron axons

[1]Department of Stem Cell and Regenerative Biology, Harvard University, 7 Divinity Avenue, Cambridge, MA 02138, USA. [2]Department of Molecular and Cellular Biology, Harvard University, 52 Oxford Street, Cambridge, MA 02138, USA. [3]Department of Brain and Cognitive Sciences, Massachusetts Institute of Technology, 43 Vassar Street, Cambridge, MA 02139, USA. [4]Neuroscience Institute Cavalieri Ottolenghi, Neuroscience Institute of Turin, Corso M. d'Azeglio 52, 10126 Turin, Italy.

*Present address: Princeton Neuroscience Institute, Princeton University, Princeton, NJ 08544, USA.
†Corresponding author. E-mail: paola_arlotta@harvard.edu

to understand whether myelin properties differ among different types of neurons. Pyramidal neurons occupy different cortical layers; have distinct molecular and long-distance connectivity properties; and compute the highest-level cognitive, sensory, and motor functions of the mammalian CNS (*5*, *6*).

We first assessed the distribution of myelin within the adult mouse somatosensory (S1) cortex. Immunohistochemistry for myelin basic protein (MBP) and the transcription factor Cux1 [a marker of layers II to IV pyramidal neurons (*7*)] showed that the lowest levels of myelin correspond to layer II/III, whereas layer IV neurons reside in an intermediate domain and layers V and VI are the most densely myelinated (Fig. 1A). The same pattern of myelin distribution was evolutionarily conserved in primates, including humans, and it is maintained in the aged cortex (fig. S1). To determine whether a correlation exists between this myelin gradient and the longitudinal deposition of myelin along axons of different neurons, we performed Golgi-Cox staining, which labels neuronal somas, dendrites, and unmyelinated axons [but not the myelinated segments of axons (*8*)]. We found that the distance between the axon hillock and the beginning of the first internode, which we refer to as premyelin axonal segment (PMAS), was inversely correlated with the distance of the neuron soma from the pia (Fig. 1B). This result suggests that neurons in different layers display different profiles of longitudinal myelination.

In order to follow individual axons at higher resolution and over long distances, we used two high-throughput EM serial reconstruction data sets spanning large volumes of the adult neocortex. The first data set spans a 500 × 1000 × 61 μm^3 volume of mouse somatosensory (S1) cortex from layer I to VI and was sectioned at 30-nm thickness. Every eighth section was imaged at a resolution of 30 nm, resulting in an image stack with 30 × 30 × 240 nm per pixel (see methods and fig. S2A). The second data set spans a 450 × 350 × 54 μm^3 volume of mouse visual cortex (V1) from layer I to the upper margin of layer IV (*9*) and is available for download at (www.openconnectomeproject.org). In order to trace individual axons, we used VAST—volume annotation and segmentation tool (see methods)—to reconstruct single neurons, their processes, and associated myelin over long distances (movie S1). These tracings can all be reproduced using the TrakEM2 plug-in of the Fiji framework (*10*).

We traced 38 axons from neurons located in layers III through VI of the S1 data set. Neurons in layer II/III could not be traced in the S1 data set because of slice folding in the outermost part of the cortex. To map myelin distribution in these more superficial layers, we therefore used the V1 data set and traced a total of 22 additional neurons located in layer II/III (Fig. 2 and table S1). A movie showing the reconstruction and tracing of a representative neuron from layer II/III is shown in movie S1. First, we normalized the length of the myelinated tracts on each axon to the total axonal length traced. In agreement with MBP distribution, we found that axons in layer V and VI have a total myelin coverage higher than axons in layers II/III (layer V to VI, 63.0 ± 5.6% coverage, $n = 12$; layer III to IV, 56.7 ± 4.2% coverage, $n = 26$; layer II/III, 37 ± 4.3% coverage, $n = 22$; means ± SEM, $P \leq 0.001$) (fig. S2, A and B, and movies S2 and S3). In addition, as indicated by the Golgi-Cox staining, the PMAS length of layer III and IV neurons was significantly longer than that of layer V and VI neurons (layer III to IV, 48.4 ± 3.5 µm, $n = 26$; layer V to VI, 33.7 ± 2.4 µm, $n = 12$; means ± SEM, $P = 0.00017$) (Fig. 1C).

Notably, the majority of the neurons traced in layer II/III displayed a pattern of longitudinal myelination that had never been described before in the CNS. Out of 22 neurons, 17 had myelinated axonal tracts of variable lengths (ranging between 18.28 µm and 57.36 µm), which were intercalated with long unmyelinated segments (up to 55.39 µm in length) (Fig. 2 and fig. S3). These myelin gaps were longer than typical nodes of Ranvier (1 to 2 µm) (*1*, *2*). In contrast to layer II/III neurons, 9 out of 12 neurons traced in layers V to VI presented long myelinated tracts interrupted by nodes of Ranvier, and three neurons showed short myelin gaps (7.3, 16.4, and 20.4 µm) (Fig. 1C, red neuron, and fig. S4). This suggests that intermittent myelination is a signature of layer II/III pyramidal neurons and that not all neurons display the same longitudinal profiles of myelination. Layer II/III pyramidal neurons are involved in elaborate cortical activities and exhibit a higher degree of molecular and electrophysiological

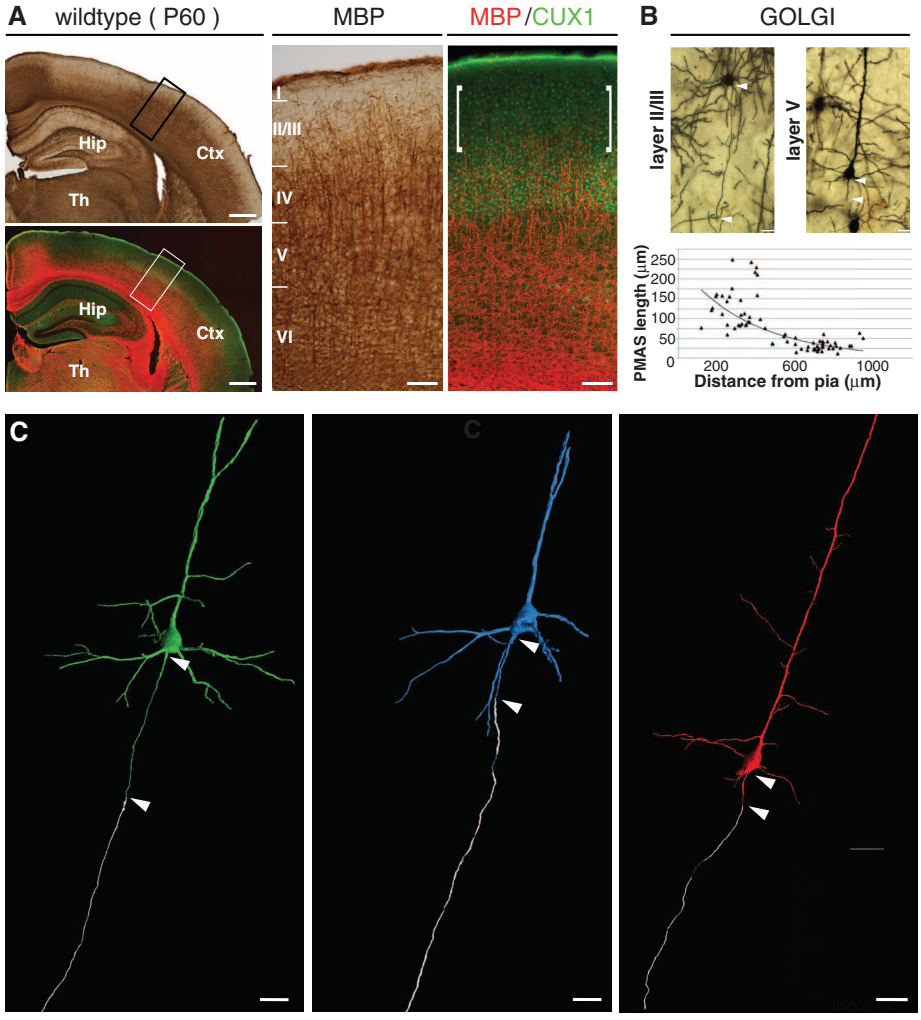

Fig. 1. Radial distribution of myelin in the adult mouse neocortex. (**A**) Immunohistochemical staining of MBP and Cux1 in coronal sections of wild-type adult neocortex. High magnifications of boxed areas show reduced levels of myelin in layer II/III (brackets). (**B**) PMAS lengths (arrowheads) in Golgi-Cox–labeled adult wild-type cortex. (Top) Representative neurons in layer II/III and layer V. (Bottom) Scatter plot of PMAS length versus distance of neuronal cell bodies from the pia ($n = 72$, $R^2 = 0.61093$). (**C**) Three-dimensional renderings of three representative neurons. The green and blue neurons were located in layer III to IV, and the red neuron was in layer V. Myelin is shown in white. Ctx, cortex; Hip, hippocampus; Th, thalamus. Scale bars: 500 µm (A) low magnification, 100 µm (A) insets, 20 µm (B), and 25 µm (C).

heterogeneity than layer V and VI neurons (*11*). The observed structural heterogeneity might contribute to the functional diversity of this complex neuronal population and be important when modeling neuronal function and network behavior in the neocortex.

In addition to the 17 neurons with intermittent myelination, we found that three neurons in layer II/III had exceptionally long PMASs (142.5, 121.6, and 101.2 μm) (Fig. 2 and fig. S3). Finally, we found two neurons whose axons were unmyelinated until the lower border of the data set (for a total distance of 208.4 μm and 193.1 μm, respectively) (Fig. 2 and fig. S3). Although we cannot exclude the possibility that these axons become myelinated farther along their path, they likely represent unmyelinated axons found in the corpus callosum (*12*). It is interesting that these three profiles of myelination can be found in neurons located in immediately adjacent positions within the same cortical layer (Fig. 2C).

To determine whether defined structural features are present along the unmyelinated segments of the layer II/III neurons that we traced, we examined them for the presence of synapses. We found that both afferent and efferent synapses exist on these unmyelinated tracts, including those of neurons with intermittent myelin (Fig. 2B, fig. S5, and table S2). Together, these features may provide a structural template for enhanced cortical plasticity.

In the peripheral nervous system, myelination is correlated with axon caliber (*1*, *2*). Although in the CNS this correlation is less stringent, because diameters of myelinated and unmyelinated axons overlap (*2*), nevertheless, axonal caliber may affect the myelin patterns that we observed. To investigate this possibility, we reconstructed the volumes of 283 cell bodies of pyramidal neurons across all layers of the S1 data set (Fig. 3A). We used these volumetric measurements as the most

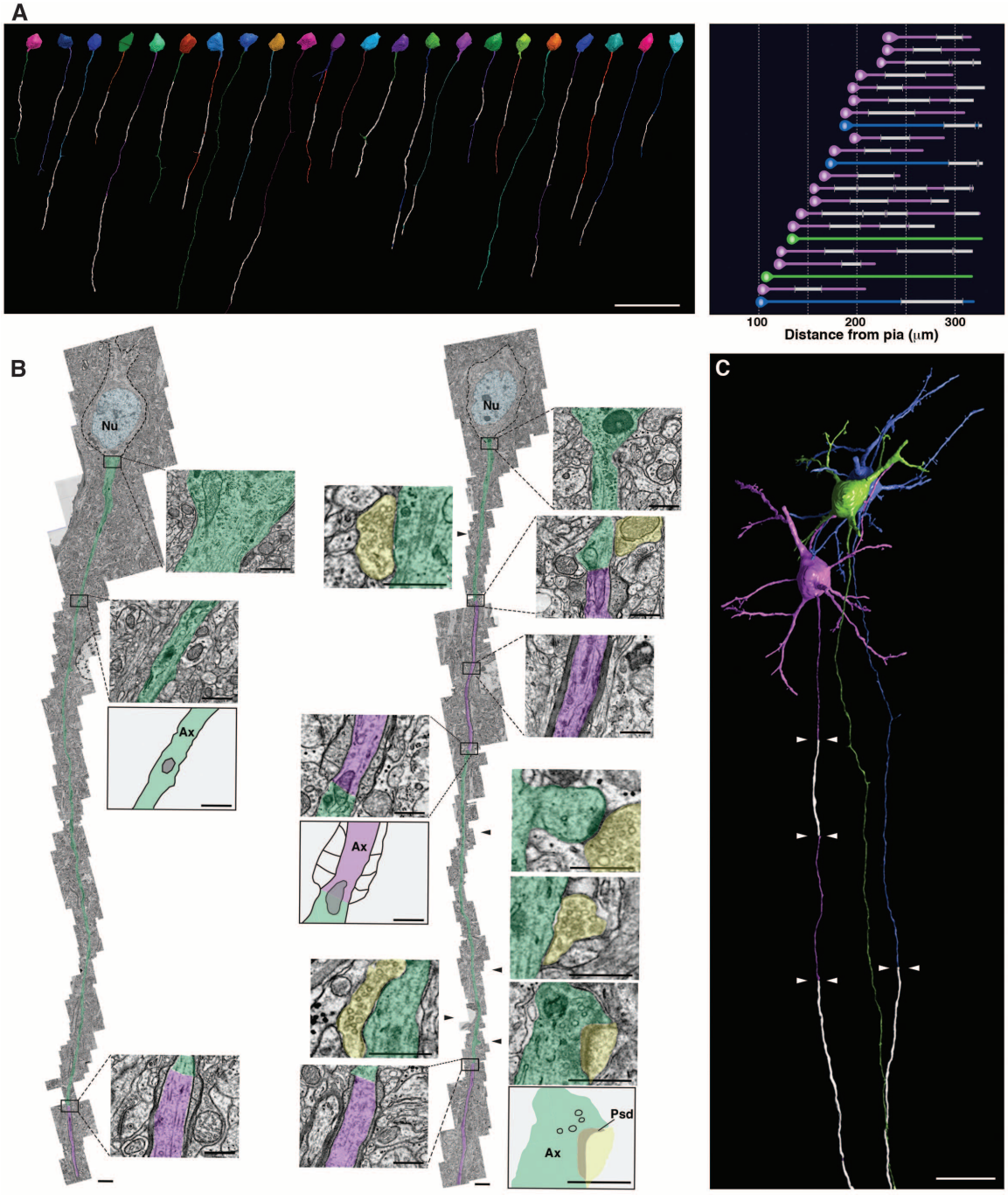

Fig. 2. Layer II/III pyramidal neurons display novel profiles of longitudinal myelination including intermittent myelin. (**A**) High-resolution rendering of myelin distribution along single axons of 22 pyramidal neurons traced and reconstructed in layer II/III of the V1 data set. (Right) Soma position and lengths of axonal tracts for all neurons rendered at left. Magenta, neurons with intermittent myelin; blue, neurons with long PMASs; green, neurons with unmyelinated axons; white, myelinated axonal segments. (**B**) Representative, serial EM reconstructions of neurons with long PMASs (left) or intermittent myelin (right). Unmyelinated axon tracts are highlighted in green and myelinated tracts in magenta. (Insets) EM images and schematic representations of selected regions from each axon. Yellow, selected synapses mapped on the intermittently myelinated axon. Ax, axon; Nu, nucleus; Psd, postsynaptic density. (**C**) High-resolution rendering of three representative neurons displaying different myelination modes. Native positions of these neurons are preserved in the rendering. Arrowheads mark the boundaries of myelinated tracts (white). Scale bars: 50 μm (A), 2 μm (B), 0.5 μm (B) insets, and 20 μm (C).

reliable indicator of average axon caliber, which is correlated with soma size (*13*, *14*). All pyramidal neurons in layers II/III, IV, and VI had comparable sizes (layer II/III, 1654.3 ± 38.6 μm^3, n = 70; layer IV, 1712.1 ± 44.4 μm^3, n = 75; and layer VI, 1592.2 ± 40.5 μm^3, n = 54; means ± SEM) (Fig. 3A). Layer V contained pyramidal neurons of different sizes (average volume = 2277.1 ± 82.4 μm^3, n = 82; mean ± SEM), including large neurons likely representing subcerebral projection neurons (Fig. 3A). Despite different soma volumes, all neurons traced in layer V had comparable profiles of myelination and PMAS lengths (fig. S4 and Fig. 3A). We also performed volumetric measurements of all neurons reconstructed in the V1 data set and found that they were all comparable in volume regardless of their myelination profiles ("long-PMAS" neurons, 1229.8 ± 110.7 μm^3; "unmyelinated" neurons, 1410.9 ± 29.1 μm^3; "intermittent myelin" neurons, 1220.2 ± 58 μm^3; means ± SEM) (Fig. 3B). Thus, we observed no correlation between neuronal soma size (and thus axon caliber) and profile of myelination.

Another possible determinant of myelin distribution may relate to availability of mature oligodendrocytes (OLs) and oligodendrocyte progenitors (OPCs) around different neurons. We quantified the radial distribution of OPCs and OLs in the cortex. Sox10$^+$ cells, which include both OLs and OPCs (*15*), were present in all layers (Fig. 3C). Thus, we quantified the distribution of OPCs and OLs separately. We found no difference in the radial distribution of OPCs, labeled by platelet-derived growth factor α (*Pdgfrα*) (*1*) (Fig. 3C). These data indicate that OPCs are not prevented from populating the upper layers of the cortex. In contrast, mature OLs, which are marked by proteolipid protein 1 (Plp1) (*1*) and adenomatous

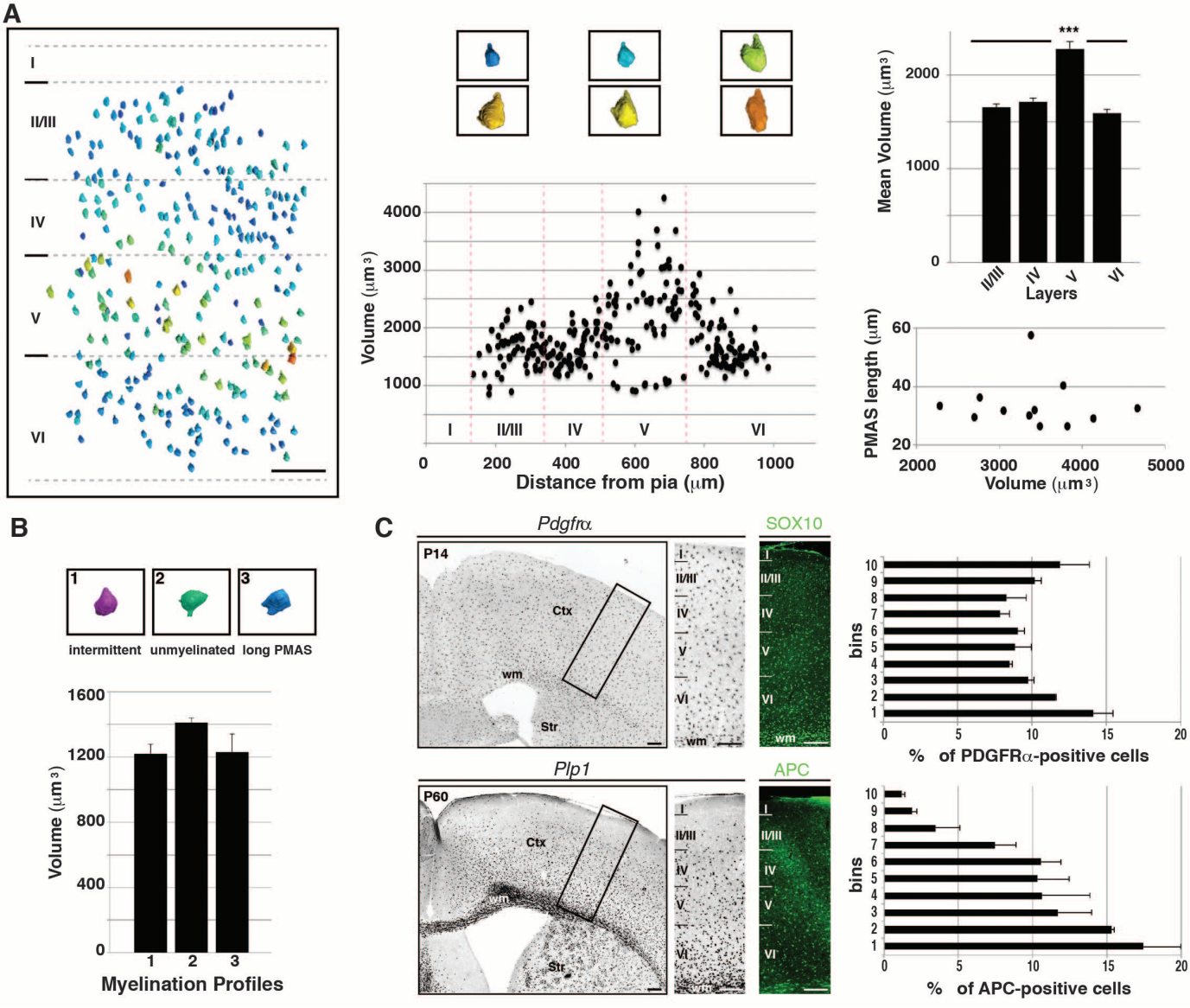

Fig. 3. Longitudinal myelination profile is independent of neuron size and availability of oligodendrocyte progenitors. (**A**) Rendering and volumetric measurements of 283 pyramidal neurons across all layers of the S1 data set. Soma size is color-coded with largest and smallest neurons rendered in orange and blue, respectively. (Center) Scatter plot of soma volumes versus distances from the pia. (Top right) Average values of the soma volumes measured in each cortical layer. (Bottom right) Scatter plot of PMAS lengths in layer V and VI versus cell body volumes. (**B**) Average values of soma volumes of 22 neurons from the V1 data set, grouped according to their myelination profiles. (**C**) (Top) In situ hybridization for PDGFRα and immunohistochemistry for Sox10 in postnatal day 14 (P14) wild-type cortex. (Right) Quantification of OPC distribution across layers. (Bottom) In situ hybridization for *Plp1* and immunohistochemistry for APC in adult wild-type cortex. (Right) Quantification of OL distribution across layers. Error bars, means ± SEM. Ctx, cortex; wm, white matter; Str, striatum. Scale bars: 150 μm (A), 200 μm (C).

polyposis coli (APC) (*16*), showed a radial distribution that matched the myelin gradient, with the vast majority residing in the deep layers (Fig. 3C). Our results indicate that the observed layer-specific differences in myelination are not due to the absence of OPCs in the upper layers but rather to their lamina-specific capacity to generate mature OLs.

Both OL development and myelin biogenesis are influenced by neuron-derived signals (*17*–*20*). Thus, the observed laminar differences in OPCs ability to give rise to OLs suggest influence of different neurons on OL development and point to a role of neuronal diversity in modulating myelin distribution in different layers. To test this possibility, we investigated how misplacement of pyramidal neurons into different layers affects myelination of the cortex using two models of aberrant neuronal migration, *Dab1*$^{-/-}$ (*21*) and *Emx1-Cre;RhoA*$^{fl/fl}$ mice (*22*). In the neocortex of the *Dab1*$^{-/-}$ mice, the radial position of pyramidal neurons is nearly inverted, with neurons of layers V and VI [labeled by Ctip2 (*6*)] ectopically located in the upper layers and those of upper layers (labeled by Cux1) located in the deep layers (*21*, *23*, *24*). In this mutant cortex, the gradient of myelination was lost, and comparable levels of myelin (labeled by MBP and Black Gold II) were detected in all layers (Fig. 4B). This altered myelination profile was reflected in the even distribution of APC^{+} OLs in all layers of the mutant cortex (Fig. 4B). As the class-specific identity of pyramidal neurons in these mice is not

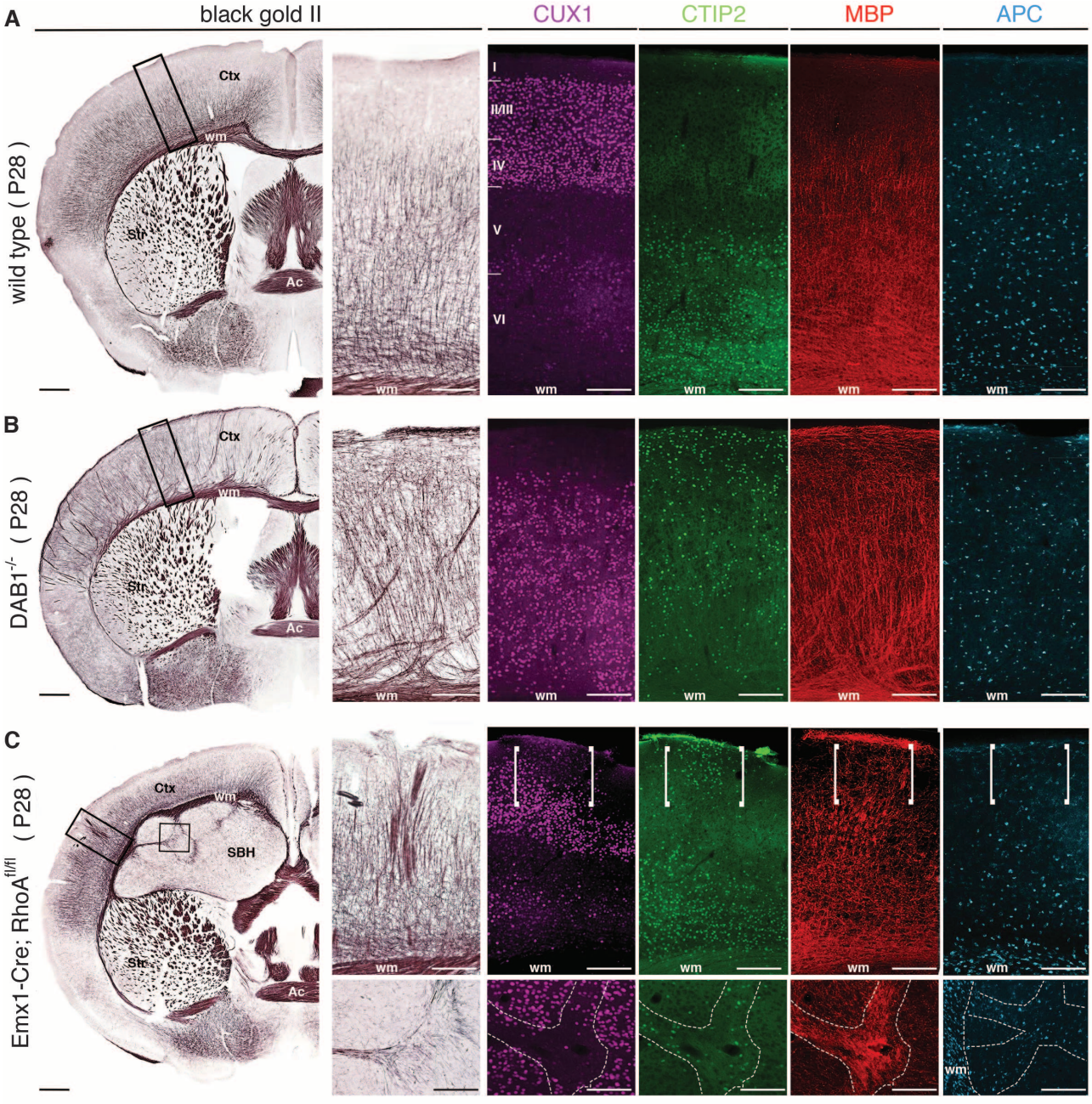

Fig. 4. Distribution of myelin depends on the laminar position of distinct classes of projection neurons. Histological staining of myelin by Black Gold II and immunohistochemistry for Cux1, Ctip2, MBP, and APC in P28 cortex of wild-type (**A**), *Dab1*$^{-/-}$ (**B**), and *Emx1-Cre;RhoA*$^{fl/fl}$ (**C**) mice with high magnifications of boxed areas. Immunohistochemistry for APC is on immediately consecutive sections. (C) (Top) Deep-layer neuron heterotopias and myelin distribution in normocortex. (Bottom) Myelin deposition in the SBH. Ac, anterior commissure; Ctx, cortex; SBH, subcortical band heterotopia; Str, striatum; wm, white matter. Scale bars: 400 μm (A) to (C), lower magnifications; 200 μm (A) to (C), higher magnifications.

affected (*25*), our results suggest that different classes of pyramidal neurons are endowed with different abilities to affect OL distribution and myelination. To further investigate this possibility, we sought to determine whether a focal alteration in pyramidal neuron position, rather than the global change present in the *Dab1*$^{-/-}$ mouse cortex, affected myelination. In the *Emx1-Cre;RhoA*$^{fl/fl}$ mice, defects in the radial glia cytoskeleton result in the generation of a secondary cortical tissue, called subcortical band heterotopia (SBH), which develops underneath a thinner neocortex (normocortex) (*22*). This model presents two types of focal abnormalities. First, SBH is mostly constituted by Cux1^{+} upper-layer pyramidal neurons with only scattered Ctip2^{+} neurons (Fig. 4C). Second, heterotopias composed of deep-layer neurons located within the upper layers can be found in the mutant normocortex (*22*). In both the SBH and the cortical heterotopias, we observed association between the presence of Ctip2^{+} deep-layer neurons and the ectopic distribution of APC^{+} OLs and myelin (Fig. 4C). Thus, changes in the laminar composition of pyramidal neurons affect the distribution of myelinating OLs, and pyramidal neurons of the upper and deep layers differentially influence myelin formation.

Here, we describe myelin distribution along single axons in the murine brain. We demonstrate that pyramidal neurons of different neocortical layers present signature profiles of myelination, which indicates that longitudinal myelin deposition is a defining feature of each neuron. This contributes to the emergence of a myelin gradient that reflects idiosyncratic interactions between pyramidal neurons and oligodendrocytes.

Although the functional significance of these heterogeneous profiles of myelination awaits future elucidation, we propose that it may have served the evolutionary expansion and diversification of the neocortex by enabling the generation of different arrays of communication mechanisms and the emergence of highly complex neuronal behaviors.

References and Notes

1. N. Baumann, D. Pham-Dinh, *Physiol. Rev.* **81**, 871–927 (2001).
2. C. Hildebrand, S. Remahl, H. Persson, C. Bjartmar, *Prog. Neurobiol.* **40**, 319–384 (1993).
3. M. Helmstaedter *et al.*, *Nature* **500**, 168–174 (2013).
4. J. W. Lichtman, W. Denk, *Science* **334**, 618–623 (2011).
5. S. Ramón y Cajal, *Histology of the Nervous System of Man and Vertebrates* (History of Neuroscience, Oxford Univ. Press, New York, 1995).
6. B. J. Molyneaux, P. Arlotta, J. R. Menezes, J. D. Macklis, *Nat. Rev. Neurosci.* **8**, 427–437 (2007).
7. M. Nieto *et al.*, *J. Comp. Neurol.* **479**, 168–180 (2004).
8. A. Fairén, A. Peters, J. Saldanha, *J. Neurocytol.* **6**, 311–337 (1977).
9. D. D. Bock *et al.*, *Nature* **471**, 177–182 (2011).
10. A. Cardona *et al.*, *PLOS ONE* **7**, e38011 (2012).
11. B. J. Molyneaux *et al.*, *J. Neurosci.* **29**, 12343–12354 (2009).
12. R. R. Sturrock, *Neuropathol. Appl. Neurobiol.* **6**, 415–420 (1980).
13. J. J. Sloper, T. P. Powell, *Philos. Trans. R. Soc. Lond. B Biol. Sci.* **285**, 173–197 (1979).
14. J. J. Sloper, T. P. Powell, *Philos. Trans. R. Soc. Lond. B Biol. Sci.* **285**, 123–139 (1979).
15. K. Kuhlbrodt, B. Herbarth, E. Sock, I. Hermans-Borgmeyer, M. Wegner, *J. Neurosci.* **18**, 237–250 (1998).
16. J. Lang *et al.*, *J. Neurosci.* **33**, 3113–3130 (2013).
17. H. Wake, P. R. Lee, R. D. Fields, *Science* **333**, 1647–1651 (2011).
18. B. A. Barres, M. C. Raff, *J. Cell Biol.* **147**, 1123–1128 (1999).
19. G. V. Michailov *et al.*, *Science* **304**, 700–703 (2004).
20. C. Taveggia, M. L. Feltri, L. Wrabetz, *Nat. Rev. Neurol.* **6**, 276–287 (2010).
21. H. O. Sweet, R. T. Bronson, K. R. Johnson, S. A. Cook, M. T. Davisson, *Mamm. Genome* **7**, 798–802 (1996).
22. S. Cappello *et al.*, *Neuron* **73**, 911–924 (2012).
23. M. L. Ware *et al.*, *Neuron* **19**, 239–249 (1997).
24. B. W. Howell, R. Hawkes, P. Soriano, J. A. Cooper, *Nature* **389**, 733–737 (1997).
25. F. Tissir, A. M. Goffinet, *Nat. Rev. Neurosci.* **4**, 496–505 (2003).

Acknowledgments: We are grateful to S. Lodato, C. Rouaux, B. Sannino, and all members of the Arlotta laboratory for insightful discussions and comments on the manuscript. We thank, in particular, Z. Trayes-Gibson for outstanding technical support; J. Macklis and W. Richardson for sharing riboprobes; and M. Gotz and S. Cappello for sharing tissue from the *Emx1-Cre;RhoA*$^{fl/fl}$ line. D.R.B. and H.S.S. were supported by the Howard Hughes Medical Institute, the Human Frontier Science Program, and the Gatsby Foundation. This work was supported by grants from NIH (NS062849 and NS078164), the New York Stem Cell Foundation, and the Harvard Stem Cell Institute to P.A. and Silvio O. Conte Centers for Basic and Translational Mental Health Research, National Institute for Mental Health, NIH (1P50MH094271); P.A. is a New York Stem Cell Foundation—Robertson Investigator.

Supplementary Materials

www.sciencemag.org/content/344/6181/319/suppl/DC1
Materials and Methods
Figs. S1 to S5
Tables S1 and S2
References (*26*–*33*)
Movies S1 to S3

16 December 2013; accepted 18 March 2014
10.1126/science.1249766

Suit(Ab)le Antibodies

We're selective. We're specific. We're scientists. We create the antibodies that are most relevant for today's research needs.

As a thoughtful producer, we take a selective approach to offering the best antibodies for each target. Our team of R&D scientists combs research and collaborates with leading institutions to identify only the most relevant antibodies for your research. Our expertise combines the pioneering work of Chemicon® and Upstate®, but our wisdom doesn't stop there. We constantly review, assess and determine which antibodies are the most suitable – those which provide the right level and type of data. It is our job to understand your needs so we can offer you the best of the best.

Put the most suitable antibodies to work for you.
www.emdmillipore.com/Ab

EMD Millipore is a division of
Merck KGaA, Darmstadt, Germany

BS-GEN-13-09105 03/2014

NEW ENGLAND BioLabs® Inc.
enabling technologies in the life sciences

Make ends meet.

Gibson Assembly® Cloning Kit

New England Biolabs has revolutionized your laboratory's standard cloning methodology. The Gibson Assembly Cloning Kit combines the power of the Gibson Assembly Master Mix with NEB 5-alpha Competent *E. coli*, enabling fragment assembly and transformation in just under two hours. Save time, without sacrificing efficiency.

Making ends meet is now quicker and easier than ever before, with the Gibson Assembly Cloning Kit from NEB.

Gibson Assembly Cloning Kit provides robust transformation efficiencies

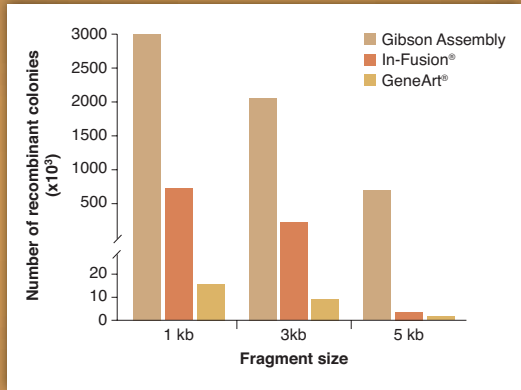

Assembly reactions containing 25 ng of linear pUC19 vector and 0.04 pmol of each fragment were performed following individual suppliers' recommended protocols and using the competent cells provided with the kit. The total number of recombinant colonies was calculated per 25 ng of linear pUC19 vector added to the assembly reaction.

NEBuilder™ for Gibson Assembly

Visit **NEBGibson.com** to view the latest tutorials and to try our primer design tool.

SGI-DNA

PNAS Congratulates 2013 Cozzarelli Prize Recipients

The *Proceedings of the National Academy of Sciences* (PNAS) has selected six outstanding articles for the 2013 Cozzarelli Prize, in recognition of their scientific excellence and originality. Winners were selected from the 3,850 research articles published in PNAS in 2013 and represent exceptional contributions to the six broadly defined classes under which the National Academy of Sciences is organized.

2013 Cozzarelli Prize Recipients

Class I: Physical and Mathematical Sciences

Prevalence of Earth-size planets orbiting Sun-like stars

Erik A. Petigura, Andrew W. Howard, and Geoffrey W. Marcy

(2013) PNAS 110:19273–19278

Class II: Biological Sciences

Task-related "cortical" bursting depends critically on basal ganglia input and is linked to vocal plasticity

Satoshi Kojima, Mimi H. Kao, and Allison J. Doupe

(2013) PNAS 110:4756–4761

Class III: Engineering and Applied Sciences

Gas production in the Barnett Shale obeys a simple scaling theory

Tad W. Patzek, Frank Male, and Michael Marder

(2013) PNAS 110:19731–19736

Class IV: Biomedical Sciences

Human placental trophoblasts confer viral resistance to recipient cells

Elizabeth Delorme-Axford, Rogier B. Donker, Jean-Francois Mouillet, Tianjiao Chu, Avraham Bayer, Yingshi Ouyang, Tianyi Wang, Donna B. Stolz, Saumendra N. Sarkar, Adrian E. Morelli, Yoel Sadovsky, and Carolyn B. Coyne

(2013) PNAS 110:12048–12053

Class V: Behavioral and Social Sciences

Historical collections reveal patterns of diffusion of sweet potato in Oceania obscured by modern plant movements and recombination

Caroline Roullier, Laure Benoit, Doyle B. McKey, and Vincent Lebot

(2013) PNAS 110:2205–2210

Class VI: Applied Biological, Agricultural, and Environmental Sciences

Neonicotinoid clothianidin adversely affects insect immunity and promotes replication of a viral pathogen in honey bees

Gennaro Di Prisco, Valeria Cavaliere, Desiderato Annoscia, Paola Varricchio, Emilio Caprio, Francesco Nazzi, Giuseppe Gargiulo, and Francesco Pennacchio

(2013) PNAS 110:18466–18471

Podcast interviews with the authors will be available at:
pnas.org/site/misc/cozzarelliprize.xhtml

PNAS
www.pnas.org

immunogenomics 2014

September 29 - October 1, 2014

HudsonAlpha Biotechnology Campus
Huntsville, Alabama, USA

Bringing together preeminent leaders and thinkers at the intersection of genomics and immunology

Our Keynote Speakers:

Christophe Benoiste
Professor, Department of Microbiology and Immunobiology, *Harvard Medical School*

Mary Ellen Conley
Federal Express Chair of Excellence and Professor, Department of Pediatrics, *University of Tennessee, College of Medicine, Memphis*

Mark Davis
Investigator, Howard Hughes Medical Institute; Professor, Department of Microbiology and Immunology; Director, Institute for Immunity, Transplantation, and Infections, *Stanford University School of Medicine*

Sponsored by

Platinum Sponsors

iRepertoire, Inc.

Gold Sponsors

UAB COMPREHENSIVE ARTHRITIS, MUSCULOSKELETAL, AND AUTOIMMUNITY CENTER

Silver Sponsors

GenapSys

illumina

Interested in sponsoring Immunogenomics 2014? Visit our website for more information.

Register today at

haig.aaas.org

follow @immunogenomics on twitter

presented by

HUDSONALPHA INSTITUTE FOR BIOTECHNOLOGY

Science AAAS

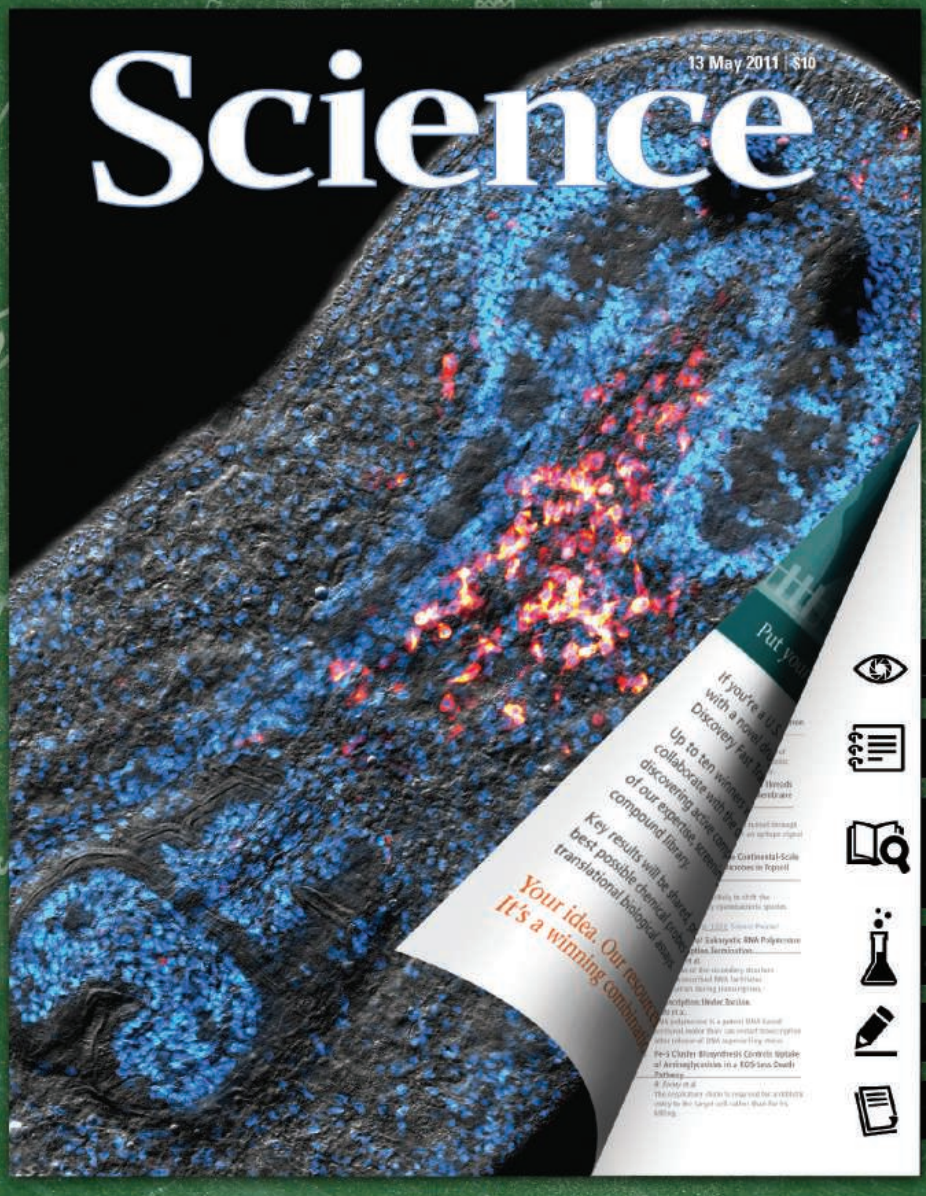

Learning Lens

Learning Notes

Connect to Learning Standards

Activities

Discussion Questions

References

Online tools to help your students analyze a professional research paper!

Science

Tell me and I forget. Teach me and I remember. Involve me and I learn. -- Benjamin Franklin

Featuring over 6 research papers at any given time, *Science* in the Classroom is specifically designed to help young researchers understand the structure and workings of professional scientific research.

Learn for yourself how *Science* in the Classroom can help your students deepen their understanding of scientific research. **Visit scienceintheclassroom.org today.**

AAAS
ADVANCING SCIENCE, SERVING SOCIETY

eppendorf
& Science

PRIZE FOR NEURO BIOLOGY

2013 Winner
Dr. Michael Yartsev
CV Starr Research Fellow
Princeton Neuroscience Institute

Application Deadline
June 15, 2014

Call for Entries

Eppendorf & Science Prize for Neurobiology
The annual Eppendorf & Science Prize for Neurobiology, an international award, honors young scientists for their outstanding contributions to neurobiological research based on methods of molecular and cell biology.
The winner and finalists are selected by a committee of independent scientists, chaired by Science's Senior Editor, Dr. Peter Stern. To be eligible, you must be 35 years of age or younger.

You could be next to win this prize and to receive
> Prize money of US$25,000
> Publication of your work in Science
> Full support to attend the Prize Ceremony held in conjunction with the Annual Meeting of the Society for Neuroscience in the USA
> An invitation to visit Eppendorf in Hamburg, Germany

It's easy to apply!

Learn more at: www.eppendorf.com/prize

eppendorf

Science
AAAS

SORPTION MICROBALANCE

XEMIS is a new high-accuracy sorption microbalance for precision weighing in extreme environments. The XEMIS allows the analysis of gas and vapor sorption by materials at pressures as high as 200 bar and at temperatures between 77 K and 500°C. It can also handle aggressive species. This combination of conditions was not previously achievable with commercial gravimetric sorption analyzers. Featuring new exosensing technology, the unique design of the XEMIS removes the sensing and control mechanisms from the microbalance chamber and out of the wetted zone. This allows sorption analysis with hazardous and aggressive species without compromising measurement accuracy or resolution. Furthermore, unparalleled weight measurement stability is provided by the symmetric geometry beam balance design. The intrinsic long-term stability of the XEMIS, with no need to rezero or recalibrate the balance, ensures the capture of true sorption behavior and provides the ability to record full kinetic data over extended timescales.

Hiden Isochema

For info: +44-(0)-1925-244678 | www.hidenisochema.com

NEURAL PROGENITORS CELLS

A new range of neural progenitor cells and cerebral cortical neurons derived from human induced pluripotent stem (iPS) cells is now available. Using cutting-edge stem cell technologies to generate high-purity human neural cells and neurons, AMSBIO is able to provide healthy and Alzheimer's disease patient-derived cerebral cortical neurons and neural progenitor cells. This accessible, in vitro human-based system offers a platform to build human cellular models to study conditions including Alzheimer's, autism, epilepsy, traumatic brain injury, and stroke. Derived using integration-free fully defined neural induction conditions, these cells are electrically active, form functional synapses in vitro and can be transplanted into animal models. Available in industrial quantities, these cerebral cortical neurons and neural progenitor cells are supplied with extensive functional and molecular characterization data. All products are supplied ready-made and remain viable in culture for months to facilitate reproducible and long-term studies.

AMS Biotechnology

For info: +44-(0)-1235-828200 | www.amsbio.com

BIOREACTOR SYSTEM

The new CellMaker PLUS is a highly flexible, robust, and easy-to-use single-use bioreactor system. The system includes improved control software and comes complete with full pH and dissolved oxygen (DO) control. The system is designed for microbial applications, especially bacterial and yeast cell culture, providing the highest DOs and improved yields of soluble protein in oxygen-hungry cell types such as *E. coli*. Production, quality control, and service of the fully CE marked system is conducted from the new Cellexus facilities in Cambridgeshire (UK) which is ISO9001 certified. The new CellMaker PLUS has been proven to provide highly efficient oxygen transfer, allowing high rates of cell growth outperforming bacterial and yeast cell culture in other systems. It uses CellMaker PLUS Bags which are unique, next generation single-use, disposable cell culture bags in which the cells are grown with fast setup times, no cleaning requirements and no cross-contamination.

Cellexus Limited

For info: +44-(0)-1354-602997 | www.cellexusinc.com

Grp78/BiP ELISA KIT

Unique enzyme-linked immunosorbent assays (ELISAs) for protein homeostasis (proteostasis), neurodegenerative disorders, and cancer research are now available with the high-sensitivity Grp78/BiP ELISA Kit. Grp78/BiP is an endoplasmic reticulum (ER)-specific homologue of Hsp70, serving as a critical stress-sensing chaperone and regulator of the unfolded protein response. This quantitative ELISA kit offers sensitivity to enable quantification of both normal and upregulated levels of Grp78/BiP, detecting as little as 8.4 ng/mL of Grp78/BiP in human, mouse, and rat cell lysates or serum samples. The assay provides quantitative results with excellent reproducibility between experiments, offering efficiency over Western blotting by requiring less sample input, and analysis of up to 40 duplicate samples in just 2.5 hours. The Grp78/BiP ELISA kit is complete, flexible, and put through rigorous fit-for-purpose validation and stability testing to ensure high precision, accuracy, sensitivity, and specificity. It is supplied with an easy-to-follow protocol, precoated microtiter plate, and liquid color-coded reagents.

Enzo Life Sciences

For info: 800-942-0430 | www.enzolifesciences.com

UNIVERSAL BLOCKING OLIGOS

By incorporating xGen Universal Blocking Oligos into target capture experiments, users can decrease the complexity and increase throughput of their target capture experiment without degradation of performance. Blocking oligos are commonly used to enhance the performance of capture experiments, through the prevention of cross-hybridization between adapter sequences. Adapters ligated to the DNA library before enrichment can hybridize to each other and cause an increase in off-target reads. Blocking oligos bind to these adapters to prevent nonspecific binding. However, when multiple samples are processed simultaneously, each adapter requires a unique blocking oligo, increasing the complexity of the experiment. xGen Universal Blocking Oligos are able to bind to all indexed adapters using a single oligonucleotide sequence, removing the need for multiple oligos. As a result, researchers can more readily multiplex their experiments for cost-effective enrichment of thousands of samples.

Integrated DNA Technologies

For info: 800-328-2661 | www.idtdna.com

Electronically submit your new product description or product literature information! Go to **www.sciencemag.org/products/newproducts.dtl** for more information.

Newly offered instrumentation, apparatus, and laboratory materials of interest to researchers in all disciplines in academic, industrial, and governmental organizations are featured in this space. Emphasis is given to purpose, chief characteristics, and availability of products and materials. Endorsement by *Science* or AAAS of any products or materials mentioned is not implied. Additional information may be obtained from the manufacturer or supplier.

CALL FOR PAPERS

www.mrs.org/fall2014

2014 MRS® FALL MEETING & EXHIBIT

November 30 - December 5, 2014 | Boston, Massachusetts

Abstract Submission Deadline June 19, 2014
Abstract Submission Opens May 19, 2014

BIOMATERIALS AND SOFT MATERIALS

- A Organic Bioelectronics
- B Multifunctional Polymeric and Hybrid Materials
- C Medical Applications of Noble Metal Nanoparticles (NMNPs)
- D Materials and Concepts for Biomedical Sensing
- E Hard-Soft Interfaces in Biological and Bioinspired Materials—Bridging the Gap between Theory and Experiment
- F Reverse Engineering of Bioinspired Nanomaterials
- G Plasma Processing and Diagnostics for Life Sciences
- H Micro/Nano Engineering and Devices for Molecular and Cellular Manipulation, Stimulation and Analysis
- I Emerging 1D and 2D Nanomaterials in Health Care

ELECTRONICS AND PHOTONICS

- J Emerging Non-Graphene 2D Atomic Layers and van der Waals Solids
- K Graphene and Graphene Nanocomposites
- L Optical Metamaterials and Novel Optical Phenomena Based on Nanofabricated Structures
- M Materials and Technology for Nonvolatile Memories
- N Frontiers in Complex Oxides
- O Oxide Semiconductors
- P Hybrid Oxide/Organic Interfaces in Organic Electronics
- Q Fundamentals of Organic Semiconductors—Synthesis, Morphology, Devices and Theory
- R Diamond Electronics and Biotechnology—Fundamentals to Applications

ENERGY AND SUSTAINABILITY

- S Advances in Materials Science, Processing and Engineering for Fuel Cells and Electrolyzers
- T Wide-Bandgap Materials for Solid-State Lighting and Power Electronics
- U Organic Photovoltaics—Fundamentals, Materials and Devices
- V Sustainable Solar-Energy Conversion Using Earth-Abundant Materials
- W Perovskite-Based and Related Novel Material Solar Cells
- Y Technologies for Grid-Scale Energy Storage
- Z Materials Challenges for Energy Storage across Multiple Scales
- AA Synthesis, Processing and Mechanical Properties of Functional Hexagonal Materials for Energy Applications
- BB Molecular, Polymer and Hybrid Materials for Thermoelectrics
- CC Advanced Materials and Devices for Thermoelectric Energy Conversion
- DD Materials for Advanced Nuclear Technologies
- EE Scientific Basis for Nuclear Waste Management XXXVIII
- FF Materials as Tools for Sustainability

NANOMATERIALS AND SYNTHESIS

- GG Nanomaterials for Harsh Environment Sensors and Related Electronic and Structural Components—Design, Synthesis, Characterization and Utilization
- HH Flame and High-Temperature Synthesis of Functional Nanomaterials—Fundamentals and Applications
- II Semiconductor Nanocrystals, Plasmonic Metal Nanoparticles, and Metal-Hybrid Structures
- JJ 3D Mesoscale Architectures—Synthesis, Assembly, Properties and Applications
- KK Directed Self-Assembly for Nanopatterning
- LL Semiconductor Nanowires—Growth, Physics, Devices, and Applications
- MM Carbon Nanotubes—Synthesis, Properties, Functionalization and Applications

THEORY, CHARACTERIZATION AND MODELING

- NN Mathematical and Computational Aspects of Materials Science
- OO *In Situ* Characterization of Dynamic Processes during Materials Synthesis and Transformation
- PP Advances in Scanning Probe Microscopy for Multimodal Imaging at the Nanoscale
- QQ Advances in Nanoscale Subsurface, Chemical and Time-Resolved Studies of Soft Matter
- RR Scaling Effects in Plasticity—Synergy between Simulations and Experiments
- SS Informatics and Genomics for Materials Development
- TT Advanced Materials Exploration with Neutrons and X-Rays—The State-of-the-Art in the International Year of Crystallography

GENERAL

- UU Structure-Property Relations in Amorphous Solids
- VV Reactive Materials—Past, Present and Future
- WW Defects and Radiation Effects in Advanced Materials
- XX Bridging Scales in Heterogeneous Materials
- YY Advanced Structural and Functional Intermetallic-Based Alloys
- ZZ Hierarchical, High-Rate, Hybrid and Roll-to-Roll Manufacturing
- AAA Undergraduate Research in Materials Science—Impacts and Benefits

Meeting Chairs

Husam N. Alshareef King Abdullah University of Science and Technology
Amit Goyal Oak Ridge National Laboratory
Gerardo Morell University of Puerto Rico
José A. Varela University of São Paulo State - UNESP
In Kyeong Yoo Samsung Advanced Institute of Technology

MRS MATERIALS RESEARCH SOCIETY®
Advancing materials. Improving the quality of life.

506 Keystone Drive • Warrendale, PA 15086-7573
Tel 724.779.3003 • Fax 724.779.8313
info@mrs.org • www.mrs.org

Don't Miss This Future MRS Meeting!

2015 MRS Spring Meeting & Exhibit
April 6-10, 2015

Moscone West & San Francisco Marriott Marquis
San Francisco, California

Promega

Better Biology, Less Work

NAD(P)/NAD(P)H-Glo Assays

The simple add-and-read NAD(P)/NAD(P)H-Glo Assays have unparalleled sensitivity and linearity making them ideal for metabolic research and HTS research applications. These assays enable direct in-well measurement of total and individual NAD/NADH or NADP/NADPH and can be used in either biochemical or cell-based applications.

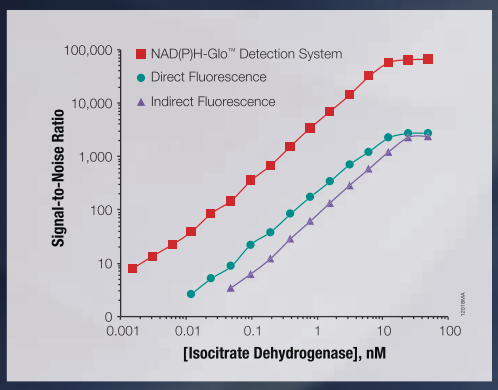

Superior sensitivity compared to fluorescent methods (Total NADH + NADPH measured).

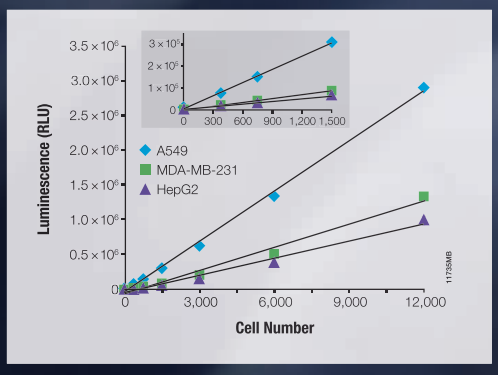

Directly measure total dinucleotide concentrations in multiwell plates using low cell numbers (Total NADP + NADPH measured).

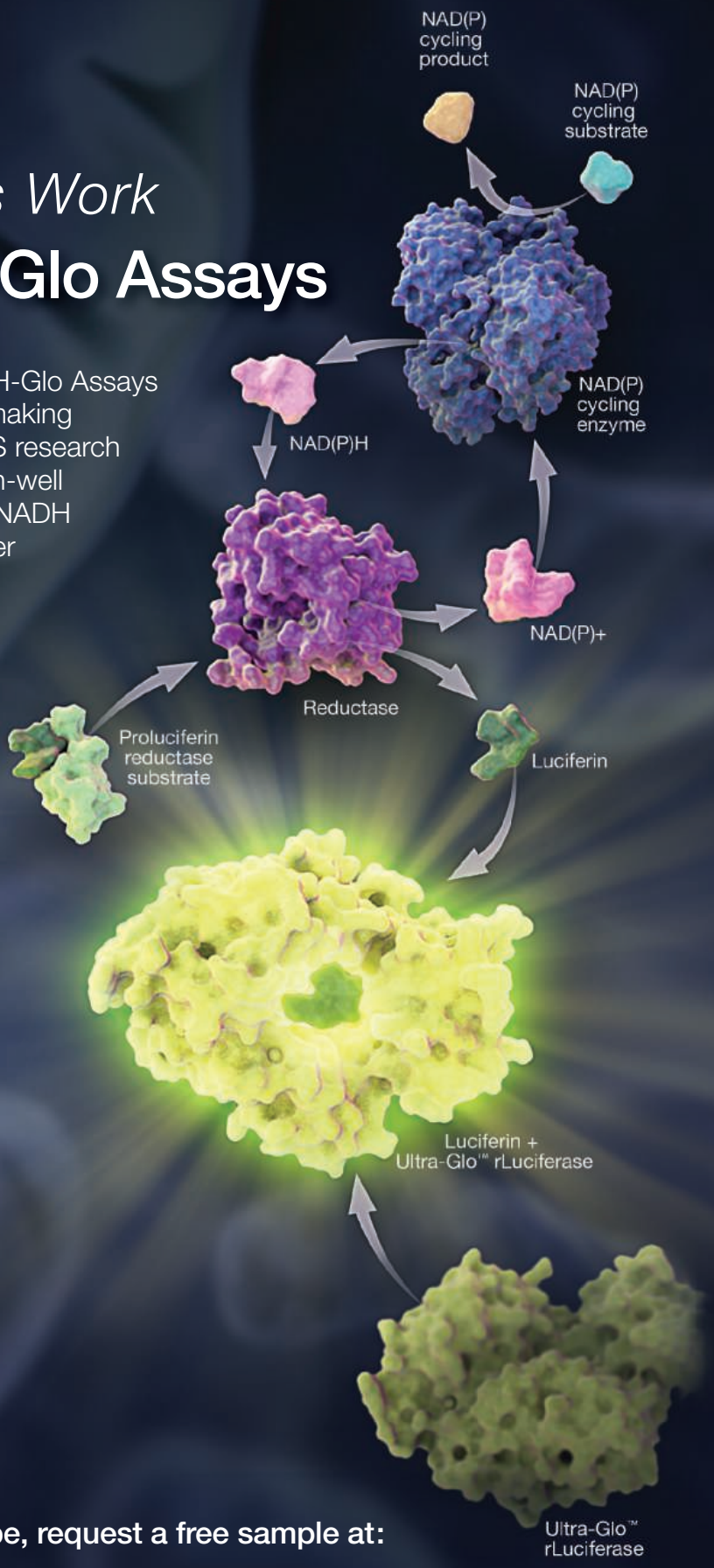

To see how easy better biology can be, request a free sample at:

www.promega.com/NADassays


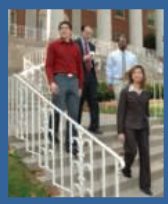
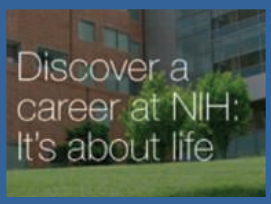


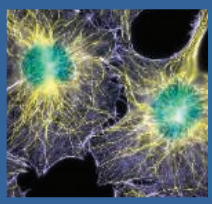

Deputy Director, National Institute of General Medical Sciences
National Institutes of Health

The National Institutes of Health is the center of medical and behavioral research for the Nation making essential medical discoveries that improve health and save lives.

Are you an exceptional candidate who can provide leadership to one of the preeminent Institutes of the National Institutes of Health?
This position offers a unique opportunity to serve as the second-in-command of the National Institute of General Medical Sciences (NIGMS) with responsibility for the execution and management of the daily operations in support of NIGMS's strategic vision and mission. The Deputy Director works collaboratively across the NIH throughout the Federal government and with other key stakeholders and organizations to further the advancement of NIGMS's mission and objectives. He/she serves as the ambassador and spokesperson for the Institute, communicating the NIGMS' position and incorporating the views/needs of key stakeholders into Institute plans and initiatives. The Deputy Director facilitates the identification and development of future leaders through mentoring programs, continuous development of skills and expertise, and recognition of achievements. In addition, he/she serves as a role model to the rest of the Institute, managing people and financial resources with integrity and fairness, while maintaining the Institute's policies and priorities.

We are looking for applicants with a commitment to scientific excellence and the energy, enthusiasm, and innovative thinking necessary to lead a dynamic and diverse organization. Applicants must possess an M.D. and/or Ph.D. and possess senior-level scientific research experience and outstanding scientific knowledge of research programs in one or more scientific areas related to cell biology, biophysics, genetics, developmental biology, pharmacology, physiology, biological chemistry, biomedical technology, bioinformatics, and/or computational biology. They should be known and respected within their profession, both nationally and internationally, as individuals of outstanding scientific competence. Applicants must also have demonstrated experience in setting, planning, implementing, and analyzing program objectives and priorities. They should have the demonstrated ability to manage financial and human resources, lead a research program involving extensive internal and external collaborations, experience managing programs related to the creation of a highly skilled and diverse biomedical research workforce.

The successful candidate for this position will be appointed at a salary commensurate with his/her qualifications and experience, and a full Federal benefits package is available including: leave, health and life insurance, retirement, long term care insurance, and savings plan (401K equivalent).
DHHS AND NIH ARE EQUAL OPPORTUNITY EMPLOYERS

If you are ready for an exciting leadership opportunity, please see the detailed vacancy announcement for mandatory qualifications requirements and application procedures at http://www.jobs.nih.gov/ (under Executive Jobs). Applications are due by 11:59 P.M. EST on May 27, 2014.

AWARDS

CALL FOR NOMINATIONS:

Sanofi and the Institut Pasteur are pleased to announce the Sanofi - Institut Pasteur 2014 Awards.

These Awards will honor four scientists, whose outstanding research in the life sciences is contributing to progress in global public health, specifically in the following fieds:

TROPICAL AND NEGLECTED DISEASES | **IMMUNOLOGY** | **DRUG RESISTANCE** | **NEUROBIOLOGY**

SANOFI - INSTITUT PASTEUR 2014 AWARDS
€ 300 000
FOR BIOMEDICAL RESEARCH

INSPIRED BY PASTEUR
SUPPORTED BY SANOFI

There will be three categories of awards:

- **One International Senior award (€ 125 000)**
- **One International Mid-career award[1] (€ 75 000)**
- **Two National Junior awards[2] (€ 50 000 each)**

More information and the nomination form are available on the website **www.sanofi-institutpasteur-awards.com**

Deadline to submit nominations: **Friday, 16th May, 2014**

Awards Ceremony: **Thursday, 20th November, 2014 in Paris**

A distinguished international Jury will choose the Awardees:
Prof. Peter C Agre, Prof. Elizabeth H. Blackburn, Prof. Pascale Cossart, Prof. Alain Fischer, Prof. Peter Gruss, Prof. Jörg H. Hacker, Prof. Jules A. Hoffmann, Dr Gary J. Nabel, Prof. Staffan Normak, Prof. Jeffrey V. Ravetch and Prof. Philippe Sansonetti.

Contact: 2014awards@pasteur.fr

[1]The candidates should not be more than 52 years old on 1-7-2014 - [2]The candidates should not be more than 45 years old on 1-7-2014 and should work in France

Institut Pasteur

www.sanofi-institutpasteur-awards.com

SANOFI

KEK
HIGH ENERGY ACCELERATOR RESEARCH ORGANIZATION

Call for Nomination for Next Director-General of KEK

KEK, High Energy Accelerator Research Organization, invites nominations for the next Director-General whose term will begin April 1, 2015.

The role of Director-General, therefore, is to promote with long-term vision and strong scientific leadership, the highly advanced, internationalized, and inter-disciplinary research activities of KEK by getting support from the public. The successful candidate is also expected to establish and carry out the medium-term goals and plans.

The term of appointment is three years. When reappointed, the term can be extended up to 9 years. We widely accept the nomination of the candidates regardless of their nationalities.

We would like to ask you to recommend the best person who satisfies requirements for the position written above.

Nomination should be accompanied by:
1) Recommendation form, 2) letter of recommendation, 3) Curriculum vitae (brief personal history of the candidate), and 4) list of major achievements (publications, academic papers, commendations and membership of councils, etc.). The nomination should be submitted to the following address **no later than May 30, 2014**:
- Documents should be written either in English or in Japanese.
- Forms are available at: **http://legacy.kek.jp/intra-e/info/2014/030109/**

Inquiries concerning the nomination should be addressed to:

General Affairs Division
General Management Department
KEK, High Energy Accelerator Research Organization
1-1 Oho, Tsukuba, Ibaraki 305-0801 Japan
Tel +81-29-864-5114 Fax +81-29-864-5560
Email: shomu@mail.kek.jp

Fritz-Haber-Institut der Max-Planck-Gesellschaft
Fritz-Haber-Institut Faradayweg 4-6 D-14195 Berlin

The Fritz-Haber-Institut der Max-Planck-Gesellschaft,
Berlin-Dahlem, Germany, invites applications for the post of a

Director

of a new department. The general research direction of the institute covers fundamental aspects of the physical chemistry of surfaces, interfaces and nanostructures. This includes the characterization of their structure, composition, dynamics, as well as the analysis and control of elementary processes. Basic research on heterogeneous catalysis currently plays an important role, together with other aspects of materials science (such as functional interfaces, photo-induced dynamics and biomolecules).

We are looking for an outstanding theoretical or experimental scientist working at the interface between physics and chemistry with the potential to become an eminent leader in the field and to set up and direct a new, successful department.

Applications will be reviewed immediately, and will be accepted until the position is filled. To apply, please send a CV to the office of the executive director (**gd_office@fhi-berlin.mpg.de,** see also **http://www.fhi-berlin.mpg.de/**). In case of questions, please contact the administrative general manager (Dr. von Helden, **g.helden@fhi-berlin.mpg.de**) or any of the four present Directors at the institute. The Fritz-Haber-Institut is an Equal Opportunity/Affirmative Action Employer. Female scientists are particularly encouraged to apply. In cases of equal qualifications, female candidates will be preferred.

CONFERENCE

AIDS 2014
20th International AIDS Conference
Melbourne, Australia
July 20-25, 2014
WWW.AIDS2014.ORG
STEPPING UP THE PACE

AIDS 2014 Late Breaker Abstract Submissions Open From 24 April 2014

The 20th International AIDS Conference welcomes submissions by emerging or established researchers for a late breaker abstract to one or more of the five scientific tracks between 24 April and 15 May 2014.

SUBMIT YOUR LATE BREAKER NOW!

www. AIDS2014.org

POSITIONS OPEN

CAREER OPPORTUNITY

Doctor of Optometry (O.D.) degree in 27 months for Ph.D.s in science and M.D.s. Excellent career opportunities for O.D./Ph.D.s and O.D./M.D.s in research, education, industry, and clinical practice. This unique program starts in March of each year, features small classes, and 12 months devoted to clinical care.

Contact the Admissions Office, **telephone: 800-824-5526** at the **New England College of Optometry, 424 Beacon Street, Boston, MA 02115.** Additional information at website: **http://www.neco.edu** or at **e-mail: admissions@neco.edu.**